FERMILAB-Proposal-845

**PROPOSAL TO FNAL**

# A DEDICATED BEAUTY EXPERIMENT FOR THE TEVATRON COLLIDER

J. Ellett, S. Erhan, D. Lynn, M. Medinnis, P. Schlein*), J Zweizig
University of California, Los Angeles, CA, U.S.A.

P. Weilhammer
CERN, Geneva, Switzerland

J. Seguinot, T. Ypsilantis
College de France, Paris, France

A. Czermak
Institute of Nuclear Physics, Cracow, Poland

K.T. Knöpfle, T. Kihm
Max-Planck Institute fur Kernphysik, Heidelberg, F.R.G.

T.Y. Chen, D. Xi
Nanjing University, Nanjing, P.R.C.

R. Dzhelyadin, V. Obraztsov, A. Ostankov
IHEP-Serpukhov, Protvino, U.S.S.R.

R. Harr, P. Karchin, C. Liapis, J. Sinnott
Yale University, New Haven, CT, U.S.A.

## Abstract

We propose a high statistics study of the physics of Beauty particles at the Tevatron $p\bar{p}$ Collider with a new dedicated detector which covers a 600 mrad forward aperture with magnetic spectrometers, RICH counters and electromagnetic calorimeters. The detector is triggered by real-time calculations on data obtained from a silicon micro-vertex detector installed inside the vacuum chamber throughout the interaction region. With $\int \mathscr{L} dt < 10\ pb^{-1}$, $\Delta M/\Gamma$ can be measured with an error of $\pm 0.1$ from the observed time oscillations in the decay of tagged $B_s$ mesons. With $\int \mathscr{L} dt \approx 200\ pb^{-1}$, rare branching fractions as small as $10^{-8}$ could be measured, although CP-Violation will only be accessible if the asymmetries are larger than about 30%.

*) Spokesperson

AR04863

## TABLE OF CONTENTS


1. **INTRODUCTION** 3

2. **PHYSICS GOALS** 5

   2.1 Overall Goals and Sensitivity to Rare Decay Channels 5
   2.2 $B_s$-Mixing (CP-Conserved) 6
   2.3 Simulation of $B_s$-Mixing Analysis 8
   2.4 Sensitivity of CP-Violation Search 12

3. **GEOMETRIC ACCEPTANCE** 14

4. **TRIGGERING & SIMULATION** 17

   4.1 Strategy 18
   4.2 Event Simulation 18
   4.3 Trigger Algorithm 19
   4.4 Trigger Performance and Expected Rates 20
   4.5 Pileup 21

5. **SPECTROMETER ELEMENTS** 21

   5.1 Silicon-Strip Microvertex Detector 22
   5.2 Vacuum Pipe 25
   5.3 Magnets 26
   5.4 Pixel Detectors 29
   5.5 Wire Chambers 30
   5.6 Ring Imaging Cherenkov (RICH) Counters 33
   5.7 Electromagnetic Calorimeter 38

6. **TRIGGER PROCESSORS & DETECTOR READOUT** 38

   6.1 Detector Readout System 39
   6.2 Level-1 Trigger Processor 41
   6.3 Level-2 Trigger Processor 45

7. **FLAVOR TAGGING: LEPTONS VS. KAONS** 45

8. **RECONSTRUCTION OF B-EVENTS, YIELDS & BACKGROUNDS** 48

   8.1 General Considerations and Lifetime Measurements 48
   8.2 $B_s$ Reconstruction; Signal Yields & Background Estimates 52
   8.3 Monte-Carlo Simulation and Analysis of RICH Counter Data 57
   8.4 Yields of Potential CP-Violating Channels 63

9. **DISCUSSION & COST ESTIMATES** 64

**APPENDIX A: Trigger Algorithm and Simulation** 66

**APPENDIX B: Liquid-Radiator RICH Resolution** 75

**APPENDIX C: Development and Test of a Large Silicon Strip System for a Hadron Collider Beauty Trigger (DRAFT – to be submitted to NIM).**

# 1. INTRODUCTION

One of the most challenging and important problems in high energy experimental physics is how best to study rare decays of Beauty particles as a probe of possible new physics beyond the Standard Model with three generations. We therefore propose a new detector dedicated to the study of B-physics (Beauty or Bottom) at the Tevatron proton-antiproton Collider.

The large cross section for $B\bar{B}$ production in hadronic interactions (e.g., 50 $\mu$barn at the Tevatron Collider and several hundred $\mu$barn at LHC and SSC), coupled with sophisticated trigger processor techniques should make possible the acquisition of enormous samples of exclusive Beauty decays at hadron colliding-beam machines. The dedicated Beauty experiment which we are proposing will allow us to make a detailed study of $B_s$ and $B_d$ mixing effects, the observation of final states with branching fractions as small as $1.7 \times 10^{-8}$ (10 events per $\int \mathscr{L} dt = 200\ pb^{-1}$), in addition to lifetime, mass and branching fraction measurements of the entire spectrum of Beauty particles. CP-Violation effects will be observable (at the $3\sigma$ level) at the Tevatron, only if the asymmetries are larger than about 0.5. Thus, the search for CP-Violation effects in Beauty decay at the Tevatron will likely only prepare the way for the next generation of experiments.

In order to allow our proposed experiment to be compared most simply, yet correctly, with other options, we give in Table 1 the few numbers and facts that are of essential importance. In the body of this proposal, we explain and justify the table entries.

*Table 1: Essential Characteristics[a] of This Proposed Experiment.*

| | |
|---|---|
| 1. $[\sigma(B\bar{B}) = 50 \cdot 10^{-2\cancel{7}\,30}\ cm^2] \times [\mathscr{L} = 10^{31}\ cm^{-2}s^{-1}]$ | $5 \cdot 10^{5\,2}\ s^{-1}$ |
| 2. Geometric Acceptance[a] | 23% or 46% |
| 3. Trigger Efficiency[b] | 20-45% |
| 4. Flavor Tagging Efficiency[c] | >35 % |
| 5. Reconstruction Efficiency[d] | 29-45% |
| 6. RICH Particle Identification ? | YES |
| 7. Electromagnetic Calorimetry ? | YES |

(a) The value for geometric acceptance depends on whether one or both forward spectrometer arms are instrumented. See discussion in Chapters 3 and 9.
(b) The trigger efficiency depends to some extent on the charged particle multiplicity of a B final state. See discussion in Chapter 4.
(c) The larger value applies to a $B_s$-Mixing experiment. See the discussion of tagging efficiency in Chapter 7.
(d) Reconstruction efficiencies are discussed in Chapter 8

For completeness, we compare the contents of Table 1 with the parameters of a new $e^+e^-$ "B-Factory". The product of our items 1,2 and 3 is $2.3 \times 10^4$ Hz, to be compared with the corrsponding result for an "idealized" $e^+e^-$ B-Factory, 10 Hz ($10^{34} \cdot 1$ nb) where, for the $e^+e^-$ case, we assume the maximum conceivable luminosity and assume acceptance and efficiencies are all 100%. It is also interesting to note that, in the next generation of pp colliders, the parameters for a hadron collider B-Factory of the type we propose give another factor of about 10 (cross section and increased acceptance from larger forward collimination).

To compare our proposed experiment with other collider options at the Tevatron, it is only necessary to compare the product of items 2, 3 and 4, since $\sigma \cdot \mathscr{L}$ will be the same for all such experiments. As explained in the following paragraphs and, in more detail, in Chapter 4 and APPENDIX A, our triggering approach is unique and does not rely on the inefficient use of lepton tags as triggers. Moreover, our extensive study of the possibilities of using charged kaons as flavor tags shows that they should be much superior to lepton tags.

The efficient triggering of heavy flavor in hadron machines was long thought to be "next to impossible". However, the success of Fermilab Experiment E691 and its successors in obtaining large clean samples of charmed particles has partly dispelled this "myth". Now, with a great deal of Monte-Carlo simulation work followed by a 3-month test experiment at the Sp$\bar{p}$S-Collider of a new type of collider microvertex detector[1] (see **APPENDIX C**), we have demonstrated that it should be possible to obtain large samples of fully reconstructed and tagged Beauty particles with minimal background.

The proposed experimental apparatus consists of a planar-silicon microvertex detector at the center of an interaction region, followed by dedicated large aperture forward spectrometer(s) installed on the outgoing beam pipes, with Ring-Imaging-CHerenkov (RICH) particle identification and electromagnetic calorimetertry. Event reconstruction is facilitated by information from the silicon microvertex detector, whose elements are installed perpendicular to and in close proximity to the circulating beams, inside the vacuum pipe and dispersed throughout the interaction region. A Level-1 trigger results from digital calculations based on the silicon data.

For the following reasons, we focus our attention in the forward directions of the p$\bar{p}$ system:

- The solid angle density of b and $\bar{b}$ quarks is considerably larger in the forward direction than elsewhere (see Chapter 3). Qualitatively, this arises because, far above threshold in the p$\bar{p}$ center of mass, the interacting partons tend to have increasingly unequal momentum.

- The momenta of B-mesons in the forward direction are much larger than at $90^0$. The decay products are therefore easier to track reliably and vertex and overall topology definition is improved. Thus, event reconstruction is enhanced. Calorimetric detection of $\gamma$'s also improves.

- Because of the relatively small solid angle coverage and planar geometry, design, construction and maintenance is easier and therefore less expensive.

- Heavy-flavored baryons (e.g., bud, cud, bcu, bsu, etc.) may be more easily produced and studied in the forward direction.

- The forward peaking of heavy flavor particles should be even more pronounced at the next generation of higher energy colliders, where the larger $b\bar{b}$ cross sections will eventually provide the yields required for CP-Violation studies. Thus, the proposed experiment would be a first example of an important class of future experiments and valuable expertise and experience would be obtained.

---

[1] A 43,000 channel silicon strip microvertex detector was run inside the Sp$\bar{p}$S vacuum pipe at 1.5 mm from the circulating beams. The observation of clean background-free events constitutes a major step in demonstrating that the silicon trigger discussed in this proposal will actually work.

ERRATUM



FERMILAB-Proposal-845

# 1. INTRODUCTION

One of the most challenging and important problems in high energy experimental physics is how best to study rare decays of Beauty particles as a probe of possible new physics beyond the Standard Model with three generations. We therefore propose a new detector dedicated to the study of B-physics (Beauty or Bottom) at the Tevatron proton-antiproton Collider.

The large cross section for $B\bar{B}$ production in hadronic interactions (e.g., 50 $\mu$barn at the Tevatron Collider and several hundred $\mu$barn at LHC and SSC), coupled with sophisticated trigger processor techniques should make possible the acquisition of enormous samples of exclusive Beauty decays at hadron colliding-beam machines. The dedicated Beauty experiment which we are proposing will allow us to make a detailed study of $B_s$ and $B_d$ mixing effects, the observation of final states with branching fractions as small as $1.7 \times 10^{-6}$ (10 events per $\int \mathscr{L} dt = 200\ pb^{-1}$), in addition to lifetime, mass and branching fraction measurements of the entire spectrum of Beauty particles. CP-Violation effects will be observable (at the $3\sigma$ level) at the Tevatron, only if the asymmetries are larger than about 0.5. Thus, the search for CP-Violation effects in Beauty decay at the Tevatron will likely only prepare the way for the next generation of experiments.

In order to allow our proposed experiment to be compared most simply, yet correctly, with other options, we give in Table 1 the few numbers and facts that are of essential importance. In the body of this proposal, we explain and justify the table entries.

*Table 1:* *Essential Characteristics[a] of This Proposed Experiment.*

| | |
|---|---|
| 1. $[\sigma(B\bar{B}) = 50 \cdot 10^{-30} cm^2] \times [\mathscr{L} = 10^{31}\ cm^{-2}s^{-1}]$ | $5 \cdot 10^2 s^{-1}$ |
| 2. Geometric Acceptance[a] | 23% or 46% |
| 3. Trigger Efficiency[b] | 20-45% |
| 4. Flavor Tagging Efficiency[c] | >35 % |
| 5. Reconstruction Efficiency[d] | 29-45% |
| 6. RICH Particle Identification ? | YES |
| 7. Electromagnetic Calorimetry ? | YES |

(a) The value for geometric acceptance depends on whether one or both forward spectrometer arms are instrumented. See discussion in Chapters 3 and 9.
(b) The trigger efficiency depends to some extent on the charged particle multiplicity of a B final state. See discussion in Chapter 4.
(c) The larger value applies to a $B_s$-Mixing experiment. See the discussion of tagging efficiency in Chapter 7.
(d) Reconstruction efficiencies are discussed in Chapter 8

For completeness, we compare the contents of Table 1 with the parameters of a new $e^+e^-$ "B-Factory". The product of our items 1,2 and 3 is 2 3. Hz, to be compared with the corrsponding result for an "idealized" $e^+e^-$ B-Factory, 10 Hz ($10^{34} \cdot 1$ nb) where, for the $e^+e^-$ case, we assume the maximum conceivable luminosity and assume acceptance and efficiencies are all 100%. It is also interesting to note that, in the next generation of pp colliders, the parameters for a hadron collider B-Factory of the type we propose give another factor of about 10 (cross section and increased acceptance from larger forward collimination).

To compare our proposed experiment with other collider options at the Tevatron, it is only necessary to compare the product of items 2, 3 and 4, since $\sigma \cdot \mathscr{L}$ will be the same for all such experiments. As explained in the following paragraphs and, in more detail, in Chapter 4 and APPENDIX A, our triggering approach is unique and does not rely on the inefficient use of lepton tags as triggers. Moreover, our extensive study of the possibilities of using charged kaons as flavor tags shows that they should be much superior to lepton tags.

The efficient triggering of heavy flavor in hadron machines was long thought to be "next to impossible". However, the success of Fermilab Experiment E691 and its successors in obtaining large clean samples of charmed particles has partly dispelled this "myth". Now, with a great deal of Monte-Carlo simulation work followed by a 3-month test experiment at the Sp$\bar{p}$S-Collider of a new type of collider microvertex detector[1] (see APPENDIX C), we have demonstrated that it should be possible to obtain large samples of fully reconstructed and tagged Beauty particles with minimal background.

The proposed experimental apparatus consists of a planar-silicon microvertex detector at the center of an interaction region, followed by dedicated large aperture forward spectrometer(s) installed on the outgoing beam pipes, with Ring-Imaging-CHerenkov (RICH) particle identification and electromagnetic calorimetertry. Event reconstruction is facilitated by information from the silicon microvertex detector, whose elements are installed perpendicular to and in close proximity to the circulating beams, inside the vacuum pipe and dispersed throughout the interaction region. A Level-1 trigger results from digital calculations based on the silicon data.

For the following reasons, we focus our attention in the forward directions of the p$\bar{p}$ system:

- The solid angle density of b and $\bar{b}$ quarks is considerably larger in the forward direction than elsewhere (see Chapter 3). Qualitatively, this arises because, far above threshold in the p$\bar{p}$ center of mass, the interacting partons tend to have increasingly unequal momentum.

- The momenta of B-mesons in the forward direction are much larger than at 90°. The decay products are therefore easier to track reliably and vertex and overall topology definition is improved. Thus, event reconstruction is enhanced. Calorimetric detection of $\gamma$'s also improves.

- Because of the relatively small solid angle coverage and planar geometry, design, construction and maintenance is easier and therefore less expensive.

- Heavy-flavored baryons (e.g., bud, cud, bcu, bsu, etc.) may be more easily produced and studied in the forward direction.

- The forward peaking of heavy flavor particles should be even more pronounced at the next generation of higher energy colliders, where the larger $b\bar{b}$ cross sections will eventually provide the yields required for CP-Violation studies. Thus, the proposed experiment would be a first example of an important class of future experiments and valuable expertise and experience would be obtained.

---

[1] A 43,000 channel silicon strip microvertex detector was run inside the Sp$\bar{p}$S vacuum pipe at 1.5 mm from the circulating beams. The observation of clean background-free events constitutes a major step in demonstrating that the silicon trigger discussed in this proposal will actually work.

In the body of this proposal we present details of the trigger design and detector which would furnish more than $10^7$ reconstructed B-Mesons per 200 pbarn$^{-1}$ integrated luminosity at the Tevatron Collider with $\sqrt{s}$ = 1.6 TeV. The actual number of reconstructed events obtained will depend on whether one or both collider arms are instrumented with spectrometers (the proposed silicon and trigger systems are bi-directional and will serve either situation). We emphasize that **all rate estimates in the proposal assume a two-arm spectrometer system, in order to demonstrate the full potential of the experiment.** See the discussion of this point in Chapter 9.

In Chapter 2 we discuss the physics goals of the experiment, in particular $B_s$-Mixing, and explain the "reach" of such an experiment at the Tevatron in studying CP-Violation and rare decay modes, if the experiment is run with sufficient priority.

Chapter 3 contains a discussion of the geometric acceptance of our proposed apparatus. In Chapter 4, we describe the trigger algorithm (see also Appendix A), which is based on real-time vertex calculations of silicon micro-vertex detector data. A Monte-Carlo simulation of the trigger is described and a performance summary is given.

Chapter 5 contains a detailed discussion of the various spectrometer elements. The silicon micro-vertex detector is also described in **APPENDIX C**, where results are given of a similar detector recently run at the Sp$\bar{p}$S-Collider. The large aperture forward detector consists of two coaxial spectrometers (2.5-100 mrad and 100-600 mrad, respectively), equiped with liquid and gas Ring-Imaging-CHerenkov (RICH) Counters. Complete electromagnetic calorimeter coverage of the spectrometer aperture would provide sensitivity for such final states as: $B_s \to D_s^* \to D_s\gamma$ and $B \to D^{0*} \to D^0\gamma$.

Chapter 6 describes how the silicon data will be analyzed in real time by a pipelined Data-Driven processor. The readout system stores event data from the spectrometer detectors in pipelined buffer memory while the processor is making a decision. A Level-2 trigger, which performs further analysis on the complete set of spectrometer data, is implemented with a large system of 50-MIPS RISC processors.

The problems of flavor tagging are dealt with in Chapter 7. Results from a Monte-Carlo simulation are given, which allow an evaluation of the relative effectiveness of lepton vs. charged kaon tagging.

Chapter 8 deals with the off-line reconstruction problems of Beauty-mesons in hadronic interactions. Results are given using reconstruction software written to analyze and find signals for different B decay modes in Monte-Carlo generated event samples. Quantitative estimates are given of the expected combinatoric background. The median momentum of detected and reconstructed B-mesons is about 45 GeV and the B proper time can be measured with a precision better than $\sigma_t/t$ = 6%. These facts allow excellent B-$\bar{B}_s$ oscillation studies to be made. Evaluations of the yields which can be expected for such an analysis and for a CP-Violation search are also given. A Monte-Carlo simulation of the analysis of RICH counter data is also given.

Finally, in Chapter 9, we discuss the desired time scale and present an estimate of the costs.

# *2. PHYSICS GOALS*

## *2.1 Overall Goals and Sensitivity to Rare Decay Channels*

Further major advances in our understanding of Beauty physics will come from experiments which produce very large samples of B-mesons and baryons, from which many different exclusive final states can be reconstructed with good mass resolution, good proper life time resolution and initial flavor tagging. Technical items are dealt with in the following chapters. Here, we simply point out that, with such data, the physics of both production and decay processes can be considerably clarified.

Analysis of the observed production processes will result in a much-needed understanding of the small-x gluon structure function of the proton. Studies of the spectroscopy of the entire series of B-mesons and baryons, including those which contain both b and c quarks (e.g., $b\bar{c}$, bcd, bcu, etc.) will also be possible. For example, reactions such as $B_c^- \rightarrow J/\psi\pi^-\pi^-\pi^+$ should be easily identifiable. Measurements of invariant masses and lifetimes of the entire spectroscopic array of states will be feasible.

The search for new physics beyond the 3-generation version of the Standard Model will be the main focus of future Beauty experiments. Unexpected values of branching fractions, mixing parameters in $B_s$ and $B_d$ decays and CP-Violation parameters will have great interest in this connection. Presumably the top mass will have been determined by the time our first results are available and will be used in making more stringent predictions that can be tested. If top has not yet been found, our results will be of even greater interest.

We now comment on the sensitivity we could expect to reach in our search for rare decay channels, if sufficient running time is given and the full (two-arms instrumented) detector is constructed. With a $b\bar{b}$ total cross section of 50 $\mu$barn at the Tevatron and an integrated luminosity, $\int\mathscr{L}dt = 200\ pb^{-1} = (10^{31}\ cm^{-2}sec^{-1} \cdot 10^7\ sec \cdot 2)$, a total of $10^{10}$ $b\bar{b}$ events are produced. The discussion below in Chapter 3 explains that, of these $10^{10}$ events, $\approx 6 \cdot 10^9$ B or $\bar{B}$ mesons will have all their decay tracks contained within the 600 mrad spectrometer apertures. From the discussions in Chapters 4 and 8 on triggering and event reconstruction, we estimate that the net triggering and reconstruction efficiency for a final state with all charged tracks is $\approx$10%. Thus, a mode with a branching fraction of about $1.7 \cdot 10^{-8}$ should yield 10 observed events. It is interesting to note that the new generation of pp colliders, with $b\bar{b}$ cross sections 5-10 times larger, with somewhat more forward collimation of B decay tracks and with somewhat larger usable luminosity may yield an additional factor of ten or so better sensitivity.

## *2.2 $B_s$-Mixing (CP-Conserved)*

We consider a prototype mixing measurement in which exclusive final states of the $B_s$, such as:

$$B_s^0 \rightarrow D_s^{*-}\pi^+\pi^+\pi^-\ , \quad D_s^{*-} \rightarrow D_s^-\gamma \tag{1}$$

are reconstructed and the proper decay time of each event is measured. The flavor of each B-Meson at production is "tagged" by observing a supplementary $K^\pm$ or $\ell^\pm$ in the spectrometer, as discussed in Chapter 7.

Four proper time distributions will be obtained from the reconstructed and tagged $B_s$ and $\bar{B}_s$ mesons:

$$T^+\ B_s(t) \tag{1}$$

$$T^-\ B_s(t) \tag{2}$$

$$T^+\ \bar{B}_s(t) \tag{3}$$

$$T^-\ \bar{B}_s(t) \tag{4}$$

where $T^+$ and $T^-$ denote the two charges of the possible tagging particles (e.g., $e^+$, $e^-$, $\mu^+$, $\mu^-$, $K^+$, $K^-$). Since a $B_s$ can be produced together with a $\bar{B}_u$, $\bar{B}_d$ or $\bar{B}_s$, the tagging particle can arise from any one of these. The latter two states are themselves subject to oscillation and can lead to the wrong sign tag, refered to in this document as "mis-tagging". Other sources of mis-tagging are, for example, background under the $B_s$ signal, other physics sources of the tagging particles, etc. Mis-tagging is estimated in Chapter 7.

In order to arrive at the equations which describe B decay time distributions (ignoring the possibility of CP violation), we start by expressing $B^0$ and $\bar{B}^0$ ($B_d$ or $B_s$) as the usual linear combination of mass eigenstates, $B_1$ and $B_2$:

$$|B^0> \; = [|B_1> \; + \; |B_2>] \; / \sqrt{2} \tag{5}$$

$$|\bar{B}^0> \; = [|B_1> \; - \; |B_2>] \; / \sqrt{2} \tag{6}$$

With the $B^0 \leftrightarrow \bar{B}^0$ transitions allowed by the second-order weak interaction, we have as the time-evolved state for an initial $B^0$:

$$\psi(t) = [e^{-iM_1t-\Gamma_1t/2} \cdot |B_1> \; + \; e^{-iM_2t-\Gamma_2t/2} \cdot |B_2>] \; / \sqrt{2} \tag{7}$$

Expanding $|B_1>$ and $|B_2>$ in terms of the observed $|B^0>$ and $|\bar{B}^0>$ states, and projecting out their amplitudes, we have as the probabilities to see $B^0$ and $\bar{B}^0$:

$$|<B^0|\psi(t)>|^2 \; = \; e^{-\Gamma t} \cdot [1 \; + \; \cos(\Delta Mt)] \; / \; 2 \tag{8}$$

$$|<\bar{B}^0|\psi(t)>|^2 \; = \; e^{-\Gamma t} \cdot [1 \; - \; \cos(\Delta Mt)] \; / \; 2 \tag{9}$$

In (8) and (9), $\Gamma \equiv \Gamma_1 \; = \; \Gamma_2$, because of the large phase space available in B decay, and $\Delta M \; = \; M_1 - M_2$.

Integrating Eqs. 8 and 9 over time, we find that the rates for no-oscillation and oscillation, respectively, go as $(2+x^2)/(1+x^2)$ and $x^2/(1+x^2)$, where $x \equiv \Delta M/\Gamma$. If we assume that a $B_s$ and its accompanying $\bar{B}$ decay independently and that only the time dependence of the $B_s$ is measured, the expressions which describe the tagged time distributions are given by Eqs. 8 and 9, multiplied by the appropriate time-averaged rate for the tag-providing $\bar{B}$. These products are shown in Table 2 for the four possible cases of tags, $T^+$ and $T^-$, with $B_s$ and $\bar{B}_s$, respectively, and for the two possible initial states.

Following the discussion on tagging in Chapter 7, we note that the $B_s$ decay time distributions for Final States 1-4 in Table 2 have the following simple forms if the initial states $B\bar{B}_s$ and $\bar{B}B_s$ occur with equal probability.[2]

$$T^+ \; B_s \;\; \text{or} \;\; T^- \; \bar{B}_s \quad : \quad A(t) \cdot e^{-t} \cdot [1 \; - \; K\cos(xt)] \tag{10}$$

$$T^+ \; \bar{B}_s \;\; \text{or} \;\; T^- \; B_s \quad : \quad A(t) \cdot e^{-t} \cdot [1 \; + \; K\cos(xt)] \tag{11}$$

$$\text{Untagged } B_s \text{ or } \bar{B}_s \quad : \quad A(t) \cdot e^{-t} \tag{12}$$

In these formulae the mixing parameter, $x \; = \; \Delta M/\Gamma$ and $t$ is the $B_s$ proper lifetime in units of mean life. K is the net "dilution" factor which results from all types of mis-tagging and decreases the amplitude of the oscillation from the value it would have were the flavor of the decaying B always correctly determined. A(t) is the acceptance function discussed in Chapter 8.

If the initial states $B\bar{B}_s$ and $\bar{B}B_s$ do not occur with equal probability, it may be seen from the entries in Table 2 that Final States 1 and 3 will have identical magnitudes for K (but opposite sign), and Final States 2 and 4 will also have identical values. For example, if initial state $B\bar{B}_s$ has probability $\alpha$ and $\bar{B}B_s$ has probability $(1-\alpha)$, it can be seen that the experimental value of K should depend on $\alpha$ in

[2] We note that this may not be the case in pp interactions and in $p\bar{p}$ interactions when the $B_s$ are produced away from small Feynman-x. A possible asymmetry in $B_s$ and $\bar{B}_s$ production due to valence quark effects has relevance to the study of CP-Violation asymmetries and must be understood empirically. This physics of the production process is also of interest in its own right.

*Table 2:* *Joint Time-Integrated, Time-Dependent Rates*[a,b,c]

| Final State | Initial State $B\bar{B}_s$ | Initial State $\bar{B}B_s$ | Equal Sum |
|---|---|---|---|
| (1) $T^+ B_s(t)$ | $(2+x^2)\cdot[1-\cos]$ | $x^2\cdot[1+\cos]$ | $1-[1/(1+x^2)]\cdot\cos$ |
| (2) $T^- B_s(t)$ | $x^2\cdot[1-\cos]$ | $(2+x^2)\cdot[1+\cos]$ | $1+[1/(1+x^2)]\cdot\cos$ |
| (3) $T^+ \bar{B}_s(t)$ | $(2+x^2)\cdot[1+\cos]$ | $x^2\cdot[1-\cos]$ | $1+[1/(1+x^2)]\cdot\cos$ |
| (4) $T^- \bar{B}_s(t)$ | $x^2\cdot[1+\cos]$ | $(2+x^2)\cdot[1-\cos]$ | $1-[1/(1+x^2)]\cdot\cos$ |

(a) To simplify the reading of this table, a common factor $e^{-\Gamma t}/(1+x^2)$ is suppressed in all terms in columns 2 and 3, as is the argument, $(\Delta Mt)$, from all cosine functions.
(b) The B or $\bar{B}$ decay which provides the tagging particle is time-integrated. The $B_s$ decay is time-dependent. Throughout this table, $x = \Delta M/\Gamma$ for the tagging B or $\bar{B}$, whereas the argument of the cosine function is for the $B_s$.
(c) In this table, the tagging particles are assumed to be secondary $K^\pm$ or leptons. They give the flavor of the B or $\bar{B}$ at time of decay (e.g., $K^+$ or $\ell^+$ result from a B, whereas a $K^-$ or $\ell^-$ result from a $\bar{B}$).

the following way (for fixed value of x):

$$T^+ B_s \text{ or } T^+ \bar{B}_s \quad : \quad K^+ = \pm[-2\alpha+(1-2\alpha)x^2]/[2\alpha+x^2] \tag{13}$$

$$T^- B_s \text{ or } T^- \bar{B}_s \quad : \quad K^- = \pm[2(1-\alpha)+(1-2\alpha)x^2]/[2(1-\alpha)+x^2] \tag{14}$$

Fig. 1 shows how K depends on $\alpha$ for both types of final states and for $x = 0.7$ and 10, respectively. An observed value of K will, of course, be a weighted average over the three contributing values of x. The effective dilution factors for different types of tags can be directly measured by studying the tags which occur with $B^\pm$ production, where the identity of a valid tag is known.

## *2.3 Simulation of $B_s$-Mixing Analysis:*

In order to demonstrate how the expected statistical significance in the determination of $x = \Delta M/\Gamma$ depends on sample size, we have generated Monte-Carlo data samples and subjected them to joint Maximum-Likelihood fits with x, $\tau$ and K as free parameters.

Event sample decay times are generated according to the distributions of Eqs. (10-11) in Section 2.2. The acceptance function is taken to be our empirical form, $A(t) = 4t^2/(1+4t^2)$, as explained in Chapter 8. We use a value of the tagging dilution constant, $K = 0.34$, which is somewhat smaller than the value 0.4 estimated in Chapter 7, to allow for Cherenkov identification efficiencies and background.

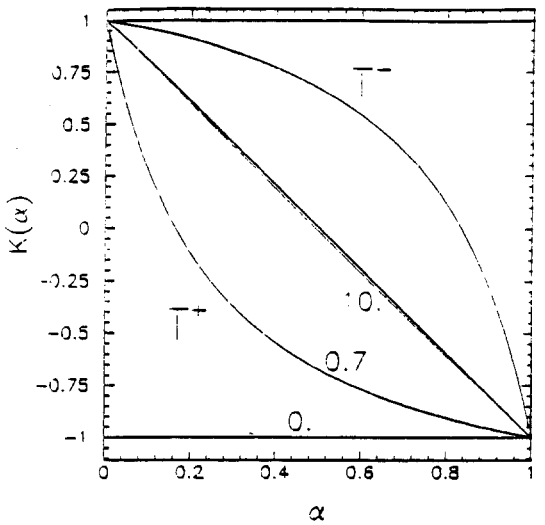


*Figure 1: Dependence Of $K^+$ and $K^-$ On $\alpha$ For Three Values Of x.* The lower left contains Eq. 8 evaluated for the three indicated values of x. The upper right contains Eq. 9 evaluated for the same values of x. The superscripts on $T^+$ and $T^-$ refer to the signs of the tagging particles.

Monte-Carlo calculations show that background is associated with B events and thus that it has an exponential proper time dependence with the same lifetime as the signal. With this assumption, the only effect of the background is to dilute the oscillation amplitude and thus reduce K. For each data sample, we also generate a sample of decay times for the corresponding sample of untagged $B_s$ (Eq. 12 is in Section 2.2) assuming, as discussed in Section 8.2, that the fraction tagged is 35%.

A simultaneous Maximum-Likelihood fit was then made to an entire data sample using, for each event, the relevant Equation (10), (11) or (12). For example, the Likelihood function for a $B_s$ tagged with a $T^+$ is:

$$\mathcal{L} = \frac{A(t) \cdot e^{-t} \cdot [1 - K\cos(xt)]}{\int A(t) \cdot e^{-t} \cdot [1 - K\cos(xt)]\, dt}$$

The sum of $-\log \mathcal{L}$ for all events is minimized using the program MINUIT.

Figs. 2(a-h) show typical generated distributions for samples of 5000 tagged events, generated at each of the x values: 0.7, 5, 10 and 15. The curves resulting from the joint Maximum-Likelihood fits are also shown for each case. Table 3 shows the fitted values of x. The following paragraphs show that a successful experiment could be performed with far fewer events.

We now investigate the dependence of the quality of the results on sample size. The parameters which best indicate the sample size required for a good measurement of $B_s$ mixing are the error in the mixing parameter ($\sigma_x$) and the significance of the oscillation amplitude ( $N_\sigma$ = K divided by the error in K). These two quantities are plotted in Fig. 3 as a function of the number of events for a fixed K value of 0.34 and an x value of 15.

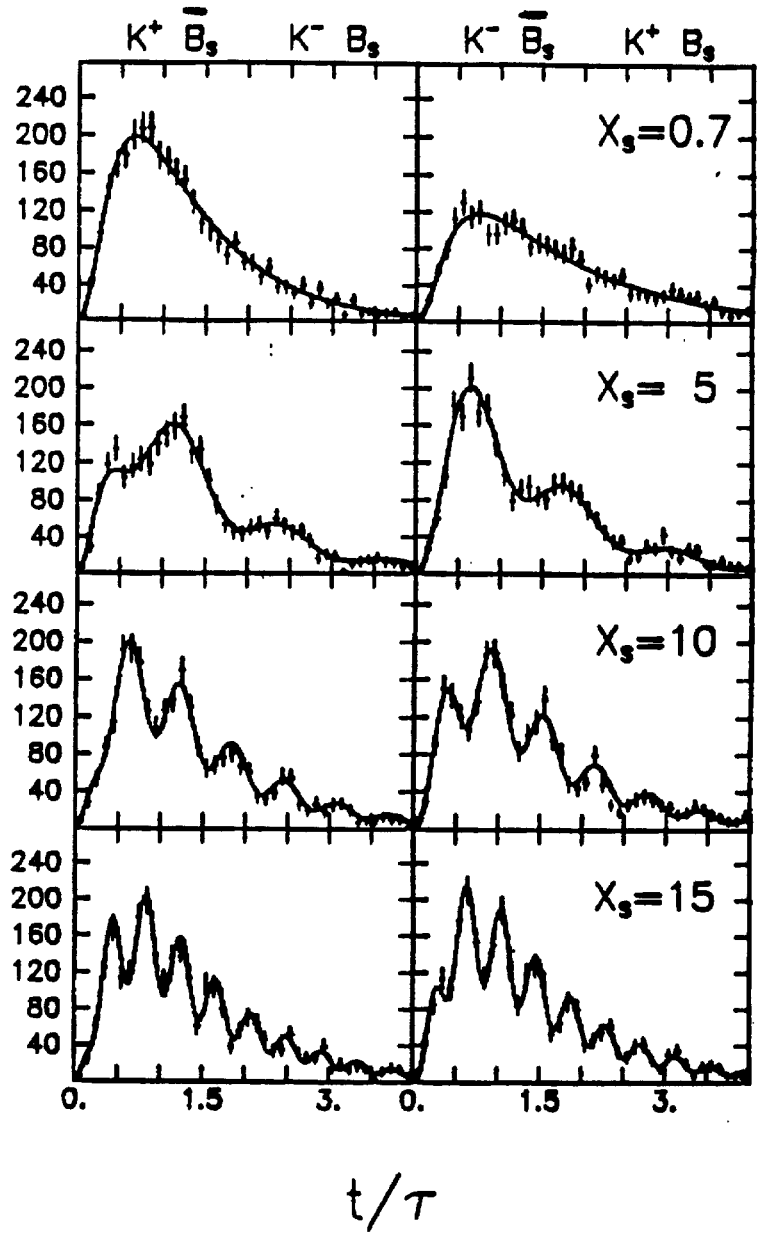


*Figure 2:* Proper time distributions for the two types of tagged events, according to Eqs. (6-7); (a,b) x = 0.7, (c,d) x = 5, (e,f) x = 10, (g,h) x = 15. The Monte-Carlo data points correspond to a sample of 5000 tagged events, as discussed in the text. The curves result from simultaneous Maximum-Likelihood fits to the data shown and the proper time distribution of the corresponding untagged sample.

We next try to find the minimum event sample size which will allow a significant measurement of the mixing parameter. We investigated the uniqueness of the solution by studying the log-Likelihood function vs. x for a large number of generated Monte-Carlo "experiments" for each sample size. Fig. 4 shows typical examples of the resulting curves. In Fig. 4(a), a typical (bad) example of the result is shown for a sample of 150 tagged events. It is obviously not possible to obtain reliable results with

*Table 3:* $x = \Delta M/\Gamma$ *Values Obtained From Fits Shown In Figs. 2*

| Input x Value | Fitted x |
|---|---|
| 0.7 | 0.70 ± 0.05 |
| 5.0 | 4.99 ± 0.03 |
| 10.0 | 9.96 ± 0.03 |
| 15.0 | 14.93 ± 0.03 |

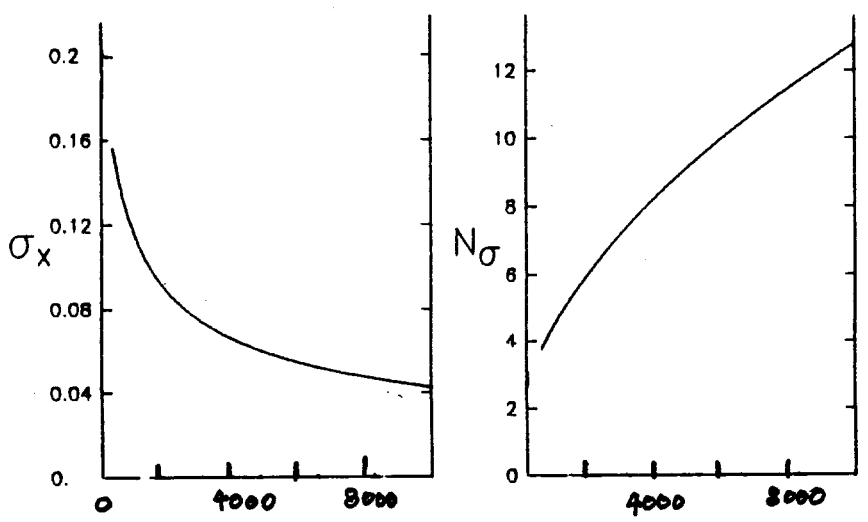


*Figure 3:* (a) Error on the mixing parameter ($\sigma_x$) vs. the number of $B_s$ signal events. (b) The significance (in standard deviations) of the oscillation amplitude (K) vs. the number of $B_s$ signal events.

such a small sample. For comparison, Figs. 4(b,c,d) show typical log-Likelihood functions plotted vs. x for tagged sample sizes of 300, 600 and 1700 events, respectively. We conclude that a sample size of about 1000 tagged events is the smallest sample size from which a meaningful result could be obtained. A run planned for 4000 tagged events should therefore allow a sufficient safety margin.

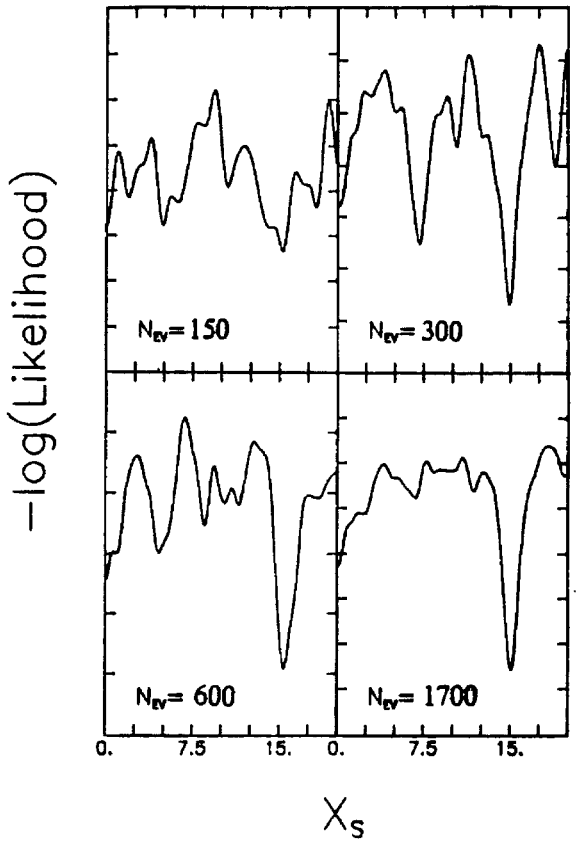


*Figure 4:* *– Log-Likelihood Function vs. x: The data samples of* 150, 300, 600 and 1700 events were all generated with x = 15. In each case, the distributions are typical examples from a study of 20 Monte-Carlo experiments.

## *2.4 Sensitivity of CP-Violation Search*

We consider a prototype of future CP-Violation measurements. The larger $b\bar{b}$ cross section and increased forward collimation expected at the next generation of machines will likely be needed to achieve the desired sensitivity to CP-Violation effects. Nonetheless, it is interesting to estimate the "reach" of such an experiment at the Tevatron Collider. We have studied the sensitivity of the proposed apparatus to a measurement of a CP-Violation asymmetry in the decay:

$$B^0_d \rightarrow J/\psi\, K_s \tag{15}$$
$$\bar{B}^0_d \rightarrow J/\psi\, K_s \tag{16}$$

Allowing for CP-Violation, the time dependences of the decay of $B_d$ and $\bar{B}_d$ into this CP eigenstate are:

$$N(B_d \rightarrow J/\psi K_s) \approx A(t) \cdot e^{-t} \cdot [1 - \sin(2\beta) \cdot \sin(xt)] \tag{17}$$
$$\bar{N}(\bar{B}_d \rightarrow J/\psi K_s) \approx A(t) \cdot e^{-t} \cdot [1 + \sin(2\beta) \cdot \sin(xt)] \tag{18}$$

where t is the proper time measured from production in units of the mean B life time, $\beta$ is an angle in the unitarity triangle and $x = \Delta M/\Gamma$ for the B (or $\bar{B}$) at production. A(t) is the detector acceptance function discussed in Chapter 8.

These time dependences imply a time-dependent asymmetry in the decay: $(\bar{N} - N)/(\bar{N} + N)$. In order to measure this asymmetry, it is necessary to tag the flavor of the B at production using the techniques described in Chapter 7. When inaccuracies inherent in the tagging are taken into account, the observed asymmetry takes the form:

$$A_{obs} = K \cdot \sin(2\beta) \tag{19}$$

where K is the net "dilution" factor, which differs from unity due to imperfect tagging, as discussed in Chapter 7.

A Monte-Carlo study was performed to determine the event sample size required to observe a given statistical significance in a measurement of a CP-Violation asymmetry. For example, Fig.s 5(a,b) show the proper time distributions for 2100 Monte-Carlo events (beyond the reach of a Tevatron experiment) each of Reactions 15 and 16, respectively, generated assuming $\sin(2\beta) = 0.20$, $x = 0.7$, a net dilution factor, $K = 0.47$, and an empirical acceptance function A(t). The curves shown are the result of a Maximum-Likelihood fit for $\sin(2\beta)$ of Eqs. 17 and 18 jointly to the data in Figs. 5(a,b). The value found is $\sin(2\beta) = 0.176 \pm 0.044$ ($4\sigma$ significance). Fig. 5(c) superimposes the two fitted curves from Figs. 5(a) and (b). The maximum deviation occurs at 2.2 mean lives, corresponding to an argument of $\pi/2$. in $\sin(xt)$, when $x = 0.7$.

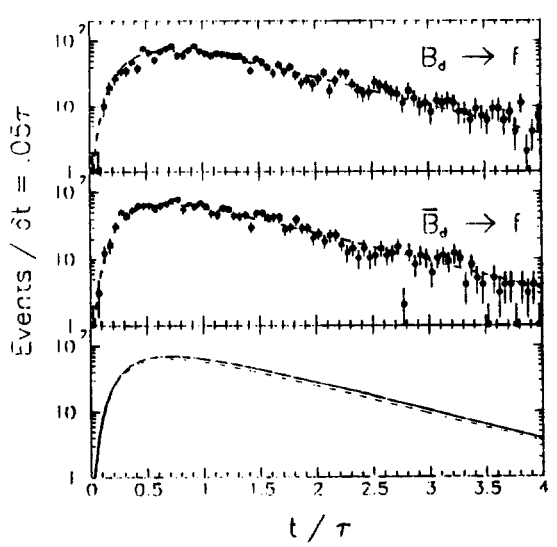


*Figure 5: Monte-Carlo Study of CP-Violation Effects in $B_d$ Decay.* (a) Proper time distribution of 2100 examples of Reaction 15 (beyond the reach of a Tevatron experiment). Fitted curve is Eq. 17; (b) Same for 2100 examples of Reaction 16. Curve is Eq. 18; (c) The two fitted curves from (a,b) are superimposed.

Fig. 6 shows the total sample sizes of tagged B and $\bar{B}$ required to observe a $3\sigma$ or a $4\sigma$ asymmetry effect as a function of $\sin(2\beta)$, assuming a net dilution factor of 0.47. As will be seen in the discussion

of yield estimates in Chapter 8, we may expect a total of only about 150 reconstructed tagged examples of Reactions (15) and (16) from runs with total $\int \mathscr{L} dt = 200\ pb^{-1}$. Thus a $3\sigma$ asymmetry effect could only be observed if $\sin(2\beta) > 0.3$.

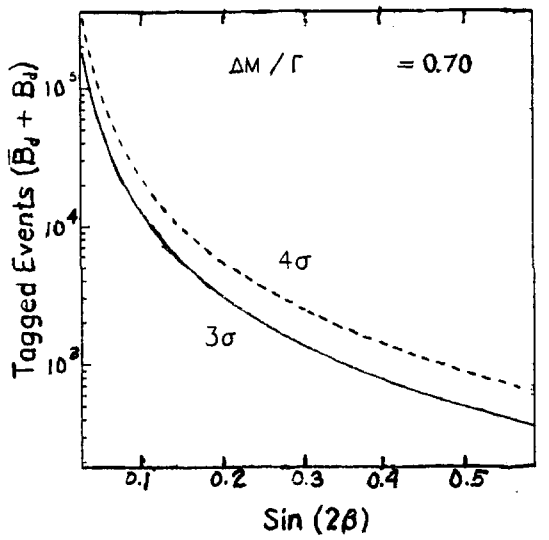


*Figure 6: Total Tagged B and $\bar{B}$ Events Required for $3\sigma$ and $4\sigma$ Effects.* Required number of tagged events is plotted vs. $\sin(2\beta)$, assuming K = 0.4.

## 3. GEOMETRIC ACCEPTANCE

Fig. 7 shows the angular distribution in the laboratory of decay tracks from B-Mesons generated via gluon-gluon fusion for $\sqrt{s} = 1.6$ TeV $p\bar{p}$ interactions using the PYTHIA Monte-Carlo program.[3] A major fraction of the Beauty signal is found in the forward direction.[4]

We have attempted to design a forward spectrometer which has the largest angular aperture consistent with uniform planar geometry. We find that, for apertures larger than about 600 mrad, detector complications and costs rise more rapidly than the benefits. We therefore choose $\theta_{max} = 600$ mrad for our proposed detector. The spectrometer which satisfies the aperture requirements discussed here and has the planar geometry required for minimal complexity is shown in Fig. 8. The spectrometer elements are described in Chapter 5.

Table 4 shows the geometric acceptance of a two-arm 600 mrad spectrometer system at $\sqrt{s} = 1.6$ TeV. All decay tracks of 30% of all B mesons produced are fully contained in the system; 30% of all $\bar{B}$ mesons are fully contained and there is a 14% overlap in which both B and $\bar{B}$ are contained. Thus, in 46% of all $B\bar{B}$ events produced, either B or $\bar{B}$, or both, are accepted. It may also be stated that, if

[3] H.-U. Bengtsson, G. Ingelman, Comput. Phys Commun. 34 (1985) 251; H.-U. Bengtsson, T. Sjostrand, Comput. Phys Commun. 46 (1987) 43.

[4] It has been pointed out by DeRujula [private communication] that the observed angular distributions may be even more sharply forward peaked than seen in Fig. 7, due to contributions from other than the low order QCD processes used in the generation of both PYTHIA and ISAJET.

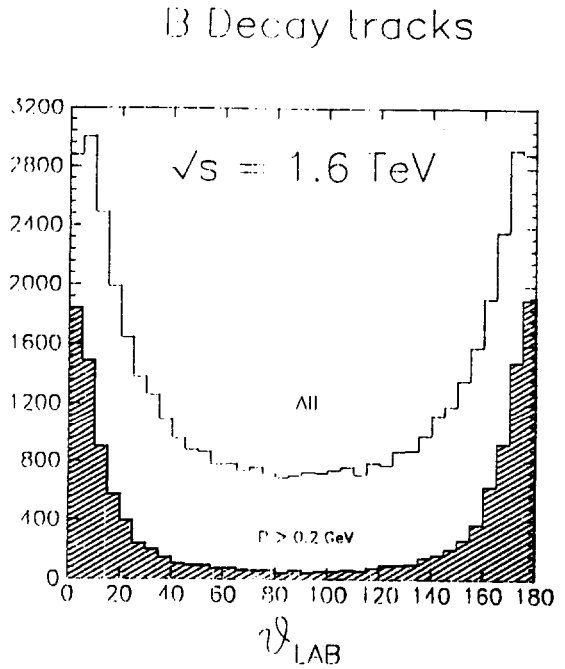


*Figure 7: $\theta_{lab}$ of B Meson Decay Tracks Generated at $\sqrt{s}$ = 1.6 TeV Using PYTHIA.* **Shaded:** Tracks from those B events which have all decay track momenta greater than 200 MeV.

N $B\bar{B}$ events are produced, one will find 0.60 N fully accepted B or $\bar{B}$ final states.

Of those events with a B fully contained in the spectrometer, 14/30 = 47% also have the $\bar{B}$ similarly contained. The same is also true for the $\bar{B}$. However, as discussed in Chapter 7, flavor tagging can be accomplished more efficiently using single particles, rather than trying to fully reconstruct the tag-providing B (or $\bar{B}$).

**Clearly, if only a single arm spectrometer is constructed, there is a 50% loss of all events, since presumably B and $\bar{B}$ mesons are rarely produced in opposite hemispheres. No fundamental loss in physics would result.**

An additional contribution to the geometric acceptance comes from the minimum angle cutoff, $\theta_{min}$, and the resultant loss of particles in the beam pipe. Such acceptance losses increase at larger Feynman-$x_F$ values. With a vacuum pipe of diameter of 2.5 cm and a window at z = 5 m from the interactions, we have a $\theta_{min}$ of 2.5 mrad, with detector sensitivity for $\theta$ > 5 mrad. This would result in a loss of less than 10% of the events contained within the 600 mrad aperture.

Fig. 9 shows the momentum distribution of all B-mesons generated by PYTHIA at $\sqrt{s}$ = 1.6 TeV. The shaded histogram is the distribution for those mesons whose laboratory angle, $\theta$, is less than 600 mrad. Finally, the solid histogram shows the momentum of B-mesons which have all decay tracks contained within the 600 mrad aperture.

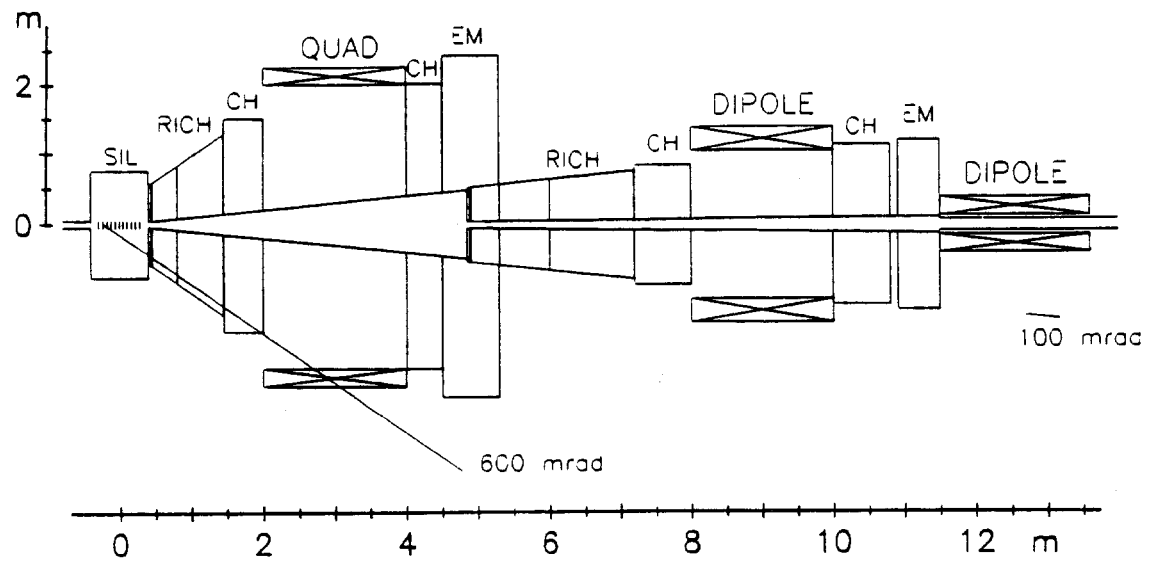


*Figure 8: Layout of one Forward Beauty Spectrometer.* The silicon microvertex system is installed inside the Tevatron vacuum pipe at the center of the interaction region. The large and small dipole magnets in the spectrometer, together with two dipole magnets on the opposite arm provide beam compensation.

*Table 4:* *Two-Arm Geometric Acceptance[a] for B and $\bar{B}$ Mesons*

| | B yes | B no |
|---|---|---|
| $\bar{B}$ yes | 14% | 16% |
| $\bar{B}$ no | 16% | 54% |

(a) Gluon-gluon fusion calculation by PYTHIA for $p\bar{p}$ interactions at $\sqrt{s}$ = 1.6 TeV. B-mesons are considered accepted if all decay tracks fall within the 600 mrad aperture of either collider arm. $\theta_{min}$ of the spectrometer is chosen to cause less than 10% additional loss of these events.

In Fig. 9, the fall-off in the accepted momentum spectrum below ≈40 GeV is an aperture effect. We note that the median momentum of accepted B mesons is ≈45 GeV or so, corresponding to a Feynman-x of 0.06. Thus, even though the spectrometers cover forward apertures, they are still sensitive to a major fraction of B mesons produced in the dominant small-x region.

Finally, we note that the mean flight path, $D = c\tau(p/m)$, is approximately 1 mm per 15 GeV momentum. Therefore, the median B momentum of about 45 GeV corresponds to a typical flight path for our reconstructed B sample of about 3 mm. Since the resolution in this quantity is better than 0.2 mm, as discussed below in Section 8.1, excellent proper time measurements can be made.

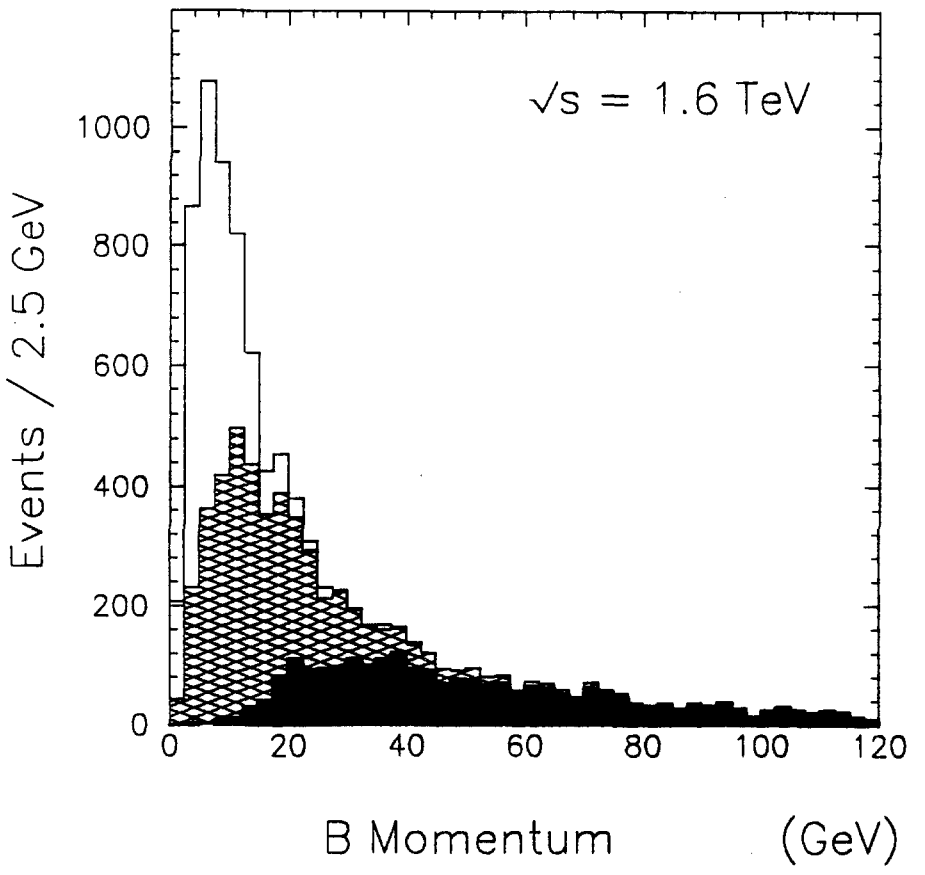


*Figure 9: Momentum Distributions of B-Mesons.* **Unshaded:** All B-mesons generated according to PYTHIA **Shaded:** Those with laboratory $\theta$ < 600 mrad. **Solid:** Those B-mesons which have all decay tracks contained within the 600 mrad aperture. The B flight path is about 1 mm per 15 GeV momentum.

## *4. TRIGGERING & SIMULATION*

The overall strategy of the trigger is to use only the silicon information to search for events which are inconsistent with having a single vertex. Before deciding on this strategy, we looked for other properties of Beauty events which would allow a more rapid and easier-to-implement trigger, such as increased transverse momentum, higher mass in the forward direction or the presence of a high transverse momentum electron. We were unable to find any such cut which does not also entail an unacceptable loss in efficiency for Beauty events.

## *4.1 Strategy*

At the Tevatron, the ratio of the $p\bar{p}$ total inelastic cross section of about 60 mb to the $b\bar{b}$ production cross section of about 50 $\mu$b is $\approx$1200/1. This indicates the required level of minimum bias suppression. Most of this suppression is accomplished on-line with a combination of Level-1 and Level-2 trigger processors, as discussed below. Monte-Carlo studies have shown that the remaining background can be suppressed by detailed topology cuts and offline Cherenkov analysis.

Although all detectors will be gated with each 395 ns bunch crossing, the readout cycle will be executed only for those crossings for which a "Level-0" trigger occurs. Level-0 is an interaction pretrigger which selects those bunch crossings that contain a $p\bar{p}$ interaction. This avoids having to read out all detectors with each bunch crossing.

The geometry of the silicon detector is described in Section 5.1. Here we simply note that there are 16 or more planes installed inside the vacuum pipe perpendicular to the beam line, with a small gap (e.g., 3 mm) through which the circulating beams pass. Each plane is divided into four quadrants and there is x and y readout of each. Because the silicon trigger algorithm is executed in real time, the silicon data must be read out as rapidly as possible. This leads us to "sparsify" on-board the detector and read out only digital information of the "hit" silicon strips.

The overall strategy of the Level-1 trigger is to use the silicon digital information to search for events which are inconsistent with having a single vertex. This is clearly a much weaker condition than requiring the presence of a nearby secondary vertex. However, it is found that a sufficiently large suppression of the minimum bias background can be obtained to allow efficient transfer of accepted events to a system of parallel processors. Moreover, the algorithm described below is sufficiently concise to allow straight-forward implementation in a Level-1 hardware trigger processor.

## *4.2 Event Simulation*

Since the effectiveness of the trigger in suppressing the minimum bias background events is such an important aspect of the proposed experiment, the problem has been studied in considerable detail. Using the CERN program GEANT,[5] complete simulations were made of the silicon detector response to PYTHIA-generated minimum bias, inclusive Beauty and Charm events. As a check of the PYTHIA generation, minimum bias events generated at $\sqrt{s}$ = 0.63 TeV were found to agree well with UA5 results[6] on minimum bias physics at the Sp$\bar{p}$S.

Following this, a trigger algorithm was created and tuned (at the Sp$\bar{p}$S energy) on Monte-Carlo data samples, to yield large suppression of minimum bias events while maintaining high trigger efficiency for Beauty events. A detailed discussion of this algorithm is found in **APPENDIX A.** This algorithm has been applied without fundamental modification to Tevatron events and its performance is discussed in Section 4.4.

There is little change in the performance of this algorithm between $\sqrt{s}$ = 0.63 and 1.6 TeV. This may be understood with reference to Table 5, which shows various quantities which characterize the event properties in the silicon. The character of the silicon data is seen to change only modestly over the larger energy range 0.63 to 16.0 TeV. The cluster density in a silicon quadrant only doubles over that large energy range.

---

[5] R. Brun, F. Bruyant, M. Maire, A.C. McPherson, P. Zanarini "Geant3", CERN report DD/EE/84 – 1, September 1987.

[6] G.J. Alner et al. (UA5 Collaboration), Physics Reports 154 (1987) 247.

*Table 5:* *Properties of Silicon Data for Minimum Bias Events From PYTHIA & GEANT.*

| | | |
|---|---|---|
| Center-of-Mass Energy, $\sqrt{s}$ (LHC & SPS) | 16.0 TeV | 0.63 TeV |
| Average No. Clusters Per Quadrant | 5.6 | 2.8 |
| Average No. Strips Hit Per Quadrant | 9.2 | 4.8 |
| Cluster Width (Strips) | 1.3 | 1.3 |
| Point Resolution | 7.6 $\mu$m | 7.6 $\mu$m |
| First Vertex Resolution (see Sec. 4.3) | 0.8 mm | 0.8 mm |

*) Silicon strip width is assumed to be 25 $\mu$m. The silicon thickness is 250 $\mu$m.

## *4.3 Trigger Algorithm*

The general strategy of the trigger algorithm is as follows:

- **The geometric centers of strip clusters are taken as "points".**
- **Line-Finding:** Lines are found in all sets of three consecutive planes using a road width of one silicon strip. Track projections which multiple scatter more than this tend not to be used in the trigger calculations ($p > 2$ GeV).
- **Duplicate Rejection:** If a single track was found in more than one detector triplet (this will occur whenever a particle traverses more than three detectors in a single view) the duplicate entries are removed from the list of tracks. In each such case, only the track defined by the first three planes the track traverses will be retained.
- **Vertex z Estimation:** The z position of the vertex is estimated by projecting all the found track projections to $x=y=0$. The resulting z positions are histogrammed, and the vertex is assumed to be at the peak bin.
- **Bad Track Removal:** All track projections are demanded to have an impact parameter of less than 1 mm. Most tracks which fail this cut are fake, mis-measured, or from strange particle decay (the great majority of tracks from beauty or charm decays have much smaller impact parameters). A large number of tracks failing this cut indicates a pileup event.
- **Vertex Calculation:** A new vertex position is calculated which minimizes the sum of the squares of error weighted impact parameters for all the remaining track projections. If the $\chi^2$ is

less than some cut value, the event will be considered to contain only a single primary vertex, and will thus be rejected by the trigger.

- **Worst Track Rejection:** If the $\chi^2$ is greater than the cut value, the track list is searched for the track with the largest contributing term. That track is then removed from the list, and the vertex calculation step is repeated. If the $\chi^2$ test still fails after two tracks have been removed, the event is assumed to have a secondary vertex.

The implementation of this trigger algorithm in hardware is discussed in Chapter 6.

## *4.4 Trigger Performance and Expected Rates*

As mentioned above, the Level-1 trigger algorithm, which was initially created and developed for the Sp$\bar{p}$S, has been applied without fundamental modification to Tevatron events. Fig. 10 shows, as a function of the $\chi^2$-cut value, the fractions of minimum bias events and events containing B-mesons which decay into two specific exclusive final states (accepted by the 600 mrad spectrometer) which survive the trigger algorithm. A $\chi^2$ cut of about 30 gives a suppression of 1/100 for minimum bias events while retaining between 25% and 50% of the B events (depending on final state multiplicity). In our simulations for the Sp$\bar{p}$S, we obtained a trigger efficiency of 1% for charm and complete offline rejection of these events. At the Tevatron, we estimate the charm trigger efficiency will be ≈2%.

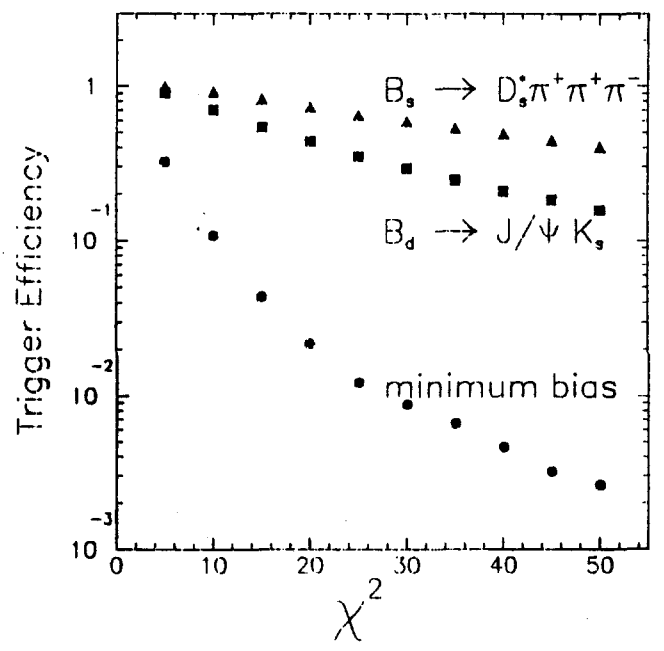


*Figure 10: Trigger Efficiency vs. $\chi^2$-Cut Value.* The fraction of events at the Tevatron which survive the Level-1 trigger algorithm. This quantity is shown for minimum bias events and the exclusive final states $B \rightarrow D^* \pi\pi\pi$ and $B \rightarrow J/\psi K_s$.

In order to estimate the trigger rates, we take a luminosity, $\mathscr{L} = 10^{31}$ cm$^{-2}$s$^{-1}$. Assuming $\sigma_{inelastic} = 60$ mb, $\sigma(c\bar{c}) = 3$ mb and $\sigma(b\bar{b}) = 50\ \mu$b, and using trigger efficiencies of 1/100, 1/50 and 1/5 (for minimum bias and inclusive $c\bar{c}$ and $b\bar{b}$, respectively), we arrive at Level-1 trigger rates of 6.0 KHz, 0.6 KHz and 0.1 KHz, respectively, or a total of 6.7 KHz. These events will be passed to a system of high performance parallel processors for the Level-2 trigger, in which a search will be made for events with multiple vertices. For the Level-2 trigger implementation, it will take a system with ≈670 50-MIPS processors to keep up with the Level-1 trigger rate, assuming an average of 0.1 sec to perform the Level-2 trigger.

### *4.5 Pileup*

With $\sigma_{inelastic} = 60$ mb, $\mathscr{L} = 10^{31}$ and the planned RF structure for the 36-bunch running mode in 1994, 16.5% of all inelastic interactions will be accompanied by one or more additional inelastic interactions in the same bunch crossing, for a total pileup rate of 99 kHz. As part of our trigger study for the Sp$\bar{p}$S-Collider (see APPENDIX A), the Level-1 trigger suppression for pileup was estimated by superimposing Monte-Carlo generated events, and passing them through the simulation software package. We found a suppression factor of 1/60. Since the interaction region size at the Tevatron is significantly longer than at the Sp$\bar{p}$S, the suppression will be even larger at the Tevatron and the Level-1 trigger rate from pileup should be smaller than 1.6 KHz. Since this rate is relatively small, compared to the 6.7 KHz event rate calculated in Section 4.4, the conclusions of that section are not modified. We have found in our Monte-Carlo studies that there is no difficulty rejecting pileup events during the offline analysis.

## *5. SPECTROMETER ELEMENTS*

A single arm of the forward Beauty detector, shown in Fig. 8, with aperture $2.5 < \theta < 600$ mrad. The angular acceptance of Spectrometer 1 is 100-600 mr, and of Spectrometer 2, 2.5-100 mr. The fractional solid angles ($\Delta\Omega/4\pi$) are 8.3% and 0.3%. In this chapter, we give detailed descriptions of the following components:

- **Silicon-strip microvertex detector;** installed at the center of the interaction region inside the vacuum chamber. Matches the forward spectrometer system and has a geometry typical of fixed-target experiments with its planes perpendicular to the circulating beams.

- **Vacuum pipe:** contains the circulating beams and passes through the various detector components. It is made of two thin windows connected by conical sections.

- **Magnets:** Spectrometer 1 contains a normal-conducting quadrupole magnet with 2 m radius. Spectrometer 2 contains a superconducting dipole with a uniform magnetic field of 2.5 Tesla and without a septum plate.

- **Pixel Devices:** Used to match the two views of the silicon tracks and to aid in connecting these with tracks found in the spectrometers. A Silicon Pad Detector is installed inside the beam pipe and the first detector elements in both spectrometers are "Pixel Drift" Chambers.

- **Wire chambers:** Chambes with jet-type drift cells are used to measure the position and direction of charged tracks before and after each magnet.

- **Ring-Imaging-CHerenkov (RICH) counters:** Liquid and gas RICH counters are used for off-line particle identification.

- **Electromagnetic calorimeters follow both spectrometers.**

## *5.1 Silicon-Strip Microvertex Detector*

**Geometry**

To match the forward spectrometer system, the silicon microvertex detector has a geometry typical of fixed-target experiments with the silicon planes perpendicular to the circulating beams. The microvertex detector system seen in Fig. 8 is installed at the center of the interaction region ($z = 0$) inside the vacuum chamber. The extended source size of the bunch crossing region and the need to minimize the extrapolation distance from measured track points in the silicon to an interaction vertex leads to a detector design in which the silicon planes are distributed along the intersection region, spaced longitudinally by about 4 cm.

A choice of ≈4 cm spacing between planes involves a compromise between simultaneously minimizing the errors in extrapolating the tracks to an event vertex and the secondary interactions and photon conversions in the material of the detector. The extrapolation errors are then dominated by the strip pitch of 25 $\mu$m for tracks with momenta above about 2 GeV.

As mentioned in the Introduction, such a silicon-strip system was recently tested at the CERN Sp$\bar{p}$S-Collider by the P238 group. A detailed description of this detector, the hardware involved and some early analysis of the data obtained is given in APPENDIX C as a DRAFT version of an article to be submitted to Nucl. Instrum. & Methods. Thus, we leave most detailed description to APPENDIX C and simply give here an abbreviated description of the detector used and explain how the final complete detector would differ from the one used for the P238 run.

Fig. 11 shows a sketch of the 6-plane P238 microvertex detector assembly which has been run in intersection region LSS5 at the Sp$\bar{p}$S as an R&D project. Each silicon plane in Fig. 11 contains eight 4.5 cm square detectors with single-sided readout, configured in four quadrants, with each quadrant comprising one x and one y plane, separated in z by 2 mm. The planes are separated by 3.8 cm and are mounted on a Roman pot assembly, such that the upper and lower halves can be retracted to a safe position at 5 cm from the beams, when there are beam manipulations. Remote control of the vertical positioning (accurate to $\pm 25\ \mu$) allows the detector assemblies to approach the beam line as close as 1.5 mm or less for data taking.

The silicon detector for the proposed Tevatron experiment will have a similar configuration but will contain a larger number[7] of detector planes. Each silicon plane will contain four double-sided readout strip detectors with pitch 25 $\mu$m and 250 $\mu$m thickness, configured in four quadrants. The planes will be separated longitudinally by 4 cm and will be mounted on rigid but movable supports such that, during beam manipulations, the upper and lower halves can be retracted to a safe position 5 cm from the beams. The detector quadrants will have dimensions approximately $6 \times 6$ cm$^2$.

Our experience with the P238 tests show that we can expect to run with a gap between upper and lower detector assemblies of less than 3 mm without significant background. Since beam sizes are smaller at the Tevatron, we may expect that this gap can be even further reduced. Clearly this places great demands on the stability and precision of the support assembly, which presumably will be patterned after the Roman pot technology developed at CERN. We also note that new monitoring elec-

[7] The large length of the Tevatron bunches poses a problem. Unless the bunch lengths can be shortened at the Tevatron, it may be necessary to suffer an acceptance loss resulting from incomplete vertex coverage. Allowing for future use of the detectors at LHC or SSC requires that the dimensions be appropriate for shorter bunch length machines.

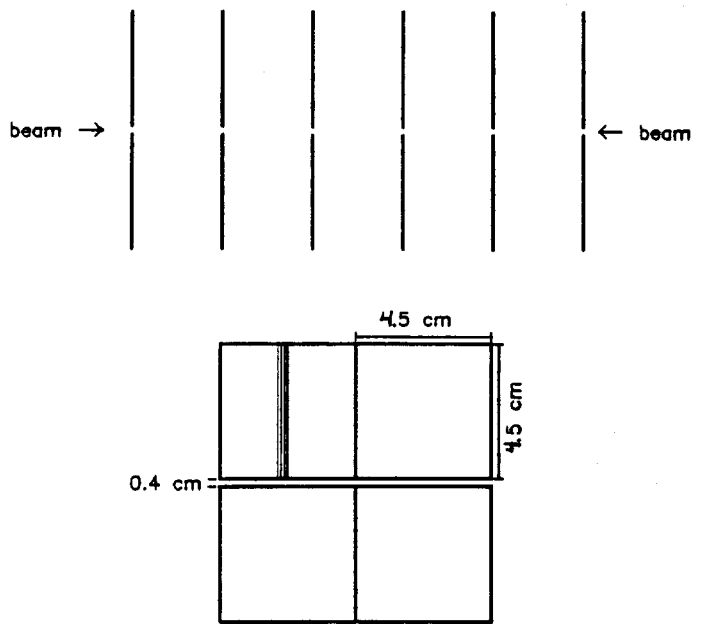


*Figure 11: Side View of the Test Version of the Silicon Detector System.* The 6-plane 43,000 channel P238 silicon system currently running at the Sp$\bar{p}$S. Planes are 3.8 cm apart in z (longitudinally) and configured perpendicular to the beam line. The beams pass between the independent upper and lower detector assemblies. The first silicon strip in each case can be as close as 2 mm from the beams Each quadrant currently contains independent x and y detectors, 4.5 cm square and 280 $\mu$m thick, and separated in z by 2 mm. The pitch is 50 $\mu$m.

tronics for the currents in the low-beta quadrupole magnets and elsewhere will be necessary in order to dump the circulating beams in less than one turn should it be necessary for the protection of the silicon.

**Installation in Vacuum**

There are two major problems with using silicon inside the ultra-high vacuum of a collider very close to circulating beams:

1. RF pick-up in the silicon generated by passage of beam bunches,

2. The need to preserve an ultra-high vacuum in the beam pipe which imposes very tight restrictions on detector materials and requires tightly sealed feed-throughs on signal paths.

An elegant solution to these problems is to separate the silicon detectors from the machine vacuum with a thin Aluminum "window" The Aluminum serves both as an RF shield and as a means of isolating the ultra-high vacuum of the machine from outgassing of detector materials and also relaxes the requirements on feed-through seals.

With the silicon detectors mounted inside a vessel, which is modeled after the CERN Roman pot mechanisms, a thin aluminum window, which approximately follows the contours of the detectors, can constitute the bottom of the "pot". Collapse of these thin windows is prevented by creating a secondary vacuum, in which the silicon detectors are found to function well, inside the Roman pots.

Such a system was successfully used by us in the P238 tests at the CERN Sp$\bar{p}$S-Collider (see below and APPENDIX C) with no signs of RF pickup. A thinner aluminum window will be used in a future installation, in order to minimize multiple scattering. The criterion is that it be thin compared to a single 250 $\mu$m thick silicon detector, while still providing adequate RF shielding. A 100 $\mu$m Aluminum shield should be a reasonable compromise.

**Recent Test Run at Sp$\bar{p}$S-Collider**

While there are many challenging hardware components in the proposed Beauty experiment, only the operation of the silicon detectors within the machine vacuum chamber had intrinsic uncertainties which could influence the overall success of the experiment. These were the unknown amounts of event-unrelated noise and beam halo tracks which would be recorded by the silicon detectors which must be run inside the vacuum pipe close to the circulating beams. Since we have shown that the PYTHIA-generated minimum bias events used in our simulation of the trigger algorithm, are in good agreement with the minimum bias data from Experiment UA5, it is likely that only such (unanticipated) event-unrelated "noise" in the silicon could, a priori, present serious difficulties.

In order to determine the magnitude of such contributions to the observed silicon signals, and thus the reliability of the proposed trigger in the complete experiment, we were fortunate to be able to run a prototype silicon system installed inside the vacuum pipe at the Sp$\bar{p}$S-Collider, in an interaction region which had a low-beta insertion (LSS5). The geometry of the 43,000 channel silicon-strip system has already been described above and is discussed in detail in APPENDIX C.

Approximately $10^7$ minimum bias events were recorded on tape, using a simple beam-beam interaction trigger. No significant background was observed. For example, Fig. 12 shows a "typical" event recorded with the detector system 1.5 mm from the beam. Six y-detectors in one quadrant are shown, with the horizontal scale given by the silicon detecter width of 4.48 cm (896 channels times the pitch of 50 $\mu$m). The vertical scale is defined by the 3.8 cm between planes.

The negligible background of event-unrelated hits in the silicon show that a large silicon strip detector centered on the interaction region can be run as close as 1.5 mm from the beam with minimal background. **It is the single most important demonstration that this experiment is viable.** Converting the silicon data to a trigger by means of powerful real time processing is a manageable task of digital engineering.

**Silicon-Strip Detectors with Readout on Both Sides**

To optimize the selectivity of the silicon microvertex detector, it will be essential to combine optimal spatial resolution with very little material in the sensitive area. This can be achieved by using both the holes and the electrons created in the detector to extract spatial information. Detectors, where strips on both sides are read out, have been developed by several groups. Our CERN group has developed ac-coupled double-sided detectors,[8] using a novel scheme to separate strips ohmically on the n-side by means of field depletion via a suitable potential applied to the readout strips. It has been demonstrated[9] that these detectors give adequate spatial resolution. Prototypes of 19.2 × 19.2 mm$^2$ sensitive area with 50 $\mu$m pitch have been tested in a high energy beam. The resolution was measured to be $\sigma$ = 8.8 $\mu$m on the p-side and 12.4 $\mu$m on the n-side, as shown in Fig. 13. These measurements

[8] B.S. Avset et al., IEEE Trans. on Nucl. Sci., Vol. 37, No. 3 (June 1990) 1153.

[9] L. Hubbeling et al., **Measurement of Spatial Resolution of a Double-Sided AC-Coupled Microstrip Detector,** to be published in the Proceedings of the 2nd London Conference on Position Sensitive Detectors (September 1990).

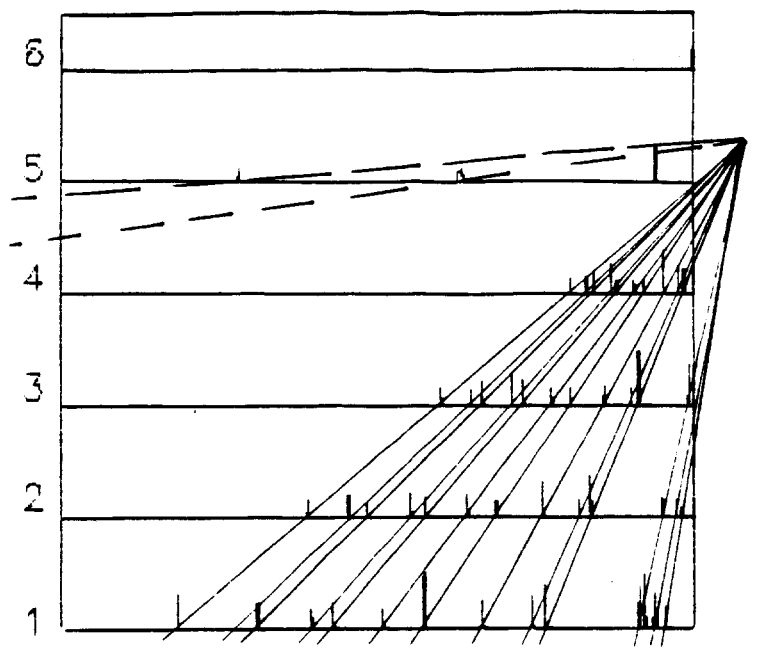


*Figure 12: Silicon Event Recorded 1.5 mm from the Sp$\bar{p}$S-Collider* Beams. One quadrant with six planes of y detectors are shown. There are 3.8 cm between planes and each detector is 4.48 cm wide. Pulse heights are shown if they are larger than $4\sigma_{noise}$. Lines are drawn by hand.

indicate that, with this technology, we should be able to achieve a spatial resolution on both sides of $\sigma \approx 5\ \mu m$.

An improved version of these detectors is at present under production for the upgrade of the DELPHI microvertex detector. For an upcoming test run for the present Beauty proposal (see below in Section 6.4), we plan to instrument some of these double-sided detectors with SVX chips and combine them with the existing P238 vertex detector for test beam and collider runs at the SPS.

## *5.2 Vacuum Pipe*

Detailed spectrometer layouts are shown in Figure 14 and Figure 15. The vacuum pipe contains two thin windows, one at z ≈30 cm and one at 475 cm, which match the apertures of the two spectrometer segments shown in Fig. 8. A conical section with an angle of 100 mr connects the windows. The last vacuum pipe section after z = 475 cm is also a conical section, but with an angle of 2.5 mr, corresponding to the minimum angle of the second spectrometer aperture (at 475 cm, this corresponds to a pipe diameter of about one inch). Although the minimum aperture of the vacuum pipe will be 2.5 mrad, we note that the sensitive regions of the chambers and other detectors will likely be somewhat larger, perhaps at 5 mrad.

Construction of the vacuum chamber from aluminum or carbon fibre (or both) will limit multiple scattering of the particles and reduce interactions of particles in material near the beam. Both of these materials have been used successfully at CERN for construction of beam pipes. Recent improvements

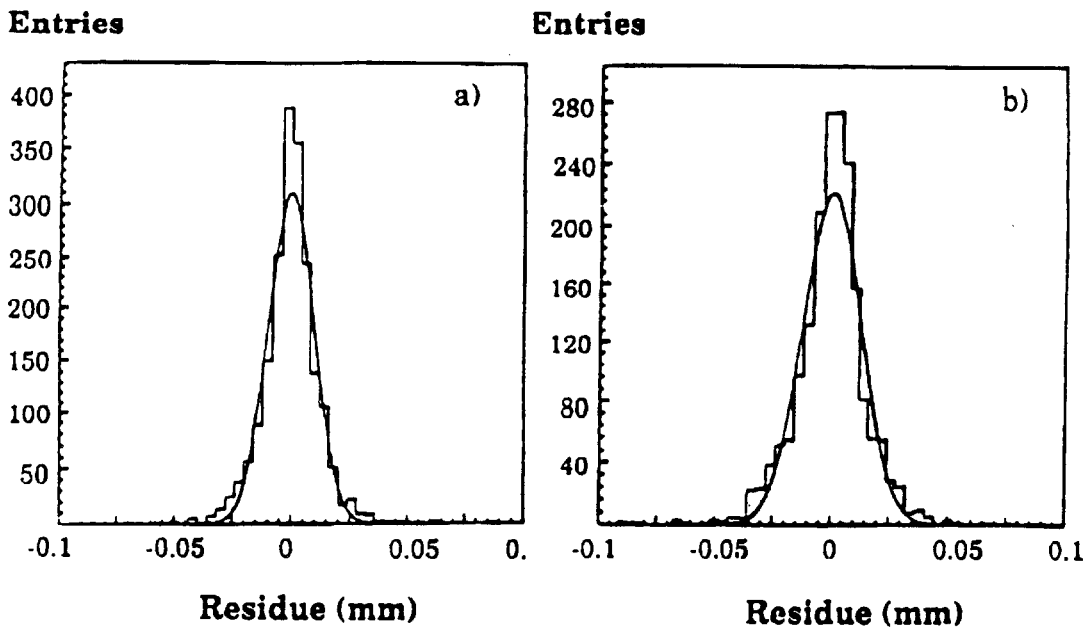


*Figure 13: Residual Distributions with Gaussian Fits:* (a) p-side, (b) n-side.

in aluminum welding used at CERN make aluminum an attractive, cost effective material for the construction of these parts where the amount of material must be minimized. Although carbon fibre is more expensive, it could provide additional immunity to secondary interactions in critical areas such as near the window of the last spectrometer where the beam pipe reaches its minimum diameter (5 cm) in the spectrometer.

## *5.3 Magnets*

The first spectrometer magnet, shown in Fig 14, is a normal-conducting quadrupole magnet of 2 m radius and $L_1 = 2$m magnetic length (3m overall length) with a pole tip field of 1.2 T and a gradient of $B_1' = 0.6$ T/m. T. Taylor of the CERN LEP division has suggested the use of such a large aperture quadrupole magnet as an alternative to large dipole spectrometer magnets with septum plates A quadrupole magnet has several advantages: (a) the absence of septum plate material near the beam minimizes interactions of outgoing particles; (b) particles with angles between 2.5 and 100 mrad receive minimal bending inside the beam pipe before they emerge and enter spectrometer 2; (c) the negligible field at the position of the silicon detectors does not distort the straight line tracks, thereby minimizing the complexity of the on-line trigger algorithm.

The average field integral seen by a charged particle produced at the origin at polar angle $\theta$ is $<BL>_1 = B_1' \cdot L_1 \cdot z_1 \cdot \tan\theta / \cos\theta$, where $z_1$ is the center of the quadrupole. In general, the momentum resolution is given by $\sigma_p = k \cdot p^2$, where $k = \sqrt{2} \cdot \sigma_\theta / [0.3 <BL>]$, and $\sigma_\theta$ is the error in the directional determination of the incident or outgoing track. For this quadrupole, with $z_1 = 3$m, $L_1 = 2$m, $B_1' = 0.6$ T/m and $k_1 = \sqrt{2} \cdot \sigma_\theta \cdot \cos\theta / [1.08 \cdot \tan\theta]$. Track sensitive detectors are installed at $r = 2$m to detect particles which strike the poles.

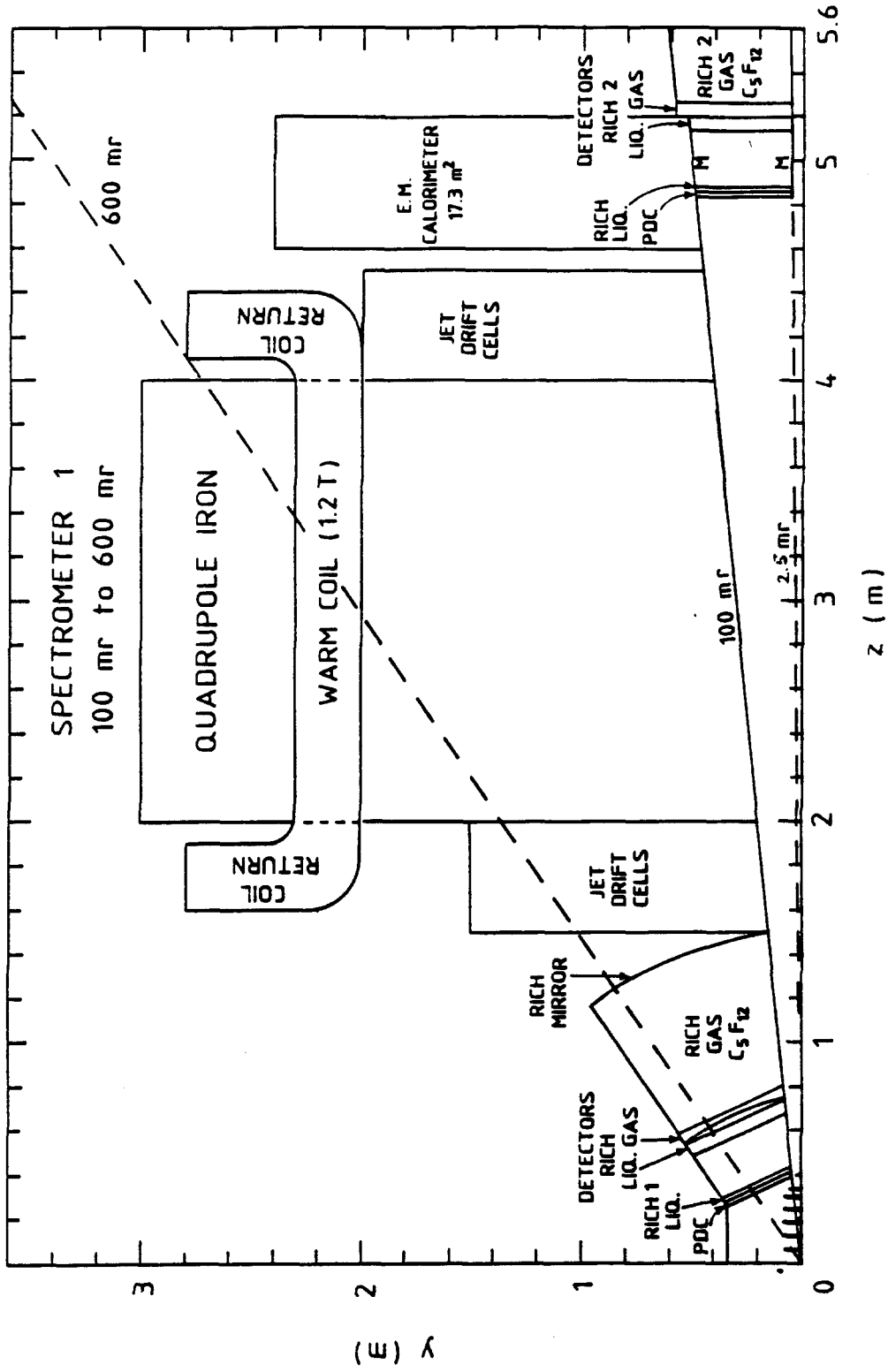


*Figure 14: Layout of Spectrometer One.*

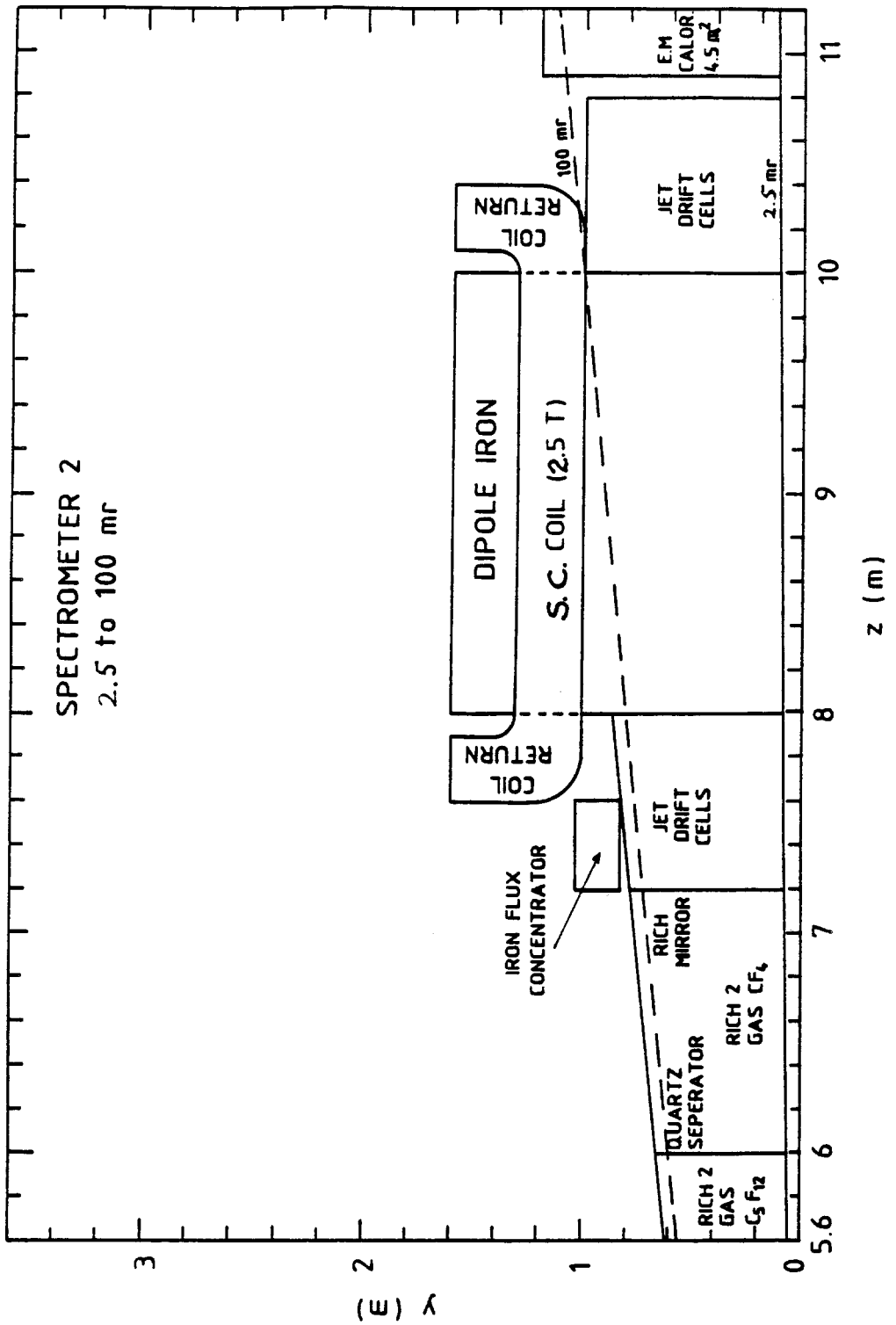


*Figure 15: Layout of Spectrometer Two.*

In Spectrometer 2, covering 2.5 to 100 mr, as shown in Fig 15, the superconducting dipole has magnetic length $L_2$ = 2m (geometrical length 3m) and uniform magnetic field of 2.5 T. The average $<BL>_2$ = 5.0 Tm. The corresponding magnet constant is: $k_2 = \sqrt{2} \cdot \sigma_\theta \cdot \cos\theta \,/\, 1.5$. The sides of the dipole will also be instrumented with track sensitive detectors in order to measure those low momentum particles which are deflected by the magnetic field into the side walls.

### *5.4 Pixel Detectors*

A silicon pixel detector and two pixel drift chambers (described below) are included in the spectrometer to match the x,y view tracks in the microvertex detector and to aid in connecting these tracks to those found in the spectrometers. Monte-Carlo calculations show that the resolution of the pixel detectors should be less than $1 \times 1$ mm$^2$.

A front view of several elements of the pixel drift chamber (PDC1) in Spectrometer 1 (see Fig. 14) is shown in Fig 16. The two dimensional position of a track traversing the 20 mm thick gap is measured with only a left-right ambiguity. The sense wires of the PDC have 2 cm length and pitch 2 mm, and are approximately parallel to the outgoing tracks, so that all ionization is collected by a single wire (or cluster). The wire coordinate and its signal arrival time provide the x,y coordinates of the track.

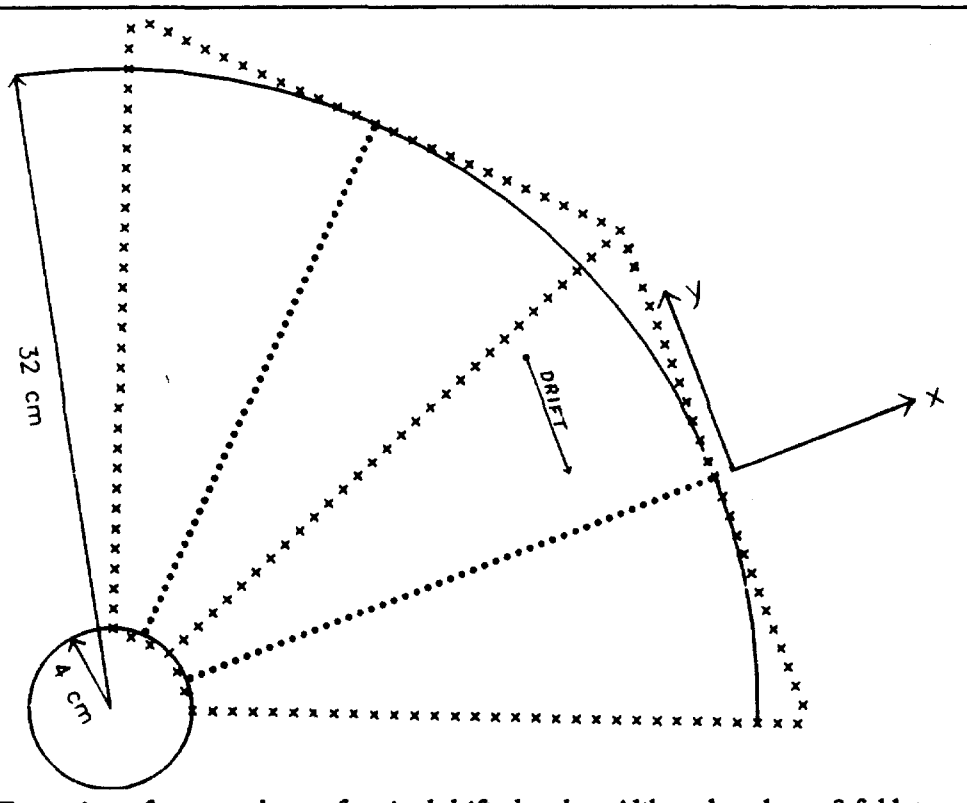


*Figure 16: Front view of one quadrant of a pixel drift chamber.* Although only an 8-fold $\phi$ symmetry is shown, PDC1 and PDC2 will actually possess 32-fold and 48-symmetries, respectively

The segmentation is determined by the requirement that the maximum drift time be less than 400 ns. With an outer radius of 32 cm and a drift velocity, $v_d \approx 8$ cm/$\mu$s, this requirement can be met if there is a 32-fold $\phi$ symmetry. The maximum drift distance is then 3.14 cm. The total number of wires in the PDC1 is 4,480 (32 × 140).

A value, $v_d \approx 8$ cm/$\mu$s, can be attained with a mixture of 90% methane and 10% isobutane. The diffusion coefficients are then: $\sigma_\ell = \sigma_t = 240\ \mu\text{m}\cdot\text{cm}^{-1/2}$. The pixel resolutions are $\sigma_x = 580\ \mu$m (with 2 mm wire pitch) and $\sigma_y = 570\ \mu$m (assuming 4-bit TDC's). The effects of diffusion change these values very little.

A similar detector, PDC2, with a larger radius of 48 cm, forms the first element of Spectrometer 2 (see figure 14). Now a 48-fold symmetry is required to satisfy the 400 ns maximum drift time and the number of sense wires are 11,040 (48 × 230). The pixel resolutions are the same as in PDC1.

The silicon pixel detector (SPD), which covers the angular range 4 to 100 mrad, is disk shaped and located inside the beam pipe, at a distance of 38 cm from the average interaction point (this assumes a distance of 1.5 mm between silicon and circulating beams). The SPD disk, with radius 3.8 cm and 250 $\mu$m thickness, will be divided into four sectors. The upper and lower halves will be mounted on the respective vertex detector positioning mechanisms so they also are retracted during beam manipulations. The pixel size will be $1 \times 1$ mm$^2$, for a total of 4500 channels.

Track segments both from the silicon detectors and from the spectrometer will be projected onto the PDC with spatial resolution better than 1 mm, in each projection, for momenta larger than 5 GeV.

## *5.5 Wire Chambers*

Jet-type drift cells will be used to measure the position and direction of charged tracks before and after each magnet. Fig. 17 shows, for example, a jet drift cell oriented so that ionization from a 350 mrad track arrives isochronously at the 10 sense wires. Similar chambers are used by the HELIOS[10] experiment at CERN and SLD[11] experiment at SLAC.

### Geometry of the Chambers

Figures 14 and 15 shows the position and dimensions of the four chambers used to measure particle directions and momenta. The four chambers all have similar cellular structures as summarized in Table 6. Chambers 1 and 2 (Spectrometer 1) each have 8 modules with 10 track samples each. Four different wire orientations are used: x, y, and u,v ($\pm 45°$). This sequence is repeated twice for a total of 80 measurements along each track. Chambers 3 and 4 (Spectrometer 2) have a somewhat different structure because of the dipole magnetic field. The cell orientation is x, u, x, v, x, u, x, v, with 16 track samples in each module. The total of 128 measurements is equivalent to 96 measurements in the bending plane.

### Cell Structure and Drift Resolution

The drift cell geometry shown in Fig. 6 has sense wires and equipotential wires strung in planes which include the intersection region center ($x=y=z=0$). Thus, the average particle direction is perpendicular to the drift direction in all cells so that isochronous charge collection results. The wires have pitch 6.25 mm and are staggered transversely by 100 $\mu$m. The maximum drift distance is 2 cm.

---

[10] D. Bettoni et al.,Nuclear Instruments and Methods A252 (1986) 272.

[11] C. Young et al., IEEE NS36 (1986).

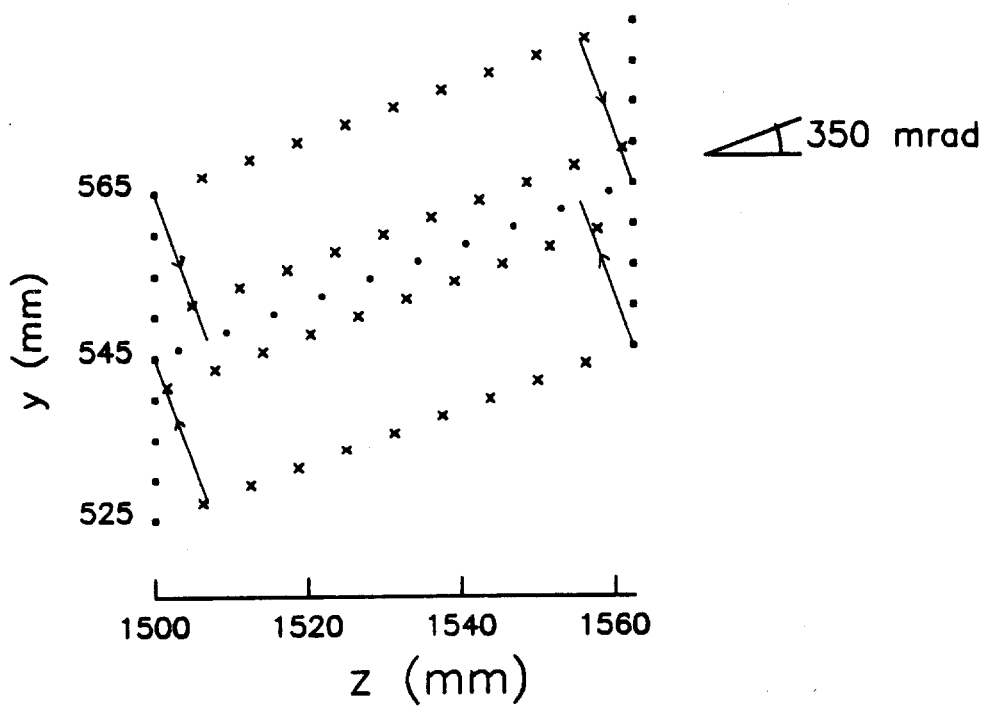


*Figure 17: A Jet drift cell in one module of Chamber 1 at $\theta = 350$ mr.* The circles are sense wires, crosses are equipotential wires, and squares are field shaping wires.

*Table 6: Chamber Properties*

| | Chamber 1 | Chamber 2 | Chamber 3 | Chamber 4 |
|---|---|---|---|---|
| Diameter × Length ($m^2$) | 3×0.5 | 4×0.5 | 1.6×0.8 | 2×0.8 |
| Sense wires | 7000 | 9600 | 5700 | 7100 |
| Orientation | x,y,u,v | x,y,u,v | x,u,x,v | x,u,x,v |
| Samples per Track | 80 | 80 | 128 | 128 |
| Drift Distance | ±2cm | ±2cm | ±2cm | ±2cm |
| S.W. Staggering | 100μm | 100μm | 100μm | 100μm |
| Drift Velocity | 20μm/nsec | 20μm/nsec | 20μm/nsec | 20μm/nsec |
| Drift Field | 4kV/cm | 4kV/cm | 4kV/cm | 4kV/cm |
| Gas | He/DME | He/DME | He/DME | He/DME |

We intend to use 70% Helium and 30% DME because of the long radiation length of this mixture (667 m) compared to that of $CO_2$ (197 m), while the diffusion characteristics and drift velocity are similar. This mixture results in an unsaturated drift velocity of 20μm/nsec in an electric field of 4 kV/

cm with a diffusion coefficient of ~80 $\mu m \cdot cm^{-1/2}$. The corresponding maximum drift time is 1 $\mu$sec for $\pm 2$ cm cells. At atmospheric pressure this mixture will produce 21 primary electrons per cm, corresponding to 13 primary electrons per wire (with 6.25 mm pitch).

The HELIOS chambers use a 90% $CO_2$ and 10% ethane gas mixture which gives a smaller drift velocity than that of the He/DME mixture we propose to use. In order to optimize track separation and reduce space-charge, HELIOS uses field wires to limit the length of the charge segment collected by a sense wire, thus obtaining a more isochronous charge collection. Their electronics makes use of pulse clipping and shaping, and multihit TDCs. In a test beam, they found a resolution of 60 $\mu$m averaged over the 2cm drift distance, and a 600$\mu$m two track separation. The SLD collaboration used 92% $CO_2$ and 8% isobutane and a cell geometry which collected 16 primary electrons per sample. Their average drift distance resolution is 55$\mu$m in $\pm 2.5$ cm cells.

Since our chambers will have substantially larger dimensions and will operate in a nonuniform magnetic field, we expect a final accuracy of 100$\mu$m averaged over the drift distance, and a two track separation of 3 mm. In order to reach such a precision, a laser alignment and calibration system will be used, together with a complete monitoring system of gas temperature and pressure, drift velocity, and electric field.

**Electronics**

A low noise preamplifier is mounted directly on the chamber frame. Ten meters away a two stage amplifier is used where a 2 nsec clipping and integration (1/t cancellation) is performed. A discriminater (with threshold set at 2 electrons on the sense wire) drives an 8-bit TDC with multihit readout. No pulse amplitude analysis is performed.

**Momentum Measurement**

The error in the track direction, $\theta$, is given by the relation

$$\sigma_\theta = [\,(\sigma_X/L)^2 \cdot (12/N) + (.01/p)^2 \cdot (L/X_0)\,]^{1/2}$$

where $\sigma_X$ is the accuracy of a single drift cell measurement and L is the distance over which the uniformly distributed N measurements are made and $X_0 = 667$ m for the He/DME mixture.

In each chamber of Spectrometer 2 we effectively have 96 measurements in the bending plane over 80 cm of track length with a single hit accuracy of 100 $\mu$m. This gives us:

$$\sigma_\theta = 44\ \mu\text{rad} \cdot \sqrt{(1+p_2{}^2/p^2)}$$

where $p_2 = 7.9$ GeV is the momentum below which the multiple scattering term dominates. The error on the Spectrometer 2 momentum measurement is given by the dipole magnet constant

$$k_2 = \sigma_p/p^2 = 4.1 \cdot 10^{-5} \cdot \cos\theta \cdot \sqrt{(1+p_2{}^2/p^2)}$$

for the 5 Tm magnet (where we have used the expression for $\sigma_p$ given above).

For Spectrometer 1 we have 40 measurements over 50 cm with 100 $\mu$m precision in the bending plane. Hence:

$$\sigma_\theta = 107\ \mu\text{rad} \cdot \sqrt{(1+p_1{}^2/p^2)}$$

with $p_1 = 2.6$ GeV and the quadrupole magnet constant is then:

$$k_1 = \sigma_p/p^2 = 1.4 \cdot 10^{-4} \cdot \cos\theta \cdot \sqrt{(1+p_1{}^2/p^2)}\ /\ \tan\theta.$$

## *5.6 Ring Imaging CHerenkov (RICH) Counters*

**Geometry and Photon Detector**

The RICH detectors are designed to identify all hadrons from B decays as well as most leptons ( $\leq$20 GeV ). Above 20 GeV electron identification is provided by the electromagnetic calorimeter. Each of the two spectrometers has a $C_6F_{14}$ freon liquid radiator of 10 mm thickness and a $C_5F_{12}$ freon gas radiator of 750 mm path length. Spectrometer 2 also has a second gas counter with a 1200 mm long higher-threshold $CF_4$ freon radiator. The two gas volumes in Spectrometer 2 are separated by a 3 mm thick fused quartz window and both ring images are detected at the focal plane, 1950 mm upstream from the spherical reflecting mirror. Fig. 18 shows the momentum ranges of unique separation for the indicated particles in the liquid and gas RICH counters.

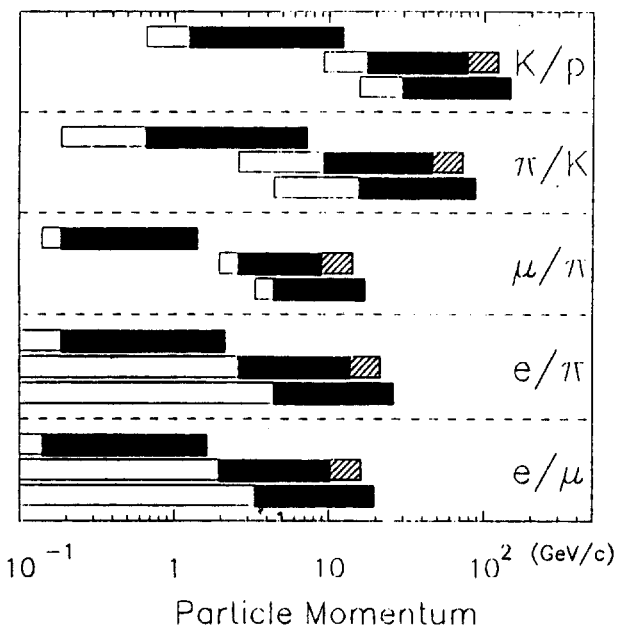


*Figure 18: Momentum Ranges of RICH Counter Identification.* For each indicated pair of particles, the upper bar in each set is for the the liquid RICH counters; the middle bar in each set is for the $C_5F_{12}$ radiators; the lower bar in each set is for the $CF_4$ radiator in Spectrometer 2. In all cases, the open bars show the momentum range between the thresholds for the lighter and heavier particles. The $3\sigma$ separation upper limits are indicated by the end of the solid bars, except for the $C_5F_{12}$ radiator in Spectrometer 2, whose upper limits extend to the ends of the hatched bars (since it is somewhat longer).

The liquid and gas radiator geometry is shown in Fig.s 14 and 15 and the proposed RICH detector geometry is shown in Fig. 19. The liquid radiator is contained by a 3 mm thick fused quartz window followed by a 25 cm Helium-filled flight path to its photon detector. This is immediately followed (back-to-back) by the gas image detector. Each detector consists of a 3 mm thick fused quartz window whose inner surface is coated with 100 $\mu$m wide metallic strips with 1 mm pitch (10% opacity) which

serve to define the equipotential surface, $V_0$. Cherenkov photons impinge upon the CsI/TMAE reflective photocathode[12] which is deposited on the pad structure shown in Fig. 19. The distance between the window and the pads is 3 mm and it is filled with 80% methane and 20% hexane at atmospheric pressure. Amplification is obtained on 20 $\mu$m diameter wires with 1 mm pitch placed 0.5 mm above the pad plane. The measured[13] pad efficiency for single photoelectrons exceeds 95% and the detector should be stable for gains up to $2 \cdot 10^6$.

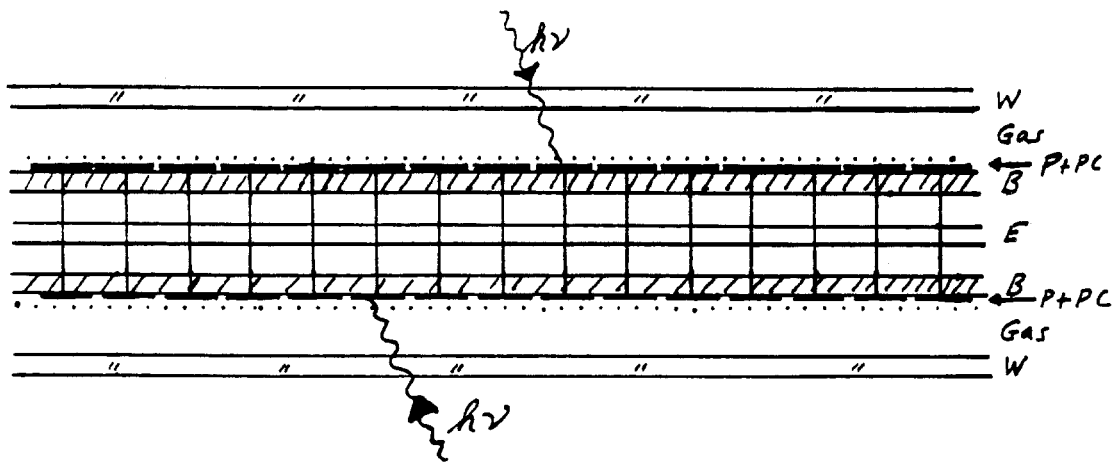


*Figure 19: Back-to-Back RICH Detector Geometry.* A schematic view of the quartz windows W, chamber body B, readout electronic E, and pad + photocathode structure P + PC. A Cherenkov photon is converted by the CsI/TMAE reflective PC and the produced primary photoelectron is amplified on a wire and induces a signal on nearby pads. The electronics readout is common to both chambers. The gas filling is 80% Methane and 20% Hexane at atmospheric pressure.

Secondary electron (feedback) production from the gas phase cannot occur since the TMAE partial pressure is negligible (i.e., TMAE gas flow is not necessary once the cathode has been sensitized). The primary avalanche process produces photons which irradiate the CsI/TMAE cathode and produce secondary avalanches. These pulses, however, merge with the primary avalanche because the amplifying wire is so near the cathode (i.e., 0.5 mm = 10 ns). The presence of hexane (with methane as the amplifying gas) defines the upper energy limit of the detector response (e.g., 7 eV) provides an absorber the $C^*$ emission lines at 7.47 and 7.95 eV (i.e., 166 and 156 nm). The $C^*$ emission line at 6.42 eV (193 nm) is then the only remaining source of feedback instability and has the same level of photon feedback as a TEA-based photoionizing gas detector. This is because the 156 and 193 nm lines are emitted with the same probability and because the quantum efficiencies of TEA and CsI/TMAE are similar at these respective wavelengths. A TEA pad detector with amplifying wires 0.5 mm from the pad plane

[12] J. Seguinot et al., **Reflective UV Photocathodes with Gas Phase Electron Extraction: Solids, Liquids and Adsorbed Thin Films;** CERN-EP/90-88 and NIM A297(1990)133.

[13] R. Arnold et al., **Experimental Study of a Fast Photon Detector with Pad Readout,** CRN/HE90-05 (available in French at CRN, Strasbourg – English version for NIM is in preparation).

has been successfully tested[13]. It showed enhanced stability to photon feedback compared to a TMAE gas detector and attained a gain of $2 \cdot 10^6$. It appears that the CsI/TMAE photocathode is suitable for fast operation ($\sigma_t$ = 10 ns) in the less dispersive energy range (6 to 7 eV), compatible with fused quartz windows.

The detector response parameter is $N_0 = (370\ eV^{-1}cm^{-1}) \cdot \Delta E \cdot \varepsilon$, where $\Delta E$ is the energy bandwidth of the detector and $\varepsilon = \int(Q \cdot T \cdot R)\, dE/\Delta E$ is the energy average of efficiencies (Q = quantum, R = reflectivity and T = transmissivity). Taking experimental values of R = T = 0.8 and an average Q = 27.5% (i.e., 12% at 6 eV and 43% at 7 eV), the detection efficiency $\varepsilon = 0.176$. The resulting response parameter, $N_0 = 65\ cm^{-1}$, is used in Table 7.

The RICH detector surface area is 0.9 $m^2$ in Spectrometer 1 and 1.1 $m^2$ in Spectrometer 2, for a total of 2.0 $m^2$ corresponding to $3.8 \times 10^5$ pads ($3 \times 3\ mm^2$ in Spectrometer 1 and $2 \times 2\ mm^2$ in Spectrometer 2). The VLSI pad readout electronics[14] comprises a fast (25 ns) Bipolar analogue chain (preamplifier, discriminator, pipeline and memory), followed by a 50 MHz CMOS 2-dimensional shift register with priority encoding, zero suppression and output bus arbitration. The prototype system reads out $10^4$ pads in less than 300 ns. The first production chips have recently been tested with partial success. We are now proceeding to a second test production with a revised layout. Production of about $4 \cdot 10^4$ channels of electronics is scheduled for spring 1991 for use in a full-scale liquid RICH counter test.

**Resolution and Particle Separation Ranges**

The chromatic error $\sigma_\theta(E)$ in the determination of the Cherenkov angle $\theta$ may be expressed as

$$\sigma_\theta(E) = (\partial\theta/\partial n) \cdot (dn/dE) \cdot \sigma_E.$$

For the $C_6F_{14}$ liquid radiator (refractive index n = 1.278 at E = 6.5 eV and dispersion $dn/dE = 9.28 \times 10^{-3}\ eV^{-1}$), the proximity focused image is characterized by (see APPENDIX B):

$$\partial\theta/\partial n = (n\tan\theta)^{-1} \cdot (n^2\beta^2) \cdot (\cos\theta_p/\alpha).$$

The first factor is the canonical factor obtained from the Cherenkov relation $n\beta\cos\theta = 1$, the second factor $n^2\beta^2$ is due to refraction at the liquid surface and the last factor $\cos\theta_p/\alpha$ depends on the particle incidence angle $\theta_p$ with respect to the normal to the radiator plane. $\alpha$ depends on the Cherenkov azimuthal angle $\phi$ via the relation:

$$\alpha = \cos\theta_p - \sin\theta_p \cdot \tan\theta \cdot \cos\phi.$$

Therefore, this last factor is unity for normal incidence and averages to 0.9 at $\theta_p = 20^0$. The energy error $\sigma_E$ of a triangular response detector is $\Delta E/\sqrt{24}$ where $\Delta E$ is the base energy width. Combining these factors gives

$$\sigma_\theta(E) = (1/1.02) \cdot (1.63) \cdot (0.9) \cdot (9.28 \cdot 10^{-3}) \cdot (1.5 / \sqrt{24}) = 4.1\ \text{mrad}.$$

At the chosen distance between the liquid radiator and detector (250 mm), the angular error $\sigma_{ze}$ due to a radiator of thickness 10 mm is about $\sigma_{ze} = 2.2$ mr when averaged over the accepted azimuthal angles $\phi$. With pad dimensions of $3 \times 3\ mm^2$, the measurement errors on the photon conversion point (x, y, z) are $\sigma_x = \sigma_y = 0.9$ mm and, with the CsI/TMAE photocathode, $\sigma_z = 0$. They contribute angular errors of 0.6 mr, 0.6 mr and 0 mr, respectively. Multiple scattering in the liquid radiator and quartz window contribute 2.8 mr/p to $\sigma_\theta$ and the uncertainty in particle direction contributes a term $(2/\pi)\ \sigma_{\theta p}$. Summing the above errors in quadrature gives a total angular error $\sigma_\theta = 4.6$ mrad per de-

[14] See Figs. 34-41 in: J. Seguinot, **Fast RICH Detectors for LHC/SSC/ELOISATRON**, Proceedings of the Symposium on Particle Identification at High Luminosity Hadron Colliders, Fermilab, Batavia, IL, 5-7 April 1989 (Ed. T.J. Gourlay and J.G. Morfin), pps. 215-253 and 671-683.

tected photon. In the liquid radiator, the threshold momenta for e, $\mu$, $\pi$, K and p are, respectively, 0, 0.13, 0.18, 0.62 and 1.18 Gev. The relevant derivatives are given in APPENDIX B and summarized in Table 7.

*Table 7: RICH Resolution and 3σ Momentum Identification Limits*

| | LIQUID | | $C_5F_{12}$ GAS 1 | | $C_5F_{12}$ GAS 2 | | $CF_4$ GAS 2 | |
|---|---|---|---|---|---|---|---|---|
| $v_i$ | $\Delta v_i$ | $\sigma_\theta$(mr) | $\Delta v_i$ | $\sigma_\theta$(mr) | $\Delta v_i$ | $\sigma_\theta$(mr). | $\Delta v_i$ | $\sigma_\theta$(mr) |
| $z_e$ (mm) | 10 | 2.24 | 750 | 0.30 | 750 | 0.12 | 1200 | 0.04 |
| $x_e$ (mm) | – | – | 1.0 | 0.00 | 1.0 | 0.00 | 1.0 | 0.00 |
| z (mm) | 0.0 | 0.00 | 0.0 | 0.00 | 0.0 | 0.00 | 0.0 | 0.00 |
| x (mm) | 3.0 | 0.64 | 3.0 | 0.81 | 2.0 | 0.20 | 2.0 | 0.20 |
| y (mm) | 3.0 | 0.64 | 3.0 | 0.81 | 2.0 | 0.20 | 2.0 | 0.20 |
| E (eV) | 1.5 | 4.0 | 1.5 | 0.35 | 1.5 | 0.35 | 1.5 | 0.27 |
| $\theta_p$(mr) | 1.0 | 0.18 | 1.0 | 0.18 | 1.0 | 0.18 | 1.0 | 0.18 |
| $\sigma_\theta$(total) | 4.64 | | 1.25 | | 0.50 | | 0.44 | |
| $k_r$ [$10^{-6}$] | 730 | | 17.9 | | 7.2 | | 5.0 | |
| $p_{3\sigma}(e\mu)$ | 1.6 | | 10.1 | | 16.0 | | 19.2 | |
| $p_{3\sigma}(e\pi)$ | 2.1 | | 13.5 | | 21.3 | | 25.6 | |
| $p_{3\sigma}(\mu\pi)$ | 1.4 | | 8.9 | | 14.1 | | 16.9 | |
| $p_{3\sigma}(\pi K)$ | 7.1 | | 45.6 | | 71.9 | | 86.3 | |
| $p_{3\sigma}(Kp)$ | 12.1 | | 77.0 | | 121.4 | | 145.7 | |

These 3σ momentum discrimination limits are shown in Fig. 18.

The allowable average magnetic field inside a RICH radiator is

$$B < (\pi/2) \cdot (\sqrt{12}) \cdot \sigma_\theta \cdot p / (0.3L)$$

to insure that particle deflection inside the radiator does not cause additional smearing of the image. In the liquid radiator, $\sigma_\theta$ = 4.6 mr and L = 0.01 m. Hence, B < 8.4 T when p = 1 GeV, which is clearly satisfied.

The momentum p at which particles of mass $m_1$ and $m_2$ are discriminated at the level of $n_\sigma$ standard deviations is given by the formula:

$$p^2 = (m_2{}^2 - m_1{}^2) / (2n_\sigma k_T)$$

where

$$k_T = n \cdot \sigma_\theta / \sqrt{(N_0 L)}.$$

Experiments with the DELPHI barrel RICH prototype[15] have demonstrated ring images with 25 photoelectrons per liquid image (L = 1 cm), corresponding to $N_0 = 65\ cm^{-1}$ for the detector band base width $\Delta E = (7.1 - 5.6)$ eV. With $\sigma_\theta = 4.6$ mrad, $N_0 = 65\ cm^{-1}$, L = 1 cm and n = 1.278, the Cherenkov constant, $k_T = 7.3 \times 10^{-4}$. Hence, particles are discriminated at a level ($n_\sigma > 3$) up to momenta p = 1.6 GeV for $e\mu$, 2.1 GeV for $e\pi$, 1.4 GeV for $\mu\pi$, 7.1 for $\pi K$ and 12.1 GeV for Kp.

The gas radiator in Spectrometer 1 consists of atmospheric pressure $C_5F_{12}$, with Cherenkov threshold $\gamma_t = 17$, corresponding to momentum thresholds of 2.4, 8.4 and 15.9 GeV for pions, kaons and protons, respectively. These thresholds overlap with the upper discrimination limits of the liquid radiator, thus assuring complete coverage for particle identification in the low energy region.

The upper limits for particle identification in the gas radiators[16] are determined by the Cherenkov angular resolution $\sigma_\theta$. The relevant variables ($v_i$) are the photon emission point, $z_e$, the particle impact parameter, $x_e$, the photon detection point, (z,x,y), the photon energy E and the particle direction $\theta_p$ relative to the detector normal. Analytic expressions for the derivatives, $\partial\theta/\partial v_i$, can be found in footnote 16. A summary of the pixel sizes, $\Delta v_i$, and their contributions, $\sigma_\theta(v_i)$, to the total error, $\sigma_\theta$, are shown in Table 7.

The average magnetic field allowable in gas RICH 1 is B < 312 gauss × p, or 0.09T at 3 GeV (just above $\pi$ threshold) and 0.3T at 10 GeV. The shielding of the quadrupole field at the position of RICH 1 (0.5m to 1.25m from the quadrupole entrance plane) appears feasible, since the field direction is azimuthal and can be easily channeled by iron plates mounted on the outer part of the RICH gas box. In gas RICH 2, with its better resolution, only 0.05T and 0.16T are allowable (at 3 GeV and 10 GeV, respectively). However, it is further away from the entrance plane of the dipole (2.0 m to 2.8 m i.e. 2.0 to 2.8 half gaps). Some loss of resolution seems likely at low momentum, where it is acceptable, since many $\sigma$'s ($n_\sigma > 10$) are available for particle discrimination.

The momentum resolution of the RICH detectors is given by the relation, $\sigma_p = k_T \cdot p^3 / (m^2\beta)$, where $k_T$ is the Cherenkov factor calculated above. For example, $\sigma_p \leq 100$ MeV at $p_\pi \leq 4.8$ GeV and $p_K \leq 11.0$ GeV in Spectrometer 1 for the $C_5F_{12}$ radiator. In Spectrometer 2, $\sigma_p \leq 100$ MeV at $p_\pi \leq 6.5$ (7.3) GeV and $p_K \leq 14.9$ (16.8) GeV for the $C_5F_{12}(CF_4)$ radiators, respectively. It appears that the momentum resolution of RICH detectors can be useful for the heavier particles (K,p).

---

[15] R.Arnold et al., NIM A270, 255 and 288 (1988).

[16] T. Ypsilantis, CERN-EP/89-150;
**Particle Identification at Hadron Colliders,** Proceedings of Symposium on Particle Identification at High Luminosity Hadron Colliders, Fermilab, Batavia, IL, 5-7 April 1989 (ed. T.J. Gourlay and J.G. Morfin) pps. 133-158;
**Particle Identification at Hadron Colliders, ECFA Study Week on Instrumentation Technology,** Barcelona, Spain, 14-21 September, 1989, CERN 89-10, Vol. 2 (ed. E. Fernandez and G. Jarlskog) pps. 661-674.

### *5.7 Electromagnetic Calorimeter System*

The electromagnetic (EM) calorimeter system is shown schematically in Figs. 14 and 15. The surface areas covered are 17.3 $m^2$ and 4.5 $m^2$ in Spectrometers 1 and 2 respectively. As is discussed in Section 8.2, the electromagnetic energy resolution required is $\sigma_E < 4\% \cdot \sqrt{E}$. This may be achieved with a totally active liquid Krypton calorimeter[17] with $\sigma_E < 1\% \cdot \sqrt{E}$ or with scintillating glass[18] with $\sigma_E < 4\% \cdot \sqrt{E}$.

In the Krypton counter, a $25X_0$ calorimeter would be 1.15 m long, have a a volume of 25 $m^3$ and weigh 61 tons. The raw material cost is ≈$4.8M.

A $25X_0$ scintillating glass (HED-1, $\rho = 3.4\ g \cdot cm^{-3}$, $X_0 = 4.12$ cm) calorimeter would be 1.03 m long, with a volume of 22.5 $m^3$ and weigh 76 tons. We estimate a cost of ≈$7.7M (including phototubes).[19]

The spatial and directional resolutions of the Krypton calorimeter are extremely good (0.1 mm and 1.5 mrad for a 10 GeV electron or photon), whereas the corresponding spatial resolution of the scintillating glass is 2 mm, and its directional resolution is very poor. The Krypton (with 5% Xenon) scintillation is fast (20 ns), compared to the scintillating glass (87 ns), and with a 100 times larger photon yield (i.e. $3 \cdot 10^4$ compared to $3 \cdot 10^2$ $MeV^{-1}$). Since the overall costs of the two calorimeters would be similar, the improved resolution of Krypton is preferable if the cryostat does not seriously deteriorate its performance.

If the EM calorimeter were made of scintillating glass, the blocks would have area 5 × 5 $cm^2$, transverse to the beams. The number of blocks in Spectrometers 1 and 2 totals ≈8700. The phototube pulse heights would be digitized to 12 bits to allow for the large dynamic range in electron and photon energies.

If Krypton were used, the calorimeter would have towers with transverse size 3 × 3 $cm^2$ with 12 ionization samples (in depth). A photodiode placed at the end of each tower detects the fast scintillation light and could be used in the trigger. The ionization is detected in the drift cells with maximum drift time of 750 ns. The fast scintillation gives excellent energy resolution ($\sigma_E < 1\% \sqrt{E}$) while the ionization signal (detected by drift) gives precise determination of the direction and position (≈1 mrad and ≈0.1 mm for a 10 GeV electron or photon, respectively).

## *6. TRIGGER PROCESSORS & DETECTOR READOUT*

The demands made on the readout system and trigger processor by the proposed experiment are particularly severe. The lack of an effective fast trigger criterion that can be calculated in less than the time between interactions means that, for each interaction, all detector information must be read out and stored in a pipeline until the Level-1 trigger decision is taken. Moreover, in order to minimize the number of events which must be stored, the estimated $10^4$ instructions per event needed for the Level-1 trigger algorithm described in Chapter 4 must be made in the shortest possible time, say 15 μsec. An additional requirement is that the fewest number of processors should be used, in order to minimize the complexity of the channel used to distribute the data from the detectors to the processors. We note that the total required computing power of the Level-1 trigger processor is given by the $10^4$ instructions per event, times the interaction rate of 600 KHz, or 6000 MIPS (million instructions per second).

---

[17] J. Seguinot et. al., CERN/DRDC/90-70,DRDC/P17;

[18] U. Buchner et. al., NIM A272(1988)695.

[19] J. Spengler MPI-H-1990-V6

The Level-1 algorithm discussed in Chapter 4 and also in APPENDIX A will be implemented using a processor with Data-Flow architecture with the processing elements imbedded in the data readout channel. The algorithm is precisely defined and amenable to implementation in hardware. Speed is of the utmost importance because it also translates directly into decreased costs for the buffer system used for the spectrometer detector information.

Five years ago, the UCLA group had a very successful experience building and using a Data-Driven processor[20] with 240 MIPS capability. This device, which was built for a Level-1 trigger for experiment UA8 at the CERN $Sp\bar{p}S$-Collider, illustrates the power of such architectures. This processor used 40 modules of two types to calculate the momentum and intercept position of fast protons traversing the UA8 roman pot spectrometers. The TDC readout, calculation and the final trigger decision were made in 1.4 $\mu$sec, of which only $\approx$450 nsec was used for the actual calculation.

The Data-Driven processor designed and built by the Nevis-Univ. Mass. group[21] for Fermilab experiment E690 is a much more powerful system and could provide our necessary online computing power this year. Thus, we have undertaken an R&D project to build and interface a version of their processor to our silicon system and test it in a beam in 1991. It is extremely cost-effective compared to, for example, a RISC processor farm of similar power. The processor configuration for our application is about one-third the size (in number of modules) of the configuration in use by E690 and should be relatively straight forward to build.

For the proposed experiment, we plan to update the technology we will actually use, to include such things as optical fiber data transmission, application specific integrated circuits (ASIC's), Digital signal processors (DSP), etc. Improvements in speed, flexibility and reliability will be sought.

Both the readout system and the Level-1 trigger processor are pipelined. Data read from the spectrometer detectors are transferred to FIFO memories in a very high speed data transport system, while the silicon vertex detector data enter the first stage of the data-driven processor described in Section 6.2. Data entering the first stage of the processor are quickly processed and sent on to the following processor segment. This frees the starting set of processor modules for the subsequent event. The results of the trigger calculation are used to direct the transfer of data through the transport system. Events emerging from the transport destination modules are sent to a VME or Fastbus-based data acquisition system for further Level-2 processing in a system of RISC processors, as well as data monitoring and recording.

## *6.1 Detector Readout System*

All detectors in the apparatus will be gated at every bunch crossing for which the readout is idle. The readout is started only if a Level-0 interaction trigger is present. Once initiated, the digitization and readout of the detector information will take two or more bunch crossings depending on the number and distribution of hits in the event. The minimum readout time is limited by the 1 $\mu$s drift time of the jet chambers. Data read from the spectrometer detectors are entered into digital pipelines (FIFO buffers) for storage until the trigger processor has completed its calculation. The data for accepted events are then passed on to the Level 2 processor farm.

Table 8 shows the numbers of detector elements, the average number of elements with hits, and the expected data lengths for each of the subdetectors in a single arm apparatus. In addition to the expected signal data length (35 Kbytes), we assume a 1% average noise rate with an average 4 bytes/hit. This yields a total average data length of 60 Kbytes/event.

---

[20] J.G. Zweizig et al.(UA8 Collaboration); Nucl. Instruments & Methods A263 (1988)188.

[21] W. Sippach et al., IEEE Trans. Nucl. Sci., 27 (1980) 578;
E.P. Hartouni et al., IEEE Trans. Nucl. Sci., 36 (1989) 1480;
B.C. Knapp, Proceedings of 4th Pisa Meeting on Advanced Detectors (1989), Nucl. Instr. & Meth. (in press - 1989)

*Table 8: Data Lengths by Detector*

| Detector | No. Elements | Hit Elements | Data Length(bytes) |
|---|---|---|---|
| Silicon | 115200 | 1000 | 4000 |
| Si Pixel | 4500 | 35 | 140 |
| Pixel DC 1 | 4480 | 18 | 72 |
| Jet Cham 1 | 7000 | 1000 | 4000 |
| Jet Cham 2 | 9600 | 1000 | 4000 |
| RICH 1 | 100000 | 1250 | 5000 |
| EM Cal 1 | 35000 | 540 | 2160 |
| Pixel DC 2 | 11040 | 15 | 60 |
| Jet Cham 3 | 5700 | 1300 | 5200 |
| Jet Cham 4 | 7100 | 1300 | 5200 |
| RICH 2 | 280000 | 1000 | 4000 |
| EM Cal 2 | 36000 | 420 | 1680 |
| Total | 615620 | | 35412 |

Emphasis is being placed on implementing a greater than usual concentration of intelligence near the front end through the use of integrated VLSI readout electronics. This will result in better compaction of the detector data and hence higher live times. As discussed in the following paragraphs, the development of VLSI readout electronics for the RICH and Silicon is already well underway.

**Silicon:** The silicon detectors will be read out using a high density (128 channels per IC) VLSI chip which employs sparse data scanning to minimize the number of cycles needed to read the data. The Berkeley SVX chip, which was developed for the CDF silicon-strip vertex detector, would be well suited to this application, but the current version may not be fast enough. However, the success of the present SVX and other chips gives us confidence that an IC which will meet our needs can be built within the time scale of this experiment.

We are presently designing a gate sequencing and readout control system for the silicon-processor interface, which we plan to test at CERN this year. In this system, the readout electronics is divided into three types of modules. A ReadOut Sequencer Module (ROSM) generates the signals necessary to gate the silicon readout chip (i.e. the SVX), and transfer the encoded hit data. Hit data is sent via a ReadOut Control Module (ROCM) associated with each set of 4 SVX daisy-chains (x and y of left and right detectors for a single half plane) to a ReadOut Link Module (ROLM) which interfaces with the Level 1 processor system. The data are then used by the processor system, and passed on for recording if the event is accepted.

**Chambers:** The chamber-hit times will be encoded and recorded using a 8-bit, 10 nsec bin, multiple hit TDC system. In this system, each sense wire signal is tested every 10 nsec starting from the bunch crossing (gate) signal. If a signal appears on a wire, the arrival time is saved in one of two 4 word × 8-bit 100 MHz FILO stacks. The encoding process will require 1$\mu$s (the maximum drift time) during which additional gates will be inhibited. This will result in a dead time of $\approx$20%. If no Level-0 signal arrives, a reset is generated and the chamber readout is aborted with no loss of live time. At the end of the readout cycle, the second FILO is enabled for readout of the next event, while data are transferred from the first set to FIFO buffers. Hit data from each chamber is transferred to the FIFOs over 20-32 parallel data streams arranged so that each stream receives approximately the same amount of data.

It would be desirable to incorporate some intelligence into the drift chamber readout electronics which would perform line-segment finding within the drift cells. This would reduce the amount of data transferred to, and saved in the FIFOs, and facilitate track reconstruction in the second level filter. This possibility is under investigation.

**RICH:** Cherenkov photons will be detected on pad detectors which are segmented into 27 groups of 64 row × 128 columns for the purposes of readout. The pad signals will be amplified and shaped by a 16-channel VLSI chip currently under development. The discriminated signals produced by these chips are latched into a 50 MHz shift register. Data readout proceeds by shifting out the hits a row at a time into a 128-bit row latch. Words which contain at least one set bit are latched in a second word from which the hit coordinates are encoded. The row number is given by counting the number of rows which have been shifted out, and the column number is determined by priority encoding. One hit is recorded and erased from the encoding register every 20 nsec until it is empty. Shifting of rows continues in parallel to the hit encoding unless a second non-zero row is found while encoding of a previous row is still in progress. One or more additional row buffers may be added to decrease the likelihood of stopping the row shifting process.

**Pixel Detectors:** The Pixel Drift Chambers will be read out with the same type of modules used for the tracking chambers. The silicon pixel detector will be read out with the same electronics used for the silicon vertex detector.

**Electromagnetic Calorimetry** The Electromagnetic Calorimetry will be read out by 64-channel 10-bit FADC modules. Each module will have 64 charge integrators with two FADCs for digitizing the latched analog signals and circuitry for suppression of empty channels.

**Data Transport System:** The data transport system is a crate-oriented, 200 Mbyte/sec synchronous backplane through which all accepted events are passed. The extremely high throughput of this system allows the transfer of all accepted event data over a single channel, facilitating the dispersal of event data to acquisition, monitor, and high level processors. Modules connected to a backplane can be either data sources or data sinks. Each source module in turn transfers all the data for one event in a broadcast mode. Any sink modules which are enabled may save the same event simultaneously. Multiple transport crates can be linked together in a tree structure for merging data from an arbitrary number of input sources or fanning out the data to an arbitrary number of destinations. A minimal programability will make it possible to configure the destination modules to select a subset of events.

## *6.2 Level-1 Trigger Processor*

Briefly, the properties of the Nevis-Univ. Mass Data-Driven processor are:

- **No centralized control:** There is no CPU in the system. The processor consists of an array of function modules, in which the arrival of data at a module initiates its operation.

- **Parallel:** Several data streams are processed in parallel. In our case, track finding in the silicon detectors is done in parallel in 8 identical processors (4 quadrants × 2 views). Other parallelism can be intrinsic to a processor structure.

- **Pipelined:** Several events are in the processor simultaneously. For example, with an interaction rate of 600 KHz and an event processing time of about 15 $\mu$s, about 10 events would be in the pipeline at a time.

- **Synchronous:** All registers in the system are latched simultaneously by a 40 MHz central clock.

- **Expandable:** The processor may be increased to solve an arbitrarily complex problem by the addition of more modules. Since there are no resources like central memory or common I/O paths, bottlenecks do not appear. Also, because there is very little overhead, an increase in the number of processor modules yields a proportional increase in processor speed. This will be a very valuable attribute in the future, when there will be a need to upgrade the data acquisition system to handle the higher luminosities which will be available at the new proton-proton colliders.

The processor modules are themselves quite simple. Each module takes one or two 24 bit (16 data + 8 control) input data words, performs some simple operation on them and produces an output which is passed on to the next module. All modules in the system are clocked synchronously and the input and output data words are latched into registers on each clock cycle. Care has been taken to provide access to all of the input and output registers in the system, either for reading data or inserting data. This greatly simplifies the task of debugging and diagnosing problems, since the state of the system can be determined and checked on a cycle by cycle basis.

Fig. 20 is a block diagram of the processor. There are five subroutines shown, which are isolated from each other by control buffers. The 3-plane line-finder, discussed below, contains most of the hardware, with 8 identical sections (corresponding to 4 quadrants × 2 views). Each of the 8 line-finders utilizes about 20 existing modules, for a total of 160 modules.

**Line-Finder**

Of the subroutines listed above, the track finding step is the most complex, and provides the greatest challenge for optimal design and construction. Fig. 21 shows a diagram of this subroutine,[22] which uses the processor modules in a configuration similar to that used by FNAL experiment E690. Depending on the required throughput, the line-finding may be performed by a single set of modules which would process each detector triplet in succession, or by many similar sets, each of which would perform the line-finding in one or a few plane triplets. With multiple independent line-finders, the effective throughput is increased by the same factor as the number of line-finders.

The following is a somewhat simplified description of the operation of the line-finding subroutine illustrated in Fig. 21. Hit strip addresses enter on the readout bus. Data from different detectors in the same quadrant appear on the same bus, and are distinguished by a 4-bit identification field (Tag). The **Buffer** modules (Labeled B in Fig. 21) select the hits from a single detector, and store them in a First-In-First-Out (FIFO) memory for eventual retransmission into the remainder of the subroutine. The hits from the first and third planes of a detector triplet are then associated into clusters by the **Associator** (A) modules and entered into lists in the **List** (L) modules. In addition, as cluster positions are entered into the lists, they are counted by the **Index Generator** (I) module. The **Index Generator** starts immediately to generate all pairs of indices of clusters in the lists. Each generated index pair causes the two **List** modules to output the cluster positions specified by those indices. The positions are then multiplied by a constant in the **Normalizer** (N) module and added together (⊕ module) resulting in a prediction of a hit position in the second plane of the triplet. If there is a hit in the second plane corresponding to the value thus predicted, it is taken to indicate the existence of a track, and the hits which define the track are added to a track list. This last function is performed by a **Map** (M) module which saves the hits from the second plane in an internal bit map. It then uses the incoming hit predictions to fetch the hits in the region of the prediction. The **Table** (T) module which follows the **Map** determines whether the neighboring hits meet the track acceptance criteria by table lookup. The hits from the first and third planes associated with the accepted lines are added to the list by the **List Counter** (Lc) modules. The resulting list of hits on tracks is then entered into buffers for use by the subsequent stages of the processor.

---

[22] We thank Bruce Knapp for his design of this hardware "subroutine"

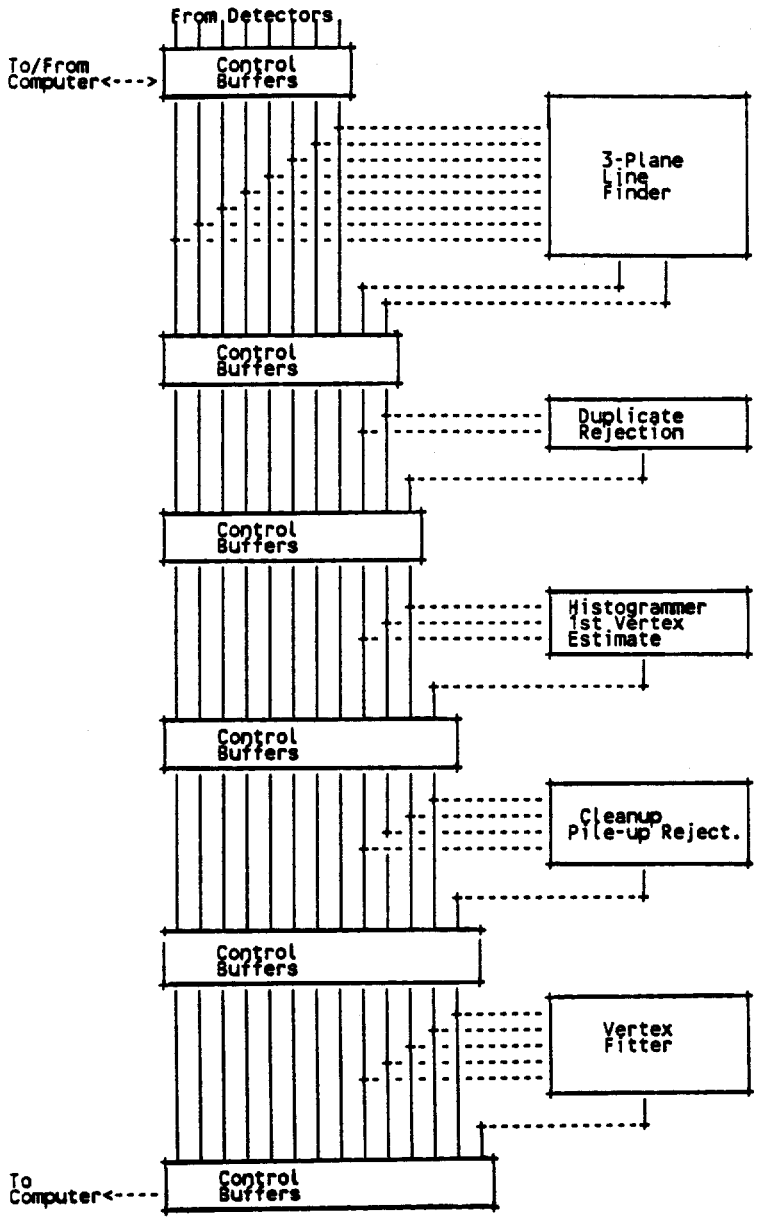


*Figure 20: Block Diagram:* Level-1 Trigger Processor with Data-Flow Architecture

The final translation of the algorithm described above into a hardware configuration will be made using emulation and analysis of the processor's response to the silicon data have obtained in our P238 Sp$\bar{p}$S-Collider test run. Preliminary design work indicates that we will need fewer than 100 additional modules for the remainder of the system, for a total of about 250 modules (compared to about 700 modules for the E690 processor). Almost all module types already exist and are in use by the E690 Collaboration. The remaining 1-2 modules are simple extensions of the existing architecture.

**Processor Emulator**

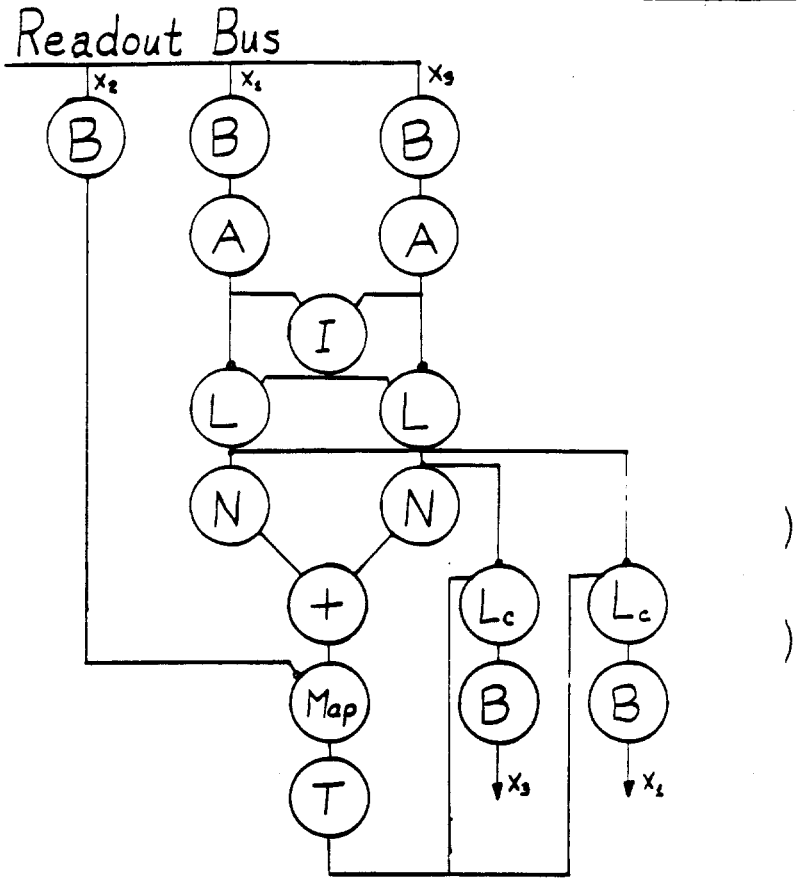


*Figure 21: Block diagram of the Data-Driven Line-Finder.*

The operation of the entire processor structure is being emulated in software. The processor emulator is a package designed to duplicate in software the action of the processor on a cycle by cycle basis. A FORTRAN subroutine is written for each type of module, of which there are about 20. One subroutine call corresponds to one clock cycle.

A processor algorithm consists of a list of boards, the specification of the contents of any memory elements on those boards and the specification of how these boards are cabled together. Such a list is known as a **Configuration File.** The emulator reads this file in its initialization phase and thus determines which board subroutines are to be called. It calls these subroutines, which in turn reserve enough memory to hold any tables which must be down-loaded as well as memory locations for the input and output registers. Storage is also reserved to hold cable contents and pointers are set up to the memory locations which hold the contents of the input and output cables. After this initialization phase, the memory locations, reserved to hold on-board tables, are loaded by simulating the cycles that would be executed by the processor hardware in performing this function.

After the initialization phase, the emulator is ready to process data. Data is loaded into the locations which correspond to the input cables and the board subroutines are called as specified in the **Configuration File.** Each board subroutine checks for data on the input cables and, if present, performs its operations and modifies the memory locations which correspond to its on-board registers and out-

put (and possibly input) cables. This procedure precisely emulates the processing performed in one clock cycle. The process is repeated for subsequent cycles until the data (and control "signals") propagate through the entire "processor" and appear in those locations which correspond to the processed data cables and the output control buffers.

Using the emulator, it is possible to precisely predict the operation of a given algorithm on any set of simulated event data. For example, the average number of clock cycles per event can be easily determined, problems of precision can be investigated and bottlenecks in the algorithm calculations can be located.

The emulator can be used not only for the design and evaluation of processor configurations, but also can serve as a powerful diagnostic tool when the same data is given to both the emulator and the hardware processor and the results of the computation compared. The operation of a single board can thus be evaluated, as can the operation of an entire subroutine.

### *6.3 Level-2 Trigger Processor*

A second level of filtering for all events which pass Level-1 will be implemented as a farm of high-speed (50 MHz or greater) RISC processors which would have access to all the data for a given event. These processors may perform some or all of the following functions:

- Perform complete track reconstruction,
- Eliminate most pileup events by requiring that the total longitudinal momentum of all tracks in either the forward or backward hemisphere does not exceed the beam momentum (as required by conservation of momentum and energy), and that there is at most one vertex with tracks in both the forward and backward hemispheres.
- Repeat the Level-1 test with matched views, and correct weighting based on the track momenta.
- Determine the event topology.

To determine the size of the RISC farm necessary to perform these functions we assume that the average event will require $5\times 10^6$ RISC instructions.[23] To handle the 6.7 KHz rate we estimate that we will need a "farm" with about 670 × 50MIPS RISC processors. Clearly, should faster processors become available, this number can be reduced.

## *7. FLAVOR TAGGING: LEPTONS VS. KAONS*

To avoid the very large event loss which arises from requiring full reconstruction of both B and $\overline{B}$ in the spectrometer, we advocate just using as tags, supplementary particles in the spectrometer which are inconsistent with coming from the primary vertex (as determined using the vertex detector information). As discussed in the following paragraphs, these can be either charged kaons or leptons. In order to understand the tagging possibilities of $K^{\pm}$ and leptons, an analysis was made of Monte-Carlo generated $B\overline{B}$ events using PYTHIA. In the event generation, no requirements are made on the hadronization or decay of the associated b-quark which provided the potential tag. Of course, these esti-

[23] Note that the $5\times 10^6$ instructions is an average figure, some events will take considerably more or less than this mean. Note also that some of the reconstruction tasks will have already been performed by the Level 1 processor (e.g. line finding in the silicon) and readout system.

mates depend greatly on the correctness of PYTHIA's hadronization scheme, which could be verified by measurements at existing hadron colliders.

For a $B_s$-Mixing experiment, charged kaons from the primary vertex can also be used, because their flavor is potentially correlated with the flavor of a reconstructed $B_s$-Meson. Such kaons have an advantage over those from secondary sources, in that there are no oscillation effects of the tag-providing system

**The Use of Muon Tags:** For events in which a Beauty meson is detected in a 600 mrad spectrometer at the Tevatron Collider, what are the momenta and angles in the laboratory of an accompanying muon ? This question is answered in Fig. 22, which is a scatter plot of $p_\mu$ vs. $\theta_\mu$ in the laboratory, for Tevatron events which contain both a B accepted in the 600 mrad spectrometer and a muon from any source with momentum transfer, $p_t > 1.2$ GeV. The correlation which is expected between a B and a $\mu$ from its partner $\bar{B}$ is clearly visible. Most muons are in the same hemisphere as the B detected near 0° and correlated within ~1 unit of rapidity. Furthermore, the muons within the spectrometer aperture of 34.9° (600 mrad) are seen to have much larger momenta than those outside the spectrometer. We can conclude that, for Beauty particles detected in the 600 mrad spectrometer, there is not much to be gained by constructing additional lepton detection outside the 600 mrad aperture.

At $\sqrt{s} = 1.6$ TeV, we find that 5.7% of B-Mesons which are accepted in the spectrometer have an accompanying $\mu^\pm$ also in the spectrometer with $p_t > 1.2$ GeV (necessary to suppress muons from the $c \to s$ transition). The tag quality factor, (good tags/all tags), is found to be 73%. The quality factor can be improved by selecting larger $p_t$, but with a loss of muons. If electron tag are also used, the fraction of tagged events could increase to an upper limit of 11.4%. However, additional losses arise from cuts needed to minimize the background from other sources. We have not attempted to estimate these losses since, as discussed in the next section, the use of $K^\pm$ tags is more promising.

**The Use of Secondary $K^\pm$ Tags:** The overall strategy is to examine supplementary kaons in the spectrometer (those not associated with the reconstructed B). There are two major sources of such kaons. They either come from the accompanying $\bar{B}$ meson or they come from the primary vertex. Those from the primary vertex are only useful for tagging reconstructed $B_s$-Mesons and we return to them below.

A $K^\pm$ which contains the s-quark at the end of the $b \to c \to s$ chain uniquely identifies the flavor of its $\bar{B}$-meson at decay. However, there are many sources of mis-tagging, such as kaons which are produced from the $s\bar{s}$ sea or from a $W^\pm$ in either the $b \to c$ or $c \to s$ transitions (which can have either sign). All these possibilities are accounted for to some approximation in the PYTHIA event generation and can be investigated by tabulating the supplementary kaons which are found in the spectrometer. For Tevatron events with $\sqrt{s} = 1.6$ TeV, 25.5% of the B-mesons in the spectrometer are found to have a supplementary $K^\pm$ with reconstructed impact parameter greater than $3\sigma$ from the primary vertex. The correct charge was found in 82.2% of these tags (good tags/all tags). Thus, secondary $K^\pm$, $\mu^\pm$ and $e^\pm$ together can tag as much as 35% of all Beauty particles reconstructed in the spectrometer.

**The Use of Primary $K^\pm$ Tags in $B_s$-Mixing Measurement:** A primary $K^+$ or $K^-$ potentially contains the $\bar{s}$ or s quark which is created in association with the s or $\bar{s}$ quark used in a reconstructed $B_s$ or $\bar{B}_s$, respectively. They should be produced nearby in rapidity. Note that the sign of such a primary $K^\pm$ has exactly the opposite tagging significance as does a secondary $K^\pm$.

Background comes from kaons produced from the $s\bar{s}$ sea in the numerous hadronization processes at the primary vertex which are not associated with the $B_s$ or $\bar{B}_s$ mesons. Such kaons can be of either flavor and thus dilute the kaon tagging. We have performed a complete detailed analysis of Monte-Carlo $B_s$ events at the lower energy $Sp\bar{p}S$-Collider and find that the primary kaons are just as effective in flavor tagging reconstructed $B_s$ mesons as are secondary kaons. 26% were tagged by secondary $K^\pm$. An additional 26% were tagged by primary $K^\pm$ and a further 7% were tagged by both types of $K^\pm$. Thus, a total of 58% of all reconstructed $B_s$ were tagged in this way. The tagging quality of these events ranged from 70-76%.

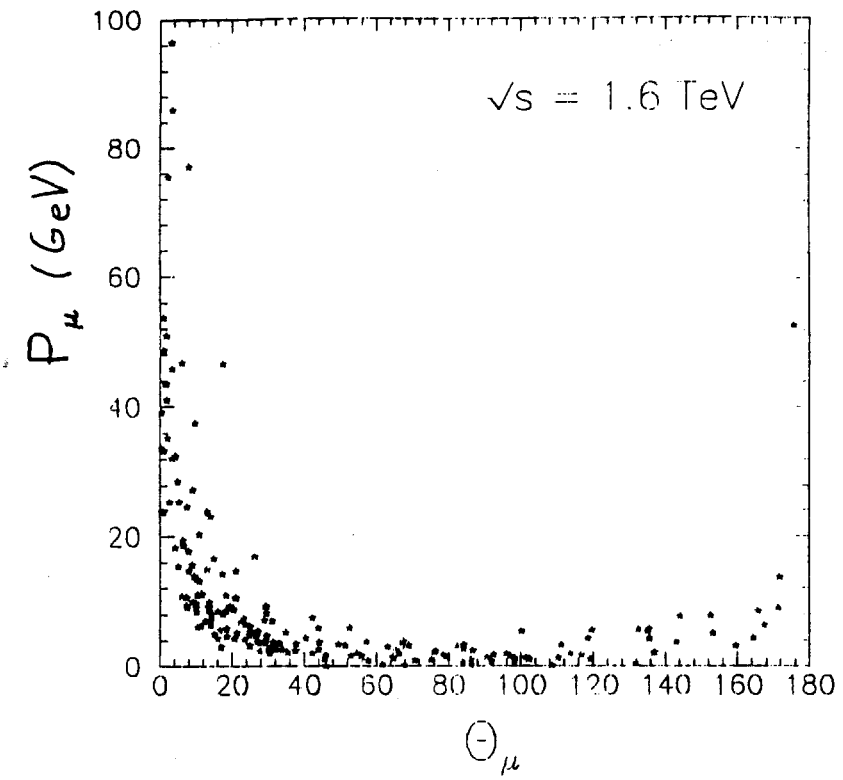


*Figure 22: Laboratory Momentum vs. Angle of* Muons Accompanying an Accepted B at the Tevatron. The detected B is on the 0° side. The muons have $p_t > 1.2$ GeV.

We are presently repeating this analysis for $B_s$ events at the Tevatron and expect that some additional contribution will indeed be offered by primary kaon tagging. However, it may be a somewhat smaller amount at the Tevatron energy because of enhanced kaon production from the $s\bar{s}$ sea.

**Dilution Effects:** There are two types of dilution (decrease in statistical effectiveness) due to mis-tagging. One arises simply from using a tagging particle (kaon or lepton) which has the wrong sign because its source is extraneous. The other arises from the fact that the B (or $\bar{B}$) which provides the tagging particle may itself oscillate and thereby give the wrong sign tag. The estimates of mis-tagging given in the previous paragraphs are obtained with the use of a Monte-Carlo generator which does not have B-oscillation built into it. Thus the estimates are of the first type of mis-tagging. As pointed out in Chapter 2, the relevant factor is not the "tag quality", but rather the quantity, $k_1$ = (good tag − bad tag)/(good + bad). For example, a "tag quality" of 0.8 yields for this dilution factor: $k_1 = 0.60$.

To estimate the dilution factor, $k_2$, from the second type of mis-tagging due to the oscillation of the tag-providing B (or $\bar{B}$), we must use the time averaged probabilities for oscillation and non-oscillation: $x^2/[2(1+x^2)]$ and $(2+x^2)/[2(1+x^2)]$, respectively. Here $x \equiv \Delta M/\Gamma$ for the source B. Because the expected decay time dependences of the tagged-B (or $\bar{B}$) are of the general form $1 \pm a(t)$, it is explicitly shown in Chapter 2 on $B_s$-Mixing that the dilution factor multiplies the a(t) term and is given by the weighted average of the quantity $1/(1+x^2)$ over the three types of tag-producing B's according to their relative production frequency.[24] A weighted average, of $[1/(1+x^2)]$ over $B_u$ (40%), $B_d$ (40%) and $B_s$ (20%) is found to be: $k_2 \approx 0.67$, if we assume x to be 0, 0.7 and 15, respectively, for

[24] P. Krawczyk, D. London & H. Steger, DESY-163 (Nov. 1988).

the 3 cases. Thus, the net dilution factor can typically be expected to be: $K = k_1 \cdot k_2 \approx 0.40$.

## 8. RECONSTRUCTION OF B-EVENTS, YIELDS & BACKGROUNDS

### 8.1 General Considerations and Lifetime Measurements

We present here a study of the problems of B event reconstruction and sources of combinatoric background which was done for a c.m. energy, $\sqrt{s} = 0.63$ TeV, where the mean momentum of reconstructed B-mesons is 35 GeV. Since this momentum is expected to be about 45 GeV at the Tevatron, and since there is not much increase in track multiplicity through the silicon detectors, the conclusions should also be valid for the Tevatron.

Software was written to reconstruct Monte Carlo Beauty events which were generated using PYTHIA. In addition to minimum bias and charm events, two types of Beauty Monte Carlo event samples were studied: (a) a general or inclusive $B\bar{B}$ sample, in which B-mesons decay according to the "natural" B decay modes given by PYTHIA, and: (b) events in which all B's decay via the particular mode under study. In both cases, PYTHIA generated an underlying event, similar in structure to a minimum bias event, in addition to the decay tracks from the B and $\bar{B}$ states. Unit vectors describing track direction and position were obtained from a full silicon detector simulation using the program GEANT. Momentum measurement errors were simulated by randomly varying the generated Monte Carlo momentum, in accordance with expected spectrometer resolutions. We assumed that x/y view matching as well as track matching between the spectrometer and silicon detector could be done without significant error.

For the exclusive decay mode samples, events whose B-meson decay products are completely contained in the spectrometer aperture are passed through the trigger algorithm simulation software. Surviving events are used to evaluate the reconstruction efficiency. Minimum bias and inclusive $B\bar{B}$ events are passed through the same software chain used for the exclusive final state in order to determine the combinatoric background level.

Studies were also made of the response of our trigger algorithm and Beauty reconstruction software to inclusive $c\bar{c}$ (charm) states. We found that the topological information in the silicon detectors, together with the larger energy release in Beauty decay, allowed us to reject background from $c\bar{c}$ states to a negligable level.

On the question of final states with a single $\pi^0$, we have not yet been able to demonstrate that acceptable signals with low-background can be extracted from the data. On the other hand, final states with a single $\gamma$, such as Reaction (20) discussed in Section 8.2, can be cleanly extracted. This should also be the case for $D^{0*} \to D^0\gamma$, as has been mentioned above. In general, we find that if an e.m. calorimeter with the superb resolution of $\sigma = 0.5\% \cdot \sqrt{E}$ is assumed, the invariant mass resolution for the B is comparable to that obtained for final states with all charged particles. See the discussion in Section 8.2.

Reconstruction software for exclusive final states proceeds in the following way. A vertex-finding algorithm which consists of the repeated application of a vertex search among tracks that do not come from previously found vertices is applied. After vertex finding each individual decay mode is reconstructed using separate subroutines. In all of these subroutines, relevant invariant masses are calculated for all possible track combinations consistent with the desired topology. Also, for most decay modes, a minimum flight path of 0.5 mm is required for the B-meson, making it possible to impose transverse momentum balance with respect to the B direction of motion. This is found to greatly suppress combinatoric background under the B signal.

We present details of the analyses of some exclusive final states in the succeeding sections. The general conclusions of these analyses are that clean signals can be found and that the chief sources of

combinatoric background to B-meson signals are: (a) those $B\bar{B}$ events which have similar topologies but which decay via modes other than the one under study; or (b) from the same mode, but where one or more tracks can not be uniquely assigned to the B decay vertex. In a sample of 4000 minimum bias events, no events survived Level-1 trigger cuts and produced a secondary vertex other than from strange particle decay. Thus we conclude that background from minimum bias is less than a third the background from events which contain Beauty.

**Analysis of:** $B^0 \rightarrow \bar{D}^0\pi^+\pi^- \rightarrow (K^+\pi^-\pi^-\pi^+)\pi^+\pi^-$

We start by calculating the invariant mass for each $K^+\pi^-\pi^-\pi^+$ track combination which is consistent with having a common vertex. For combinations with a mass near to that of the $\bar{D}^0$, we loop over the remaining $\pi^+\pi^-$ pairs which have a common vertex at least 0.5 mm downstream of the primary vertex but no further downstream than the $\bar{D}^0$ vertex. Finally, we reconstruct the momentum vectors of the $B^0$ and $\bar{D}^0$ requiring that the $\bar{D}^0$ momentum vector be collinear with the line connecting the $B^0$ and $\bar{D}^0$ vertices and that the $B^0$ momentum vector be collinear with the line connecting the $B^0$ vertex with the primary vertex. For these events, the $\bar{D}^0\pi^+\pi^-$ invariant mass is calculated.

Fig. 23 shows the $K^+\pi^-\pi^-\pi^+$ and $\bar{D}^0\pi^+\pi^-$ invariant mass spectra. In both Figs. 23(a,b), the unshaded histograms show all possible track combinations with no cuts on vertex topology. The shaded histograms show the effects of imposing the vertex topology and momentum conservation cuts referred to in the preceding paragraph.

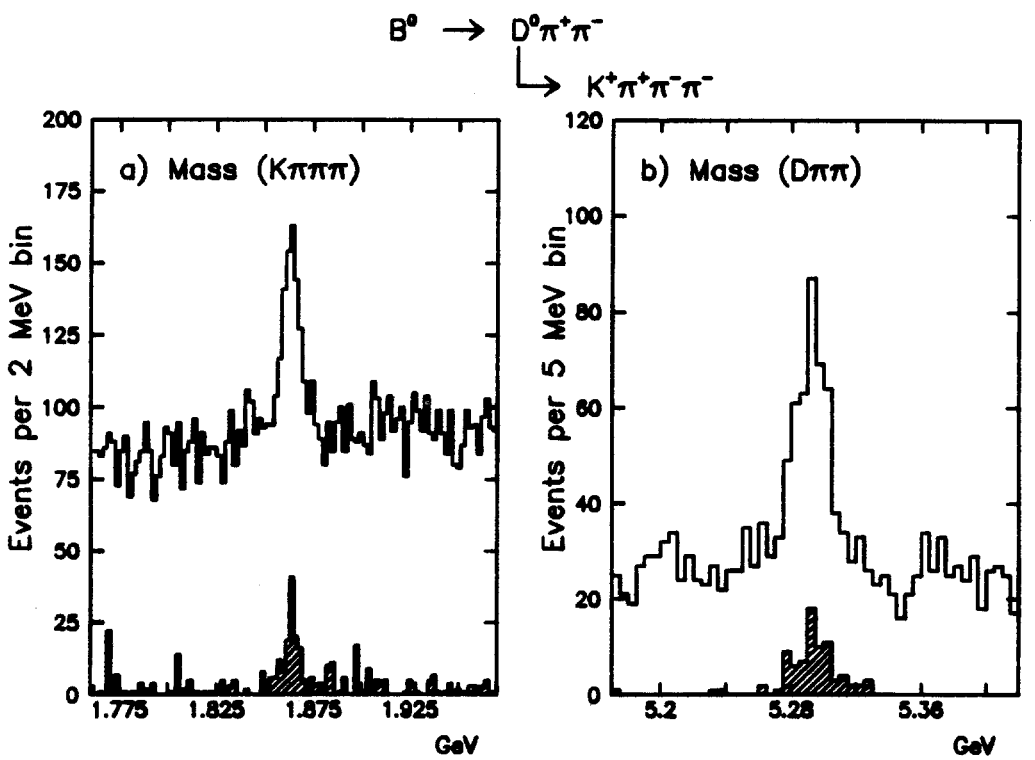


*Figure 23: Invariant Mass Spectra for the Final State* $\bar{D}^0\pi^+\pi^-$. (a) $\bar{D}^0$ signal in $K^+\pi^-\pi^-\pi^+$ spectrum; (b) $B^0$ signal in $\bar{D}^0\pi^+\pi^-$ spectrum, both with no vertex cuts. The shaded areas in each plot show the signals which remain after applying the vertex cuts discussed in the text.

This figure does not reflect the true background level since it contains only the combinatoric background from events containing $B^0$ mesons decaying according to the reaction $\bar{D}^0\pi^+\pi^-$. When background generated from all other sources is included, the B-signal/background ratio is estimated to be larger than 5/1.

**Analysis of:** $B^0 \rightarrow D^{*-}\pi^+\pi^+\pi^- \rightarrow ((K^+\pi^-\pi^-\pi^+)\pi^-)\pi^+\pi^+\pi^-$

We start by calculating the invariant mass of all $K^+\pi^-\pi^-\pi^+$ combinations which are consistent with a common vertex. For each such combination which has a mass near to the $\bar{D}^0$ mass, we calculate the $\pi^-K^+\pi^-\pi^-\pi^+$ invariant mass using all remaining $\pi^-$ tracks in the spectrometer. Fig 24(a) shows the distribution of the mass difference between these two combinations. The peak is quite clean. For combinations which are consistent with being from the decay of a $D^{*-}$, we calculate $(\pi^-K^+\pi^-\pi^-\pi^+)\pi^+\pi^+\pi^-$ invariant mass. We demand that the $D^{*-}/D^0$ mass difference be small, and use the momentum conservation cut described above and somewhat less stringent cuts on event topology. The $(D^{*-}) - (\bar{D}^0)$ mass constraint is sufficiently powerful that a reconstruction efficiency of more than 40% can be obtained. The resulting mass distribution is shown in Fig. 24(b). For this mode, we find that little background is contributed by events with B's decaying inclusively, thus the figure represents the true background level.

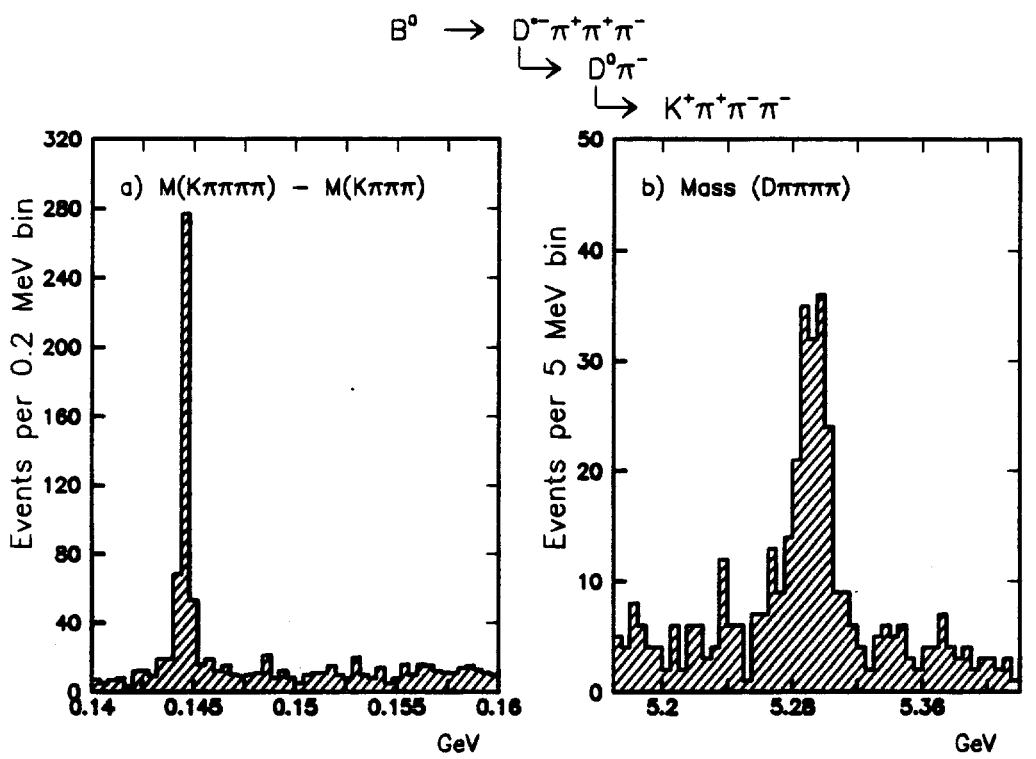


*Figure 24:* (a) The distribution of the difference in invariant mass between $K^+\pi^-\pi^-\pi^+$ and $\pi^-(K^+\pi^-\pi^-\pi^+)$ combinations as explained in the text. (b) The $B^0$ signal in the $(\pi^-K^+\pi^-\pi^-\pi^+)\pi^+\pi^+\pi^-$ mass spectrum when $\pi^-(K^+\pi^-\pi^-\pi^+)$ satisfies the $\bar{D}^{*-}$ mass constraint, $K^+\pi^-\pi^-\pi^+$ satisfies the $\bar{D}^0$ mass constraint and after topology and momentum conservation cuts have been applied.

**Analysis of $B^0 \rightarrow J/\psi^0 K^0 \rightarrow (e^+e^-)(\pi^+\pi^-)$**

The analysis proceeds by forming the invariant mass for all $e^+e^-$ pairs. The resulting mass plot is shown in Fig. 25(a). Next, the invariant mass for all $\pi^+\pi^-$ combinations is calculated and $K^0$ candidates defined by requiring that this mass be near the $K^0$ mass. We then calculate the invariant mass for all $J/\psi^0$ candidates (defined only by a mass cut) with all $K^0$ candidates. The resulting mass plot (with no vertex cuts) is shown in Fig. 25(b).

The $J/\psi^0$ cut alone suppresses virtually all background from $B^0$ decays. Background from direct $J/\psi^0$ production has not been studied but a combination of topology and transverse momentum cuts should reduce it to manageable levels with some sacrifice of signal.

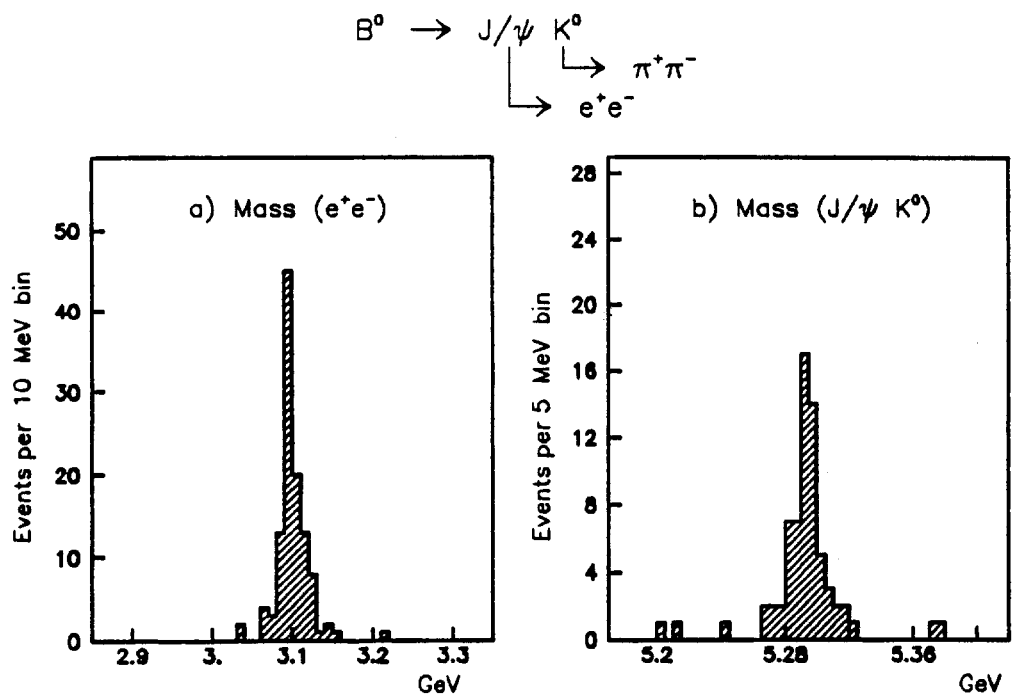


*Figure 25: Invariant Mass Spectra for the Final State $J/\psi\ K^0$.* (a) $J/\psi$ signal in $e^+e^-$ spectrum; (b)$B^0$ signal in $J/\psi\ K^0$ spectrum, both with no vertex cuts.

**Lifetime Measurements**

The mean reconstructed B-meson momentum of about 45 GeV/c (see Fig. 9 in Chapter 3) and the mean distance of 2 cm between event vertices and first silicon detector plane allow rather good measurements of proper flight time for each event.

Fig. 26 displays the simulated proper time distribution (in units of B mean life) expected for a 9000 event sample.

It is seen in Fig. 26 that we have excellent acceptance in t above about one mean life. The departure from a pure exponential in Fig. 26 illustrates the combined effect of the geometrical acceptance

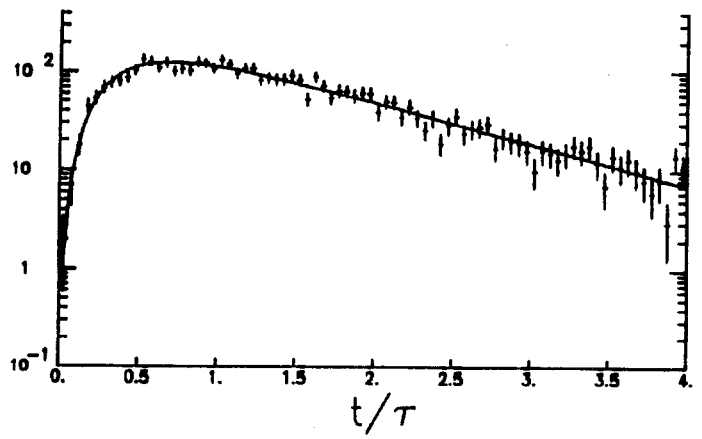


*Figure 26:* Simulated proper time distribution (in units of B mean life) for 9000 reconstructed $B_s$ events. The departure from a pure exponential illustrates the acceptance effects of geometry, trigger and event reconstruction. The superimposed curve is the empirical acceptance function $A(t) = 4t^2/(1+4t^2)$ multiplied by $e^{-t}$ This curve is a reasonably good fit to the B events which have been accepted by our trigger simulation and reconstruction programs.

(aperture) and trigger efficiency. The acceptance function, $A(t) = 4t^2/(1+4t^2)$, approximately describes the net acceptance and is used in the generation of Monte-Carlo events in the mixing and CP violation studies summarized in Chapter 2. This function is multiplied by $e^{-t}$ and superimposed on the generated data in Fig. 26. In our mixing studies, simultaneous fits to the data shown in Fig. 26 and to the subset which is flavor tagged (as described in Chapter 7) are performed to obtain the B mean life, $x = \Delta M/\Gamma$ and the dilution factor, K.

The experimental resolution in the measured proper time is obtained by comparing the generated $B_s$ flight path with its reconstructed value for a large number of Monte-Carlo events. This difference quantity is plotted in Fig. 27 and is seen to have a standard deviation, $\sigma_z = 180\ \mu m$.

The error in proper time, $\sigma_t$, is obtained from the relation $z = ctp/m$ and $\sigma_z = 180\ \mu m$. With a mean $p = 45$ GeV, we find $\sigma_t = 5.8$ %. For a number of reasons, the expected value will be somewhat smaller than this. First, the data in Fig. 27 are calculated using a distance of 6 cm between silicon detector planes used in the P238 silicon configuration. We have since decided to decrease this distance to 4 cm. Second, it is likely that the algorithm used in the calculation of the data in Fig. 27 can be further improved.

## 8.2 $B_s$ Reconstruction: Signal Yields & Background Estimates

The previous section contains a discussion of the B-meson reconstruction procedure and combinatoric background problem in some detail, for specific exclusive final states. However, for a $B_s$-mixing measurement, we anticipate using a final state such as:

$$\begin{aligned} B_s &\to D_s^* \pi\pi\pi \\ &\quad\ \to D_s \gamma \\ &\qquad\ \to \phi\pi \\ &\qquad\qquad \to K^+K^- \end{aligned} \tag{20}$$

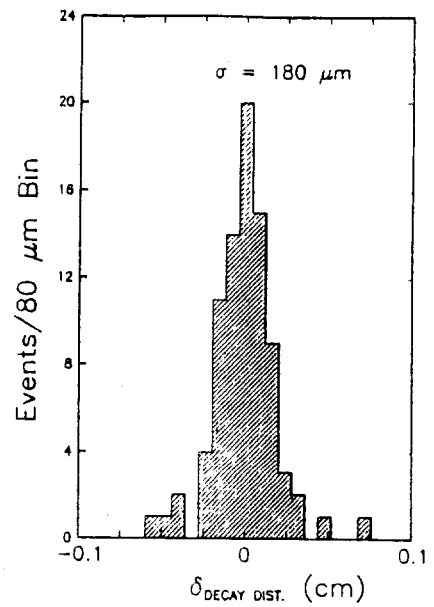


*Figure 27:* Difference between Monte-Carlo generated and reconstructed B track length. The width of this distribution (standard deviation, $\sigma_Z$ = 180 $\mu$m) gives the uncertainty in our measurement of the B track length. As discussed in the text, several improvements in software and hardware will result in $\sigma_Z$ actually being smaller than this value.

which introduces a new factor, namely the effect of using electromagnetic calorimeter information in the $B_s$-meson reconstruction.[25] We have thus studied the effect of calorimeter energy and spatial resolutions on both the reconstruction yield and the $B_s$ signal/background ratio.

Following the procedures of the last section, we construct the invariant mass difference, $M(D_s^*) - M(D_s)$ for the $B_s$ decay in Reaction 20. We plot the resulting mass difference distributions in Fig. 28 for 12 combinations of calorimeter parameters. Calorimeter energy resolutions ($\sigma/\sqrt{E}$) of 0.5%, 1%, 2% and 4% and spatial resolutions of 0.3 mm, 1.0 mm and 10 mm are considered. In constructing these plots, we randomly vary all charged track and $\gamma$ parameters in accordance with the expected energy and angular resolutions. Since the purpose of these plots is to demonstrate the effect of different calorimeter resolutions on the invariant mass resolution, we do not include the combinatoric background resulting from all possible track combinations – only the correct $B_s$ decay tracks are used.

Although there is very little dependence of the invariant mass difference resolution on calorimeter spatial resolution seen in Fig. 28, there is a very large dependence on its energy resolution. For a $0.5\% \cdot \sqrt{E}$ calorimeter, the FWHM is 2 MeV, while for $4\% \cdot \sqrt{E}$, the FWHM increases to about 12 MeV. As will be demonstrated below, the effect of this poorer resolution is to allow more combinatoric background into the signal region and also to lose some signal because some of the tails in the $M(D_s^*) - M(D_s)$ distribution will be cut off. In addition, a larger fraction of the $\gamma$'s from $D^*$'s combine with other $\gamma$'s in the event to form a $\pi^0$ mass; these are then cut out in our selection procedure.

[25] With electromagnetic calorimetry, we would also have the capability to detect B final states which contain $D^{*0} \to D^0\gamma$ (BR = 48%) for the first time, thereby opening the door to the study of entire new classes of final states..

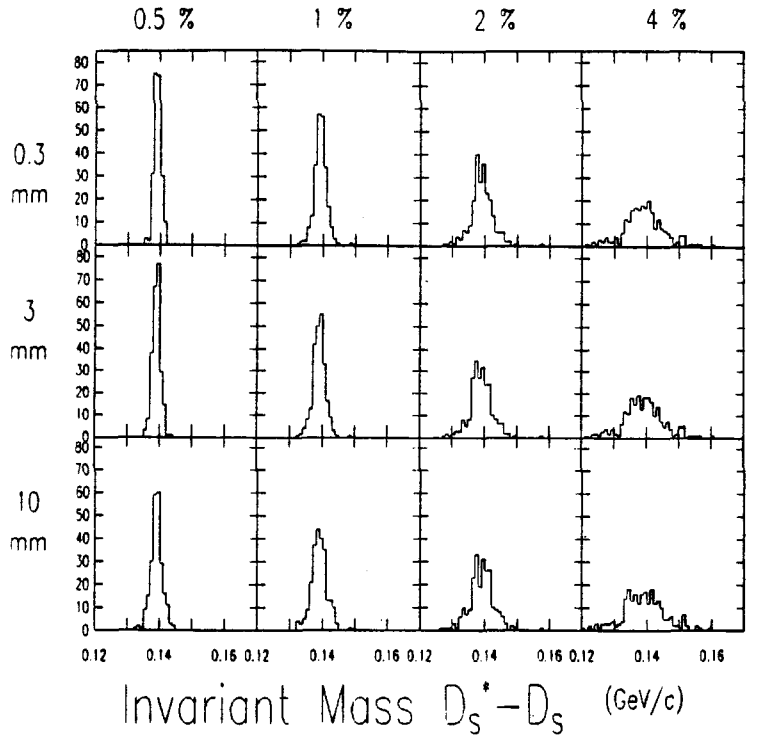


*Figure 28:* Invariant mass differences, $M(D_s^*) - M(D_s)$, for the indicated 12 combinations of electromagnetic calorimeter energy and spatial resolutions. The spatial resolution is the standard deviation, $\sigma_x$. The mass bins are 1 MeV. No combinatoric background is shown. In each case, the energy resolution $\sigma_E/E$ is the indicated constant (e.g. k = 0.5%) divided by $\sqrt{E}$ in GeV.

Using appropriate mass cuts in Figs. 28 to select most of the signal peaks leads to the $B_s$ invariant mass distributions shown in Figs. 29 for the same sets of calorimeter parameters. Although there is a significant dependence of the mass resolution on calorimeter parameters, the dependence is weak, due to the fact that, in general, the $\gamma$ possesses only a small part of the $B_s$ energy (average $\gamma$ energy is about 1 GeV for a $B_s$ energy of 35 GeV).

Before discussing the matter of how the signal/background ratio depends on calorimeter resolution, we show in Fig. 30(a) the expected $B_s$ signal for the best calorimeter case ($0.5\% \cdot \sqrt{E}$ and 0.3 mm), with all combinatoric background. Fig. 30(b) shows the expected $D_s$ signal with its combinatoric background.

The $B_s$ signal size and signal/background ratio have been evaluated for all 12 sets of calorimeter resolutions considered (we include the expected background from the general B event sample, in addition to the combinatoric background arising from Reaction (20). Figs. 31 shows the signal/background results. For the $4\% \cdot \sqrt{E}$ and $0.5\% \cdot \sqrt{E}$ calorimeters, the signal/background is about 4 and 10, respectively. The degradation of the $B_s$ reconstruction efficiency with worsening calorimeter energy resolution is also noticable. We find 29% and 43%, respectively for the two calorimeter types.

**Yields of $B_s$-Mesons**

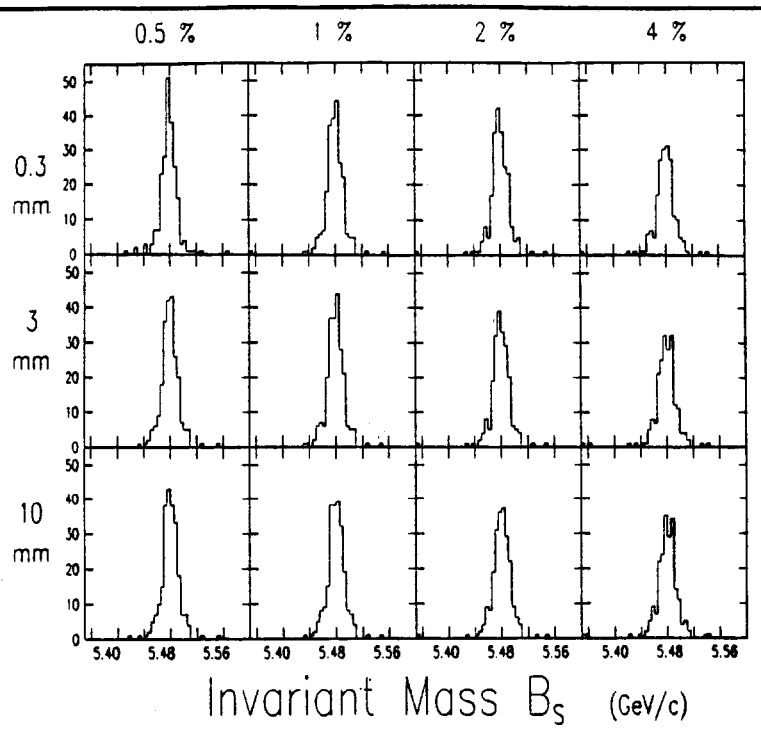


*Figure 29:* Reconstructed $B_s$ Invariant Mass for the indicated 12 combinations of electromagnetic calorimeter energy and spatial resolutions as in Fig. 28. In each case, an appropriate cut is made on the mass difference, $M(D^*) - M(D_s)$, of the corresponding plot in Fig. 28. The mass bins are 5 MeV. No combinatoric background is shown.

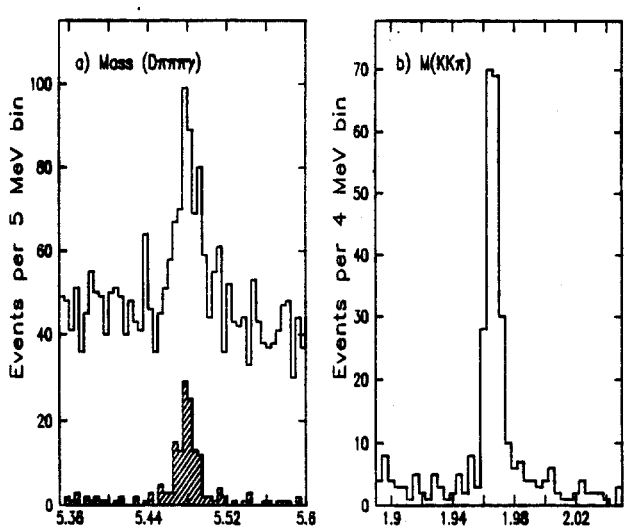


*Figure 30:* (a) Reconstructed $D^*_{\pi\pi\pi}$ invariant mass and (b) $KK\pi\gamma$ invariant mass. Both plots assume calorimeter energy resolution $\sigma_E = 0.5\% \cdot \sqrt{E}$ and position resolution = 0.3 mm. All expected combinatoric background is shown.

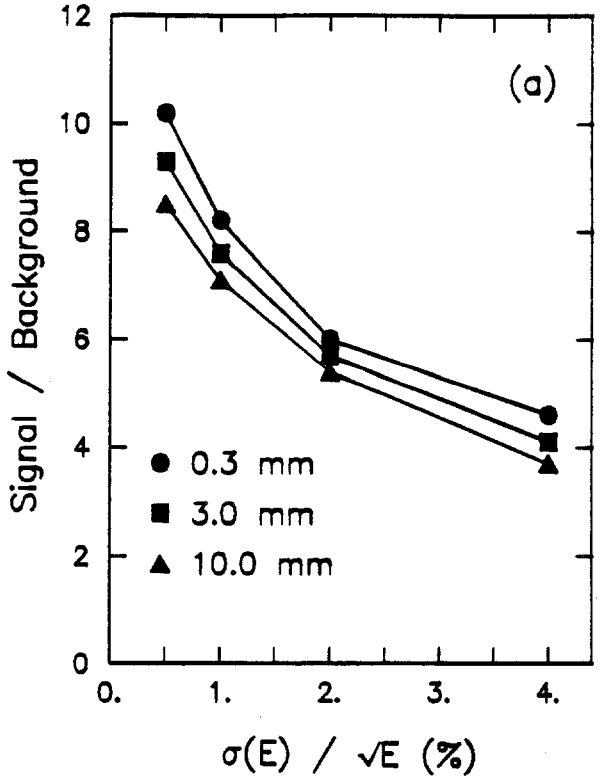


*Figure 31: $B_s$ Signal/background vs. Calorimeter Resolution:* The $B_s$ Signal/Background is shown vs. k in $\sigma_E = k\% \cdot \sqrt{E}$. Curves are given for three different spatial resolutions of the calorimeter.

We base our estimate of the expected yields of reconstructed and tagged $B_s$ and $\bar{B}_s$ mesons for a run with integrated luminosity, $\int \mathscr{L} dt = 10\ pb^{-1}$. The following losses and efficiencies are tabulated in Table 9:

- **$B_s$ Production Probability:** We assume that a $\bar{b}$-quark has a 12% probability[26] to combine with an s-quark to make a $B_s$-meson. This should allow, for example, for the loss of excited $B_s$ which can decay into B + K.

- **2-Arm Geometric Acceptance:** As discussed in Chapter 3, the decay tracks of 30% of all PYTHIA-generated $B_s$ mesons and 30% of all $\bar{B}_s$ mesons are fully contained by a system of two 600 mrad aperture forward spectrometers. There is a 14% overlap, in which both are contained.

- **$B_s$ Branching Ratios:** We assume BR = 9% for the total of all reactions of the type:

$$B_s \rightarrow D_s^* + n\pi^\pm\ ,\ D_s + n\pi\ ,\ D_u + Kn\pi$$

[26] V. Khoze [private communication].

The ARGUS group has reported a branching ratio[27] BR = 6.7%, for final states of the type $B_d \rightarrow D^* + n\pi$ with n = 1,2,3 We also assume that the $D_s^*$ to direct $D_s$ ratio is 3/1 and that the final state $D_u K n\pi$ contributes at least 0.2 %, giving us the total of 9%. Since it seems likely that we shall also be able to reconstruct such final states with n > 3, our effective useful BR should be larger than this.

- **$D_s^\pm$ Branching Ratio:** We take BR = 5% for all known charged final states:[28] $K^+K^-\pi^\pm$, $K^+K^-3\pi$, $K^0K^\pm$

- **$D_s^*$ Branching Ratio:** We assume that all $D_s^*$ decay via the mode: $D_s^* \rightarrow D_s\,\gamma$

- **Live time:** We assume a net 70% live time for the experiment.

- **Trigger Efficiency:** The trigger simulation is discussed in detail in Chapter 4. We find an efficiency of about 45% for Reaction 20 at the Tevatron.

- **Tagging Efficiency:** The tagging efficiency is estimated in Chapter 7 to be larger than 35%. We assume a value of 35% in constructing Table 9

- **Reconstruction Efficiency:** As mentioned above, a $\sigma = 4\% \cdot \sqrt{E}$ e.m. calorimeter yields a reconstruction efficiency of 29% for an average $B_s$ momentum of 35 GeV. The larger $B_s$ momenta at the Tevatron and somewhat larger track multiplicity may decrease this. Thus, for the Table 9 estimates, we assume the conservative value of 15%.

A total of ≈2700 tagged reconstructed $B_s$ events is about four times the estimated need in Chapter 2. Since 10 $pb^{-1}$ is an integrated luminosity that may be reached in a 10 day run in 1994, we see that a $B_s$-Mixing measurement constitutes a relatively modest goal for this experiment.

## *8.3 Monte-Carlo Simulation and Analysis of RICH Counter Data*

We have attempted to make a realistic estimate of the RICH identification efficiencies by simulating the RICH counter response to events containing $B_s$ decays. These simulated RICH data are then analyzed, in order to extract identification information for the particles.

We have started by doing an accurate simulation of the Liquid RICH counter in the first (100-600 mrad) spectrometer. Particle identification in the Liquid RICH counters are the most difficult for the following reasons:

- The number of particles which produce Cherenkov light in the liquid radiator is larger than in the gas counters (pion threshold is about 0.2 GeV in the liquid and is about 2.6 GeV in the gas counters).

- The "rings" are only rings for particles at normal incidence. Away from normal incidence, the light is seen in conic sections which have been truncated by light loss due to total internal reflection in the liquid radiator.

---

[27] H. Schroeder, Rapporteur Talk at XXIV International Conference in HEP (August 1988 - Munich, FRG) and DESY 88-101.

[28] [P. Karchin, Rapporteur Talk at SLAC Lepton-Photon Conference (August 1989)].

*Table 9:* *$B_s$ & $\bar{B}_s$ Event Yields at the Tevatron Collider*

$5 \times 10^8$ $b\bar{b}$ using: $\int \mathscr{L} dt = 10$ pbarn$^{-1}$ ($10^{31} \times 10^6$)
$\sigma(b\bar{b}) = 50\ \mu b$.

| | | |
|---|---|---|
| $6.0 \times 10^7$ $B_s$ | $6.0 \times 10^7$ $\bar{B}_s$ | 0.12 = $B_s$ Production |
| $1.8 \times 10^7$ | $1.8 \times 10^7$ | 0.30 = 2-Arm Geometrical Acceptance |
| $8.1 \times 10^4$ | $8.1 \times 10^4$ | $4.5 \cdot 10^{-3}$ = Branching Ratios ($B_s \to D_s^*$, $D_s$ and $DK^-$ with $n\pi$) ($D_s^* \to D_s\,\gamma$) ($D_s \to KK\pi$, $KK3\pi$, $K^0K$) |
| $5.7 \times 10^4$ | $5.7 \times 10^4$ | 0.70 = Live Time |
| $2.6 \times 10^4$ | $2.6 \times 10^4$ | 0.45 = Trigger Efficiency ($D_s^*\ 3\pi \to D_s\gamma\ 3\pi$) |
| $8.9 \times 10^3$ | $8.9 \times 10^3$ | 0.35 = Tagging Efficiency |
| $1.3 \times 10^3$ | $1.3 \times 10^3$ | 0.15 = Reconstruction Efficiency (allowing for $\gamma$) |
| $2.7 \times 10^3$ | | Total Reconstructed $B_s$ and $\bar{B}_s$ Events |

- The radii of the liquid RICH "rings" are large. Thus, there is considerable overlap of the rings from different particles. There is also some light loss to the walls of the counter.

In order to obtain an overall efficiency for the RICH identification procedure, we have generated 200 $B_s$ events, in which all particles in the final state $K^+K^-\gamma 4\pi$ are contained in the spectrometer aperture. Fig. 32(a) shows the momentum distribution for kaons which emerge from the decay of the $B_s$. Fig. 32(b) shows the momentum for kaons in the spectrometer which are not from the $B_s$ decay (they provide the candidate tagging sample discussed in Chapter 7).

To illustrate the enormous difference between the signals in the detector planes of both types of counters, we show in Figs. 33(a,b) the detector planes for typical events in the liquid and gas RICH counters, respectively. For the gas counter, the signals from nine events are superimposed. Note also that the noise signals referred to below are not shown in these figures.

Because the rings in the gas RICH are much much smaller and relatively well isolated, for the purposes of this study, we provisionally assume that the Gas RICH counter perfectly identifies all particles for which at least 4 photons are detected. We are in the process of extending our modeling to the entire system and should soon have a more complete answer. We first describe the RICH counter simulation, then the reconstruction algorithm and finally present the results of this study.

**RICH Data Simulation**

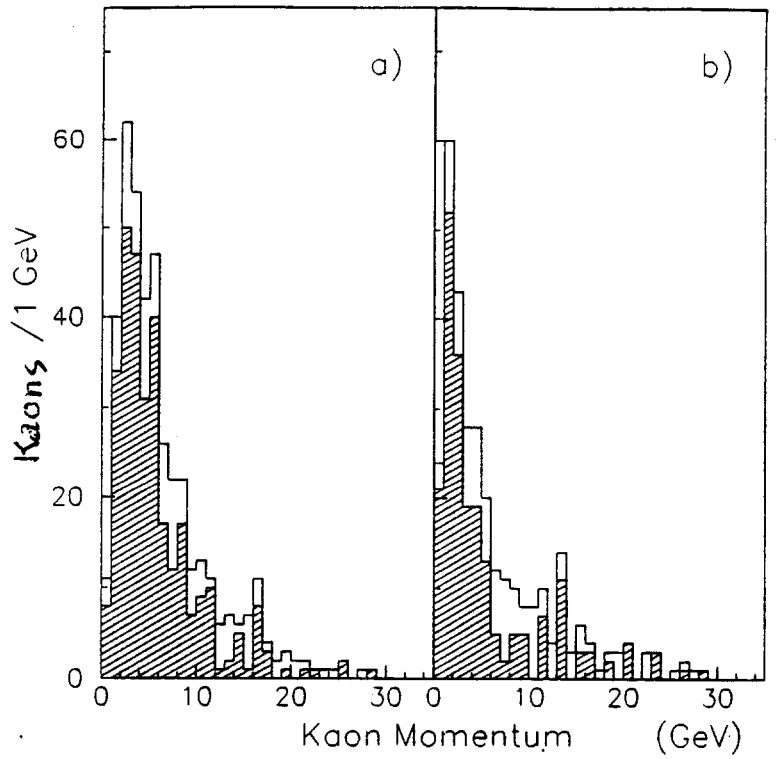


*Figure 32:* (a) Momentum distribution of $K^{\pm}$ which emerge from $B_s \to D_s^* 3\pi$ decay. Shaded histogram shows those that enter the first spectrometer (100-600 mrad); (b) Momentum distribution of $K^{\pm}$ in the detector, which do not come from the decay of $B_s$. Shaded histogram is same as in (a).

As explained above in Section 5.6, each liquid RICH counter consists of a 1 cm thick radiator which is followed by a 3mm thick quartz window. Cherenkov photons which are emitted in the radiator pass through the window into a 25 cm long, helium-filled volume. After traversing the helium, the photons pass through a second quartz window into the photon detector.

For ease of simulation, all windows, detectors and radiators were assumed to have surfaces perpendicular and parallel to the beam axis. This differs slightly from the proposed geometry in which the normals to the windows are along the average particle direction (see Fig. 14). This approximation slightly decreases the number of photons detected in a ring image (because of increased losses due to total internal reflection), but should have little effect on the the ring reconstruction problem. In fact, the average number of "detected" photons generated by the program (20) is very close to the 23.4 photons, measured[29] for a $\beta = 1$ track normally incident on a similar prototype module.

All physical effects relating to the generation and propagation of the Cherenkov photons were carefully simulated. Tracks entering the RICH radiator are multiple-scattered between emission of photons. The photons are propagated through the radiator, the two quartz windows and the helium space, taking into account the energy-dependent index of refraction and absorption lengths in each medium. Reflection probabilities are calculated at each interface between two materials with differing indices of refraction and photons were eliminated if reflection takes place. The distance each photon

[29] R. Arnold et al. [CRN/HE 87-08]

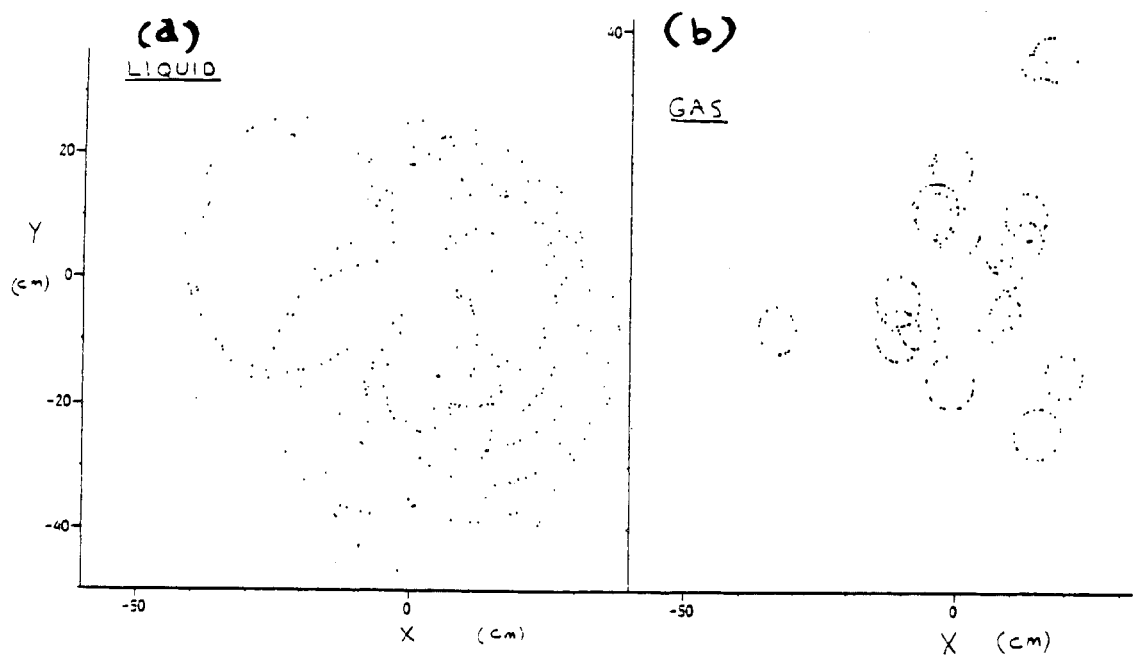


*Figure 33:* (a) Photon Images for One Typical Event in Detector Plane of Liquid RICH; (b) Photon Images in Detector Plane of Gas RICH. The signals from 9 events are superimposed in the gas RICH figure. Noise signals referred to in the text are not shown in either figure.

indices of refraction and photons were eliminated if reflection takes place. The distance each photon travels in the detector before absorption is then calculated, and the detected photon position is digitized, assuming $3 \times 3$ mm$^2$ pads.

Cherenkov light is also generated by all tracks as they traverse the quartz windows (this effect is expected to account for the major fraction of noise photons). These photons are propagated through the counter to the detector in the manner described above. It may be noted that the counter configuration used in the present simulation (perpendicular to the beam axis, rather than rotated as in Fig. 14) overestimates the number of photons from this source, since most photons from tracks normally incident on the quartz are internally reflected in the windows.

**Analysis of Simulated RICH Data**

The input to our provisional reconstruction algorithm is the list of tracks and their trajectories and momenta, as well as the list of hit RICH detector pads produced by the simulation program. As described below, we assume that, if a particle's velocity is above Cherenkov threshold for pions in the gas RICH counter, the gas counter gives a correct particle identification.

For a given measured charged track, the analysis is based on the reconstruction of a Cherenkov emission angle, $\theta$, for each detected photon (at present, each struck 3 x 3 mm$^2$ pad is interpreted as one photon). A straightforward ray calculation, which includes refraction at the interfaces, gives two equations for the coordinates (x,y) of converted photons in the photon detector as a function of $\theta$. and the azimuthal Cherenkov emission angle, $\phi$. For each track, we use these equations and standard numerical techniques to give $\theta$ and $\phi$ for each detected photon (if a solution exists).

The subsequent analysis is facilitated by the removal of hits in the Liquid RICH detector, which constitute background from two sources:

- For the relatively few tracks in each event which are above Cherenkov threshold in the Gas RICH, a random number, n, is generated according to a Poisson distribution, whose mean is the expected $\beta$-dependent photo-electron yield (20 for $\beta = 1$). If $n > 4$, we assume that the Gas RICH counter correctly identifies this track (tracks whose momenta are between pion and kaon thresholds in that counter, and which have no light, are assumed to be kaons). We then remove, from the Liquid RICH hit list, all photons from these tracks which are within 2 standard deviations of their expected $\theta$ (this standard deviation is discussed in Section 5.6).

- Cherenkov photons produced in the quartz detector window are removed by removing all hits produced in a 1 cm radius circle about the point where the particle enters the photon detector.

Since, as discussed above, the gas RICH counter is assumed to correctly identify all tracks which are above about 2.6 GeV (pion threshold in that counter), we now investigate with our detailed simulation how well the liquid RICH counter can be used to identify tracks with momentum below 2.6 GeV. Fig. 34 shows a histogram of the values of $\theta$ for an identified kaon track in a typical $B_s$ event after the above cleanup procedure. A peak is seen at an angle which corresponds to the Cherenkov emission angle for the track in question. In general, the situation may not be so obvious.

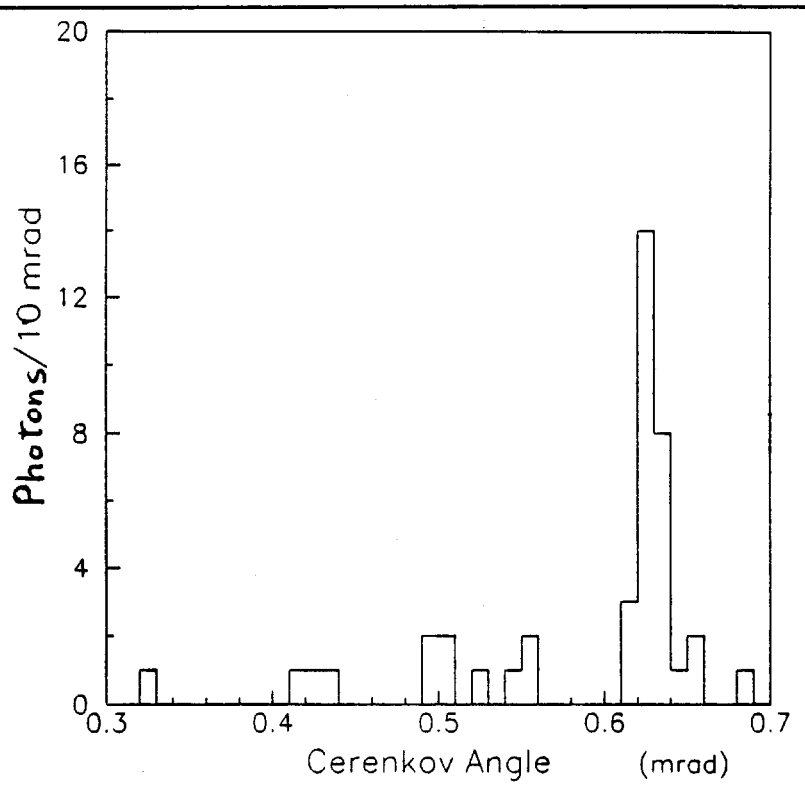


*Figure 34:* Histogram of reconstructed Cherenkov emission angles for a typical kaon track that is identified by the liquid RICH counter. The momentum of this kaon is 1.7 GeV.

In order to quantify the RICH identification picture, we have tentatively employed the following, somewhat arbitrary, algorithm. For each track with momentum below 2.6 GeV, and for each possible mass identity, we count the number of the photons within a "road" of width, $2\sigma$, where $\sigma$ is the expected standard deviation on $\theta$ referred to above. A photon count thus results for each mass identity possibility. For the particle to be uniquely identified as a particular type, the algorithm requires:

- The photon count, $n_\gamma > 5$, within the "road" for that particle type.
- For all other particle types, their photon counts, $n_\gamma' < n_\gamma - 4$.

We are also exploring other more sophisticated algorithms but this relatively simple one already gives rather good results. Table 10 gives the results of the analysis for the sample of 200 events. The rows are the "true" identities of the tracks and the columns are the identities deduced using the above algorithm.

*Table 10:* *RICH Counter Identification Matrix for 200 $B_s$ Events**

| | | Identification from RICH counters | | | |
|---|---|---|---|---|---|
| | | p | K | $\pi$ | pK$\pi$ |
| "True" ID | p | 22 | 22 | | 26 |
| | K | 3 | 372 | 5 | 62 |
| | $\pi$ | 10 | 30 | 1277 | 673 |

(*) For simplification, muons are not included here. Their contribution is small, however.

We see in Table 10 that 85% of all "real" kaons are called kaons by the RICH counters. On the other hand, of all tracks that are called kaons by the RICH counters, 88% of these are real kaons. As commented above, we are fairly confident that these efficiencies can be improved, as we use increasingly more sophisticated reconstruction algorithms.

## *8.4 Yields of Potential CP-Violating Channels*

Table 11 gives a summary of the various factors which determine the event sample size available for a CP-Violation measurement at the Tevatron Collider. The estimates assume a 50 $\mu$b cross section for $B\bar{B}$ production and are given for an integrated luminosity, $\int \mathscr{L} dt = 200$ pbarn$^{-1}$. Referring to Fig. 6, we can see that the 1150 tagged events obtained in this run would permit a $3\sigma$ or more measurement of $\sin(2\beta)$ only for asymmetries larger than about 0.3.

*Table 11:* $B^0_d \to J/\psi\, K^0_s$ *Event Yields at Tevatron Collider*

$10^{10}$ $b\bar{b}$ using: $\int \mathscr{L} dt = 200$ pbarn$^{-1}$ ($10^{31} \cdot 2 \cdot 10^7$)
$\sigma(b\bar{b}) = 50$ $\mu$b.

| | | | |
|---|---|---|---|
| $4.0 \times 10^9$ $B_d$ | $4.0 \times 10^9$ $\bar{B}_d$ | 0.40 | = $B_d$ Production |
| $1.2 \times 10^9$ | $1.2 \times 10^9$ | 0.30 | = 2-Arm Geometrical Acceptance |
| $4.7 \times 10^4$ | $4.7 \times 10^4$ | $3.9 \cdot 10^{-5}$ | = Branching Ratios $B \to J/\psi K_s \to \ell^+\ell^-\pi^+\pi^-$ |
| $3.3 \times 10^4$ | $3.3 \times 10^4$ | 0.70 | = Live Time |
| $6.6 \times 10^3$ | $6.6 \times 10^3$ | 0.20 | = Trigger Efficiency |
| $2.3 \times 10^3$ | $2.3 \times 10^3$ | 0.35 | = Tagging Efficiency |
| $5.7 \times 10^2$ | $5.7 \times 10^2$ | 0.25 | = Reconstruction Efficiency |
| $11.5 \times 10^2$ | | | Total Reconstructed $J/\psi K_s$ Events |

Our preliminary estimates indicate that substantial radiation damage may occur during the course of a 200 pb$^{-1}$ run and it may be necessary to replace the silicon once or twice during the course of a CP experiment. However, radiation damage to the silicon at high luminosities is not a fundamental limitation, although it will probably be necessary to regard the silicon detectors as expendable, at a cost which is quite tolerable compared to the cost of the entire detector and of running the machine.

# *9. DISCUSSION & COST ESTIMATES*

**Discussion**

Assuming eventual approval by summer 1991, we would endeavor to have the experiment designed, built and tested in time for a run beginning during the last half of 1994. There remains one key question to answer:

- **Should one or two spectrometer arms be instrumented ?**

To answer this question, there are two important points to note. This experiment would be the first of its kind and it would seem desirable to build one arm and after running and obtaining experience with it, to consider "how things should have been done". But, equally important is our observation that CP-Violation is probably beyond the reach of any Tevatron collider experiment. On the other hand, physics items such as $B_s$-Mixing are easily done with the available luminosity and the loss of 50% statistics that a single instrumented arm implies. **Thus, we propose to build a single arm spectrometer system** at this time.

**Cost Estimates**

The major items which we consider here are 1) The silicon vertex detector, 2) The tracking system (wire and pixel drift chambers), 3) RICH, 4) Electromagnetic Calorimeters, 5) Magnets, 6) Trigger Processors, 7) Readout system, 8) Other computing needs, and 9) Mechanical devices for transport and support.

The wire drift chambers contain about 30000 sense wires with building costs estimated at \$24/wire. The electronics costs add an additional \$48/wire giving a total of \$72/wire. The pixel drift chambers, which have about 15000 wires, will use cheaper electronics and cost \$48/wire. The total electronic and mechanical costs are thus estimated to be \$2,880K. An additional \$144K will be needed for a laser alignment system and a gas delivery system for a system total of \$3,024K.

The RICH detectors contain about 7 $m^2$ of quartz costing \$168K. Mechanical construction of the 2.0 $m^2$ of RICH detector is estimated at \$80K, The gas system at \$40K, liquid transport and cleaning system \$40K and mirrors \$16K. Other items include thermal regulation, Freon liquids and gasses, and mechanical mounts. The largest item is the readout electronics for $3.8 \times 10^5$ channels which is estimated to cost \$3/channel for the RICHIP. Development of this chip is almost finished and a 15,000 pad detector is expected to be equipped soon. Pad detectors have recently been tested and work as expected. A full scale operating detector is scheduled for spring 1991, and a full scale test of the combined radiator and detector system will take place early in 1992. Design, construction and testing of the full RICH system during the ensuing two years appears eminently feasible. The total cost of the RICH system is estimated to be \$1,604K.

*Table 12: Experiment Cost Estimates in U.S. Dollars*

| Device | Quantity | Unit Cost | Total (K$) |
|---|---|---|---|
| **Silicon Vertex Detector System** | | | |
| Si Detectors | 96 | 5,000 | 480 |
| Readout electronics | $4 \cdot 10^5$ | 0.50/ch | 200 |
| Mechanical Support | | | 200 |
| VLSI Development | | | 200 |
| Subtotal | | | 1,080 |
| **Wire Chambers (Tracking & Pixel)** | | | |
| Mechanical | $4.5 \cdot 10^4$ | 24 | 1,080 |
| Electronic Preamp | $4.5 \cdot 10^4$ | 8 | 360 |
| Multihit TDC(8 bits, 4 ns) | $3.0 \cdot 10^4$ | 32 | 960 |
| Multihit TDC(4 bits, 25 ns) | $1.5 \cdot 10^4$ | 8 | 120 |
| Cables, Housing, Power | $4.5 \cdot 10^4$ | 8 | 360 |
| Laser Alignment | | | 100 |
| Gas Transport | | | 40 |
| Subtotal | | | 3,020 |
| **RICH System** | | | |
| Quartz Windows | 7 $m^2$ | 24K/$m^2$ | 168 |
| Detectors | 2 $m^2$ | 40K/$m^2$ | 80 |
| Gas System | | | 40 |
| Liquid transport & cleaning | | | 40 |
| Mirrors | | | 16 |
| Thermal Regulation | | | 40 |
| Mechanical Mounts | | | 40 |
| Liquids & Gases | | | 40 |
| Electronics | $3.8 \cdot 10^5$ | 3/ch | 1,140 |
| Subtotal | | | 1,604 |
| **Electromagnetic Calorimeter** | | | |
| Subtotal | | | 7,700 |
| **Magnets** | | | |
| Quadrupole ($\phi$4m·2m) | | | 1,600 |
| Superconducting Dipole (2·2·2$m^3$) | | | 2,600 |
| Subtotal | | | 4,200 |

*Table 12: Experiment Cost Estimates in U.S. Dollars*

| Device | Quantity | Unit Cost | Total (K$) |
|---|---|---|---|
| **Data-Driven Trigger Processor** | | | |
| Computational Modules | 300 | 300 | 90 |
| Control, Power, and Housing | | | 50 |
| Development | | | 200 |
| Subtotal | | | 340 |
| **Readout System** | | | |
| Detector Encoding | 200 | 800 | 160 |
| Data Buffering/Transport | 200 | 800 | 160 |
| Housing & Power | 30 | 3,200 | 96 |
| Subtotal | | | 416 |
| **Other Computing** | | | |
| Online Host Computer | | | 80 |
| Monitoring/Selection $\mu$P Farm | 700 | 2,000 | 1,400 |
| Subtotal | | | 1,480 |
| **Mechanical** | | | |
| Supports | | | 80 |
| Transport | | | 80 |
| Subtotal | | | 160 |
| TOTAL | | | 20,000 |
| CONTINGENCIES (20%) | | | 4,000 |
| GRAND TOTAL | | | 24,000 |

## APPENDIX A – Trigger Algorithm & Simulation

This is a detailed description of the Monte-Carlo study of the trigger algorithm and its performance which was done for a c.m. energy, $\sqrt{s}$ = 0.63 TeV, where the mean B momentum is 35 GeV. Since the mean momentum at the Tevatron only increases to about 45 GeV, and since there is not much increase in track multiplicity through the silicon detectors, the conclusions should still be valid.

**Silicon Data Simulation and Detector Response** In order to understand the properties of the silicon system, we have generated Monte-Carlo event samples of different types using the Lund program, PYTHIA 4.8, imbedded in the CERN detector simulation Monte-Carlo program, GEANT (We have compared PYTHIA event distributions with the corresponding distributions from UA5 data and have found reasonable agreement).

Silicon response data for the various classes of Monte-Carlo events are simulated in GEANT. We have included the following effects into the generation:

- **Multiple Scattering** Both Gaussian and Moliere scattering were tried. The Gaussian form results in a somewhat more pessimistic estimate of the trigger suppression for minimum bias events and we use it for the results presented below.
- **Nuclear Interactions** We have tried both the Tatina and Geisha packages, but see little difference between the two. The samples discussed below were generated with the Tatina package.
- **$\pi^0$ decays** $\pi^0$s are allowed to decay into either $\gamma\gamma$ or $\gamma e^+e^-$.
- **$\gamma \to e^+e^-$ conversions in the detector** Here, as above, the electrons are added to the track list and are followed through the detector as far as they go.
- **$\delta$-rays** Charged particles traversing the detector are allowed to generate electrons with energies above 10 keV, which are subsequently tracked until they stop.

The first step in generating the silicon response is to assign a quantity representing the amount of energy deposited in the detector by each charged track in an event. For example, Fig. 35 shows the distribution of energy generated for tracks with momenta greater than 10 GeV which impinge on the detector at normal incidence. The energy deposited by delta rays associated with the tracks is included.

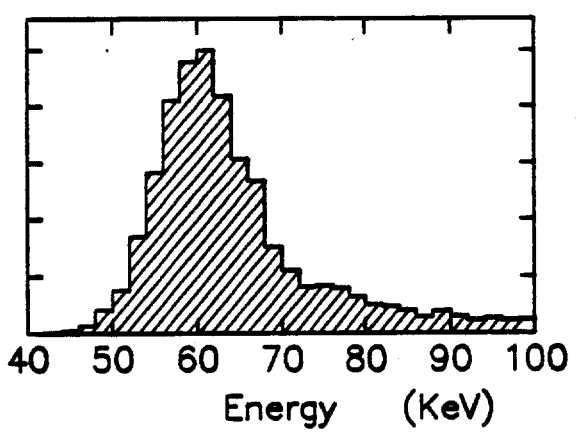


*Figure 35: Energy Deposition in 200 μm of Silicon*

The energy is divided between strips based on the path length spent in the depletion layer of each strip. Next, the number of electron/hole pairs is calculated assuming 270 pairs per KeV of deposited

energy. Detector noise is accounted for by generating a normally distributed random number with a width ($\sigma$) of 1000 electrons and adding it to the signal. The resulting total charge is then compared to a threshold of 4000 electrons, and a yes/no response is generated for each strip. We decided not to make use of pulse height information, since it is currently impossible to read out such information from a real detector at a high enough rate to satisfy the requirements of our on line trigger calculations. This algorithm results in a detector which is essentially fully efficient for tracks impinging at angles less than about 500 mrad, but rapidly loses efficiency for larger angle tracks.

## TRIGGER ALGORITHM AND SIMULATION:

Fig. 36 shows the flow diagram of the proposed trigger. We describe each step of the algorithm in detail. We refer to a coordinate system in which z is along the beam direction, with x (horizontal) and y (vertical) perpendicular to z.

### • POINT FINDING

First, the raw silicon hit information is transformed into points independently in the xz and yz planes. The problem here is to dispose of the clusters (contiguous hit strips). Fig. 37(a) is the distribution of the number of contiguous hit strips generated in the Monte-Carlo simulation. The average cluster width is 1.6 strips. A point is defined as the geometrical center of a cluster. A comparison of the points found in this way with the original track coordinates shows that they have a resolution of 16 $\mu$m (full width half maximum) as demonstrated in figure 37(c).

The distribution of the number of points per silicon detector (i.e. one quadrant of one plane) is shown in Fig. 37(b). Although the charged track multiplicity is high, one quadrant sees on average, less than 1/8 of the total, resulting in the rather modest mean multiplicity of 2.5 points per quadrant.

### • TRACK FINDING

Next, straight lines in both hemispheres, which traverse at least three planes of silicon, are found independently in their xz and yz projections. We demand that the points be collinear to better than $\pm 25$ $\mu$m. This rather stringent cut corresponds to the multiple scattering of a 2 GeV/c track and thus tends to reject tracks with lower momentum which could degrade the vertex algorithm. Figure 38(a) shows the number of tracks found in the xz vs. yz projections using this procedure. The correlation is clear, although mainly because of the loss of lowest momentum tracks, there is a smearing. On average, the algorithm finds about 13 tracks in each view. Fig. 38(b) is a histogram of the number of particles which have traversed at least 3 detector planes minus the number of tracks found per event. As can be seen from this figure, the algorithm usually finds fewer tracks than are actually present (the overall efficiency is about 80%) because of the loss discussed above of tracks with momentum less than 2 GeV which fail the collinearity test.

### • ESTIMATE PRIMARY VERTEX

We use the tracks found above to estimate the position of the vertex. As shown below, this step is mainly needed to define the subset of found tracks whose origins are near the primary vertex.

We histogram together in 5 mm bins the z intercept of all found tracks in both the xz and yz views. (We use only the two hits closest to the beam to estimate the track parameters.) A z-intercept histogram of a typical event from the minimum bias sample is shown in Fig. 39(a). Part (b) of this figure contains a histogram from a typical B event. For both events, most tracks are contained in two bins. There is seen to be very little difference on this scale between minimum bias events and B events.

We next loop over the histogram bins and find the two adjacent bins which contain the most hits. For our first estimate of the event vertex, we assume that the z coordinate is the average position of these 2 bins, weighted by the number of hits in each bin, and that $x=y=0$. Using this method, the vertex is located with a precision of 1 mm along the z axis.

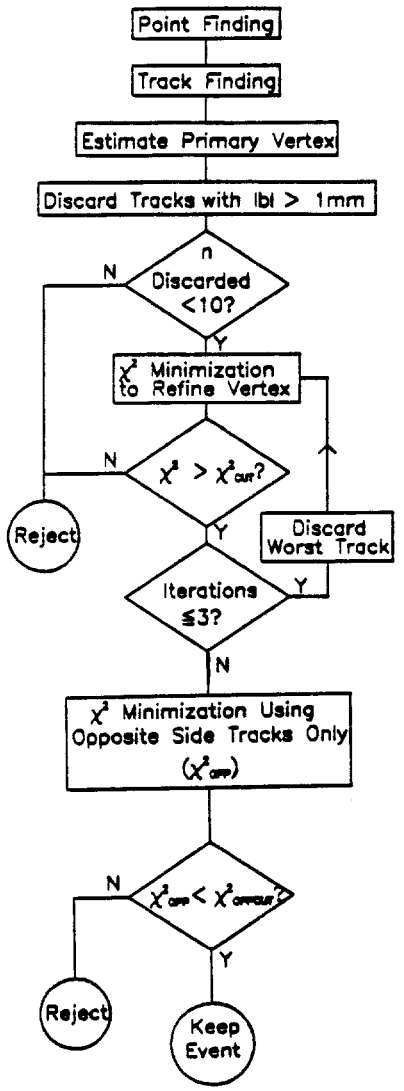


*Figure 36: The Trigger Algorithm*

- **EXCLUDE TRACKS WITH IMPACT PARAMETERS > 1 mm**

This cut serves the dual purpose of discarding tracks which come neither from the primary vertex nor a B decay vertex (such as strange particle decay products or spurious tracks) and as a basis for rejection of pileup (multiple interactions in a bunch crossing) as is discussed below and earlier in Section 3.2.

We define the impact parameter as the distance between the point on the track at the z of the first vertex estimate and the z axis. Fig. 40 shows the impact parameter distributions for various classes of

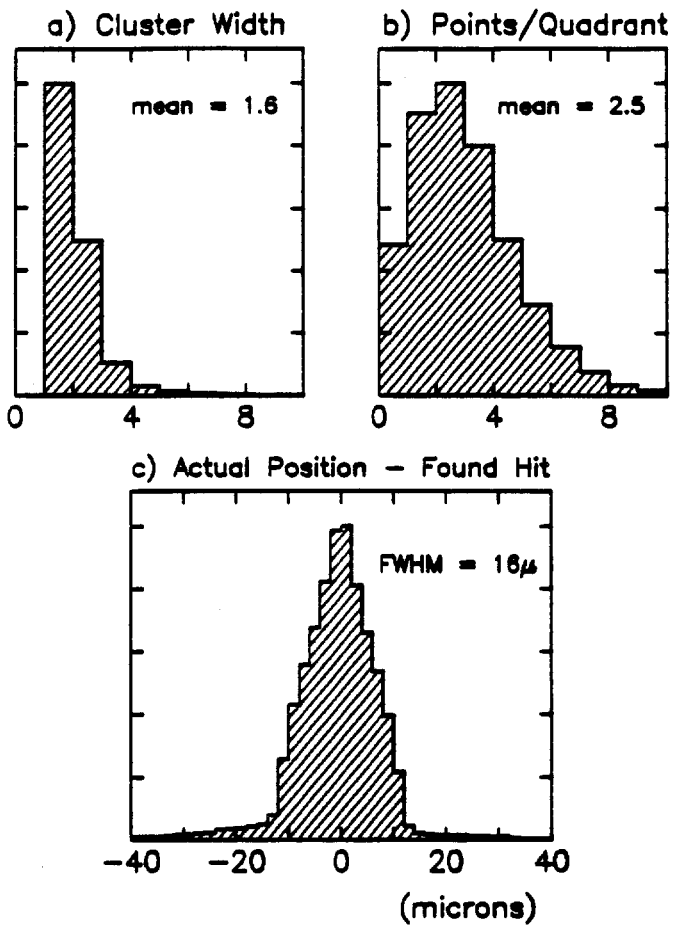


*Figure 37: Point finding details*

tracks. Fig. 40(a) is for tracks from the primary vertex only. Most of these tracks are in two 200 $\mu$m bins. Very few are actually outside the 1 mm cut. On the other hand, Fig. 40(b) shows that tracks from $K^0$ and $\Lambda$ decay have a considerably broader distribution. Roughly half of all $K^0$ and $\Lambda$ decay tracks are thrown out by this cut. The impact parameter distribution for tracks from B decays is somewhat broader than that of primary vertex tracks as can be seen in Fig. 40(d). On average the 1 mm cut discards about 1 more track from B events than from minimum bias events.

- **REJECT EVENT IF MORE THAN 10 TRACKS HAVE b > 1 mm**

This cut is aimed at pileup suppression. Fig. 40(c) shows the impact parameter distribution obtained from Monte-Carlo generated double events (two minimum bias events in one bunch crossing). Except for the broad tail, the distribution is very similar to Fig. 40(a). The histograming method used to find the first vertex estimate usually picks out one or the other vertex when two events occur at the same time. The tracks from the found vertex are mainly in the b = 0 peak, while the tracks from the second vertex form a broad background, also centered at b = 0.

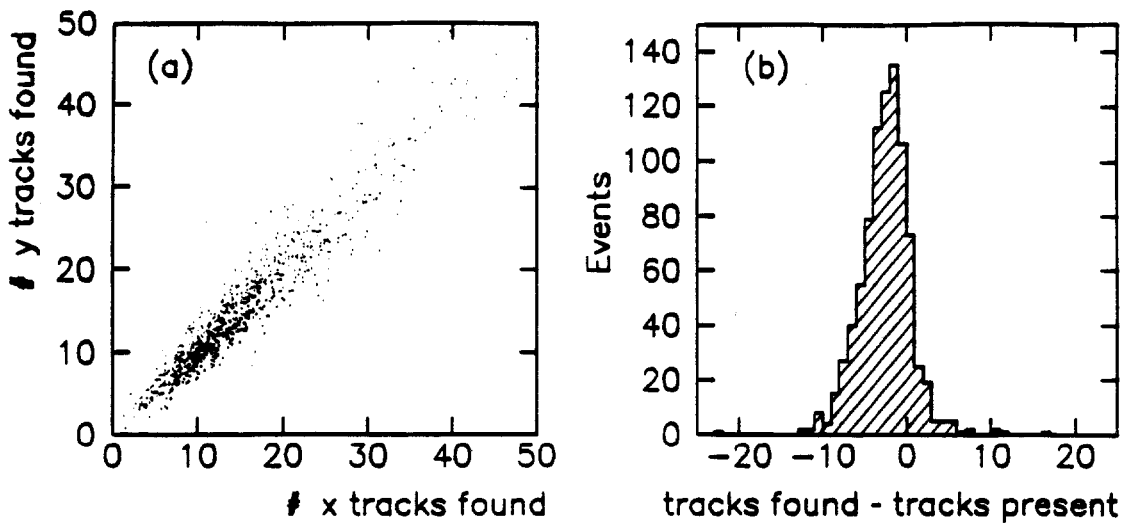


*Figure 38:* (a) The number of y-view tracks found, vs. number of x-view found. (b) the number of tracks found minus number of tracks present.

Fig. 41 shows the number of tracks per event whose impact parameters exceed 1 mm for three classes of events. Demanding that fewer than ten tracks be excluded results in a loss of a few percent of B events while suppressing pileup by a factor of ten.

- **VERTEX FINDING BY $\chi^2$ MINIMIZATION**

Events which pass the above track cut proceed to the next phase which consists of refining the vertex estimate by minimization of the $\chi^2$ given by:

$$\chi^2 = \sum_{i=1}^{N_x} \frac{b_{xi}^2}{\sigma_{xi}^2} + \sum_{i=1}^{N_y} \frac{b_{yi}^2}{\sigma_{yi}^2}$$

This equation contains independent sums over x and y view tracks. $b_{xi}$ ($b_{yi}$) is the impact parameter of the i'th track in the x (y) view. Here, the impact parameter is the distance between the point on the track at the z of the vertex and the vertex point which is no longer constrained to be at $x = y = 0$. Track parameters are estimated using the two measured points closest to the first vertex estimate. A weight, $\sigma_{xi}$ or $\sigma_{yi}$, is assigned to each impact parameter based on the track's slope (which gives a very rough indication of the track's momentum) and the extrapolation distance between the vertex and the closest measured point on the track.

Fig. 42 shows the $\chi^2$/DOF (Degree of Freedom) distribution obtained from a sample of minimum bias events. The distribution is far from the ideal $\chi^2$/DOF distribution. It peaks at $\chi^2$/DOF

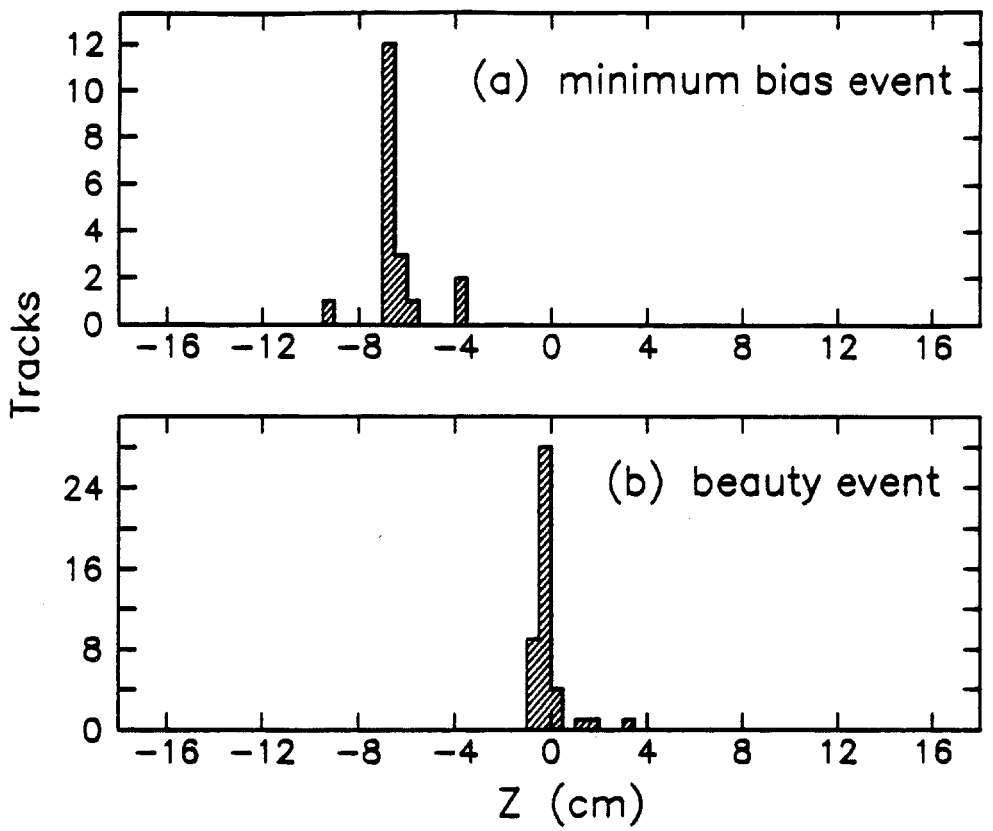


*Figure 39:* z-Intercept Distributions for (a) Typical Minimum Bias Event (b) Typical $B\bar{B}$ Event

= 4 and has a tail extending to very high values. This is due in part to the presence of non-vertex tracks in the sum and to the rather crude estimate of track momentum that is used in evaluating the weight.

- **$\chi^2$ CUT AND ITERATION**

The $\chi^2$-distribution shown in Fig. 42 with its very long tail (not shown) is insufficient to obtain the required suppression of minimum bias events without simultaneously rejecting an unacceptably large portion of the B events. However, we find that if we discard the track with the largest contribution to the $\chi^2$ and refit, we can obtain substantially greater minimum bias suppression with acceptable additional losses of B events. The procedure is optimized by iterating and discarding up to 3 tracks. The results of applying this procedure to minimum bias, $b\bar{b}$ and $c\bar{c}$ event samples are shown in the next section.

Additional suppression of minimum bias events relative to B events can be obtained by using only the tracks which point in the hemisphere opposite the spectrometer and forming a $\chi^2_{opp}$. The basic rationale behind this is the observation that if a B meson is produced and decays into the spectrometer, the accompanying $\bar{B}$ meson is very likely to be in the same hemisphere and therefore $\chi^2_{opp}$ should be small. However, a minimum bias event which happens to have a large $\chi^2$ is equally likely to

## APPENDIX B – Liquid-Radiator Rich Resolution

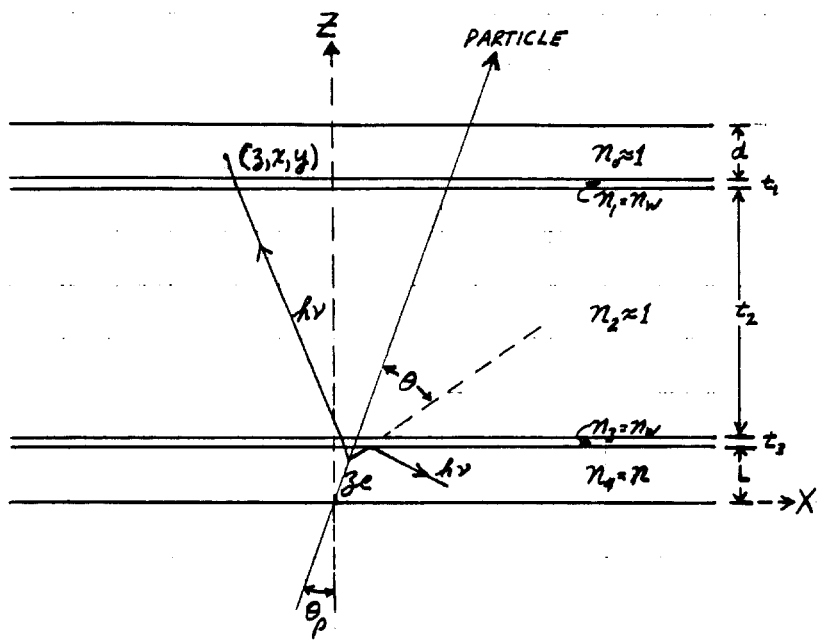


*Figure 43: Liquid-Radiator Geometry.*

The xz plane is defined to contain the radiator normal (z) and the particle momentum vector ($\vec{p}$) as shown in Fig. 43 The photon emission point $z_e$ along the particle direction varies between $-L/(2\cdot\cos\theta_p) < z_e < +L/(2\cdot\cos\theta_p)$ and is unmeasurable. Hence $\sigma_{ze} = L / (\sqrt{12}\cdot\cos\theta_p)$. The photon energy is also unmeasurable and has an energy width $\Delta E$ determined by the detector response, in this case $\sigma_E = \Delta E/\sqrt{24} = .31$ eV. The photons are detected at points (z, x, y) in the detector volume with r.m.s. errors $\sigma_z$, $\sigma_x$ and $\sigma_y$. The Cherenkov angle $\theta$ may be reconstructed from the measured quantities z, x, y, $\theta_p$, $z_e = \langle z_e \rangle = 0$, $n = \langle n \rangle = 1.278$ with the formulas (valid for vanishingly thin window and radiator)

$$\cos\theta = (\sin\theta_p/n)\cdot(x/r) + (\cos\theta_p/n)\sqrt{[n^2-(x^2+y^2)/r^2]}$$

$$\tan\phi = y / [x\cos\theta_p - \sin\theta_p \cdot \sqrt{(n^2r^2-x^2-y^2)}]$$

The derivatives of these reconstruction formulas allow calculation of the angular error at a given $\phi$ via the relation $\sigma_\theta = (\partial\theta/\partial v_i)\,\sigma_{vi}$ The derivatives are:

$$\partial\theta/\partial x = (\beta\sqrt{K/z})[K\cos\phi/\alpha - \sin\theta_p \tan\theta \sin^2\phi/\beta^2]$$

$$\partial\theta/\partial y = (\beta\sqrt{K/z})\sin\phi[1/\beta^2 - \cos\theta_p(n^2-1)/\alpha]$$

$$\partial\theta/\partial z = -(K/z\alpha)(\cos\theta_p \tan\theta + \sin\theta_p \cos\phi)$$

$$\partial\theta/\partial\theta_p = -\cos\phi$$

$$\partial\theta/\partial z_e = (\tan\theta\sqrt{K/z\beta})[(\beta^2 K/\alpha^2)(1-\sin^2\theta_p \sin^2\phi) + \sin^2\theta_p \sin^2\phi]$$

$$\partial\theta/\partial n = (n\tan\theta)^{-1}(n^2\beta^2)(\cos\theta_p/\alpha)$$

with $\alpha = \cos\theta_p - \sin\theta_p \tan\theta \cos\phi$ and $K = 1 - n^2 + \alpha^2/\beta^2$.

APPENDIX C

EUROPEAN ORGANIZATION FOR NUCLEAR RESEARCH

DRAFT

18 December 1990

# Development and Test of a Large Silicon Strip System for a Hadron Collider Beauty Trigger


J. Ellett, S. Erhan, P. Kreuzer[1], D. Lynn, M. Medinnis, P. Schlein, J. Zweizig
University of California*), Los Angeles, U.S.A.

A. Czermak[2], G. Engelmann, O. Klingsheim[3], K. Ley, A. Rudge, H. Wahl, P. Weilhammer
CERN, Geneva, Switzerland

G. Borreani
University of Ferrara and INFN, Italy

R. Ely, C. Haber
Lawrence Berkeley Laboratory, Berkeley, CA, U.S.A.

W. Hofmann, B. Wilkens
Max Planck Institut fur Kernphysik, Heidelberg, F.R.G.

M. Calvetti, M. Punturo
University of Perugia and INFN, Italy

Y. Guz, Y. Ivanuschenkov
IHEP-Serpukhov, Protvino, U.S.S.R.

C. Biino, S. Palestini, L. Pesando
University of Torino and INFN, Italy

R. Harr, P. Karchin
Yale University**), New Haven, Connecticut, U.S.A.


## Abstract


Large aperture forward spectrometers with planar geometry perpendicular to the beam line are the natural detectors to accomodate the expected forward peaking of heavy flavor production at high energy hadron colliders. Such systems, together with silicon strip detectors for triggering, which are configured perpendicular to and close to the beam inside the vacuum pipe at the center of the interaction region should make possible the exploitation of hadron colliders as Beauty Factories. We have designed, built and tested such a silicon system at the CERN Sp$\bar{p}$S-Collider. Running 1.5 mm from the Sp$\bar{p}$S beams, clean background-free events are seen.



To be submitted to Nuclear Instruments and Methods


---


*) Supported by U.S. National Science Foundation, Grants PHY90-08221 and PHY85-09175.
**) Supported by the U.S. Department of Energy


1) Ecole Polytechnique, Lausanne, Switzerland
2) Visitor from Institute of Nuclear Physics, Krakow, Poland.
3) Present Address: Stavanger Tekniske Fagskole, Stavanger, Norway.

# Contents


**1 Introduction** **1**

**2 The Detector** **2**
2.1 Overview . . . . . 2
2.2 Silicon Detectors . . . . . 2
2.3 SVX Chips . . . . . 2
2.4 Hybrid Design . . . . . 3
2.5 Detector Mount . . . . . 3
2.6 Assembly and Testing . . . . . 4

**3 Installation and Roman Pots** **5**
3.1 Roman Pots . . . . . 5
3.2 Positioning Mechanism . . . . . 5
3.3 Pumping system . . . . . 5

**4 Silicon Power System** **6**

**5 Triggering and Readout System** **6**

**6 System Performance & Data Analysis** **8**

**7 Conclusions** **9**


# 1 Introduction

The exploitation of hadron colliders as beauty factories would be impossible without a high resolution vertex detector and an efficient and highly selective beauty trigger. A scheme for realizing such a detector and trigger was explored and extensively modeled in the context of a proposal to the CERN SPS committee[1]. Although this proposal was for an experiment at the Sp$\bar{p}$S-collider, it was recognized that the apparatus built for the Sp$\bar{p}$S collider experiment could serve as a basis for the more elaborate apparatus needed to cope with the higher energies of the next generation of hadron colliders. Indeed, the long range goal of the collaboration is an experiment with sufficient sensitivity to measure CP violation parameters in the decay of B mesons. The attainment of this goal awaits the high luminosites and high cross-sections of the next generation of hadron colliders.

We report here on the design and construction of a test version of the proposed detector and present a preliminary analysis of the results obtained with it during the Fall 1990 Sp$\bar{p}$S-collider run. The purposes of this test were to assess the feasibility of operating a silicon detector at a few millimeters from the beam axis, and to gather data for the off-line testing of trigger algorithms based on silicon hit information, which would select events containing beauty production.

Fig. 1(a) shows a side view of the detector used for this test. Part (b) of this figure shows a perspective drawing. The detectors are organized into 6 planes perpendicular to the beam axis. Each plane has 8 silicon detectors: 4 with vertical (x-view) and 4 with horizontal (y-view) strips.

The "fixed-target" type geometry was adopted to accomodate the anticipated sharp peaking of B production in the beam directions[1]. The forward peaking of reconstructable B mesons is even sharper since the decay products of B mesons produced near Feynman-x = 0 tend to have low momentum and therefore become easily lost in pattern recognition. The detector was therefore optimized for particles traveling in the forward and backward directions, at angles less than about 600 milliradians.

In order to minimize extrapolation distance to the primary vertex, the detector was positioned at the center of the interaction region and the gap between upper and lower halves was reduced to the minimum distance consistent with clean running conditions. The detector is

mounted in a device (called a Roman Pot) which allows retraction of the detector to a safe distance during beam manipulations and setups.

The detector assembly and associated systems are discussed in Sections 1 through 5. A discussion of the performance of the detector during the collider test run and a preliminary analysis of the data taken during that run is presented in Section 6.

# 2 The Detector

## 2.1 Overview

A photograph of a detector with its associated readout hybrid is shown in Fig. 2. The assembly pictured here was appropriate for readout of the horizontal coordinate. The silicon detector is on the left in this view. The seven chips next to the detector are SVX pre-amplifier/readout chips. A Kapton readout cable is shown plugged into connectors near the right-hand edge of the hybrid.

The detectors were supported by aluminum brackets glued to the back of the alumina hybrids. Fig. 3 shows a side view of two detector planes. Each detector is shown attached to its hybrid and heat sink. The distance between adjacent x- and y-view detectors was 2 mm and the distance between the center lines of adjacent planes was 3.8 cm.

As shown in Fig. 4, the aluminum support brackets were afixed to a water-cooled mounting plate which was in turn attached to a vacuum bulkhead. As shown in Fig.s 3 and 4, a thin corrugated window separated the detector volume from the main SPS vacuum. Since the window was required to be thin, the detector volume was also evacuated.

## 2.2 Silicon Detectors

The silicon strip detectors were fabricated by the Central Institute for Industrial Research (S.I.) in Oslo and are functionally similar to those used by the DELPHI experiment[2]. They have an active area of $44.8 \times 44.8\,\mathrm{mm}^2$ and thickness $280\,\mu\mathrm{m}$. Each detector has a total of 1793 diodes with a pitch of $25\mu\mathrm{m}$, only half of which (every second one) is read out. The charge deposited on diodes between read out strips capacitively induces signal on neighboring strips, thus enhancing charge sharing and improving spatial resolution. Metal strips, which are bonded to preamplifier inputs, run the length of the diodes and couple capacitively to the underlying p-strips via a 200 nm thick oxide layer. Each p-strip is connected to a common bias bus through individual $\sim 6\,\mathrm{M}\Omega$ polysilicon bias resistors. We find more than a 99% yield of good strips and leakage currents in the range of 50 pA/strip to 1 nA/strip.

## 2.3 SVX Chips

A detailed discussion of the properties of the Lawrence Berkeley designed SVX-D chip can be found elsewhere[3]. We present only a functional description relevant to the design of the support electronics.

The SVX-D is a CMOS chip which contains 128 charge-sensitive preamplifiers with an overall gain of about 15 mv/fc as well as circuitry for multiplexing and optionally "sparsifying" pulse-height information (i.e. reading out only those strips whose charge is above a set threshold).

In addition to the 128 preamplifier inputs, the SVX has the following input/output lines:

- A set of eight bi-directional data lines which is used to read addresses of hit strips, to set and reset various switches in the pre-amplifiers, and to write a chip number during initialization.
- Three control signals which determine the function of the data lines.
- A calibration line by which charge is injected to set a threshold for sparse readout.
- Input and output priority signals which allow daisy-chaining of an arbitrary number of SVX chips.

- A gated analog line which, during readout, outputs a voltage proportional to the charge on the strip currently being read out. The analog line is only active when the chip currently has priority.

The SVX requires two sources of power, an analog power of six volts which is supplied to the bottom of the chip as well as a bonding pad, and a digital power of between five and six volts which is supplied to a bonding pad.

For each strip read out, the SVX first outputs the chip number (which is written to the chip during initialization) followed by the strip number onto the eight data lines while simultaneously outputting the analog pulse height onto a common bus.

## 2.4 Hybrid Design

Each silicon detector (896 strips) requires seven SVX chips, which were mounted on ceramic alumina hybrid circuit boards. There were two different but similar hybrid designs for the x- and y-view detectors. The two designs were needed since connections could only be made near the outer vertical edges due to space limitations.

Both hybrid types contain five main layers silk-screened onto the alumina substrate. The lowest two layers have horizontal and vertical gold traces intended to bring the control, data, calibration, and analog signals to and from the SVX chips. An SVX analog power plane, an SVX digital power plane, and then a ground plane are layered above. Dielectric material electrically isolates the various layers. Surface mount capacitors provide filtering for the SVX power. The SVX chips are glued with conducting epoxy onto an exposed section of the analog power plane. Connections to the input/output pads of the SVX chips and the gold traces on the hybrid are made via an ultrasonic wire bonding process using one mil diameter aluminum wire. Two sixteen-pin surface mount connectors manufactured by DuPont (Microflex) were mounted on each hybrid.

## 2.5 Detector Mount

The individual silicon detectors were glued to hybrids along one edge, with a two millimeter overlap. The hybrids were then glued to aluminum brackets, which also served as heat sinks, using silver-impregnated epoxy for good heat conduction. The gluing was done under microscope and on a vacuum jig with a precision of ten microns perpendicular to the strips and one hundred microns parellel to the strips. The detectors were positioned for gluing with reference to alignment holes on the heat sink and to the heat sink surface which abuts the mounting plates. Each assembled detector was attached to its mounting plate with a single screw. The x-view detectors were held in position with alignment pins.

The two water-cooled mounting plates (for top and bottom hodoscopes) each consisted of two 2 cm thick plates glued together. Before gluing, a channel for cooling water was machined into the inner surface of one of the disks and matching slots were machined into both disks for the passage of readout cables. Fig. 5 shows a photograph of a partially assembled hodoscope. Five of the six planes had been mounted at the time the photograph was taken. The x- and y-view detectors for each quadrant were mounted with diode strips facing each other across a 2 mm gap. The cable slots for the sixth (as yet unmounted) plane are visible on the right-hand side of this photograph.

Each mounting plate was attached to vacuum bulkheads by means of four precisely-machined aluminum bars. The vacuum bulkheads were made from 3 cm thick aluminum plates, which bolted onto the Roman Pot assembly (described below). Signals to and from the SVX chips traversed from vacuum to atmosperhic pressure on printed-circuit boards ("feed-through boards") which were glued with Araldite into the bulkheads. The bulkheads also contained ports for vacuum pumps and cooling water. Fig. 6 shows the same five-plane assembly pictured in Fig. 5 after it had been joined to the vacuum bulkhead. The bulkhead is at the bottom of the figure. The vacuum-side portions of the printed-circuit boards can be seen traversing the bulkhead and a cooling-water tube is visible in the forground.

## 2.6 Assembly and Testing

Upon receipt from the manufacturer, the silicon detector wafers were subjected to a thorough visual inspection at a microscope station with the intention of catching physical defects such as shorts between strips, breaks in the bias and guard rings or diffusion strips, and poorly cut wafer edges.

After visual inspection, electrical measurements were made of the coupling capacitance and the interstrip capacitance and resistance. Additionally, the leakage currents of the guard ring and bias strip were monitored for a period of 40 to 50 hours. Typically, bias strip currents were in the range $0.1 - 1.0\,\mu$amps while the guard ring currents would increase over a period of about one day from an initial value of about $1 - 10\,\mu$amps to $20 - 100\,\mu$amps and then stabilize. Approximately 10% of the detectors were rejected either for physical or electrical defects.

The SVX chips were tested at Lawrence Berkeley Lab using a procedure developed for the CDF $\mu$vertex detector. Our batch had the unusually low yield of 13% good chips. Using the test results, an attempt was made to match as closely as possible the nominal analog output voltage for each set of seven SVX chips on a given detector. No additional tests were performed on the SVX chips before mounting on the hybrid assembly.

The alumina hybrids were designed by our group and manufactured at CERN. After manufacture, they were visually inspected for obvious defects, then passive components (resistors, capacitors and connectors) were mounted. The hybrids were tested for continuity between bonding pads and connectors and for shorts between adjacent lines. The SVX chips were then glued in place and wire-bonded to the hybrids.

At this point, the hybrid assembly was tested. The test setup was similar to the experimental readout system which is discussed in Sec. 5. It consisted of a MicroVax controlling a CAMAC crate which contained a sequencer module (SRS)[4] to generate the SVX clocking signals, and a readout module (SDA)[4] to read and store the analog and digital address information from the SVX's. A test board provided the electrical interface to the detector assembly and contained a variable charge injection circuit as well as oscilloscope test points. The following checks were made:

- analog output voltage responds to charge injection onto the calibration line;
- priority propagates through the SVX chain;
- average analog outputs of most channels are correct;
- noise levels of most channels are small;
- correlated shifts of baselines (common-mode) on all channels of a chip not too large;
- no (or few) skipped, out of sequence, or multiple occurrences of digital addresses.

Problems detected by the testing were repaired, sometimes with the use of a probe station for tracking down less obvious malfunctions. Not all problems were considered serious enough to warrant the risk of creating a worse condition by attempting repairs. An example would be a channel which was always skipped during readout.

After gluing the hybrids to the heat sinks and the detectors to the hybrids, the 896 readout strips were bonded to the inputs of the SVX preamplifiers using a semi-automatic bonding machine. This process took approximately two to three hours per detector. The detector pictured in Fig. 2 does not have an attached aluminum heat sink (it was a test assembly) but otherwise shows a detector at this stage of assembly.

The above tests were then repeated with the detector attached and biased. As a final test each detector was scanned with a tightly focused, pulsed LED light source to verify that all (or most) channels responded and to get a rough measure of the relative analog gain differences between the SVX's. The detectors were then assembled onto the mounting plates as shown in Fig. 5.

# 3 Installation and Roman Pots

## 3.1 Roman Pots

The silicon detector must be isolated from the Sp$\bar{p}$S machine vacuum for two reasons:

1. The pressure in the vacuum system around experimental areas of the Sp$\bar{p}$S must be in the low $10^{-10}$ mbar range. However, the gas load ($\sim 10^{-3}$ mbar $* \ell/s$) of the complete silicon detector assembly precludes pumping to this pressure range.

2. The detector must be electromagnetically shielded from the beam bunches which set up strong image currents in the vacuum chamber walls which could cause very serious noise pickup in the detectors.

Thus, a metallic, vacuum-tight separation with low outgassing rate was needed. The separator was also required to present a minimum thickness to particles traversing the detector's active volume in order to minimize multiple scattering, particularly of small angle tracks. We therefore developed a special aluminium vacuum vessel which had a very thin ($200\mu$ m) corrugated Al-foil in the sensitive volumes of the detectors as shown in Fig. 3. Since such a thin Al-foil could not withstand the pressure difference of one atmosphere, the silicon detector assembly was designed such that it could be pumped down to about $10^{-4}$ mbar and therefore exclude all forces on the Al-foil.

For reasons of expediency, the whole arrangement, pot and silicon detector, had to be designed such that it could be fitted into the existing Roman Pot driving mechanism which is described below.

Fig. 7 shows the aluminum vacuum vessel with its two corrugated side walls. This piece was machined from a single piece of aluminum using a numerical-controlled milling machine. The free space between the two side walls, which housed the silicon detector planes, was later covered with the 200 $\mu$m thin Al-foil.

The corrugated shape of the Al-foil was produced using special tools as shown in Fig. 8 and afterwards annealed in order to stabilize the corrugated shape. It was then glued to the side walls of the pot with a special silver charged Araldite to ensure good electrical contact between the Al-foil and pot, and thus maintain adequate electromagnetic shielding. Fig. 9 shows a close-up of the corrugated region of the pot, after installation of the Al-foil.

Since the total surface of glue ($\sim 50\,\mu$m thick line over the length of the corrugated shape) exposed to the Ultra High Vacuum (UHV) system of the SPS is less than 1% of the surface of the complete pot, its contribution to the total outgassing rate is negligible. Fig. 10 shows a detail of the connection of the Al-foil to the pot.

## 3.2 Positioning Mechanism

Given the short time allowed for construction of equipment for this test, it was not possible to design and build an optimized positioning mechanism. We therefore used, with minimal compromise, an existing Roman Pot mechanism which had previously been used for diffractive measurements by two experiments at the Sp$\bar{p}$S-collider. A photograph of the mechanism is shown in Fig. 11.

The mechanism allows detectors, mounted inside pots above and below the beam, to be displaced along the vertical axis. The pot flanges are connected to the vacuum chamber of the machine by bellows. During beam manipulations, the inner edge of the vacuum shield was retracted to a distance of about 5 cm from the nominal beam position. During data-taking runs, the two pots were brought close to the beam axis as shown in Fig. 4. The pot position was adjusted and monitored using a linear position transducer with an accuracy better than 50 $\mu$m.

## 3.3 Pumping system

Fig. 12 shows the schematic layout of the special pumping system installed for this test. The line between the SPS sector valves VVS1 and VVS2 represents the SPS vacuum system with

the pot assembly in the center. VPRS1 to VPRS3 are turbomolecular pumps backed by rotary vane pumps. VG1, VG2 and VG-SPS are vacuum gauges and V1 to V4 are roughing valves. On each side of the pot, a combination of a 400 $\ell$/s sputter-ion with a 1000 $\ell$/s sublimation pump (VPS) was installed for UHV production.

The initial pump down from atmospheric pressure of the SPS vacuum system and of the pots down to about $10^{-1}$ mbar is made with VPRS1 via the valve V1 and V2. Below a pressure of $10^{-1}$ mbar, measured on VG2 and VG-SPS, valve V2 closes automatically and VPRS1 is pumping via V1 only the pots. At the same time V3 and V4 are opened to pump the SPS vacuum system with the help of VPRS2 and VPRS3. After a bakeout at 150 °C of the SPS vacuum system, UHV production with the VPS's was started.

In case of a sudden pressure rise higher than $10^{-1}$ mbar in the SPS vacuum system or in the pots, VVS1 and VVS2 as well as the roughing valve V1 close and the separation valve V2 open in order to equalize the pressures in both vacuum systems and therefore avoid damage to the detector or thin Al-foil of the pot.

After a short power cut the pumping system restarts automatically. If there is however a slow pressure rise above $10^{-1}$ mbar due to an extended power failure of a few hours, the complete pumping system will be blocked and can, for safety reasons, only be manually restarted.

The best pressure obtained in the SPS vacuum system after a few weeks of pumping was about $5 \times 10^{-10}$ mbar with a residual gas composition mainly composed of hydrogen and water vapor. The pressure in the pots was maintained at about $5 \times 10^{-4}$ mbar.

## 4 Silicon Power System

The power system supplies the DC voltages to run the detectors, with the requirements that these voltages have low noise ($<$ 1 mV at the detector) and that every bias current is monitored. The system consists of a switch panel in the counting room for individual control of each of the 48 detectors; the supplies, mounted in a rack next to the detector; and a monitoring system composed of a CAMAC multiplexer and ADC module, read out by a Caviar unit in the counting room. The use of opto-couplers to switch individual detectors assures total electrical isolation of the control circuitry thus minimizing noise pick-up.

The SVX analog and digital voltages as well as voltages to power the PID boards (described below) were generated by commercial supplies (Ultronix).

Ninety volt batteries (Eveready No. 490) were used to bias the detector back planes, since suitably decoupled batteries provide ripple-free voltage, and make individual detector current monitoring relatively simple. Four batteries were mounted in a double-width NIM module. The output voltage for each channel could be independently adjusted in the range 0 to 90 V and was determined by a combination of an external reference voltage, common to all supplies and potentiometers for each channel as shown in Fig. 13. Two Darlington connected transistors provide a low output impedance, and independence from battery voltage changes. With typical bias voltages of 50 V and currents of 1 to 100 $\mu$A (due mainly to guard ring leakage), battery life is greater than 6 months.

The voltages and currents of all supplies were continuously monitored by a CAMAC analog scanner and DVM (Lecroy LG5310), and displayed in the counting room in bar graph form. The SVX analog and digital voltages and the detector bias voltage are interlocked to insure that they could be turned on only in the correct order.

## 5 Triggering and Readout System

The control signals necessary for operation of the SVX chips were generated by the Lawrence Berkeley designed SRS (SVX Readout Sequencer)[4] CAMAC module. This module contains an AMD2910 sequencer and 12 kbytes of program memory which may be downloaded from the host computer. Approximately 6 kbytes of the memory are used to store bit patterns which are sent to front panel outputs to drive the SVX's. The AMD2910 addresses successive locations of the internal memory to access these bit patterns, but may jump to any specified address depending

on the state of front panel input signals (e.g. scintillator trigger signal). This permits access to the different sets of bit patterns required either by the sampling sequence or by the SVX readout sequence.

The SRS control signals were converted to differential levels and sent over a 50 m flat twisted pair cable to the interaction region, where a repeater board converted them to single ended TTL levels. The control signals then traveled another two meters over two flat cables to twelve Plug-In-Driver (PID) printed circuit boards of the top and bottom half detectors. This signal path is indicated in Fig. 14 for the upper detector hodoscope. As shown in this figure, there is one PID board for each detector plane. The PID boards plug into feed-through boards which together with short Kapton cables, relay signals to and from the hybrids, through the vacuum bulkhead . Two analog output daisy-chains from each PID board are routed to the control room on shielded twisted-pair cable.

The purpose of the PID was to:

- fan out control and data signals to the hybrids;
- daisy chain the readout of the x- and y-view hybrids from each quadrant to produce two daisy-chains of 1792 channels per PID board (for a total of 24 daisy-chains);
- convert the single-ended SVX analog output signals to differential levels which are sent to the counting room via approximately 50 m of shielded twisted pair cables;
- mulitplex the digital data signals (strip number and chip number) from the SVX chips onto a bus common to all PID boards. Signals from any daisy-chain could be selected from the counting room for diagnostic purposes. (This bus is not shown in Fig. 14.)

The detector readout was triggered by a coincidence of scintillation counters, which detected particles produced at polar angles between 0.027 and 0.11 rad. The trigger was sensitive to approximately 45% of the total cross section and introduced minimal bias.

Synchronization with the beam crossing was accomplished by means of a signal from a directional coupler which sensed the beam passage. When live, the SRS generated a double-correlated sample and hold sequence for every beam bunch crossing (3.8 $\mu$sec). Upon receipt of a scintillator trigger, the SRS initiated and controlled the SVX readout.

We did not utilize the sparsification feature of the SVX since, in the short time available to us, we were not able to adequately evaluate its performance. We were particulary concerned that charge fluctuations at the inputs to the preamplifiers on time scales comparable to the readout cycle would result in common baseline shifts which would render the sparsification useless. Rather, we chose the CERN-designed SIROCCO II[5] (SIlicon ReadOut Camac COntroller) module for analog to digital conversion. This module features optional hit sparsification as well as common mode and pedestal subtraction. It contains a 10-bit flash ADC, and internal memory to store pedestals and pedestal subtracted pulse heights for up to 2048 channels. Twenty four of these modules were used (one for each daisy chain).

Readout to the host computer (MicroVAX II) was implemented using standard CAMAC and ROMULUS/REMUS modules. Silicon hit data together with pulse-height, pulse arrival time and scaler information from the scintillators were written to 8 mm tape cassettes using Exabyte tape drives.

Data was collected with full detector readout as well as under SIROCCO II sparsification. Approximately 1.4 million events were written in the full readout mode. The data acquisition rate was limited to approximately 3 Hz by the tape writing speed. The full event size was 172 kbytes.

For readout sparsification, the threshold was set at three times the average r.m.s. noise found in the two daisy-chained detectors for each SIROCCO II . Only channels passing the threshold were read out and written to tape. In order to monitor pedestal stability and common mode noise, 21 additional "monitor" channels (2% of the total), were always read out. Thresholds for hot channels were set such that those channels were never read out. The event size was typically 9 kbytes, and the acquisition rate was approximately equal to 35 Hz. About 5 million events have so far been collected in this mode.

# 6 System Performance & Data Analysis

The silicon Microvertex detector was tested under high luminosity (typically $2 \times 10^{30} cm^{-2} s^{-1}$) collider operating conditions during the Fall 1990 run. The most important result obtained from run is that it is possible to cleanly and routinely run a silicon detector at a distance of 1.5 mm[1] (approximately 15 beam widthes) from the beam.

In more detail:

1. We saw no increase in scintillator counting rates as the pot window was brought from 5 cm to 1.5 mm, indicating that the beam scrapers which were positioned at 6 beam widthes were still effectively shadowing the detector assembly. We found however, that when positioning the window to a distance of 1.2 mm from the beam, we experienced an increase in scintillator counting rates of about a factor of two, which can be accounted for if aproximately one halo track per bunch crossing interacts in the aluminum shield. Thus, we chose to run regularly at the 1.5 mm distance.

2. We saw no evidence for run-to-run variations in the average vertical position of the beams and were thus able to set the detectors to the same position at the start of every Sp$\bar{p}$S fill. Preliminary analysis of reconstructed verticies shows that over the course of a run, the Sp$\bar{p}$S beams were steady to better than 100 $\mu$m.

3. Forty seven of the 48 detectors functioned properly when installed into the Roman Pots and subjected to vacuum. The back-plane of the one failed detector developed a short to ground. Two SVX chips (256 channels) of another detector failed during the run due to a power glitch. Of the remaining 46 detectors, 386 ( 1% of remaining channels) were unusable due to high noise levels caused mainly by defects in the silicon (e.g. holes in the $SiO_2$ layer resulting in shorts between a diode and its readout strip). Therefore, a total of 96.4% of the 43008-strip system was found to work.

4. Electronic effects, such as pedestal shifts, due to RF pickup of the passing beams was not seen.

5. Total detector leakage current decreased when the detector was put into vacuum and remained low during the course of the run. Typical total leakage currents varied between 1 and 20 $\mu$amps while in vacuum. This compares to values in the range of 100 to 200 $\mu$amps as measured on the test bench in air.

6. Strip noise showed no noticable increase during the course of the run, thus no significant radiation damage was observed. This is further illustrated by Fig. 15(a) which shows the rms noise levels in units of ADC channels of a typical detector as a function of channel number. The data for this plot were taken near the end of the collider run. Since the beam passes nearest to strip 896, the radiation dose from interactions increases with increasing strip number. The fact that the rms noise shows no corresponding increase indicates that no significant interaction-induced radiation damage had occurred.

7. Based on an event scan, the number of tracks coming from a sources outside the p$\bar{p}$ interaction region (e.g. "beam halo") was neglible.

8. The detectors and associated readout electronics displayed excellent signal to noise characteristics. The average cluster[2] pulse height distribution for a typical detector is plotted in Fig. 15(b) for all clusters with width less than four strips and (cross-hatched) all clusters with width equal two. The average of the uncut distribution is 94.5 ADC counts while the average of the cluster width equal two distribution is 74.9 ADC counts. Dividing

[1] The inner edge of the aluminum window was positioned at 1.5 mm. The edge of the sensitive region of the silicon was 3.0 mm from the beam.

[2] A cluster is defined as a contiguous series of strips each with a pulse height more than 4 times the rms noise and with total cluster pulse height more than 5 times the rms of all strips in the cluster

this last value by the average rms noise shown in Fig. 15(a) of about 2.2 ADC counts gives an average signal to single channel noise of 34.0. (When no cut is made on cluster width, the average signal to single channel noise is 43.4 but there is evidence for significant contribution from hits originating from two nearby tracks.)

9. The distribution of cluster hit multiplicity in one typical detector is shown in Fig. 16(a). The average hit multiplicity per detector is 1.8. The distribution of hits as a function of strip number is shown in Fig. 16(b). The comparison of these and other distributions with Monte Carlo is under study.

10. Event dispays tend to be clean and contain few clusters which are not associated with tracks from a common vertex. Fig. 17 shows a relatively high multiplicity but otherwise typical event.

## 7 Conclusions

A large silicon system was assembled and operated at very short distance from the Sp$\bar{p}$S-collider beam, in the LSS5 high luminosity interaction region.

The detector performance was satisfactory with signal to noise ratios in the range 20 to 30, which allows an on-line pedestal subtraction and zero suppression with high efficiency.

The background due to beam halo particles, and the effect of RF induced signal from bunch crossing was found to be negligible.

The success of this test leads to the conclusion that a detector of this kind might be very effective in tagging beauty particles produced in the forward region in high energy hadronic collider, at the level of both on-line trigger and off-line analysis.

## References


[1] Proposal P238, Study of Beauty Physics at the SPS-Collider with Real-Time Use of Silicon Microvertex Information, CERN-SPSC/88-33;
P238Add.1, Measurement of $B_s$ Mixing, CERN-SPSC/89-43;
P238Add.2, Request For Collider Test of Silicon Microvertex Detector, CERN-SPSC/89-55;
P238Add.3, Further Comments on Collider Test of Silicon Microvertex Detector, CERN-SPSC/89-61.

[2] M. Caccia et al., NIM A260 (87)124.

[3] S.A. Kleinfelder et al., IEEE Trans. Nucl. Sci. 35 (1989) 171.

[4] F. Kirsten and C. Haber, IEEE Trans. Nucl. Sci. 37 (1990) 288.

[5] A. Lang and J.P. Vanuxem.

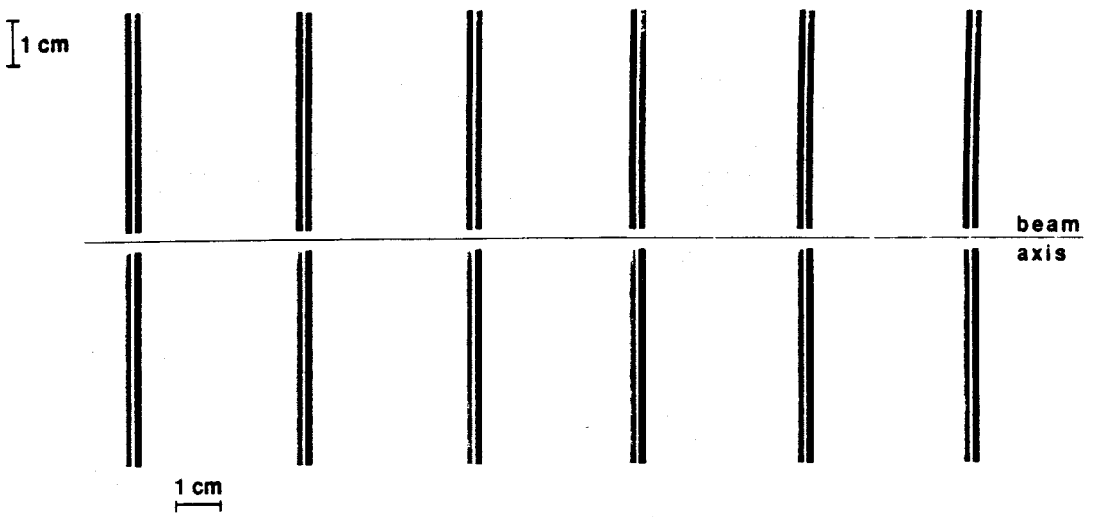


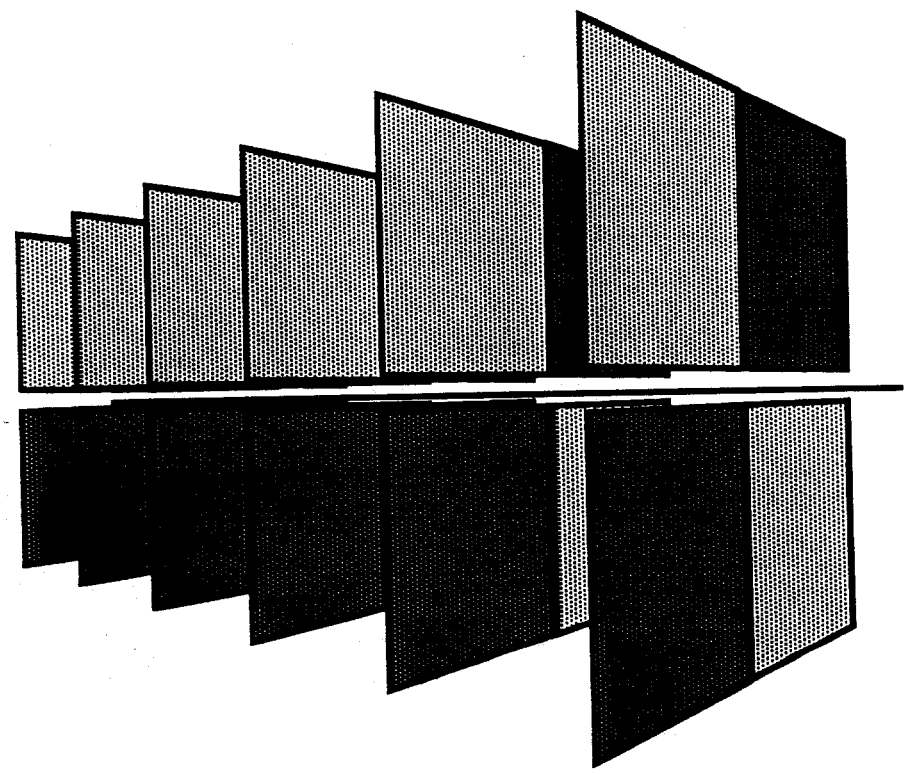

Figure 1: (a) Side view of the detector configuration. The black lines indicate the x-view detector positions and the gray lines indicate the y-view detector positions. (b) Perspective drawing of detector. Only four of the eight detectors in each plane are visible. The strip orientation of the hidden detectors is perpendicular to that of the detectors they face.

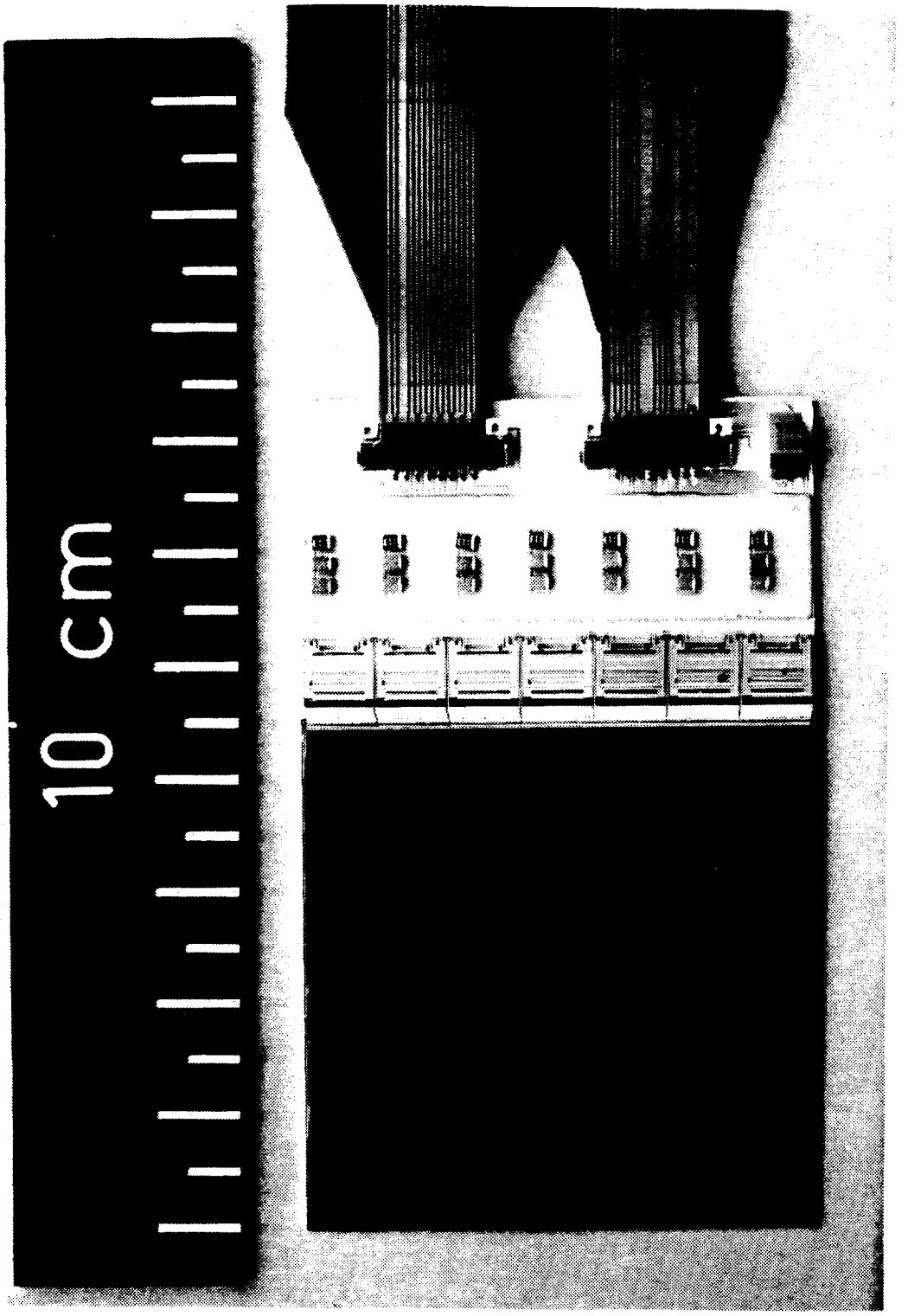


Figure 2: Photograph of a single silicon strip detector with its associated alumina hybrid and readout chips.

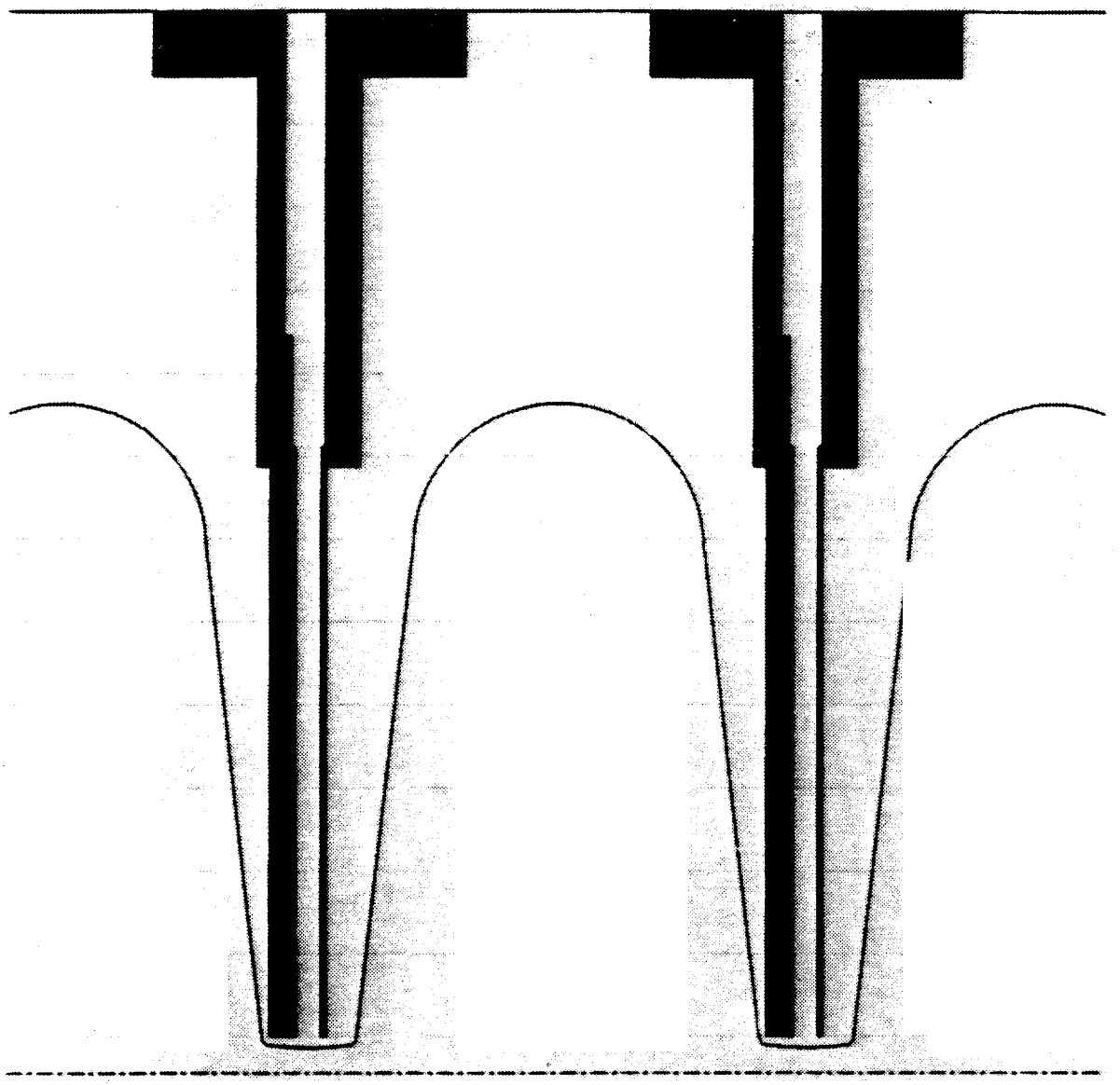

Figure 3: Side view showing two detector planes. The y-view detectors for each plane are on the left of the corresponding x-view detectors.

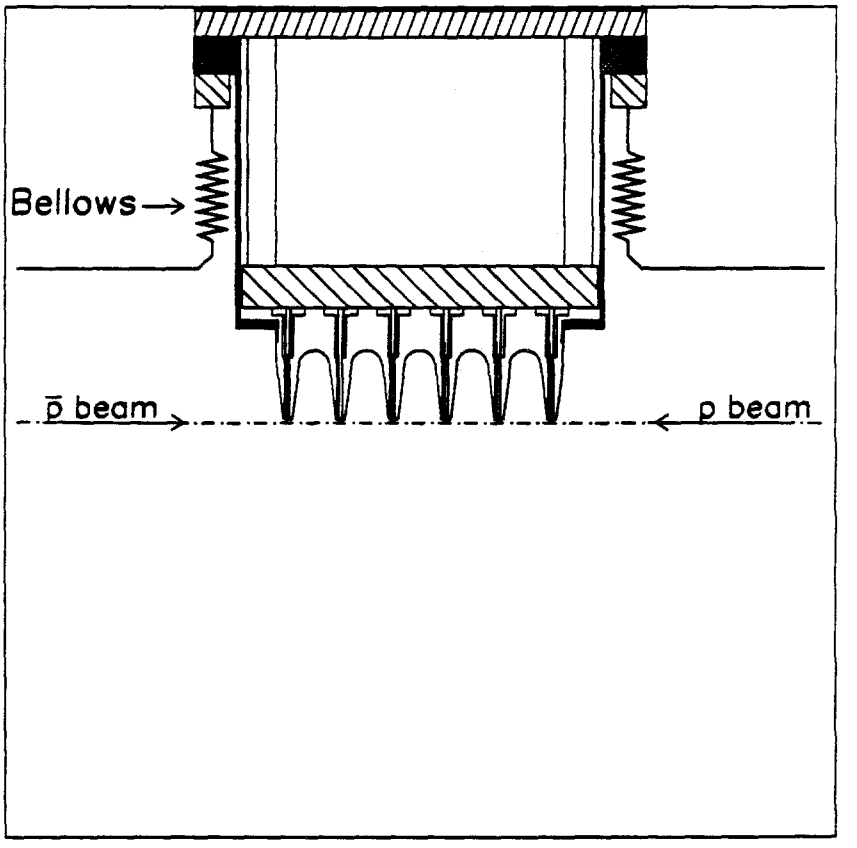


Figure 4: Sketch of the upper silicon half-detector mounted inside a Roman Pot. The bottom of the corrugated window is shown at a distance of 1.5 mm from the beam.

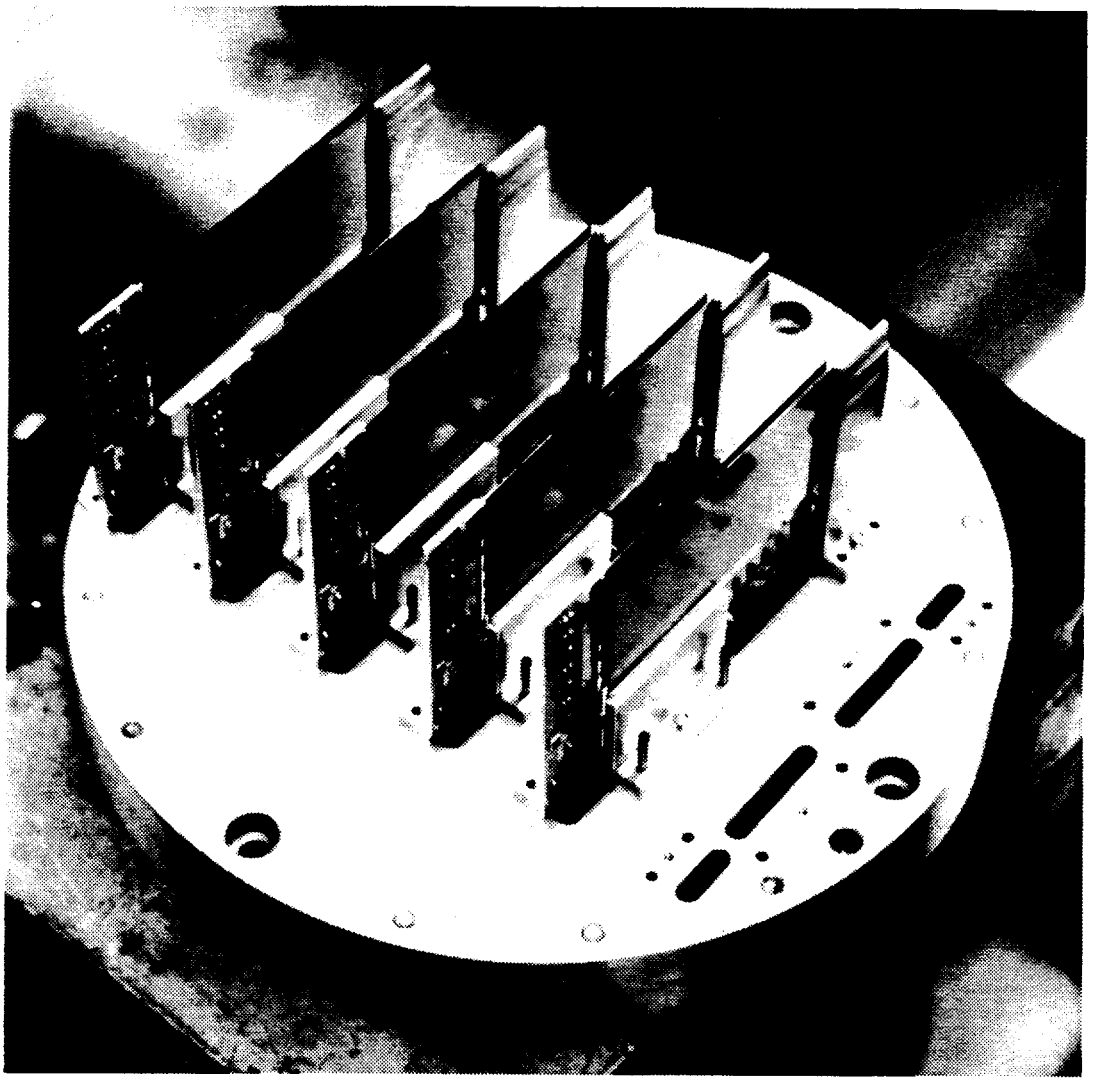

Figure 5: Photograph of a partially assembled half-detector. Five of the six planes had been mounted at the time the photograph was taken.

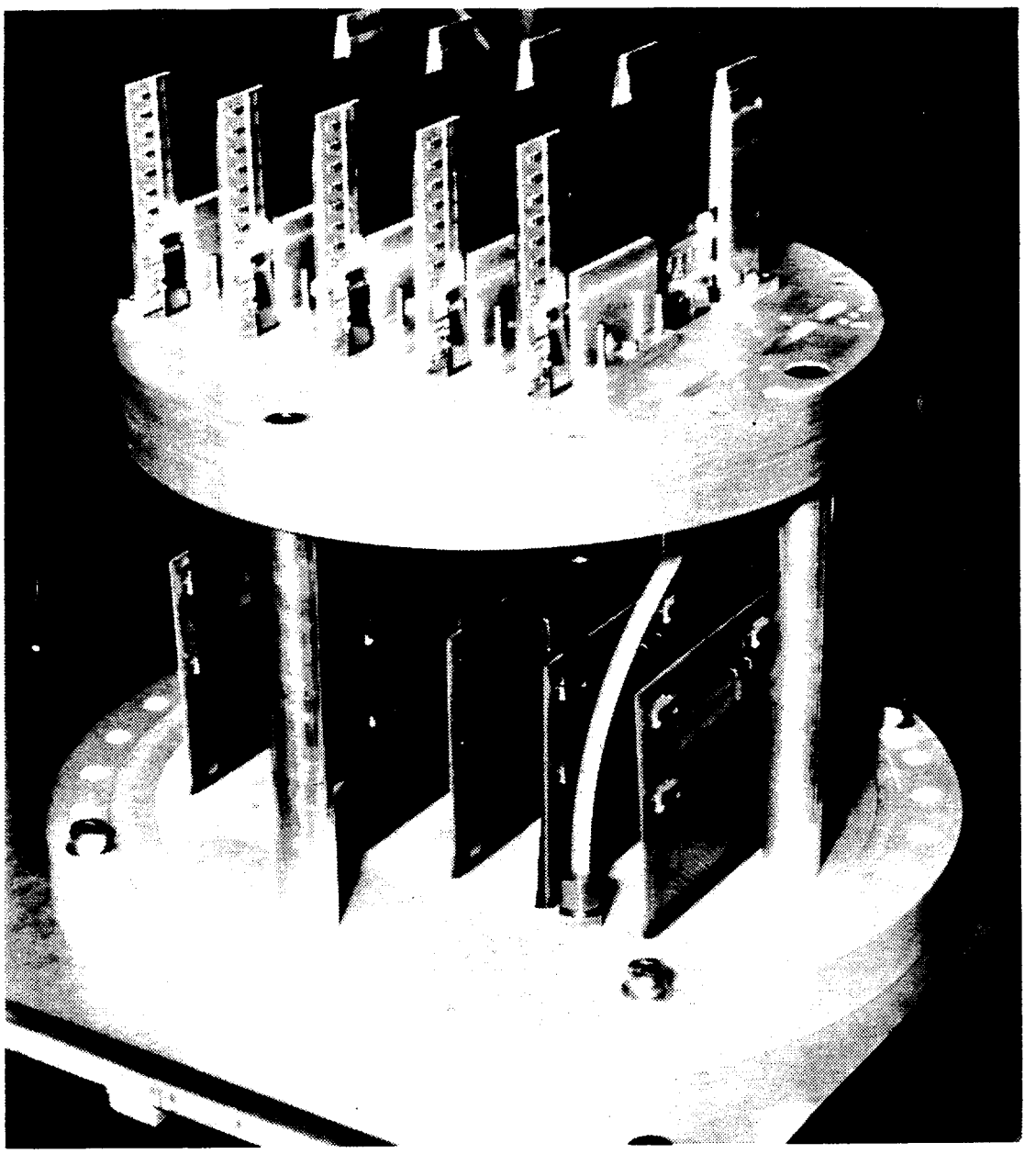

Figure 6: Photograph of the five-plane assembly joined to a vacuum bulkhead.

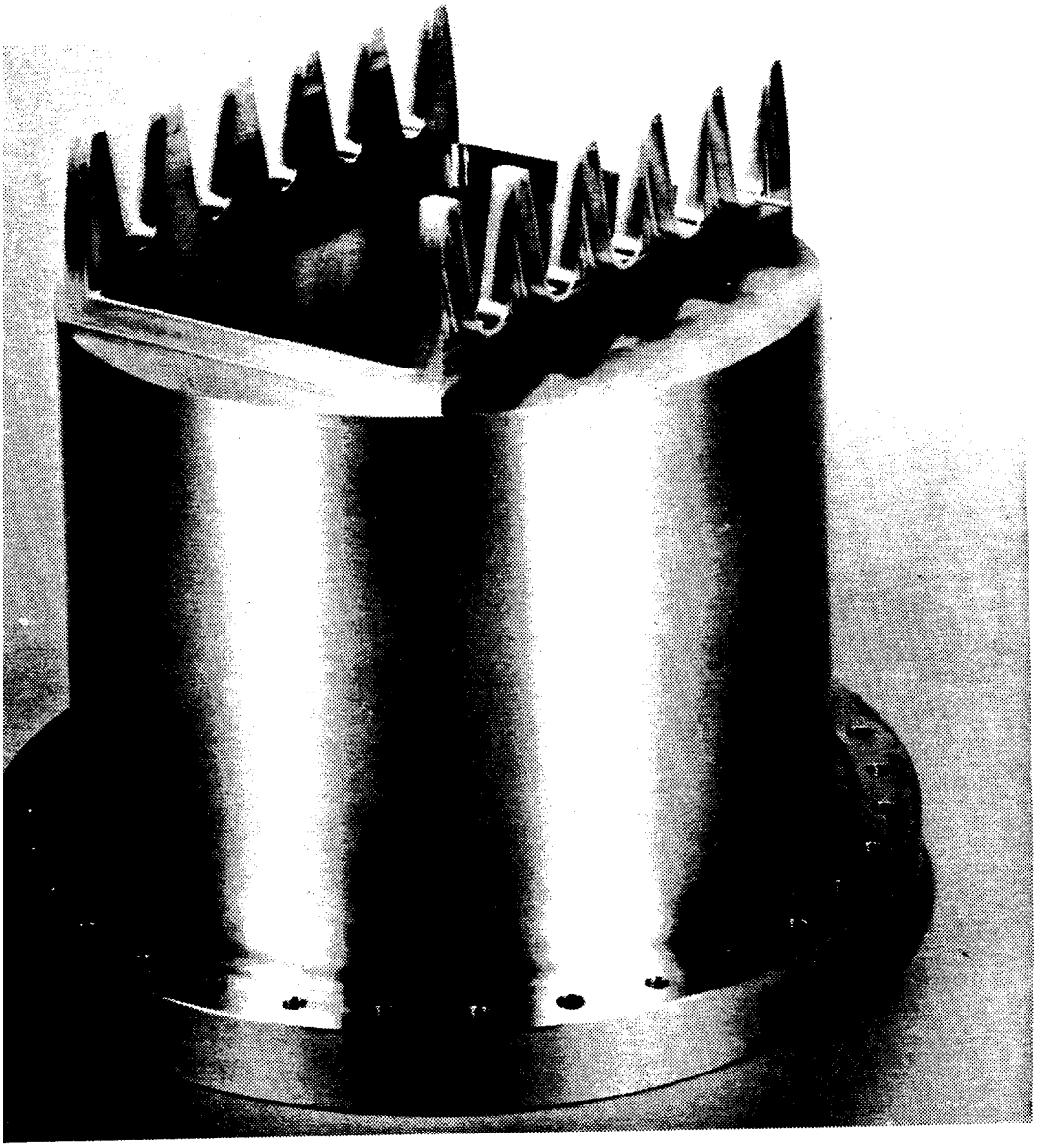

Figure 7: Photograph of a Roman Pot, taken before mounting of the corrugated window.

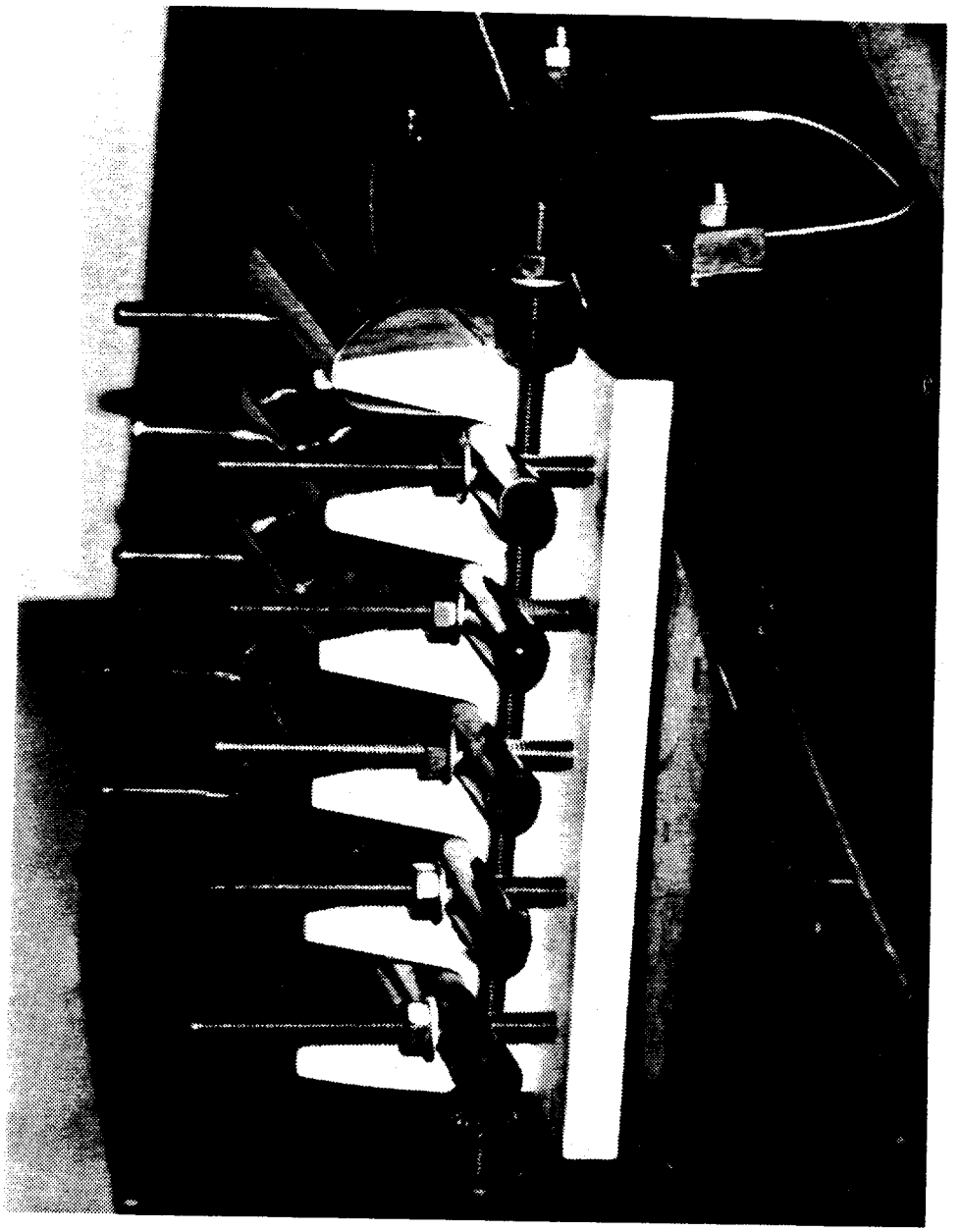

Figure 8: Jig used for pre-forming the 200 $\mu$m aluminum window.

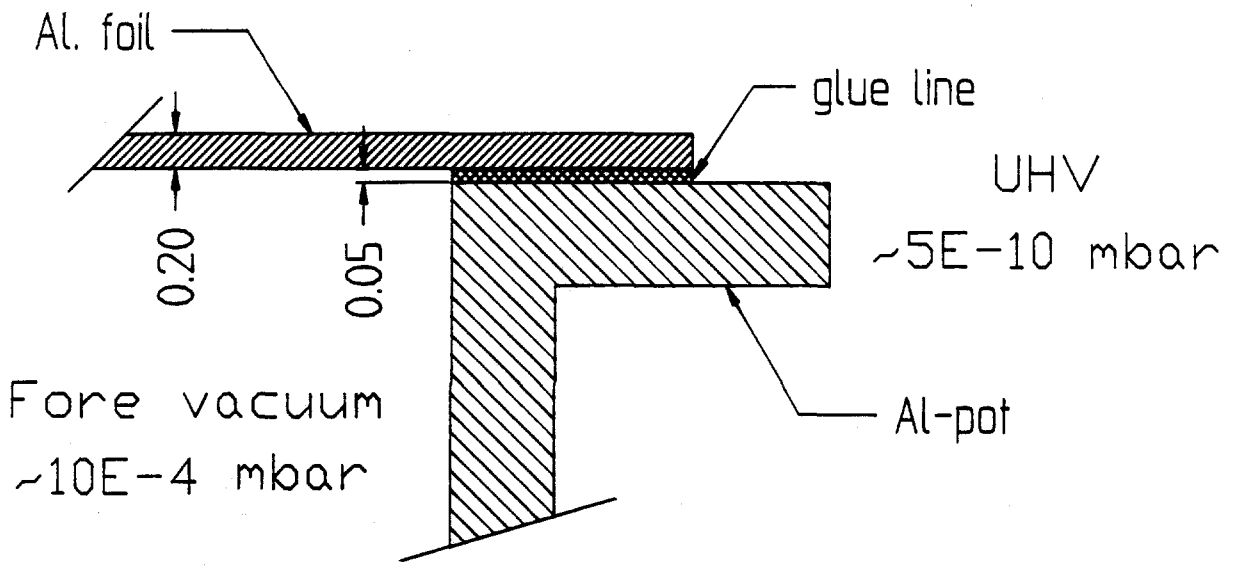


**Figure 10: Detail of the joint between the 200 $\mu$m window and the Roman Pot.**

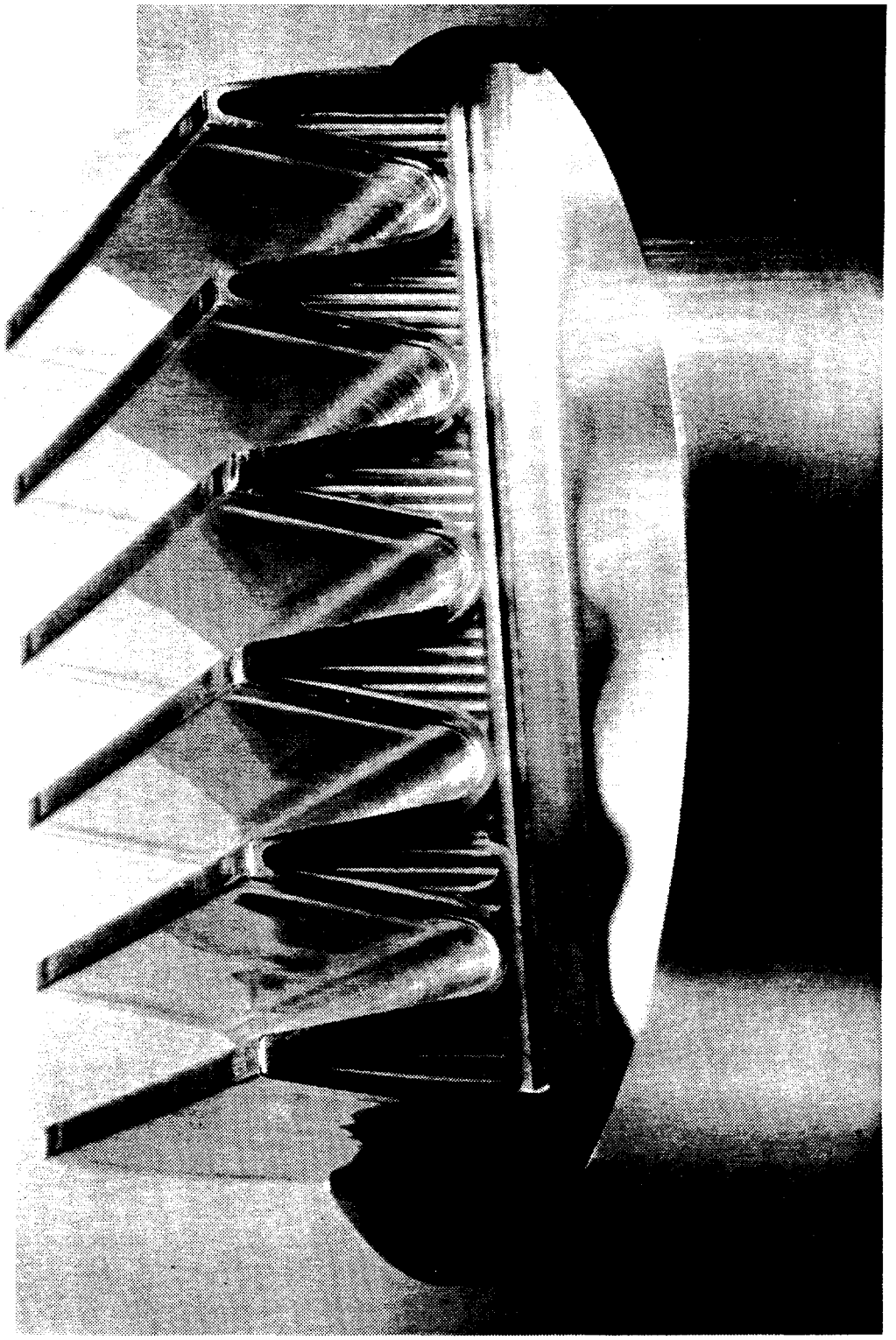

Figure 9: Close up photograph of the corrugated window on the Roman Pot designed for this test.

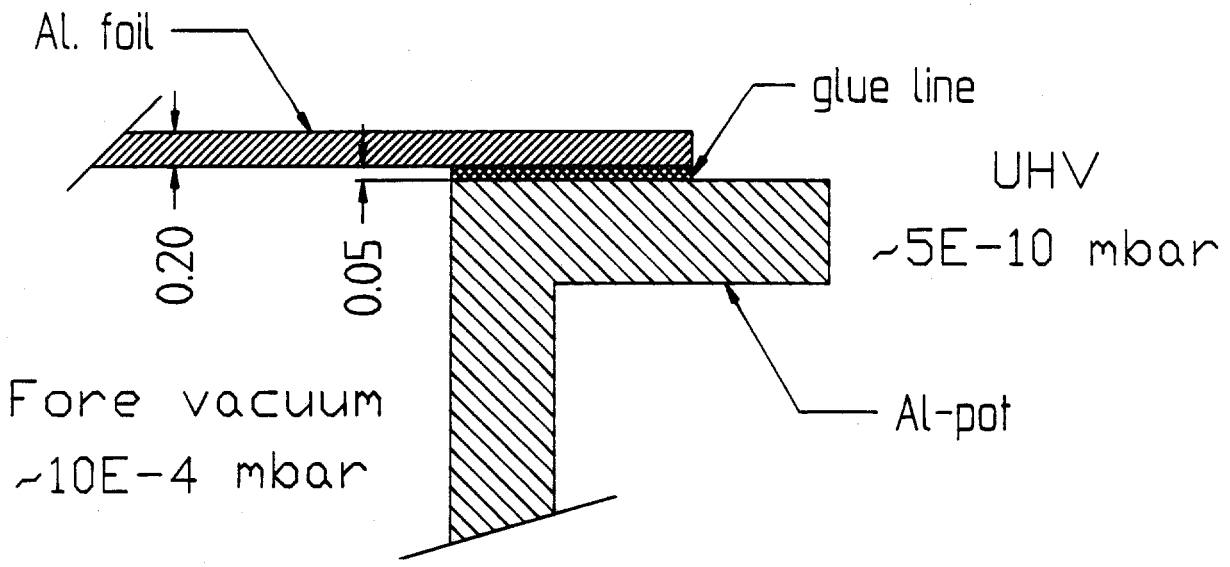


**Figure 10: Detail of the joint between the 200 $\mu$m window and the Roman Pot.**

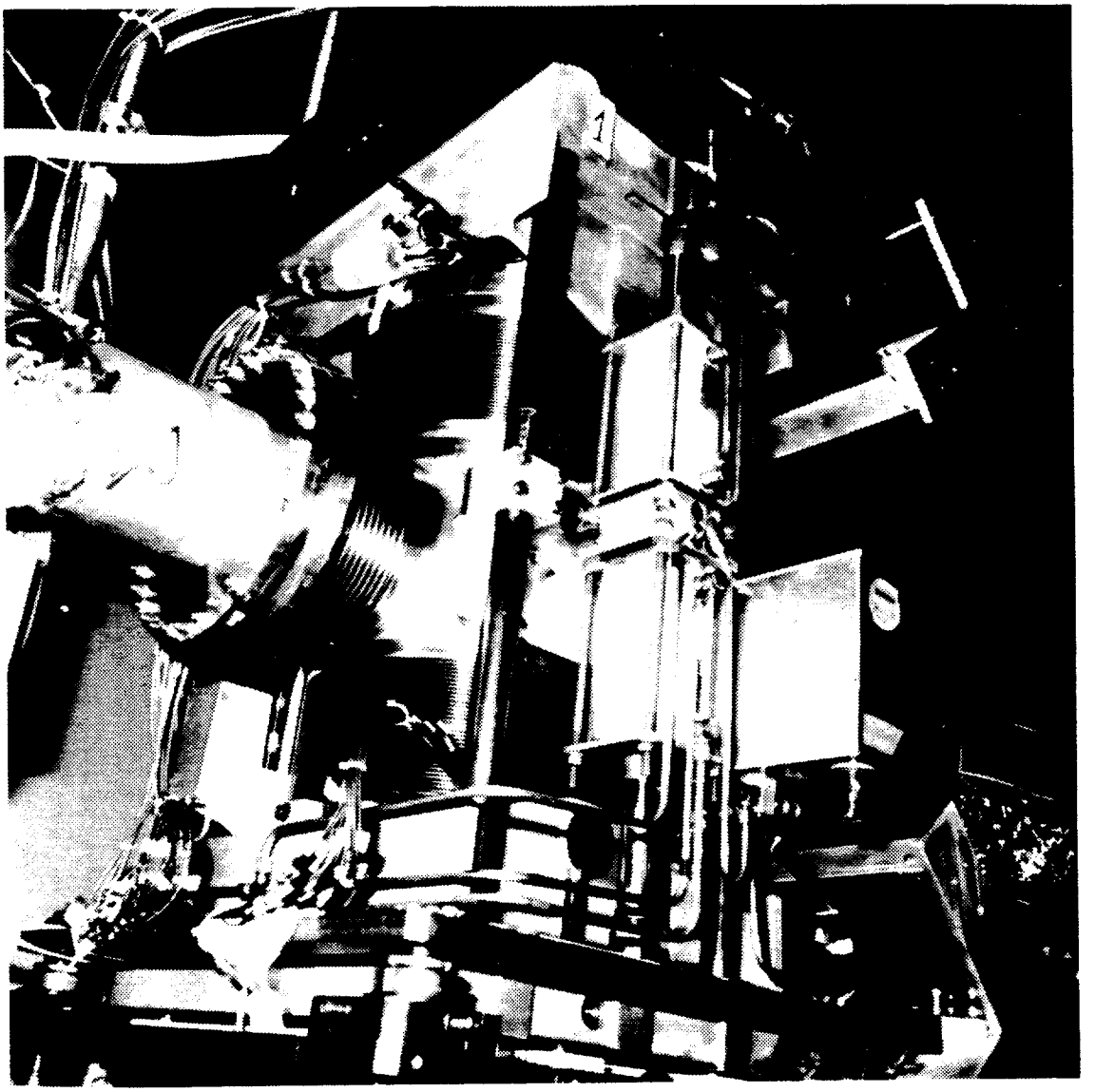

Figure 11: Pot positioning mechanism, after installation in LSS5.

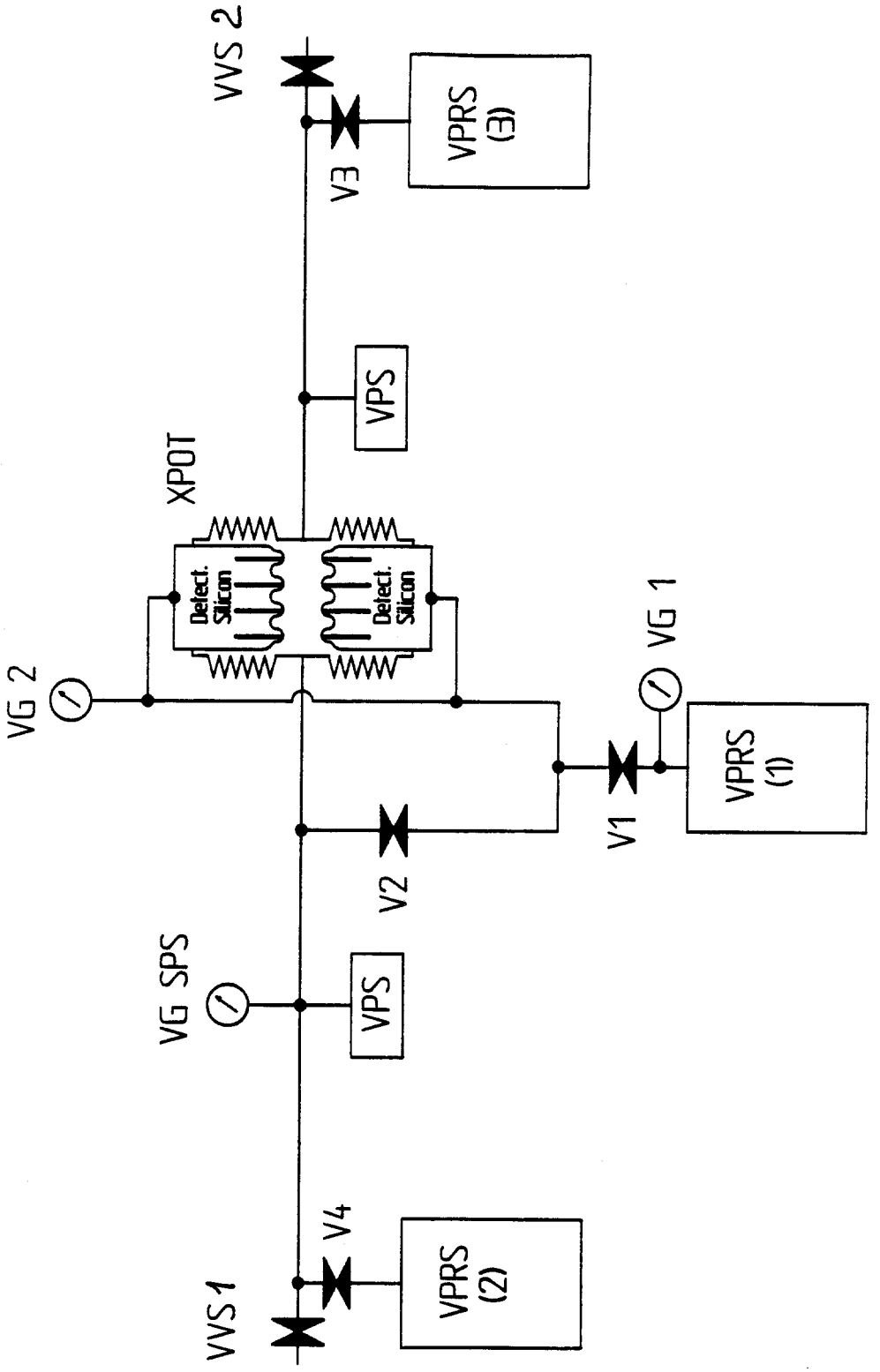


**Figure 12: Schematic layout of the vacuum pumping system.**

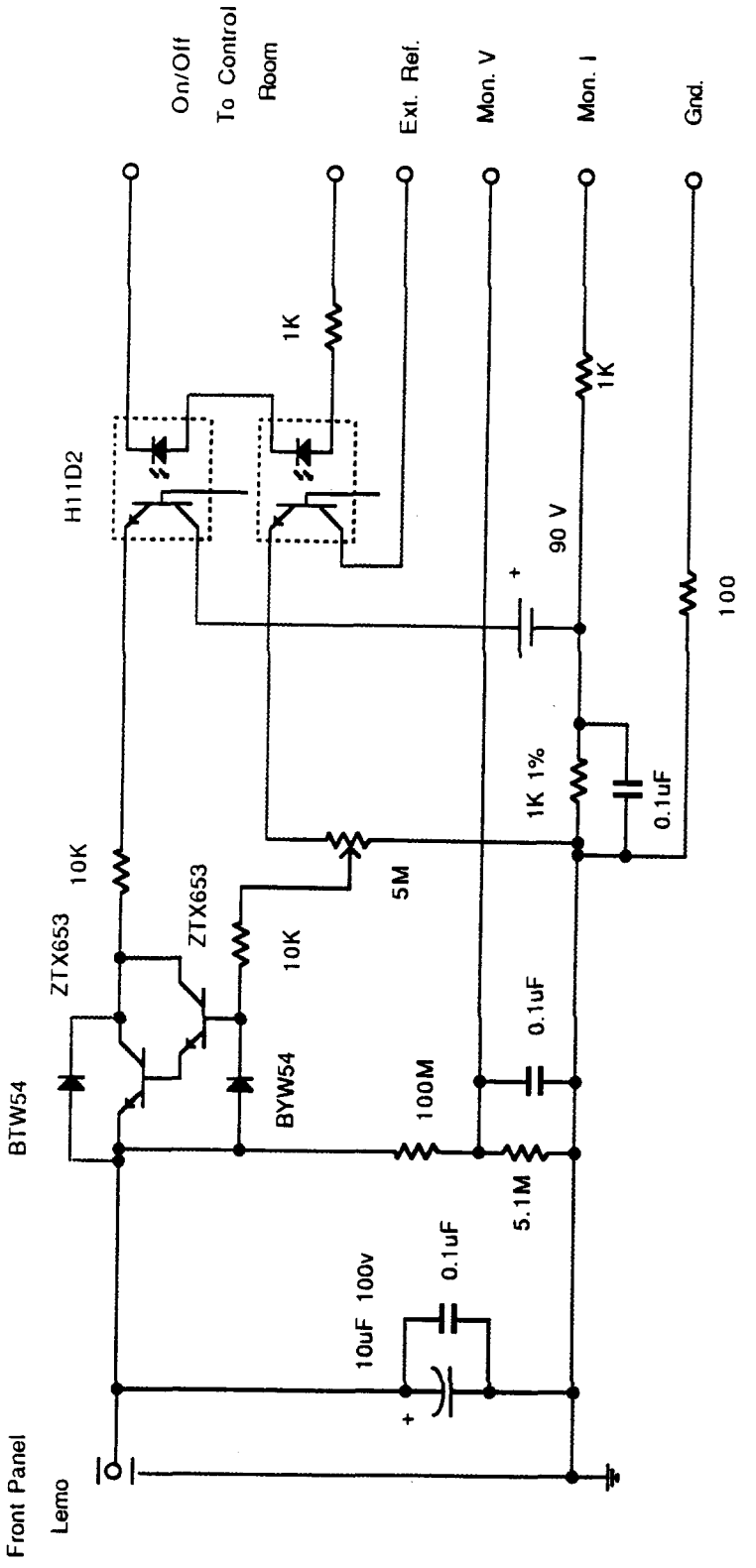


Figure 13: Power supply bias and control circuit.

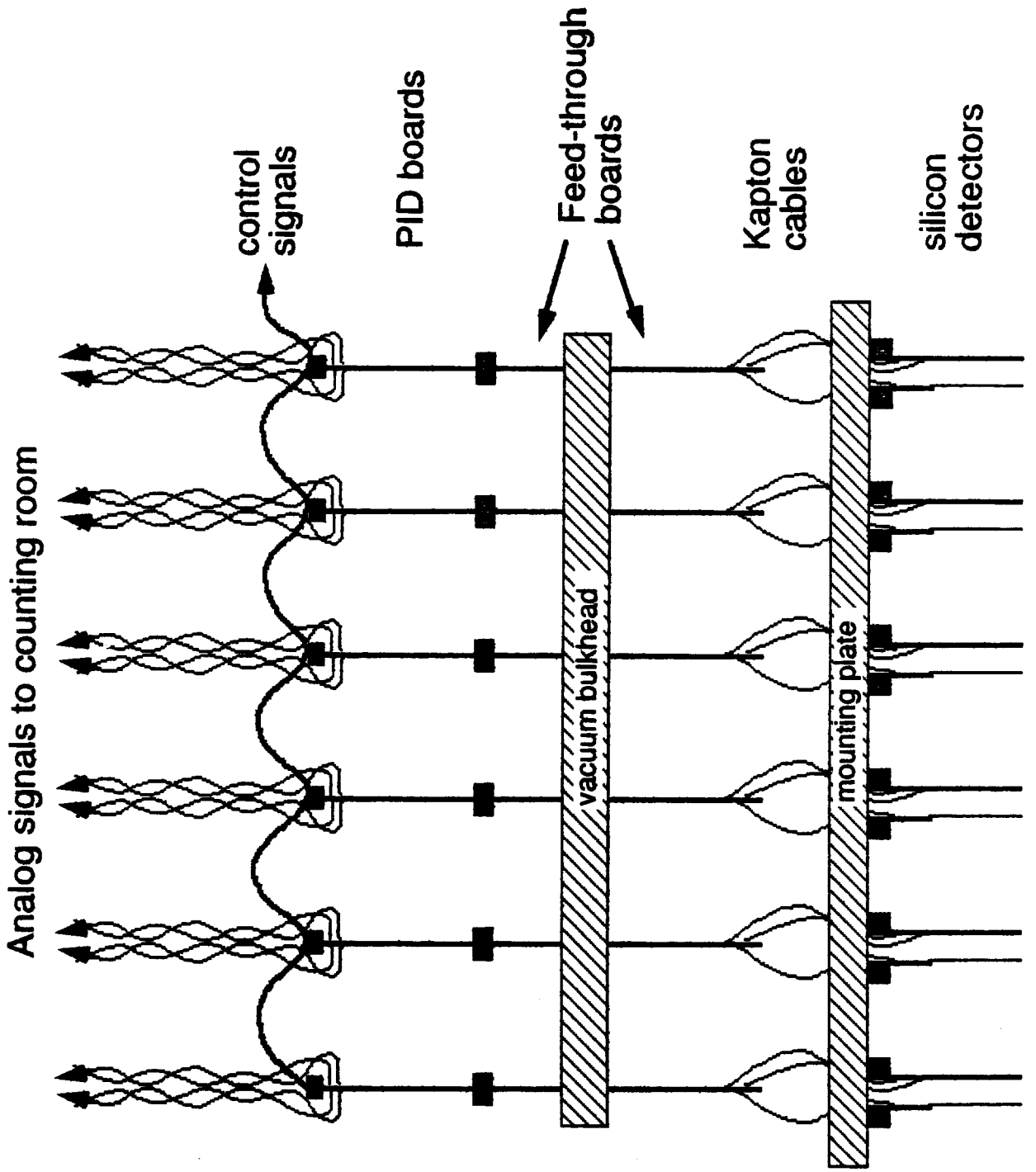


Figure 14: Schematic of readout and control pathes for one detector hodoscope.

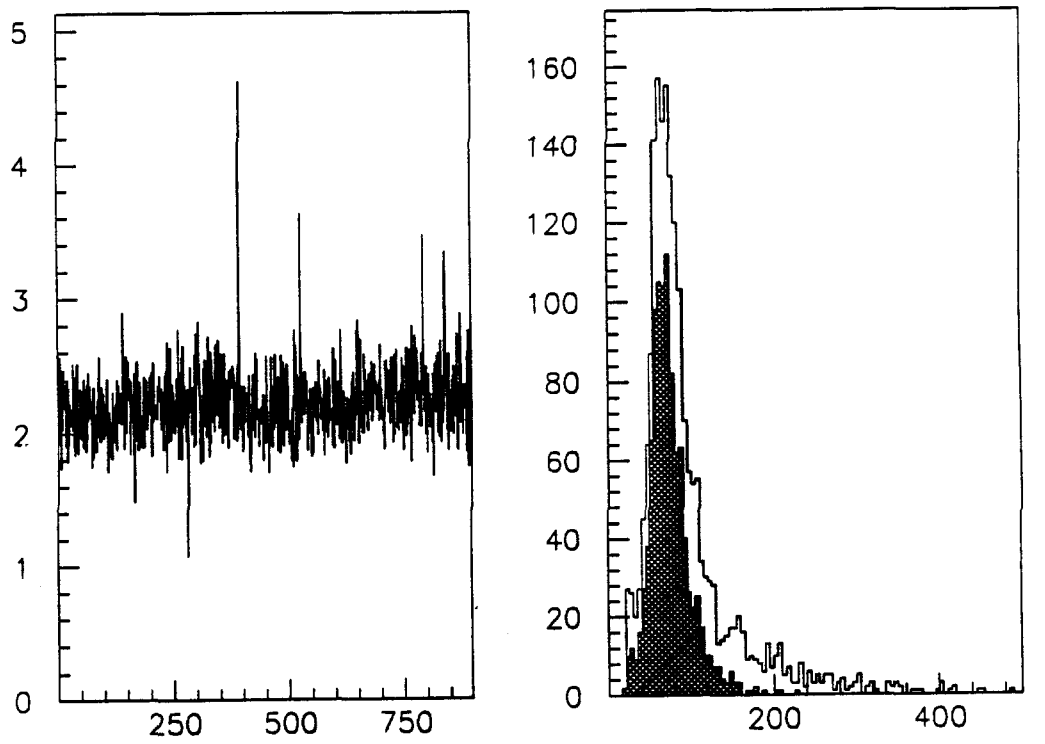


Figure 15: (a) The rms noise of a typical detector plotted vs. channel number. (b) Cluster pulse height distributions. The unhatched histogram is for all clusters with width less than four strips. The hatched histogram is for all width=2 clusters.

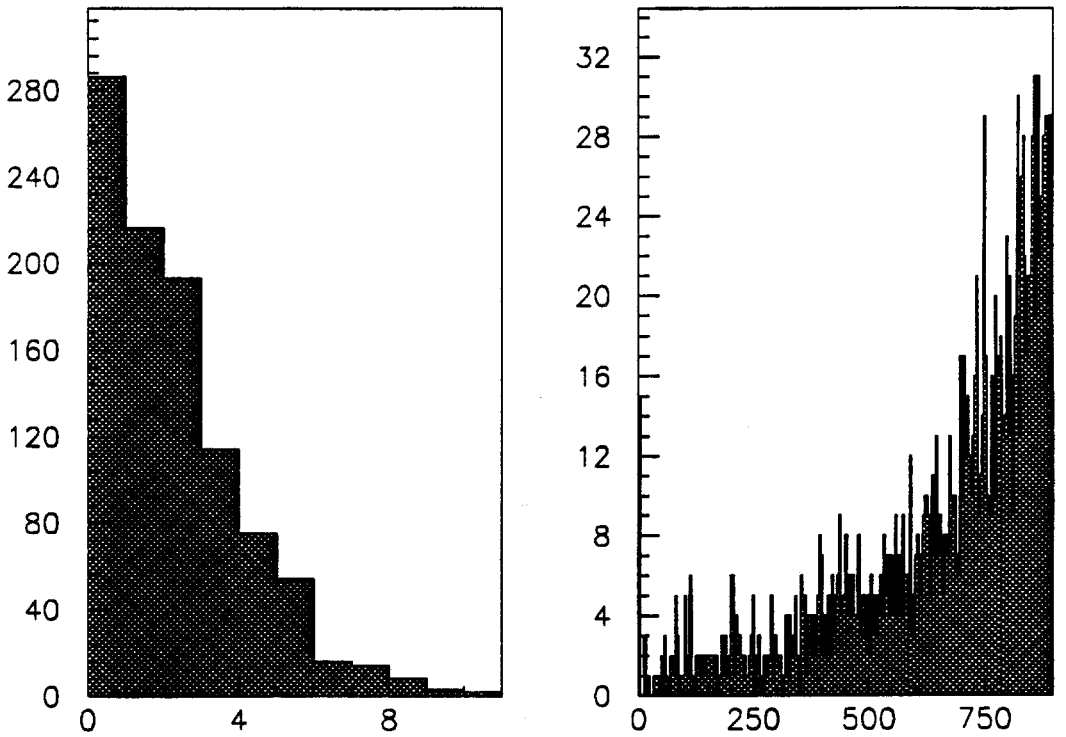


**Figure 16: (a) Hit multiplicity distribution on one detector. The average hit multiplicity is 1.8. (b) Hit distribution vs. channel number for a typical detector.**

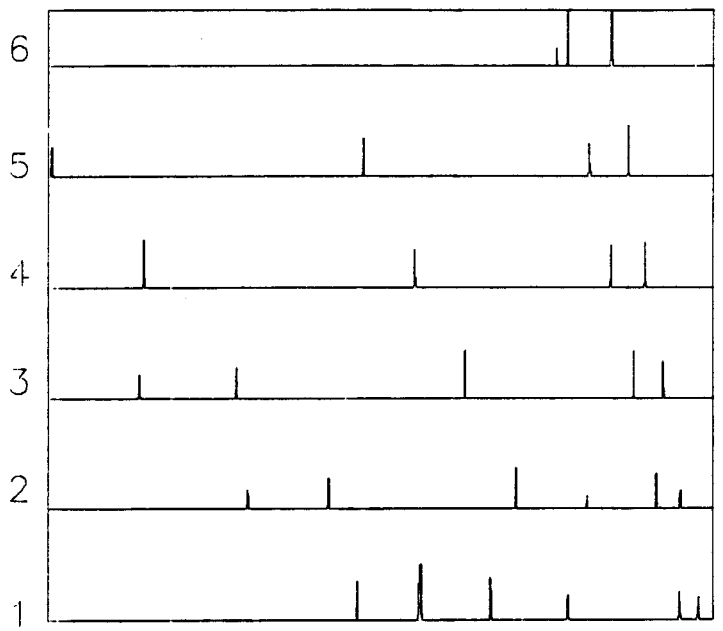


**Figure 17: Pulse height distribution vs.channel for the six planes of one detector quadrant for a single event. Only pulse heights greater than 4 times the rms noise are plotted.**

845

7 January, 1991

**PROPOSAL TO FNAL**

# A DEDICATED BEAUTY EXPERIMENT FOR THE TEVATRON COLLIDER


J. Ellett, S. Erhan, D. Lynn, M. Medinnis, P. Schlein*), J Zweizig
University of California, Los Angeles, CA, U.S.A.

P. Weilhammer
CERN, Geneva, Switzerland

J. Seguinot, T. Ypsilantis
College de France, Paris, France

A. Czermak
Institute of Nuclear Physics, Cracow, Poland

K.T. Knöpfle, T. Kihm
Max-Planck Institute fur Kernphysik, Heidelberg, F.R.G.

T.Y. Chen, D. Xi
Nanjing University, Nanjing, P.R.C.

R. Dzhelyadin, V. Obraztsov, A. Ostankov
IHEP-Serpukhov, Protvino, U.S.S.R.

R. Harr, P. Karchin, C. Liapis, J. Sinnott
Yale University, New Haven, CT, U.S.A.


## Abstract


We propose a high statistics study of the physics of Beauty particles at the Tevatron $p\bar{p}$ Collider with a new detector [illegible] which covers a 600 mrad forward aperture with magnetic spectrometers, RICH counters and electromagnetic calorimeters. The detector is triggered by real-time calculations on data obtained from a silicon-micro-vertex detector installed inside the vacuum chamber throughout the interaction region. With $\int \mathcal{L}dt < 10\ pb^{-1}$, $\Delta M/M$ can be measured with an error of $\pm 0.1$ from the observed mass [illegible] in the decay of tagged $B_s$ mesons. With $\int \mathcal{L}dt \approx 200\ pb^{-1}$, rare branching fractions as small as $10^{-6}$ would be measured, although CP-Violation will only be accessible if the asymmetry is larger than about 30%.


*) Spokesperson

## TABLE OF CONTENTS


1. **INTRODUCTION** 3

2. **PHYSICS GOALS** 5

   2.1 Overall Goals and Sensitivity to Rare Decay Channels 5
   2.2 $B_s$-Mixing (CP-Conserved) 6
   2.3 Simulation of $B_s$-Mixing Analysis 8
   2.4 Sensitivity of CP-Violation Search 12

3. **GEOMETRIC ACCEPTANCE** 14

4. **TRIGGERING & SIMULATION** 17

   4.1 Strategy 18
   4.2 Event Simulation 18
   4.3 Trigger Algorithm 19
   4.4 Trigger Performance and Expected Rates 20
   4.5 Pileup 21

5. **SPECTROMETER ELEMENTS** 21

   5.1 Silicon-Strip Microvertex Detector 22
   5.2 Vacuum Pipe 25
   5.3 Magnets 26
   5.4 Pixel Detectors 29
   5.5 Wire Chambers 30
   5.6 Ring Imaging Cherenkov (RICH) Counters 33
   5.7 Electromagnetic Calorimeter 38

6. **TRIGGER PROCESSORS & DETECTOR READOUT** 38

   6.1 Detector Readout System 39
   6.2 Level-1 Trigger Processor 41
   6.3 Level-2 Trigger Processor 45

7. **FLAVOR TAGGING: LEPTONS VS. KAONS** 45

8. **RECONSTRUCTION OF B-EVENTS, YIELDS & BACKGROUNDS** 48

   8.1 General Considerations and Lifetime Measurements 48
   8.2 $B_s$ Reconstruction; Signal Yields & Background Estimates 52
   8.3 Monte-Carlo Simulation and Analysis of RICH Counter Data 57
   8.4 Yields of Potential CP-Violating Channels 63

9. **DISCUSSION & COST ESTIMATES** 64

**APPENDIX A: Trigger Algorithm and Simulation** 66

**APPENDIX B: Liquid-Radiator RICH Resolution** 75

**APPENDIX C: Development and Test of a Large Silicon Strip System for a Hadron Collider Beauty Trigger (DRAFT – to be submitted to NIM).**

FERMILAB-Proposal-845

# 1. INTRODUCTION

One of the most challenging and important problems in high energy experimental physics is how best to study rare decays of Beauty particles as a probe of possible new physics beyond the Standard Model with three generations. We therefore propose a new detector dedicated to the study of B-physics (Beauty or Bottom) at the Tevatron proton-antiproton Collider.

The large cross section for $B\bar{B}$ production in hadronic interactions (e.g., 50 $\mu$barn at the Tevatron Collider and several hundred $\mu$barn at LHC and SSC), coupled with sophisticated trigger processor techniques should make possible the acquisition of enormous samples of exclusive Beauty decays at hadron colliding-beam machines. The dedicated Beauty experiment which we are proposing will allow us to make a detailed study of $B_s$ and $B_d$ mixing effects, the observation of final states with branching fractions as small as $1.7 \times 10^{-6}$ (10 events per $\int \mathscr{L} dt = 200\ pb^{-1}$), in addition to lifetime, mass and branching fraction measurements of the entire spectrum of Beauty particles. CP-Violation effects will be observable (at the $3\sigma$ level) at the Tevatron, only if the asymmetries are larger than about 0.5. Thus, the search for CP-Violation effects in Beauty decay at the Tevatron will likely only prepare the way for the next generation of experiments.

In order to allow our proposed experiment to be compared most simply, yet correctly, with other options, we give in Table 1 the few numbers and facts that are of essential importance. In the body of this proposal, we explain and justify the table entries.

*Table 1:* *Essential Characteristics[a] of This Proposed Experiment.*

| | |
|---|---|
| 1. $[\sigma(B\bar{B}) = 50 \cdot 10^{-30} cm^2] \times [\mathscr{L} = 10^{31}\ cm^{-2}s^{-1}]$ | $5 \cdot 10^2 s^{-1}$ |
| 2. Geometric Acceptance[a] | 23% or 46% |
| 3. Trigger Efficiency[b] | 20-45% |
| 4. Flavor Tagging Efficiency[c] | >35% |
| 5. Reconstruction Efficiency[d] | 29-45% |
| 6. RICH Particle Identification ? | YES |
| 7. Electromagnetic Calorimetry ? | YES |

(a) The value for geometric acceptance depends on whether one or both forward spectrometer arms are instrumented. See discussion in Chapters 3 and 9.
(b) The trigger efficiency depends to some extent on the charged particle multiplicity of a B final state. See discussion in Chapter 4.
(c) The larger value applies to a $B_s$-Mixing experiment. See the discussion of tagging efficiency in Chapter 7.
(d) Reconstruction efficiencies are discussed in Chapter 8

For completeness, we compare the contents of Table 1 with the parameters of a new $e^+e^-$ "B-Factory". The product of our items 1,2 and 3 is 2 3. Hz, to be compared with the corrsponding result for an "idealized" $e^+e^-$ B-Factory, 10 Hz ($10^{34} \cdot 1$ nb) where, for the $e^+e^-$ case, we assume the maximum conceivable luminosity and assume acceptance and efficiencies are all 100%. It is also interesting to note that, in the next generation of pp colliders, the parameters for a hadron collider B-Factory of the type we propose give another factor of about 10 (cross section and increased acceptance from larger forward collimination).

To compare our proposed experiment with other collider options at the Tevatron, it is only necessary to compare the product of items 2, 3 and 4, since $\sigma \cdot \mathscr{L}$ will be the same for all such experiments. As explained in the following paragraphs and, in more detail, in Chapter 4 and APPENDIX A, our triggering approach is unique and does not rely on the inefficient use of lepton tags as triggers. Moreover, our extensive study of the possibilities of using charged kaons as flavor tags shows that they should be much superior to lepton tags.

The efficient triggering of heavy flavor in hadron machines was long thought to be "next to impossible". However, the success of Fermilab Experiment E691 and its successors in obtaining large clean samples of charmed particles has partly dispelled this "myth". Now, with a great deal of Monte-Carlo simulation work followed by a 3-month test experiment at the Sp$\bar{p}$S-Collider of a new type of collider microvertex detector[1] (see APPENDIX C), we have demonstrated that it should be possible to obtain large samples of fully reconstructed and tagged Beauty particles with minimal background.

The proposed experimental apparatus consists of a planar-silicon microvertex detector at the center of an interaction region, followed by dedicated large aperture forward spectrometer(s) installed on the outgoing beam pipes, with Ring-Imaging-CHerenkov (RICH) particle identification and electromagnetic calorimetertry. Event reconstruction is facilitated by information from the silicon microvertex detector, whose elements are installed perpendicular to and in close proximity to the circulating beams, inside the vacuum pipe and dispersed throughout the interaction region. A Level-1 trigger results from digital calculations based on the silicon data.

For the following reasons, we focus our attention in the forward directions of the p$\bar{p}$ system:

- The solid angle density of b and $\bar{b}$ quarks is considerably larger in the forward direction than elsewhere (see Chapter 3). Qualitatively, this arises because, far above threshold in the p$\bar{p}$ center of mass, the interacting partons tend to have increasingly unequal momentum.

- The momenta of B-mesons in the forward direction are much larger than at 90°. The decay products are therefore easier to track reliably and vertex and overall topology definition is improved. Thus, event reconstruction is enhanced. Calorimetric detection of $\gamma$'s also improves.

- Because of the relatively small solid angle coverage and planar geometry, design, construction and maintenance is easier and therefore less expensive.

- Heavy-flavored baryons (e.g., bud, cud, bcu, bsu, etc.) may be more easily produced and studied in the forward direction.

- The forward peaking of heavy flavor particles should be even more pronounced at the next generation of higher energy colliders, where the larger $b\bar{b}$ cross sections will eventually provide the yields required for CP-Violation studies. Thus, the proposed experiment would be a first example of an important class of future experiments and valuable expertise and experience would be obtained.

---

[1] A 43,000 channel silicon strip microvertex detector was run inside the Sp$\bar{p}$S vacuum pipe at 1.5 mm from the circulating beams. The observation of clean background-free events constitutes a major step in demonstrating that the silicon trigger discussed in this proposal will actually work.

In the body of this proposal we present details of the trigger design and detector which would furnish more than $10^7$ reconstructed B-Mesons per 200 pbarn$^{-1}$ integrated luminosity at the Tevatron Collider with $\sqrt{s}$ = 1.6 TeV. The actual number of reconstructed events obtained will depend on whether one or both collider arms are instrumented with spectrometers (the proposed silicon and trigger systems are bi-directional and will serve either situation). We emphasize that **all rate estimates in the proposal assume a two-arm spectrometer system, in order to demonstrate the full potential of the experiment.** See the discussion of this point in Chapter 9.

In Chapter 2 we discuss the physics goals of the experiment, in particular $B_s$-Mixing, and explain the "reach" of such an experiment at the Tevatron in studying CP-Violation and rare decay modes, if the experiment is run with sufficient priority.

Chapter 3 contains a discussion of the geometric acceptance of our proposed apparatus. In Chapter 4, we describe the trigger algorithm (see also Appendix A), which is based on real-time vertex calculations of silicon micro-vertex detector data. A Monte-Carlo simulation of the trigger is described and a performance summary is given.

Chapter 5 contains a detailed discussion of the various spectrometer elements. The silicon micro-vertex detector is also described in **APPENDIX C**, where results are given of a similar detector recently run at the Sp$\bar{p}$S-Collider. The large aperture forward detector consists of two coaxial spectrometers (2.5-100 mrad and 100-600 mrad, respectively), equiped with liquid and gas Ring-Imaging-CHerenkov (RICH) Counters. Complete electromagnetic calorimeter coverage of the spectrometer aperture would provide sensitivity for such final states as: $B_s \to D_s^* \to D_s\gamma$ and $B \to D^{0*} \to D^0\gamma$.

Chapter 6 describes how the silicon data will be analyzed in real time by a pipelined Data-Driven processor. The readout system stores event data from the spectrometer detectors in pipelined buffer memory while the processor is making a decision. A Level-2 trigger, which performs further analysis on the complete set of spectrometer data, is implemented with a large system of 50-MIPS RISC processors.

The problems of flavor tagging are dealt with in Chapter 7. Results from a Monte-Carlo simulation are given, which allow an evaluation of the relative effectiveness of lepton vs. charged kaon tagging.

Chapter 8 deals with the off-line reconstruction problems of Beauty-mesons in hadronic interactions. Results are given using reconstruction software written to analyze and find signals for different B decay modes in Monte-Carlo generated event samples. Quantitative estimates are given of the expected combinatoric background. The median momentum of detected and reconstructed B-mesons is about 45 GeV and the B proper time can be measured with a precision better than $\sigma_t/t$ = 6%. These facts allow excellent B-$\bar{B}_s$ oscillation studies to be made. Evaluations of the yields which can be expected for such an analysis and for a CP-Violation search are also given. A Monte-Carlo simulation of the analysis of RICH counter data is also given.

Finally, in Chapter 9, we discuss the desired time scale and present an estimate of the costs.

# 2. PHYSICS GOALS

## 2.1 Overall Goals and Sensitivity to Rare Decay Channels

Further major advances in our understanding of Beauty physics will come from experiments which produce very large samples of B-mesons and baryons, from which many different exclusive final states can be reconstructed with good mass resolution, good proper life time resolution and initial flavor tagging. Technical items are dealt with in the following chapters. Here, we simply point out that, with such data, the physics of both production and decay processes can be considerably clarified.

Analysis of the observed production processes will result in a much-needed understanding of the small-x gluon structure function of the proton. Studies of the spectroscopy of the entire series of B-mesons and baryons, including those which contain both b and c quarks (e.g., $b\bar{c}$, bcd, bcu, etc.) will also be possible. For example, reactions such as $B_c^- \rightarrow J/\psi\pi^-\pi^-\pi^+$ should be easily identifiable. Measurements of invariant masses and lifetimes of the entire spectroscopic array of states will be feasible.

The search for new physics beyond the 3-generation version of the Standard Model will be the main focus of future Beauty experiments. Unexpected values of branching fractions, mixing parameters in $B_s$ and $B_d$ decays and CP-Violation parameters will have great interest in this connection. Presumably the top mass will have been determined by the time our first results are available and will be used in making more stringent predictions that can be tested. If top has not yet been found, our results will be of even greater interest.

We now comment on the sensitivity we could expect to reach in our search for rare decay channels, if sufficient running time is given and the full (two-arms instrumented) detector is constructed. With a $b\bar{b}$ total cross section of 50 $\mu$barn at the Tevatron and an integrated luminosity, $\int\mathscr{L}dt = 200\ pb^{-1} = (10^{31}\ cm^{-2}sec^{-1} \cdot 10^7\ sec \cdot 2)$, a total of $10^{10}$ $b\bar{b}$ events are produced. The discussion below in Chapter 3 explains that, of these $10^{10}$ events, $\approx 6 \cdot 10^9$ B or $\bar{B}$ mesons will have all their decay tracks contained within the 600 mrad spectrometer apertures. From the discussions in Chapters 4 and 8 on triggering and event reconstruction, we estimate that the net triggering and reconstruction efficiency for a final state with all charged tracks is $\approx$10%. Thus, a mode with a branching fraction of about $1.7 \cdot 10^{-8}$ should yield 10 observed events. It is interesting to note that the new generation of pp colliders, with $b\bar{b}$ cross sections 5-10 times larger, with somewhat more forward collimation of B decay tracks and with somewhat larger usable luminosity may yield an additional factor of ten or so better sensitivity.

## *2.2 $B_s$-Mixing (CP-Conserved)*

We consider a prototype mixing measurement in which exclusive final states of the $B_s$, such as:

$$B_s^0 \rightarrow D_s^{*-}\pi^+\pi^+\pi^- , \quad D_s^{*-} \rightarrow D_s^-\gamma \tag{1}$$

are reconstructed and the proper decay time of each event is measured. The flavor of each B-Meson at production is "tagged" by observing a supplementary $K^\pm$ or $\ell^\pm$ in the spectrometer, as discussed in Chapter 7.

Four proper time distributions will be obtained from the reconstructed and tagged $B_s$ and $\bar{B}_s$ mesons:

$$T^+\ B_s(t) \tag{1}$$

$$T^-\ B_s(t) \tag{2}$$

$$T^+\ \bar{B}_s(t) \tag{3}$$

$$T^-\ \bar{B}_s(t) \tag{4}$$

where $T^+$ and $T^-$ denote the two charges of the possible tagging particles (e.g., $e^+$, $e^-$, $\mu^+$, $\mu^-$, $K^+$, $K^-$). Since a $B_s$ can be produced together with a $\bar{B}_u$, $\bar{B}_d$ or $\bar{B}_s$, the tagging particle can arise from any one of these. The latter two states are themselves subject to oscillation and can lead to the wrong sign tag, refered to in this document as "mis-tagging". Other sources of mis-tagging are, for example, background under the $B_s$ signal, other physics sources of the tagging particles, etc. Mis-tagging is estimated in Chapter 7.

In order to arrive at the equations which describe B decay time distributions (ignoring the possibility of CP violation), we start by expressing $B^0$ and $\bar{B}^0$ ($B_d$ or $B_s$) as the usual linear combination of mass eigenstates, $B_1$ and $B_2$:

$$|B^0> \; = [|B_1> \; + \; |B_2>] \, / \sqrt{2} \tag{5}$$

$$|\bar{B}^0> \; = [|B_1> \; - \; |B_2>] \, / \sqrt{2} \tag{6}$$

With the $B^0 \leftrightarrow \bar{B}^0$ transitions allowed by the second-order weak interaction, we have as the time-evolved state for an initial $B^0$:

$$\psi(t) = [e^{-iM_1t-\Gamma_1t/2} \cdot |B_1> \; + \; e^{-iM_2t-\Gamma_2t/2} \cdot |B_2>] \, / \sqrt{2} \tag{7}$$

Expanding $|B_1>$ and $|B_2>$ in terms of the observed $|B^0>$ and $|\bar{B}^0>$ states, and projecting out their amplitudes, we have as the probabilities to see $B^0$ and $\bar{B}^0$:

$$|<B^0|\psi(t)>|^2 \; = e^{-\Gamma t} \cdot [1 \; + \; \cos(\Delta Mt)] \, / \, 2 \tag{8}$$

$$|<\bar{B}^0|\psi(t)>|^2 \; = e^{-\Gamma t} \cdot [1 \; - \; \cos(\Delta Mt)] \, / \, 2 \tag{9}$$

In (8) and (9), $\Gamma \equiv \Gamma_1 \; = \; \Gamma_2$, because of the large phase space available in B decay, and $\Delta M \; = \; M_1 - M_2$.

Integrating Eqs. 8 and 9 over time, we find that the rates for no-oscillation and oscillation, respectively, go as $(2+x^2)/(1+x^2)$ and $x^2/(1+x^2)$, where $x \equiv \Delta M/\Gamma$. If we assume that a $B_s$ and its accompanying $\bar{B}$ decay independently and that only the time dependence of the $B_s$ is measured, the expressions which describe the tagged time distributions are given by Eqs. 8 and 9, multiplied by the appropriate time-averaged rate for the tag-providing $\bar{B}$. These products are shown in Table 2 for the four possible cases of tags, $T^+$ and $T^-$, with $B_s$ and $\bar{B}_s$, respectively, and for the two possible initial states.

Following the discussion on tagging in Chapter 7, we note that the $B_s$ decay time distributions for Final States 1-4 in Table 2 have the following simple forms if the initial states $B\bar{B}_s$ and $\bar{B}B_s$ occur with equal probability.[2]

$$T^+ \, B_s \text{ or } T^- \, \bar{B}_s \quad : \quad A(t) \cdot e^{-t} \cdot [1 \; - \; K\cos(xt)] \tag{10}$$

$$T^+ \, \bar{B}_s \text{ or } T^- \, B_s \quad : \quad A(t) \cdot e^{-t} \cdot [1 \; + \; K\cos(xt)] \tag{11}$$

$$\text{Untagged } B_s \text{ or } \bar{B}_s \quad : \quad A(t) \cdot e^{-t} \tag{12}$$

In these formulae the mixing parameter, $x \; = \; \Delta M/\Gamma$ and $t$ is the $B_s$ proper lifetime in units of mean life. K is the net "dilution" factor which results from all types of mis-tagging and decreases the amplitude of the oscillation from the value it would have were the flavor of the decaying B always correctly determined. A(t) is the acceptance function discussed in Chapter 8.

If the initial states $B\bar{B}_s$ and $\bar{B}B_s$ do not occur with equal probability, it may be seen from the entries in Table 2 that Final States 1 and 3 will have identical magnitudes for K (but opposite sign), and Final States 2 and 4 will also have identical values. For example, if initial state $B\bar{B}_s$ has probability $\alpha$ and $\bar{B}B_s$ has probability $(1-\alpha)$, it can be seen that the experimental value of K should depend on $\alpha$ in

---

[2] We note that this may not be the case in pp interactions and in $p\bar{p}$ interactions when the $B_s$ are produced away from small Feynman-x. A possible asymmetry in $B_s$ and $\bar{B}_s$ production due to valence quark effects has relevance to the study of CP-Violation asymmetries and must be understood empirically. This physics of the production process is also of interest in its own right.

*Table 2:* *Joint Time-Integrated, Time-Dependent Rates*[a,b,c]

| Final State | Initial State $B\bar{B}_s$ | Initial State $\bar{B}B_s$ | Equal Sum |
|---|---|---|---|
| (1) $T^+ B_s(t)$ | $(2+x^2)\cdot[1-\cos]$ | $x^2 \cdot[1+\cos]$ | $1-[1/(1+x^2)]\cdot\cos$ |
| (2) $T^- B_s(t)$ | $x^2 \cdot[1-\cos]$ | $(2+x^2)\cdot[1+\cos]$ | $1+[1/(1+x^2)]\cdot\cos$ |
| (3) $T^+ \bar{B}_s(t)$ | $(2+x^2)\cdot[1+\cos]$ | $x^2 \cdot[1-\cos]$ | $1+[1/(1+x^2)]\cdot\cos$ |
| (4) $T^- \bar{B}_s(t)$ | $x^2 \cdot[1+\cos]$ | $(2+x^2)\cdot[1-\cos]$ | $1-[1/(1+x^2)]\cdot\cos$ |

(a) To simplify the reading of this table, a common factor $e^{-\Gamma t}/(1+x^2)$ is suppressed in all terms in columns 2 and 3, as is the argument, $(\Delta Mt)$, from all cosine functions.
(b) The B or $\bar{B}$ decay which provides the tagging particle is time-integrated. The $B_s$ decay is time-dependent. Throughout this table, $x = \Delta M/\Gamma$ for the tagging B or $\bar{B}$, whereas the argument of the cosine function is for the $B_s$.
(c) In this table, the tagging particles are assumed to be secondary $K^\pm$ or leptons. They give the flavor of the B or $\bar{B}$ at time of decay (e.g., $K^+$ or $\ell^+$ result from a B, whereas a $K^-$ or $\ell^-$ result from a $\bar{B}$).

the following way (for fixed value of x):

$$T^+ B_s \text{ or } T^+ \bar{B}_s \quad : \quad K^+ = \pm[-2\alpha+(1-2\alpha)x^2]/[2\alpha+x^2] \tag{13}$$

$$T^- B_s \text{ or } T^- \bar{B}_s \quad : \quad K^- = \pm[2(1-\alpha)+(1-2\alpha)x^2]/[2(1-\alpha)+x^2] \tag{14}$$

Fig. 1 shows how K depends on $\alpha$ for both types of final states and for $x = 0.7$ and 10, respectively. An observed value of K will, of course, be a weighted average over the three contributing values of x. The effective dilution factors for different types of tags can be directly measured by studying the tags which occur with $B^\pm$ production, where the identity of a valid tag is known.

## *2.3 Simulation of $B_s$-Mixing Analysis:*

In order to demonstrate how the expected statistical significance in the determination of $x = \Delta M/\Gamma$ depends on sample size, we have generated Monte-Carlo data samples and subjected them to joint Maximum-Likelihood fits with x, $\tau$ and K as free parameters.

Event sample decay times are generated according to the distributions of Eqs. (10-11) in Section 2.2. The acceptance function is taken to be our empirical form, $A(t) = 4t^2/(1+4t^2)$, as explained in Chapter 8. We use a value of the tagging dilution constant, $K = 0.34$, which is somewhat smaller than the value 0.4 estimated in Chapter 7, to allow for Cherenkov identification efficiencies and background.

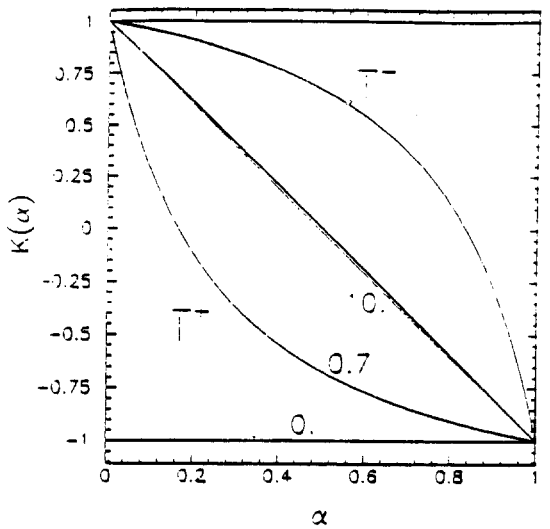


*Figure 1: Dependence Of $K^+$ and $K^-$ On $\alpha$ For Three Values Of x.* The lower left contains Eq. 8 evaluated for the three indicated values of x. The upper right contains Eq. 9 evaluated for the same values of x. The superscripts on $T^+$ and $T^-$ refer to the signs of the tagging particles.

Monte-Carlo calculations show that background is associated with B events and thus that it has an exponential proper time dependence with the same lifetime as the signal. With this assumption, the only effect of the background is to dilute the oscillation amplitude and thus reduce K. For each data sample, we also generate a sample of decay times for the corresponding sample of untagged $B_s$ (Eq. 12 is in Section 2.2) assuming, as discussed in Section 8.2, that the fraction tagged is 35%.

A simultaneous Maximum-Likelihood fit was then made to an entire data sample using, for each event, the relevant Equation (10), (11) or (12). For example, the Likelihood function for a $B_s$ tagged with a $T^+$ is:

$$\mathcal{L} = \frac{A(t) \cdot e^{-t} \cdot [1 - K\cos(xt)]}{\int A(t) \cdot e^{-t} \cdot [1 - K\cos(xt)]\, dt}$$

The sum of $-\log \mathcal{L}$ for all events is minimized using the program MINUIT.

Figs. 2(a-h) show typical generated distributions for samples of 5000 tagged events, generated at each of the x values: 0.7, 5, 10 and 15. The curves resulting from the joint Maximum-Likelihood fits are also shown for each case. Table 3 shows the fitted values of x. The following paragraphs show that a successful experiment could be performed with far fewer events.

We now investigate the dependence of the quality of the results on sample size. The parameters which best indicate the sample size required for a good measurement of $B_s$ mixing are the error in the mixing parameter ($\sigma_K$) and the significance of the oscillation amplitude ( $N_\sigma$ = K divided by the error in K). These two quantities are plotted in Fig. 3 as a function of the number of events for a fixed K value of 0.34 and an x value of 15.

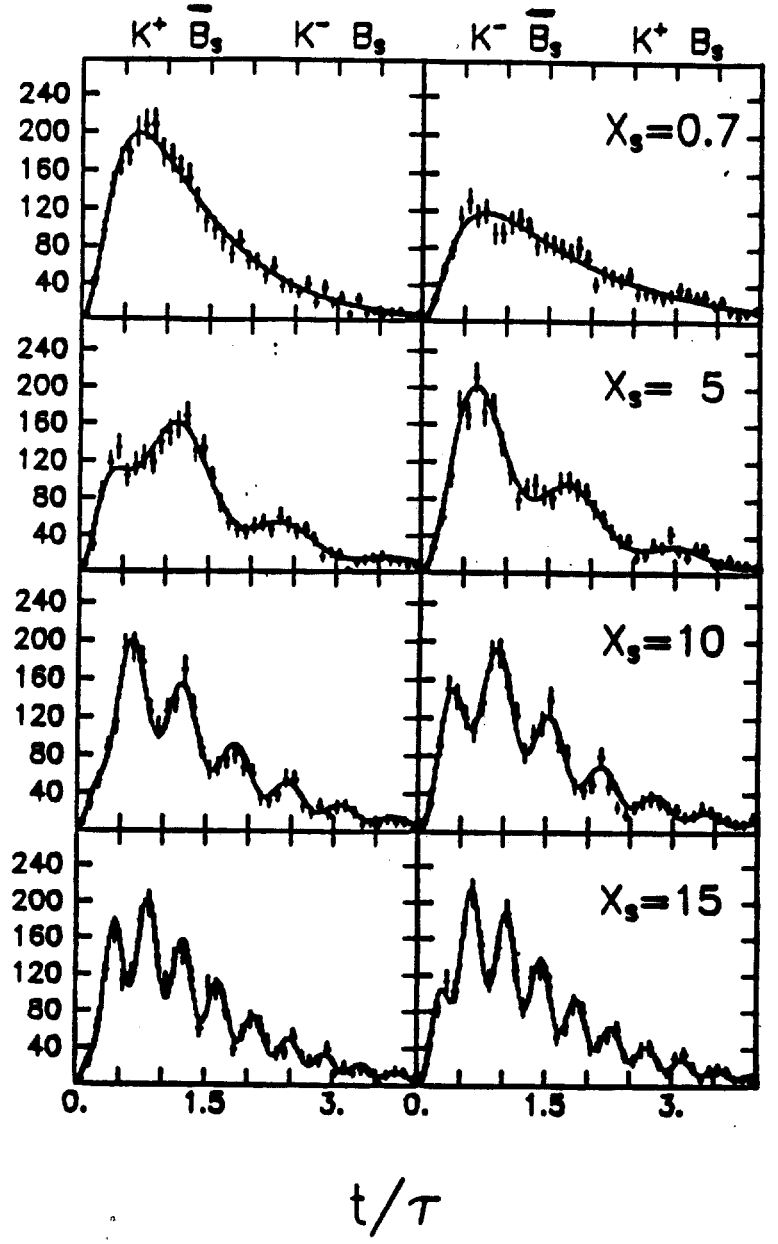


*Figure 2:* Proper time distributions for the two types of tagged events, according to Eqs. (6-7); (a,b) x = 0.7, (c,d) x = 5, (e,f) x = 10, (g,h) x = 15. The Monte-Carlo data points correspond to a sample of 5000 tagged events, as discussed in the text. The curves result from simultaneous Maximum-Likelihood fits to the data shown and the proper time distribution of the corresponding untagged sample.

We next try to find the minimum event sample size which will allow a significant measurement of the mixing parameter. We investigated the uniqueness of the solution by studying the log-Likelihood function vs. x for a large number of generated Monte-Carlo "experiments" for each sample size. Fig. 4 shows typical examples of the resulting curves. In Fig. 4(a), a typical (bad) example of the result is shown for a sample of 150 tagged events. It is obviously not possible to obtain reliable results with

*Table 3:* $x = \Delta M/\Gamma$ *Values Obtained From Fits Shown In Figs. 2*

| Input x Value | Fitted x |
|---|---|
| 0.7 | 0.70 ± 0.05 |
| 5.0 | 4.99 ± 0.03 |
| 10.0 | 9.96 ± 0.03 |
| 15.0 | 14.93 ± 0.03 |

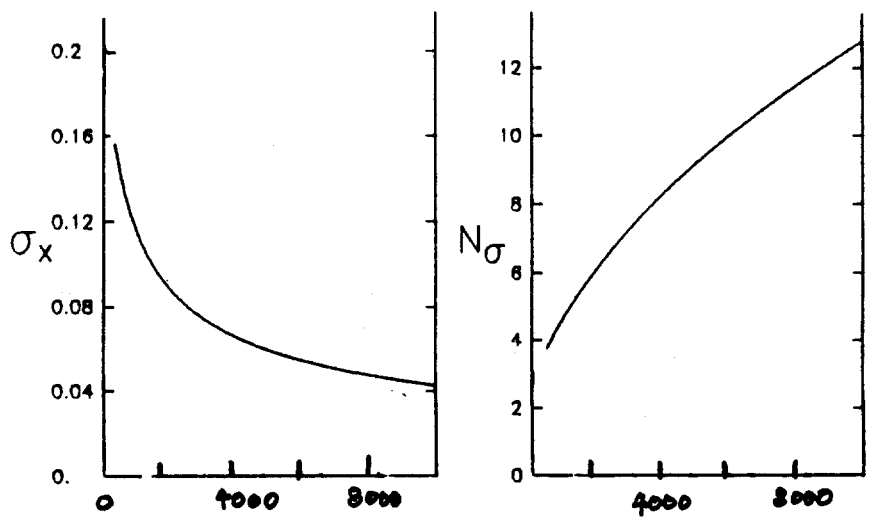


*Figure 3:* (a) Error on the mixing parameter ($\sigma_x$) vs. the number of $B_s$ signal events. (b) The significance (in standard deviations) of the oscillation amplitude (K) vs. the number of $B_s$ signal events.

such a small sample. For comparison, Figs. 4(b,c,d) show typical log-Likelihood functions plotted vs. x for tagged sample sizes of 300, 600 and 1700 events, respectively. We conclude that a sample size of about 1000 tagged events is the smallest sample size from which a meaningful result could be obtained. A run planned for 4000 tagged events should therefore allow a sufficient safety margin.

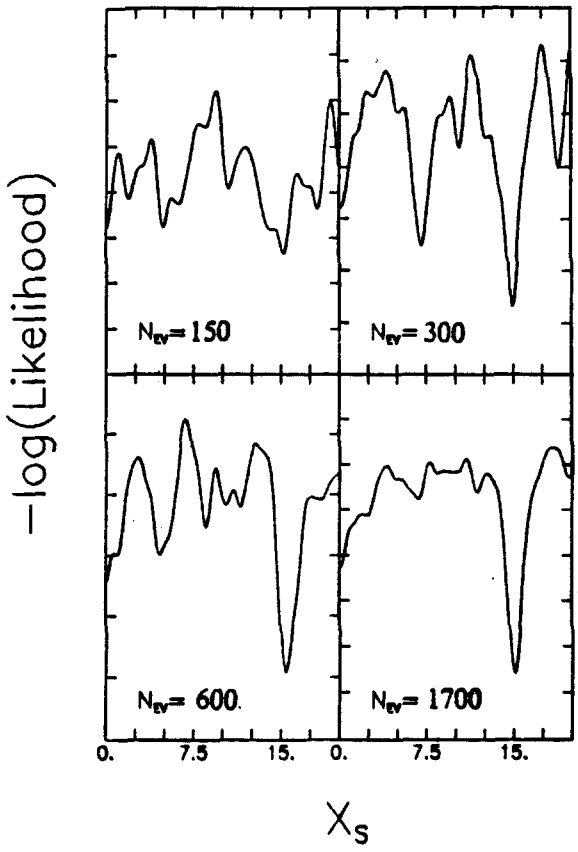


*Figure 4:* *−Log-Likelihood Function vs. x: The data samples of* 150, 300, 600 and 1700 events were all generated with x = 15. In each case, the distributions are typical examples from a study of 20 Monte-Carlo experiments.

## *2.4 Sensitivity of CP-Violation Search*

We consider a prototype of future CP-Violation measurements. The larger $b\bar{b}$ cross section and increased forward collimation expected at the next generation of machines will likely be needed to achieve the desired sensitivity to CP-Violation effects. Nonetheless, it is interesting to estimate the "reach" of such an experiment at the Tevatron Collider. We have studied the sensitivity of the proposed apparatus to a measurement of a CP-Violation asymmetry in the decay:

$$B^0_d \rightarrow J/\psi\, K_s \tag{15}$$
$$\bar{B}^0_d \rightarrow J/\psi\, K_s \tag{16}$$

Allowing for CP-Violation, the time dependences of the decay of $B_d$ and $\bar{B}_d$ into this CP eigenstate are:

$$N(B_d \rightarrow J/\psi K_s) \approx A(t) \cdot e^{-t} \cdot [1 - \sin(2\beta) \cdot \sin(xt)] \tag{17}$$
$$\bar{N}(\bar{B}_d \rightarrow J/\psi K_s) \approx A(t) \cdot e^{-t} \cdot [1 + \sin(2\beta) \cdot \sin(xt)] \tag{18}$$

where t is the proper time measured from production in units of the mean B life time, $\beta$ is an angle in the unitarity triangle and $x = \Delta M/\Gamma$ for the B (or $\bar{B}$) at production. A(t) is the detector acceptance function discussed in Chapter 8.

These time dependences imply a time-dependent asymmetry in the decay: $(\bar{N}-N)/(\bar{N}+N)$. In order to measure this asymmetry, it is necessary to tag the flavor of the B at production using the techniques described in Chapter 7. When inaccuracies inherent in the tagging are taken into account, the observed asymmetry takes the form:

$$A_{obs} = K \cdot \sin(2\beta) \tag{19}$$

where K is the net "dilution" factor, which differs from unity due to imperfect tagging, as discussed in Chapter 7.

A Monte-Carlo study was performed to determine the event sample size required to observe a given statistical significance in a measurement of a CP-Violation asymmetry. For example, Fig.s 5(a,b) show the proper time distributions for 2100 Monte-Carlo events (beyond the reach of a Tevatron experiment) each of Reactions 15 and 16, respectively, generated assuming $\sin(2\beta) = 0.20$, $x = 0.7$, a net dilution factor, $K = 0.47$, and an empirical acceptance function A(t). The curves shown are the result of a Maximum-Likelihood fit for $\sin(2\beta)$ of Eqs. 17 and 18 jointly to the data in Figs. 5(a,b). The value found is $\sin(2\beta) = 0.176 \pm 0.044$ ($4\sigma$ significance). Fig. 5(c) superimposes the two fitted curves from Figs. 5(a) and (b). The maximum deviation occurs at 2.2 mean lives, corresponding to an argument of $\pi/2$. in $\sin(xt)$, when $x = 0.7$.

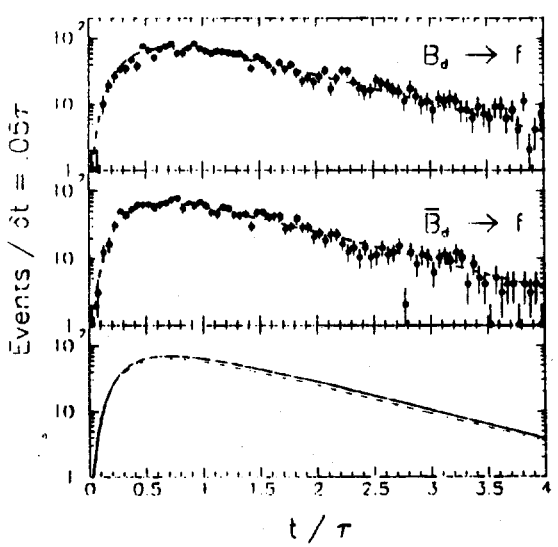


*Figure 5: Monte-Carlo Study of CP-Violation Effects in $B_d$ Decay.* (a) Proper time distribution of 2100 examples of Reaction 15 (beyond the reach of a Tevatron experiment). Fitted curve is Eq. 17; (b) Same for 2100 examples of Reaction 16. Curve is Eq. 18; (c) The two fitted curves from (a,b) are superimposed.

Fig. 6 shows the total sample sizes of tagged B and $\bar{B}$ required to observe a $3\sigma$ or a $4\sigma$ asymmetry effect as a function of $\sin(2\beta)$, assuming a net dilution factor of 0.47. As will be seen in the discussion

of yield estimates in Chapter 8, we may expect a total of only about 1150 reconstructed tagged examples of Reactions (15) and (16) from runs with total $\int \mathscr{L} dt = 200\ pb^{-1}$. Thus a $3\sigma$ asymmetry effect could only be observed if $\sin(2\beta) > 0.3$.

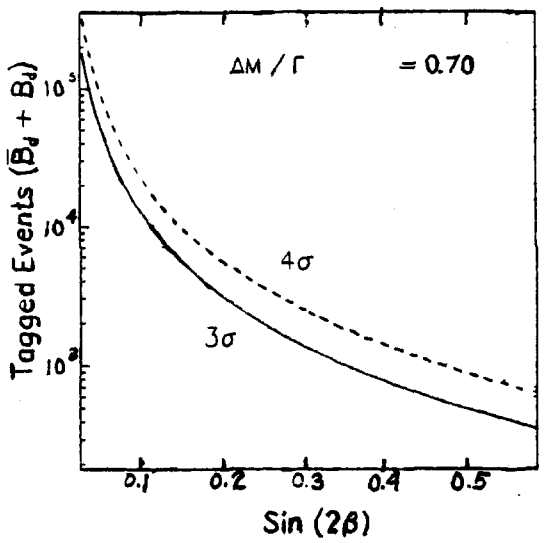


*Figure 6: Total Tagged B and $\bar{B}$ Events Required for $3\sigma$ and $4\sigma$ Effects.* Required number of tagged events is plotted vs. $\sin(2\beta)$, assuming K = 0.4.

## 3. GEOMETRIC ACCEPTANCE

Fig. 7 shows the angular distribution in the laboratory of decay tracks from B-Mesons generated via gluon-gluon fusion for $\sqrt{s} = 1.6$ TeV $p\bar{p}$ interactions using the PYTHIA Monte-Carlo program.[3] A major fraction of the Beauty signal is found in the forward direction.[4]

We have attempted to design a forward spectrometer which has the largest angular aperture consistent with uniform planar geometry. We find that, for apertures larger than about 600 mrad, detector complications and costs rise more rapidly than the benefits. We therefore choose $\theta_{max} = 600$ mrad for our proposed detector. The spectrometer which satisfies the aperture requirements discussed here and has the planar geometry required for minimal complexity is shown in Fig. 8. The spectrometer elements are described in Chapter 5.

Table 4 shows the geometric acceptance of a two-arm 600 mrad spectrometer system at $\sqrt{s} = 1.6$ TeV. All decay tracks of 30% of all B mesons produced are fully contained in the system; 30% of all $\bar{B}$ mesons are fully contained and there is a 14% overlap in which both B and $\bar{B}$ are contained. Thus, in 46% of all $B\bar{B}$ events produced, either B or $\bar{B}$, or both, are accepted. It may also be stated that, if

[3] H.-U. Bengtsson, G. Ingelman, Comput. Phys Commun. 34 (1985) 251; H.-U. Bengtsson, T. Sjostrand, Comput. Phys Commun. 46 (1987) 43.

[4] It has been pointed out by DeRujula [private communication] that the observed angular distributions may be even more sharply forward peaked than seen in Fig. 7, due to contributions from other than the low order QCD processes used in the generation of both PYTHIA and ISAJET.

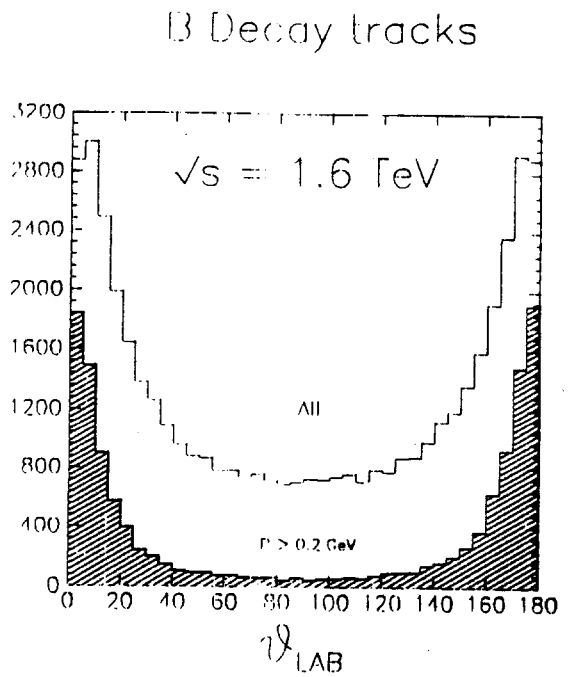


*Figure 7: $\theta_{lab}$ of B Meson Decay Tracks Generated at $\sqrt{s}$ = 1.6 TeV Using PYTHIA.* **Shaded:** Tracks from those B events which have all decay track momenta greater than 200 MeV.

N $B\bar{B}$ events are produced, one will find 0.60 N fully accepted B or $\bar{B}$ final states.

Of those events with a B fully contained in the spectrometer, 14/30 = 47% also have the $\bar{B}$ similarly contained. The same is also true for the $\bar{B}$. However, as discussed in Chapter 7, flavor tagging can be accomplished more efficiently using single particles, rather than trying to fully reconstruct the tag-providing B (or $\bar{B}$).

**Clearly, if only a single arm spectrometer is constructed, there is a 50% loss of all events, since presumably B and $\bar{B}$ mesons are rarely produced in opposite hemispheres. No fundamental loss in physics would result.**

An additional contribution to the geometric acceptance comes from the minimum angle cutoff, $\theta_{min}$, and the resultant loss of particles in the beam pipe. Such acceptance losses increase at larger Feynman-$x_F$ values. With a vacuum pipe of diameter of 2.5 cm and a window at z = 5 m from the interactions, we have a $\theta_{min}$ of 2.5 mrad, with detector sensitivity for $\theta$ > 5 mrad. This would result in a loss of less than 10% of the events contained within the 600 mrad aperture.

Fig. 9 shows the momentum distribution of all B-mesons generated by PYTHIA at $\sqrt{s}$ = 1.6 TeV. The shaded histogram is the distribution for those mesons whose laboratory angle, $\theta$, is less than 600 mrad. Finally, the solid histogram shows the momentum of B-mesons which have all decay tracks contained within the 600 mrad aperture.

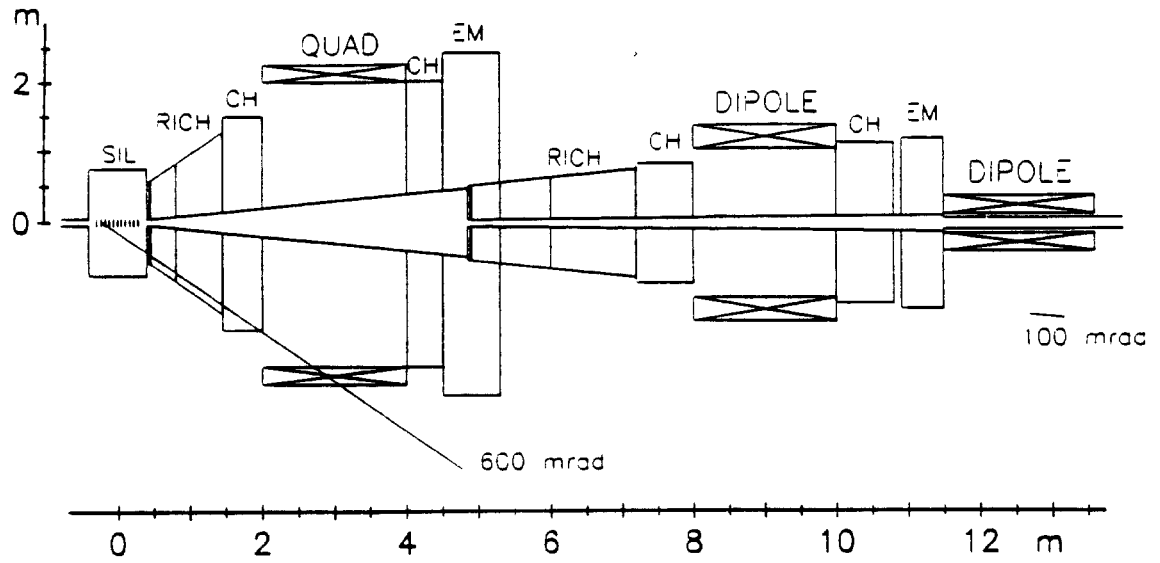


*Figure 8: Layout of one Forward Beauty Spectrometer.* The silicon microvertex system is installed inside the Tevatron vacuum pipe at the center of the interaction region. The large and small dipole magnets in the spectrometer, together with two dipole magnets on the opposite arm provide beam compensation.

*Table 4:* *Two-Arm Geometric Acceptance[a] for B and $\bar{B}$ Mesons*

| | B yes | B no |
|---|---|---|
| $\bar{B}$ yes | 14% | 16% |
| $\bar{B}$ no | 16% | 54% |

(a) Gluon-gluon fusion calculation by PYTHIA for $p\bar{p}$ interactions at $\sqrt{s}$ = 1.6 TeV. B-mesons are considered accepted if all decay tracks fall within the 600 mrad aperture of either collider arm. $\theta_{min}$ of the spectrometer is chosen to cause less than 10% additional loss of these events.

In Fig. 9, the fall-off in the accepted momentum spectrum below ≈40 GeV is an aperture effect. We note that the median momentum of accepted B mesons is ≈45 GeV or so, corresponding to a Feynman-x of 0.06. Thus, even though the spectrometers cover forward apertures, they are still sensitive to a major fraction of B mesons produced in the dominant small-x region.

Finally, we note that the mean flight path, $D = c\tau(p/m)$, is approximately 1 mm per 15 GeV momentum. Therefore, the median B momentum of about 45 GeV corresponds to a typical flight path for our reconstructed B sample of about 3 mm. Since the resolution in this quantity is better than 0.2 mm, as discussed below in Section 8.1, excellent proper time measurements can be made.

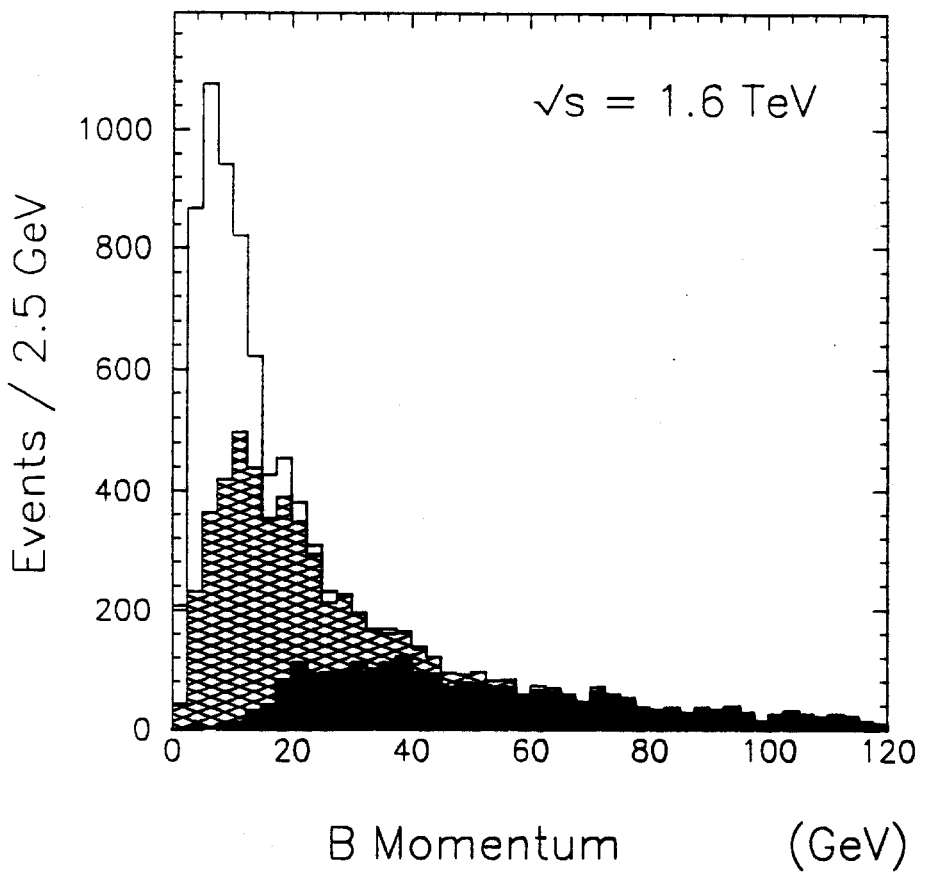


*Figure 9: Momentum Distributions of B-Mesons.* **Unshaded:** All B-mesons generated according to PYTHIA **Shaded:** Those with laboratory $\theta$ < 600 mrad. **Solid:** Those B-mesons which have all decay tracks contained within the 600 mrad aperture. The B flight path is about 1 mm per 15 GeV momentum.

## 4. TRIGGERING & SIMULATION

The overall strategy of the trigger is to use only the silicon information to search for events which are inconsistent with having a single vertex. Before deciding on this strategy, we looked for other properties of Beauty events which would allow a more rapid and easier-to-implement trigger, such as increased transverse momentum, higher mass in the forward direction or the presence of a high transverse momentum electron. We were unable to find any such cut which does not also entail an unacceptable loss in efficiency for Beauty events.

### *4.1 Strategy*

At the Tevatron, the ratio of the $p\bar{p}$ total inelastic cross section of about 60 mb to the $b\bar{b}$ production cross section of about 50 $\mu$b is $\approx$1200/1. This indicates the required level of minimum bias suppression. Most of this suppression is accomplished on-line with a combination of Level-1 and Level-2 trigger processors, as discussed below. Monte-Carlo studies have shown that the remaining background can be suppressed by detailed topology cuts and offline Cherenkov analysis.

Although all detectors will be gated with each 395 ns bunch crossing, the readout cycle will be executed only for those crossings for which a "Level-0" trigger occurs. Level-0 is an interaction pretrigger which selects those bunch crossings that contain a $p\bar{p}$ interaction. This avoids having to read out all detectors with each bunch crossing.

The geometry of the silicon detector is described in Section 5.1. Here we simply note that there are 16 or more planes installed inside the vacuum pipe perpendicular to the beam line, with a small gap (e.g., 3 mm) through which the circulating beams pass. Each plane is divided into four quadrants and there is x and y readout of each. Because the silicon trigger algorithm is executed in real time, the silicon data must be read out as rapidly as possible. This leads us to "sparsify" on-board the detector and read out only digital information of the "hit" silicon strips.

The overall strategy of the Level-1 trigger is to use the silicon digital information to search for events which are inconsistent with having a single vertex. This is clearly a much weaker condition than requiring the presence of a nearby secondary vertex. However, it is found that a sufficiently large suppression of the minimum bias background can be obtained to allow efficient transfer of accepted events to a system of parallel processors. Moreover, the algorithm described below is sufficiently concise to allow straight-forward implementation in a Level-1 hardware trigger processor.

### *4.2 Event Simulation*

Since the effectiveness of the trigger in suppressing the minimum bias background events is such an important aspect of the proposed experiment, the problem has been studied in considerable detail. Using the CERN program GEANT,[5] complete simulations were made of the silicon detector response to PYTHIA-generated minimum bias, inclusive Beauty and Charm events. As a check of the PYTHIA generation, minimum bias events generated at $\sqrt{s}$ = 0.63 TeV were found to agree well with UA5 results[6] on minimum bias physics at the Sp$\bar{p}$S.

Following this, a trigger algorithm was created and tuned (at the Sp$\bar{p}$S energy) on Monte-Carlo data samples, to yield large suppression of minimum bias events while maintaining high trigger efficiency for Beauty events. A detailed discussion of this algorithm is found in **APPENDIX A.** This algorithm has been applied without fundamental modification to Tevatron events and its performance is discussed in Section 4.4.

There is little change in the performance of this algorithm between $\sqrt{s}$ = 0.63 and 1.6 TeV. This may be understood with reference to Table 5, which shows various quantities which characterize the event properties in the silicon. The character of the silicon data is seen to change only modestly over the larger energy range 0.63 to 16.0 TeV. The cluster density in a silicon quadrant only doubles over that large energy range.

---

[5] R. Brun, F. Bruyant, M. Maire, A.C. McPherson, P. Zanarini "Geant3", CERN report DD/EE/84 – 1, September 1987.

[6] G.J. Alner et al. (UA5 Collaboration), Physics Reports 154 (1987) 247.

*Table 5:* *Properties of Silicon Data for Minimum Bias Events From PYTHIA & GEANT.*

| | | |
|---|---|---|
| Center-of-Mass Energy, $\sqrt{s}$ (LHC & SPS) | 16.0 TeV | 0.63 TeV |
| Average No. Clusters Per Quadrant | 5.6 | 2.8 |
| Average No. Strips Hit Per Quadrant | 9.2 | 4.8 |
| Cluster Width (Strips) | 1.3 | 1.3 |
| Point Resolution | 7.6 $\mu$m | 7.6 $\mu$m |
| First Vertex Resolution (see Sec. 4.3) | 0.8 mm | 0.8 mm |

*) Silicon strip width is assumed to be 25 $\mu$m. The silicon thickness is 250 $\mu$m.

### *4.3 Trigger Algorithm*

The general strategy of the trigger algorithm is as follows:

- **The geometric centers of strip clusters are taken as "points".**
- **Line-Finding:** Lines are found in all sets of three consecutive planes using a road width of one silicon strip. Track projections which multiple scatter more than this tend not to be used in the trigger calculations ($p > 2$ GeV).
- **Duplicate Rejection:** If a single track was found in more than one detector triplet (this will occur whenever a particle traverses more than three detectors in a single view) the duplicate entries are removed from the list of tracks. In each such case, only the track defined by the first three planes the track traverses will be retained.
- **Vertex z Estimation:** The z position of the vertex is estimated by projecting all the found track projections to $x = y = 0$. The resulting z positions are histogrammed, and the vertex is assumed to be at the peak bin.
- **Bad Track Removal:** All track projections are demanded to have an impact parameter of less than 1 mm. Most tracks which fail this cut are fake, mis-measured, or from strange particle decay (the great majority of tracks from beauty or charm decays have much smaller impact parameters). A large number of tracks failing this cut indicates a pileup event.
- **Vertex Calculation:** A new vertex position is calculated which minimizes the sum of the squares of error weighted impact parameters for all the remaining track projections. If the $\chi^2$ is

less than some cut value, the event will be considered to contain only a single primary vertex, and will thus be rejected by the trigger.

- **Worst Track Rejection:** If the $\chi^2$ is greater than the cut value, the track list is searched for the track with the largest contributing term. That track is then removed from the list, and the vertex calculation step is repeated. If the $\chi^2$ test still fails after two tracks have been removed, the event is assumed to have a secondary vertex.

The implementation of this trigger algorithm in hardware is discussed in Chapter 6.

## *4.4 Trigger Performance and Expected Rates*

As mentioned above, the Level-1 trigger algorithm, which was initially created and developed for the Sp$\bar{p}$S, has been applied without fundamental modification to Tevatron events. Fig. 10 shows, as a function of the $\chi^2$-cut value, the fractions of minimum bias events and events containing B-mesons which decay into two specific exclusive final states (accepted by the 600 mrad spectrometer) which survive the trigger algorithm. A $\chi^2$ cut of about 30 gives a suppression of 1/100 for minimum bias events while retaining between 25% and 50% of the B events (depending on final state multiplicity). In our simulations for the Sp$\bar{p}$S, we obtained a trigger efficiency of 1% for charm and complete offline rejection of these events. At the Tevatron, we estimate the charm trigger efficiency will be ≈2%.

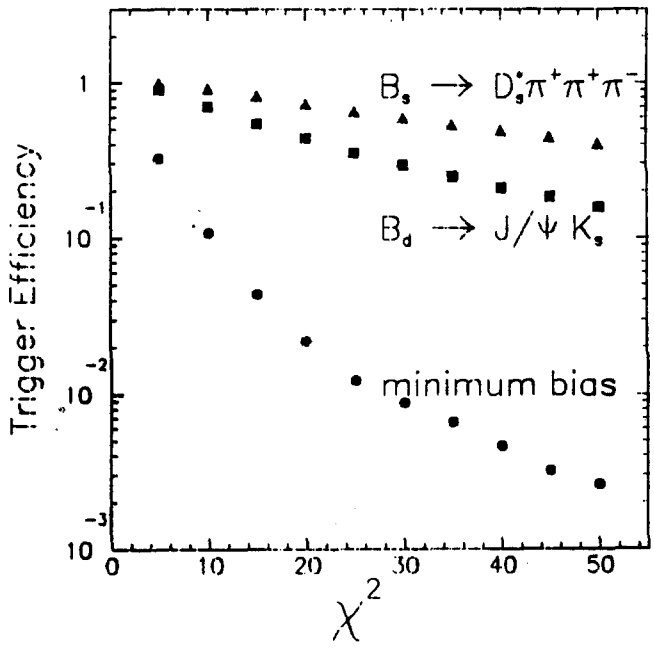


*Figure 10: Trigger Efficiency vs. $\chi^2$-Cut Value.* The fraction of events at the Tevatron which survive the Level-1 trigger algorithm. This quantity is shown for minimum bias events and the exclusive final states $B \rightarrow D^* \pi\pi\pi$ and $B \rightarrow J/\psi K_s$.

In order to estimate the trigger rates, we take a luminosity, $\mathscr{L} = 10^{31}$ cm$^{-2}$s$^{-1}$. Assuming $\sigma_{inelastic} = 60$ mb, $\sigma(c\bar{c}) = 3$ mb and $\sigma(b\bar{b}) = 50\ \mu$b, and using trigger efficiencies of 1/100, 1/50 and 1/5 (for minimum bias and inclusive $c\bar{c}$ and $b\bar{b}$, respectively), we arrive at Level-1 trigger rates of 6.0 KHz, 0.6 KHz and 0.1 KHz, respectively, or a total of 6.7 KHz. These events will be passed to a system of high performance parallel processors for the Level-2 trigger, in which a search will be made for events with multiple vertices. For the Level-2 trigger implementation, it will take a system with ≈670 50-MIPS processors to keep up with the Level-1 trigger rate, assuming an average of 0.1 sec to perform the Level-2 trigger.

### *4.5 Pileup*

With $\sigma_{inelastic} = 60$ mb, $\mathscr{L} = 10^{31}$ and the planned RF structure for the 36-bunch running mode in 1994, 16.5% of all inelastic interactions will be accompanied by one or more additional inelastic interactions in the same bunch crossing, for a total pileup rate of 99 kHz. As part of our trigger study for the Sp$\bar{p}$S-Collider (see APPENDIX A), the Level-1 trigger suppression for pileup was estimated by superimposing Monte-Carlo generated events, and passing them through the simulation software package. We found a suppression factor of 1/60. Since the interaction region size at the Tevatron is significantly longer than at the Sp$\bar{p}$S, the suppression will be even larger at the Tevatron and the Level-1 trigger rate from pileup should be smaller than 1.6 KHz. Since this rate is relatively small, compared to the 6.7 KHz event rate calculated in Section 4.4, the conclusions of that section are not modified. We have found in our Monte-Carlo studies that there is no difficulty rejecting pileup events during the offline analysis.

## *5. SPECTROMETER ELEMENTS*

A single arm of the forward Beauty detector, shown in Fig. 8, with aperture $2.5 < \theta < 600$ mrad. The angular acceptance of Spectrometer 1 is 100-600 mr, and of Spectrometer 2, 2.5-100 mr. The fractional solid angles ($\Delta\Omega/4\pi$) are 8.3% and 0.3%. In this chapter, we give detailed descriptions of the following components:

- **Silicon-strip microvertex detector;** installed at the center of the interaction region inside the vacuum chamber. Matches the forward spectrometer system and has a geometry typical of fixed-target experiments with its planes perpendicular to the circulating beams.

- **Vacuum pipe:** contains the circulating beams and passes through the various detector components. It is made of two thin windows connected by conical sections.

- **Magnets:** Spectrometer 1 contains a normal-conducting quadrupole magnet with 2 m radius. Spectrometer 2 contains a superconducting dipole with a uniform magnetic field of 2.5 Tesla and without a septum plate.

- **Pixel Devices:** Used to match the two views of the silicon tracks and to aid in connecting these with tracks found in the spectrometers. A Silicon Pad Detector is installed inside the beam pipe and the first detector elements in both spectrometers are "Pixel Drift" Chambers.

- **Wire chambers:** Chambes with jet-type drift cells are used to measure the position and direction of charged tracks before and after each magnet.

- **Ring-Imaging-CHerenkov (RICH) counters:** Liquid and gas RICH counters are used for off-line particle identification.

- **Electromagnetic calorimeters follow both spectrometers.**

## *5.1 Silicon-Strip Microvertex Detector*

**Geometry**

To match the forward spectrometer system, the silicon microvertex detector has a geometry typical of fixed-target experiments with the silicon planes perpendicular to the circulating beams. The microvertex detector system seen in Fig. 8 is installed at the center of the interaction region ($z = 0$) inside the vacuum chamber. The extended source size of the bunch crossing region and the need to minimize the extrapolation distance from measured track points in the silicon to an interaction vertex leads to a detector design in which the silicon planes are distributed along the intersection region, spaced longitudinally by about 4 cm.

A choice of ≈4 cm spacing between planes involves a compromise between simultaneously minimizing the errors in extrapolating the tracks to an event vertex and the secondary interactions and photon conversions in the material of the detector. The extrapolation errors are then dominated by the strip pitch of 25 $\mu$m for tracks with momenta above about 2 GeV.

As mentioned in the Introduction, such a silicon-strip system was recently tested at the CERN Sp$\bar{p}$S-Collider by the P238 group. A detailed description of this detector, the hardware involved and some early analysis of the data obtained is given in APPENDIX C as a DRAFT version of an article to be submitted to Nucl. Instrum. & Methods. Thus, we leave most detailed description to APPENDIX C and simply give here an abbreviated description of the detector used and explain how the final complete detector would differ from the one used for the P238 run.

Fig. 11 shows a sketch of the 6-plane P238 microvertex detector assembly which has been run in intersection region LSS5 at the Sp$\bar{p}$S as an R&D project. Each silicon plane in Fig. 11 contains eight 4.5 cm square detectors with single-sided readout, configured in four quadrants, with each quadrant comprising one x and one y plane, separated in z by 2 mm. The planes are separated by 3.8 cm and are mounted on a Roman pot assembly, such that the upper and lower halves can be retracted to a safe position at 5 cm from the beams, when there are beam manipulations. Remote control of the vertical positioning (accurate to $\pm 25\ \mu$) allows the detector assemblies to approach the beam line as close as 1.5 mm or less for data taking.

The silicon detector for the proposed Tevatron experiment will have a similar configuration but will contain a larger number[7] of detector planes. Each silicon plane will contain four double-sided readout strip detectors with pitch 25 $\mu$m and 250 $\mu$m thickness, configured in four quadrants. The planes will be separated longitudinally by 4 cm and will be mounted on rigid but movable supports such that, during beam manipulations, the upper and lower halves can be retracted to a safe position 5 cm from the beams. The detector quadrants will have dimensions approximately $6 \times 6$ cm$^2$.

Our experience with the P238 tests show that we can expect to run with a gap between upper and lower detector assemblies of less than 3 mm without significant background. Since beam sizes are smaller at the Tevatron, we may expect that this gap can be even further reduced. Clearly this places great demands on the stability and precision of the support assembly, which presumably will be patterned after the Roman pot technology developed at CERN. We also note that new monitoring elec-

---

[7] The large length of the Tevatron bunches poses a problem. Unless the bunch lengths can be shortened at the Tevatron, it may be necessary to suffer an acceptance loss resulting from incomplete vertex coverage. Allowing for future use of the detectors at LHC or SSC requires that the dimensions be appropriate for shorter bunch length machines.

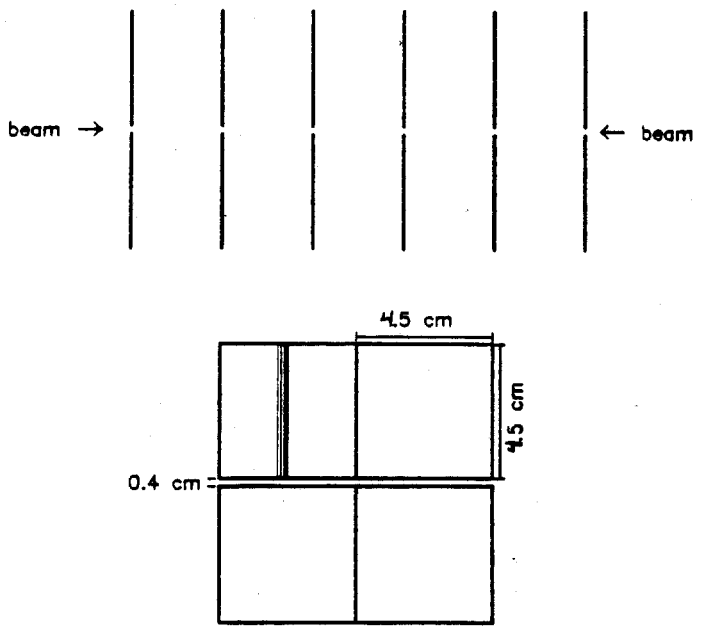


*Figure 11: Side View of the Test Version of the Silicon Detector System.* The 6-plane 43,000 channel P238 silicon system currently running at the Sp$\bar{p}$S. Planes are 3.8 cm apart in z (longitudinally) and configured perpendicular to the beam line. The beams pass between the independent upper and lower detector assemblies. The first silicon strip in each case can be as close as 2 mm from the beams Each quadrant currently contains independent x and y detectors, 4.5 cm square and 280 $\mu$m thick, and separated in z by 2 mm. The pitch is 50 $\mu$m.

tronics for the currents in the low-beta quadrupole magnets and elsewhere will be necessary in order to dump the circulating beams in less than one turn should it be necessary for the protection of the silicon.

**Installation in Vacuum**

There are two major problems with using silicon inside the ultra-high vacuum of a collider very close to circulating beams:

1. RF pick-up in the silicon generated by passage of beam bunches,

2. The need to preserve an ultra-high vacuum in the beam pipe which imposes very tight restrictions on detector materials and requires tightly sealed feed-throughs on signal paths.

An elegant solution to these problems is to separate the silicon detectors from the machine vacuum with a thin Aluminum "window" The Aluminum serves both as an RF shield and as a means of isolating the ultra-high vacuum of the machine from outgassing of detector materials and also relaxes the requirements on feed-through seals.

With the silicon detectors mounted inside a vessel, which is modeled after the CERN Roman pot mechanisms, a thin aluminum window, which approximately follows the contours of the detectors, can constitute the bottom of the "pot". Collapse of these thin windows is prevented by creating a secondary vacuum, in which the silicon detectors are found to function well, inside the Roman pots.

Such a system was successfully used by us in the P238 tests at the CERN Sp$\bar{p}$S-Collider (see below and APPENDIX C) with no signs of RF pickup. A thinner aluminum window will be used in a future installation, in order to minimize multiple scattering. The criterion is that it be thin compared to a single 250 $\mu$m thick silicon detector, while still providing adequate RF shielding. A 100 $\mu$m Aluminum shield should be a reasonable compromise.

**Recent Test Run at Sp$\bar{p}$S-Collider**

While there are many challenging hardware components in the proposed Beauty experiment, only the operation of the silicon detectors within the machine vacuum chamber had intrinsic uncertainties which could influence the overall success of the experiment. These were the unknown amounts of event-unrelated noise and beam halo tracks which would be recorded by the silicon detectors which must be run inside the vacuum pipe close to the circulating beams. Since we have shown that the PYTHIA-generated minimum bias events used in our simulation of the trigger algorithm, are in good agreement with the minimum bias data from Experiment UA5, it is likely that only such (unanticipated) event-unrelated "noise" in the silicon could, a priori, present serious difficulties.

In order to determine the magnitude of such contributions to the observed silicon signals, and thus the reliability of the proposed trigger in the complete experiment, we were fortunate to be able to run a prototype silicon system installed inside the vacuum pipe at the Sp$\bar{p}$S-Collider, in an interaction region which had a low-beta insertion (LSS5). The geometry of the 43,000 channel silicon-strip system has already been described above and is discussed in detail in APPENDIX C.

Approximately $10^7$ minimum bias events were recorded on tape, using a simple beam-beam interaction trigger. No significant background was observed. For example, Fig. 12 shows a "typical" event recorded with the detector system 1.5 mm from the beam. Six y-detectors in one quadrant are shown, with the horizontal scale given by the silicon detecter width of 4.48 cm (896 channels times the pitch of 50 $\mu$m). The vertical scale is defined by the 3.8 cm between planes.

The negligible background of event-unrelated hits in the silicon show that a large silicon strip detector centered on the interaction region can be run as close as 1.5 mm from the beam with minimal background. **It is the single most important demonstration that this experiment is viable.** Converting the silicon data to a trigger by means of powerful real time processing is a manageable task of digital engineering.

**Silicon-Strip Detectors with Readout on Both Sides**

To optimize the selectivity of the silicon microvertex detector, it will be essential to combine optimal spatial resolution with very little material in the sensitive area. This can be achieved by using both the holes and the electrons created in the detector to extract spatial information. Detectors, where strips on both sides are read out, have been developed by several groups. Our CERN group has developed ac-coupled double-sided detectors,[8] using a novel scheme to separate strips ohmically on the n-side by means of field depletion via a suitable potential applied to the readout strips. It has been demonstrated[9] that these detectors give adequate spatial resolution. Prototypes of 19.2 × 19.2 mm$^2$ sensitive area with 50 $\mu$m pitch have been tested in a high energy beam. The resolution was measured to be $\sigma$ = 8.8 $\mu$m on the p-side and 12.4 $\mu$m on the n-side, as shown in Fig. 13. These measurements

---

[8] B.S. Avset et al., IEEE Trans. on Nucl. Sci., Vol. 37, No. 3 (June 1990) 1153.

[9] L. Hubbeling et al., **Measurement of Spatial Resolution of a Double-Sided AC-Coupled Microstrip Detector**, to be published in the Proceedings of the 2nd London Conference on Position Sensitive Detectors (September 1990).

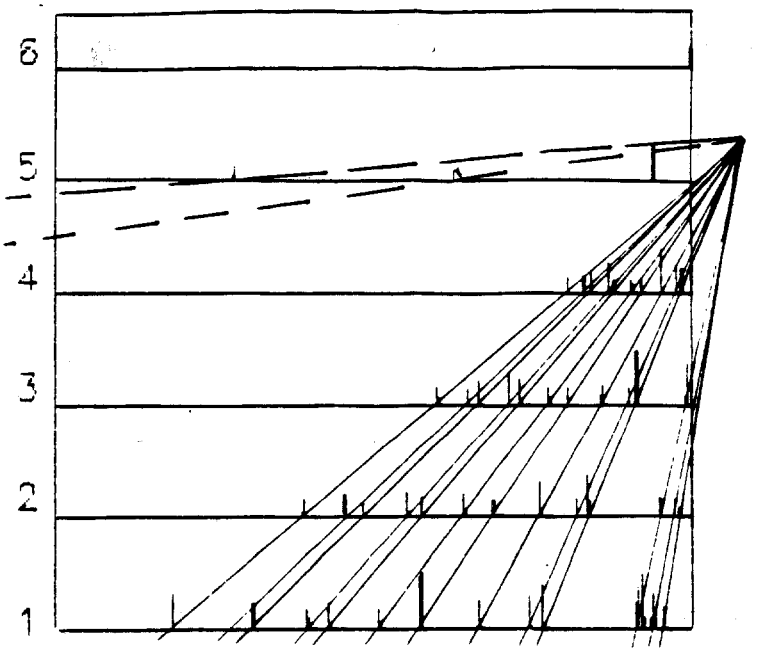


*Figure 12: Silicon Event Recorded 1.5 mm from the Sp$\bar{p}$S-Collider* Beams. One quadrant with six planes of y detectors are shown. There are 3.8 cm between planes and each detector is 4.48 cm wide. Pulse heights are shown if they are larger than $4\sigma_{noise}$. Lines are drawn by hand.

indicate that, with this technology, we should be able to achieve a spatial resolution on both sides of $\sigma \approx 5\ \mu m$.

An improved version of these detectors is at present under production for the upgrade of the DELPHI microvertex detector. For an upcoming test run for the present Beauty proposal (see below in Section 6.4), we plan to instrument some of these double-sided detectors with SVX chips and combine them with the existing P238 vertex detector for test beam and collider runs at the SPS.

## *5.2 Vacuum Pipe*

Detailed spectrometer layouts are shown in Figure 14 and Figure 15. The vacuum pipe contains two thin windows, one at z ≈30 cm and one at 475 cm, which match the apertures of the two spectrometer segments shown in Fig. 8. A conical section with an angle of 100 mr connects the windows. The last vacuum pipe section after z = 475 cm is also a conical section, but with an angle of 2.5 mr, corresponding to the minimum angle of the second spectrometer aperture (at 475 cm, this corresponds to a pipe diameter of about one inch). Although the minimum aperture of the vacuum pipe will be 2.5 mrad, we note that the sensitive regions of the chambers and other detectors will likely be somewhat larger, perhaps at 5 mrad.

Construction of the vacuum chamber from aluminum or carbon fibre (or both) will limit multiple scattering of the particles and reduce interactions of particles in material near the beam. Both of these materials have been used successfully at CERN for construction of beam pipes. Recent improvements

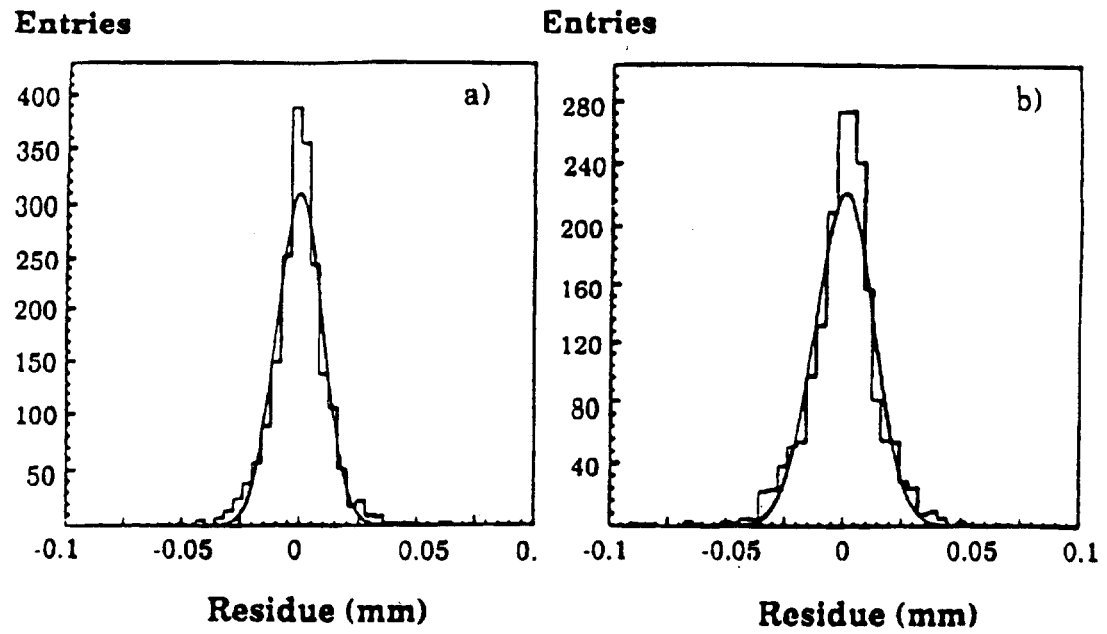


*Figure 13: Residual Distributions with Gaussian Fits:* (a) p-side, (b) n-side.

in aluminum welding used at CERN make aluminum an attractive, cost effective material for the construction of these parts where the amount of material must be minimized. Although carbon fibre is more expensive, it could provide additional immunity to secondary interactions in critical areas such as near the window of the last spectrometer where the beam pipe reaches its minimum diameter (5 cm) in the spectrometer.

## *5.3 Magnets*

The first spectrometer magnet, shown in Fig 14, is a normal-conducting quadrupole magnet of 2 m radius and $L_1 = 2$m magnetic length (3m overall length) with a pole tip field of 1.2 T and a gradient of $B_1' = 0.6$ T/m. T. Taylor of the CERN LEP division has suggested the use of such a large aperture quadrupole magnet as an alternative to large dipole spectrometer magnets with septum plates A quadrupole magnet has several advantages: (a) the absence of septum plate material near the beam minimizes interactions of outgoing particles; (b) particles with angles between 2.5 and 100 mrad receive minimal bending inside the beam pipe before they emerge and enter spectrometer 2; (c) the negligible field at the position of the silicon detectors does not distort the straight line tracks, thereby minimizing the complexity of the on-line trigger algorithm.

The average field integral seen by a charged particle produced at the origin at polar angle $\theta$ is $<BL>_1 = B_1' \cdot L_1 \cdot z_1 \cdot \tan\theta / \cos\theta$, where $z_1$ is the center of the quadrupole. In general, the momentum resolution is given by $\sigma_p = k \cdot p^2$, where $k = \sqrt{2} \cdot \sigma_\theta / [0.3 < BL >]$, and $\sigma_\theta$ is the error in the directional determination of the incident or outgoing track. For this quadrupole, with $z_1 = 3$m, $L_1 = 2$m, $B_1' = 0.6$ T/m and $k_1 = \sqrt{2} \cdot \sigma_\theta \cdot \cos\theta / [1.08 \cdot \tan\theta]$. Track sensitive detectors are installed at $r = 2$m to detect particles which strike the poles.

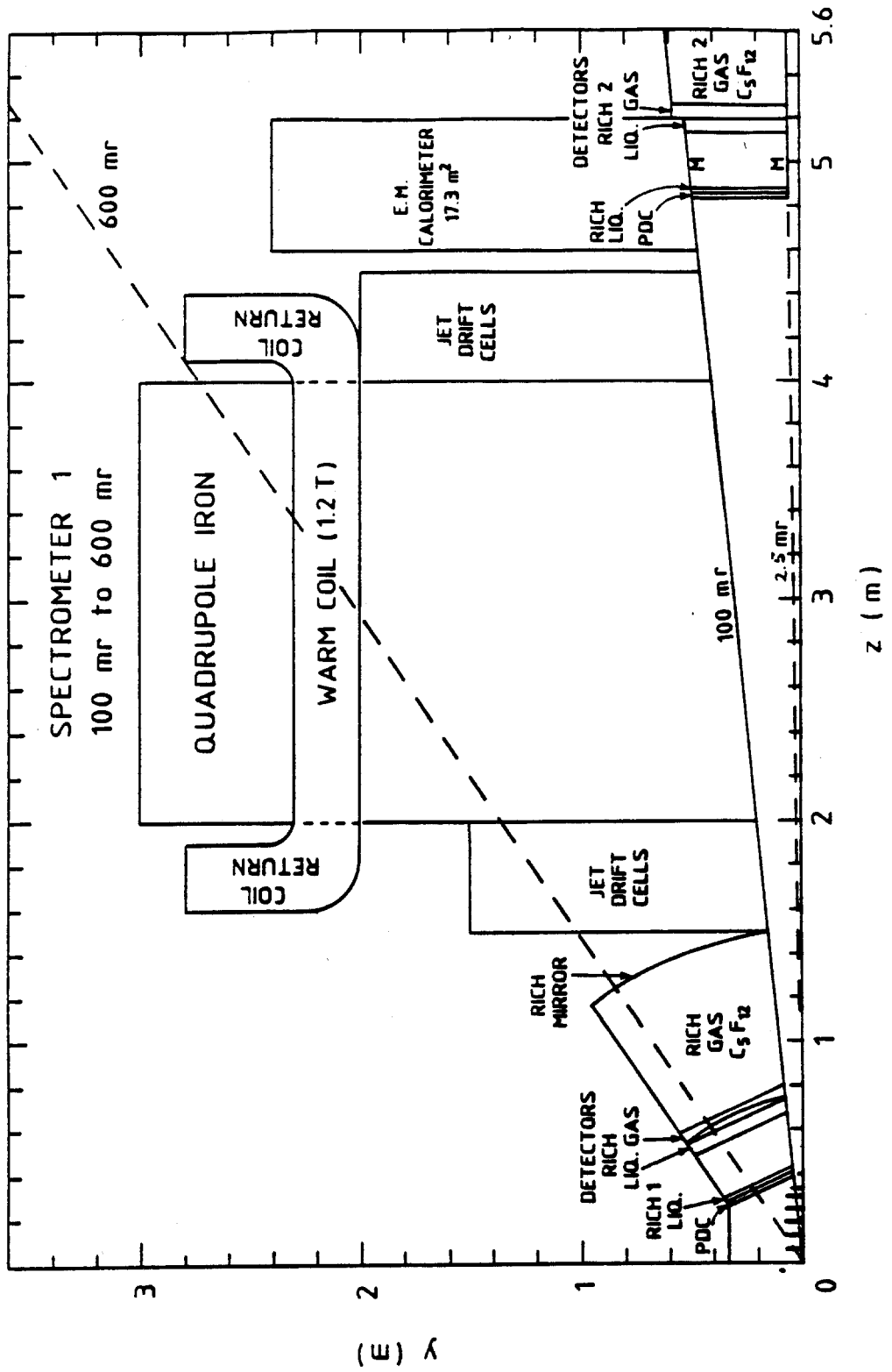


*Figure 14: Layout of Spectrometer One.*

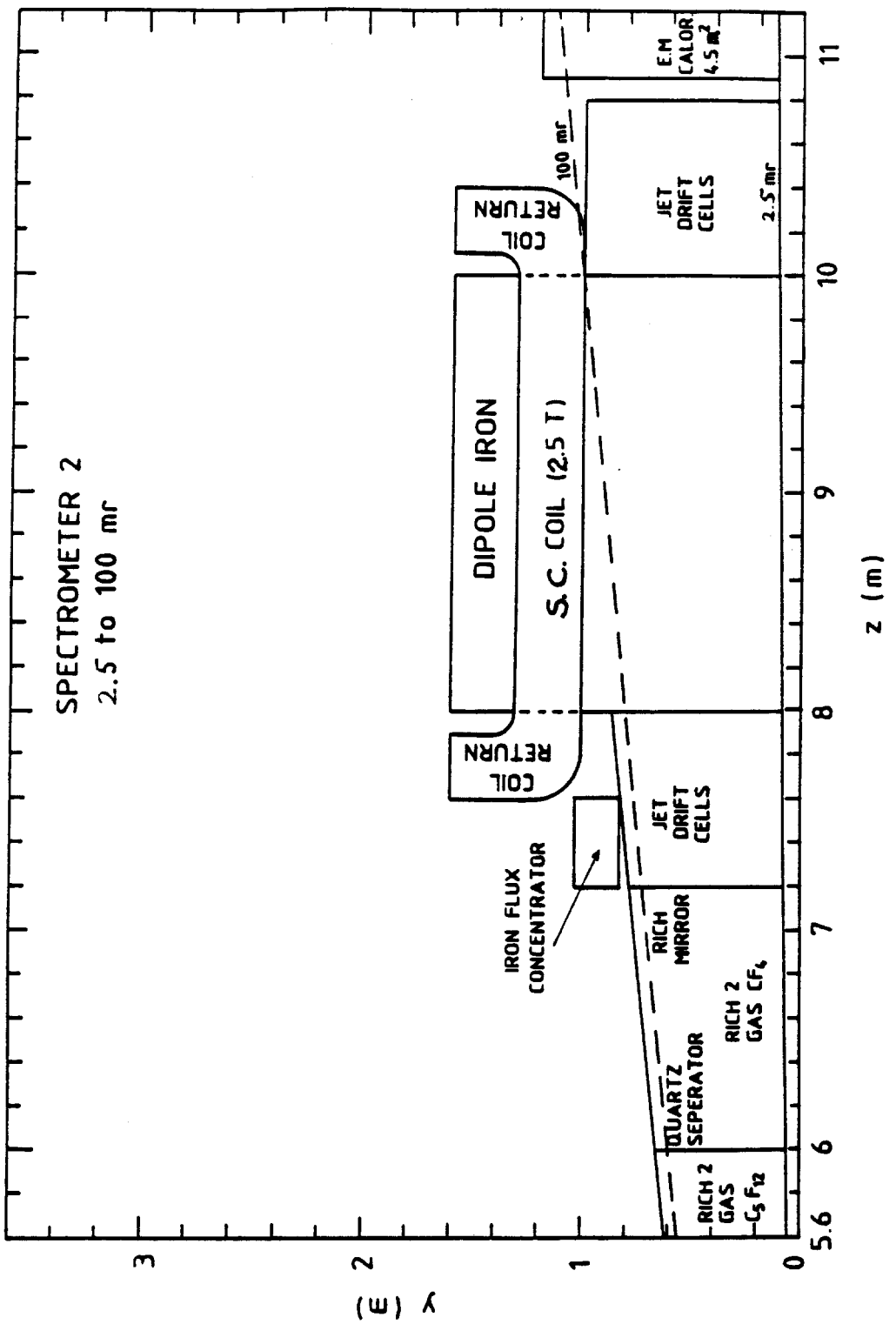


*Figure 15: Layout of Spectrometer Two.*

In Spectrometer 2, covering 2.5 to 100 mr, as shown in Fig 15, the superconducting dipole has magnetic length $L_2$ = 2m (geometrical length 3m) and uniform magnetic field of 2.5 T. The average $<BL>_2$ = 5.0 Tm. The corresponding magnet constant is: $k_2 = \sqrt{2} \cdot \sigma_\theta \cdot \cos\theta \,/\, 1.5$. The sides of the dipole will also be instrumented with track sensitive detectors in order to measure those low momentum particles which are deflected by the magnetic field into the side walls.

### *5.4 Pixel Detectors*

A silicon pixel detector and two pixel drift chambers (described below) are included in the spectrometer to match the x,y view tracks in the microvertex detector and to aid in connecting these tracks to those found in the spectrometers. Monte-Carlo calculations show that the resolution of the pixel detectors should be less than $1 \times 1$ mm$^2$.

A front view of several elements of the pixel drift chamber (PDC1) in Spectrometer 1 (see Fig. 14) is shown in Fig 16. The two dimensional position of a track traversing the 20 mm thick gap is measured with only a left-right ambiguity. The sense wires of the PDC have 2 cm length and pitch 2 mm, and are approximately parallel to the outgoing tracks, so that all ionization is collected by a single wire (or cluster). The wire coordinate and its signal arrival time provide the x,y coordinates of the track.

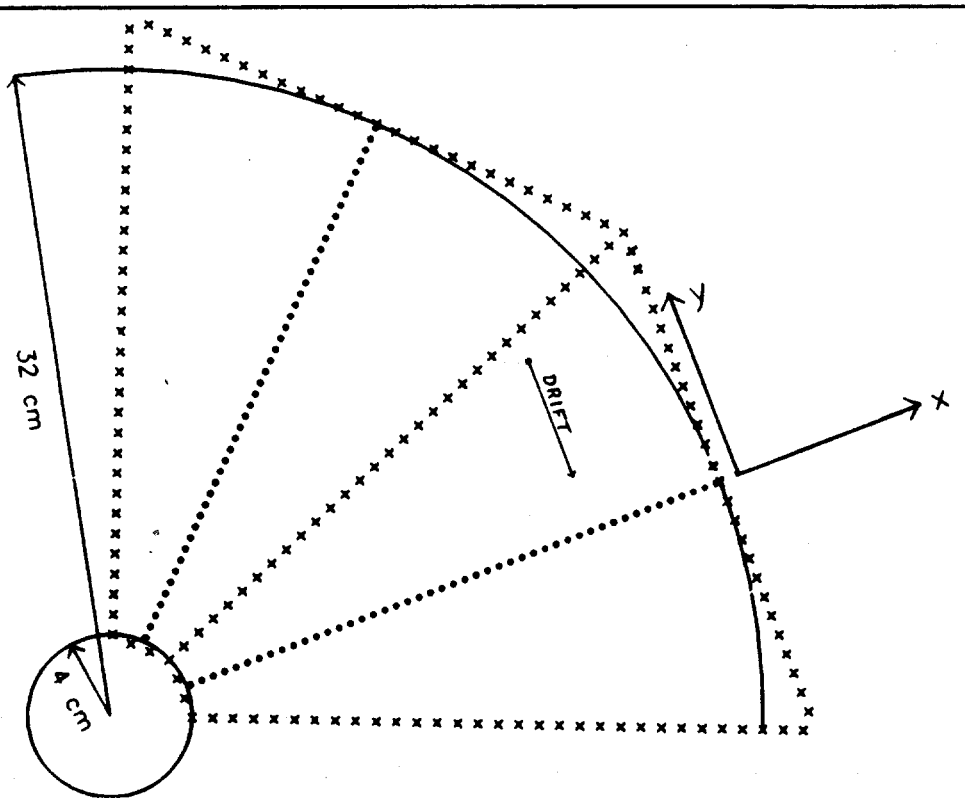


*Figure 16: Front view of one quadrant of a pixel drift chamber.* Although only an 8-fold $\phi$ symmetry is shown, PDC1 and PDC2 will actually possess 32-fold and 48-symmetries, respectively

The segmentation is determined by the requirement that the maximum drift time be less than 400 ns. With an outer radius of 32 cm and a drift velocity, $v_d \approx 8$ cm/$\mu$s, this requirement can be met if there is a 32-fold $\phi$ symmetry. The maximum drift distance is then 3.14 cm. The total number of wires in the PDC1 is 4,480 (32 × 140).

A value, $v_d \approx 8$ cm/$\mu$s, can be attained with a mixture of 90% methane and 10% isobutane. The diffusion coefficients are then: $\sigma_\ell = \sigma_t = 240\ \mu\text{m}\cdot\text{cm}^{-1/2}$. The pixel resolutions are $\sigma_x = 580\ \mu$m (with 2 mm wire pitch) and $\sigma_y = 570\ \mu$m (assuming 4-bit TDC's). The effects of diffusion change these values very little.

A similar detector, PDC2, with a larger radius of 48 cm, forms the first element of Spectrometer 2 (see figure 14). Now a 48-fold symmetry is required to satisfy the 400 ns maximum drift time and the number of sense wires are 11,040 (48 × 230). The pixel resolutions are the same as in PDC1.

The silicon pixel detector (SPD), which covers the angular range 4 to 100 mrad, is disk shaped and located inside the beam pipe, at a distance of 38 cm from the average interaction point (this assumes a distance of 1.5 mm between silicon and circulating beams). The SPD disk, with radius 3.8 cm and 250 $\mu$m thickness, will be divided into four sectors. The upper and lower halves will be mounted on the respective vertex detector positioning mechanisms so they also are retracted during beam manipulations. The pixel size will be $1 \times 1$ mm$^2$, for a total of 4500 channels.

Track segments both from the silicon detectors and from the spectrometer will be projected onto the PDC with spatial resolution better than 1 mm, in each projection, for momenta larger than 5 GeV.

## *5.5 Wire Chambers*

Jet-type drift cells will be used to measure the position and direction of charged tracks before and after each magnet. Fig. 17 shows, for example, a jet drift cell oriented so that ionization from a 350 mrad track arrives isochronously at the 10 sense wires. Similar chambers are used by the HELIOS[10] experiment at CERN and SLD[11] experiment at SLAC.

### Geometry of the Chambers

Figures 14 and 15 shows the position and dimensions of the four chambers used to measure particle directions and momenta. The four chambers all have similar cellular structures as summarized in Table 6. Chambers 1 and 2 (Spectrometer 1) each have 8 modules with 10 track samples each. Four different wire orientations are used: x, y, and u,v ($\pm 45°$). This sequence is repeated twice for a total of 80 measurements along each track. Chambers 3 and 4 (Spectrometer 2) have a somewhat different structure because of the dipole magnetic field. The cell orientation is x, u, x, v, x, u, x, v, with 16 track samples in each module. The total of 128 measurements is equivalent to 96 measurements in the bending plane.

### Cell Structure and Drift Resolution

The drift cell geometry shown in Fig. 6 has sense wires and equipotential wires strung in planes which include the intersection region center ($x = y = z = 0$). Thus, the average particle direction is perpendicular to the drift direction in all cells so that isochronous charge collection results. The wires have pitch 6.25 mm and are staggered transversely by 100 $\mu$m. The maximum drift distance is 2 cm.

---

[10] D. Bettoni et al.,Nuclear Instruments and Methods A252 (1986) 272.

[11] C. Young et al., IEEE NS36 (1986).

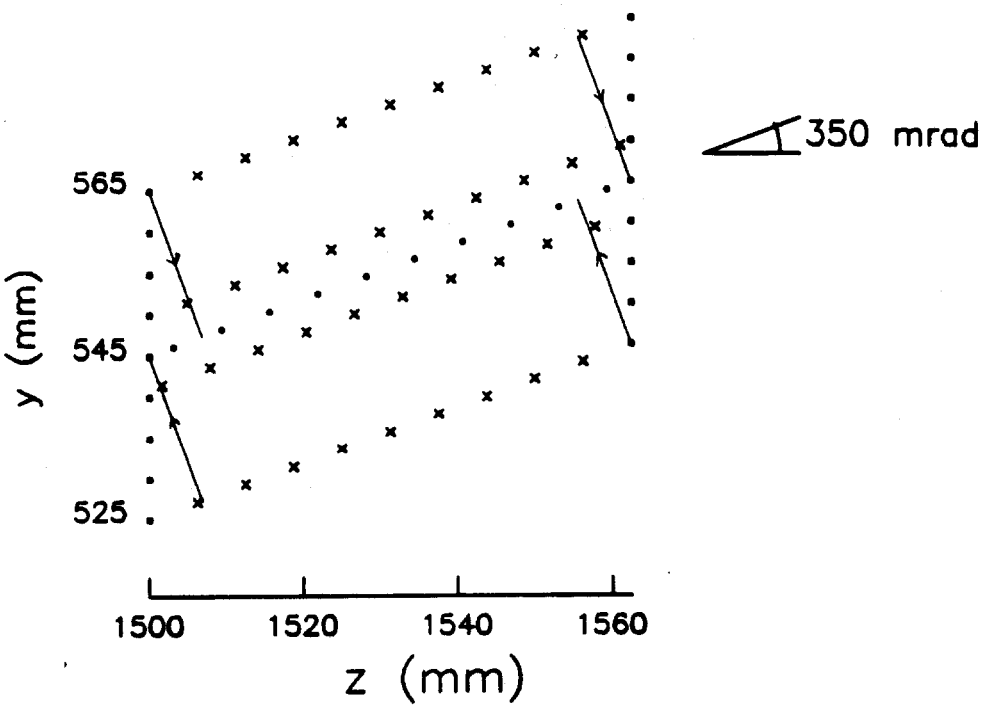


*Figure 17: A Jet drift cell in one module of Chamber 1 at $\theta = 350$ mr.* The circles are sense wires, crosses are equipotential wires, and squares are field shaping wires.

*Table 6: Chamber Properties*

| | Chamber 1 | Chamber 2 | Chamber 3 | Chamber 4 |
|---|---|---|---|---|
| Diameter × Length ($m^2$) | 3×0.5 | 4×0.5 | 1.6×0.8 | 2×0.8 |
| Sense wires | 7000 | 9600 | 5700 | 7100 |
| Orientation | x,y,u,v | x,y,u,v | x,u,x,v | x,u,x,v |
| Samples per Track | 80 | 80 | 128 | 128 |
| Drift Distance | ±2cm | ±2cm | ±2cm | ±2cm |
| S.W. Staggering | 100μm | 100μm | 100μm | 100μm |
| Drift Velocity | 20μm/nsec | 20μm/nsec | 20μm/nsec | 20μm/nsec |
| Drift Field | 4kV/cm | 4kV/cm | 4kV/cm | 4kV/cm |
| Gas | He/DME | He/DME | He/DME | He/DME |

We intend to use 70% Helium and 30% DME because of the long radiation length of this mixture (667 m) compared to that of $CO_2$ (197 m), while the diffusion characteristics and drift velocity are similar. This mixture results in an unsaturated drift velocity of 20μm/nsec in an electric field of 4 kV/

cm with a diffusion coefficient of ~80 $\mu m \cdot cm^{-1/2}$. The corresponding maximum drift time is 1 $\mu$sec for $\pm 2$ cm cells. At atmospheric pressure this mixture will produce 21 primary electrons per cm, corresponding to 13 primary electrons per wire (with 6.25 mm pitch).

The HELIOS chambers use a 90% $CO_2$ and 10% ethane gas mixture which gives a smaller drift velocity than that of the He/DME mixture we propose to use. In order to optimize track separation and reduce space-charge, HELIOS uses field wires to limit the length of the charge segment collected by a sense wire, thus obtaining a more isochronous charge collection. Their electronics makes use of pulse clipping and shaping, and multihit TDCs. In a test beam, they found a resolution of 60 $\mu$m averaged over the 2cm drift distance, and a 600$\mu$m two track separation. The SLD collaboration used 92% $CO_2$ and 8% isobutane and a cell geometry which collected 16 primary electrons per sample. Their average drift distance resolution is 55$\mu$m in $\pm 2.5$ cm cells.

Since our chambers will have substantially larger dimensions and will operate in a nonuniform magnetic field, we expect a final accuracy of 100$\mu$m averaged over the drift distance, and a two track separation of 3 mm. In order to reach such a precision, a laser alignment and calibration system will be used, together with a complete monitoring system of gas temperature and pressure, drift velocity, and electric field.

**Electronics**

A low noise preamplifier is mounted directly on the chamber frame. Ten meters away a two stage amplifier is used where a 2 nsec clipping and integration (1/t cancellation) is performed. A discriminater (with threshold set at 2 electrons on the sense wire) drives an 8-bit TDC with multihit readout. No pulse amplitude analysis is performed.

**Momentum Measurement**

The error in the track direction, $\theta$, is given by the relation

$$\sigma_\theta = [\, (\sigma_X/L)^2 \cdot (12/N) + (.01/p)^2 \cdot (L/X_0)\,]^{1/2}$$

where $\sigma_X$ is the accuracy of a single drift cell measurement and L is the distance over which the uniformly distributed N measurements are made and $X_0 = 667$ m for the He/DME mixture.

In each chamber of Spectrometer 2 we effectively have 96 measurements in the bending plane over 80 cm of track length with a single hit accuracy of 100 $\mu$m. This gives us:

$$\sigma_\theta = 44\ \mu\text{rad} \cdot \sqrt{(1+p_2{}^2/p^2)}$$

where $p_2 = 7.9$ GeV is the momentum below which the multiple scattering term dominates. The error on the Spectrometer 2 momentum measurement is given by the dipole magnet constant

$$k_2 = \sigma_p/p^2 = 4.1 \cdot 10^{-5} \cdot \cos\theta \cdot \sqrt{(1+p_2{}^2/p^2)}$$

for the 5 Tm magnet (where we have used the expression for $\sigma_p$ given above).

For Spectrometer 1 we have 40 measurements over 50 cm with 100 $\mu$m precision in the bending plane. Hence:

$$\sigma_\theta = 107\ \mu\text{rad} \cdot \sqrt{(1+p_1{}^2/p^2)}$$

with $p_1 = 2.6$ GeV and the quadrupole magnet constant is then:

$$k_1 = \sigma_p/p^2 = 1.4 \cdot 10^{-4} \cdot \cos\theta \cdot \sqrt{(1+p_1{}^2/p^2)} \,/\, \tan\theta.$$

## *5.6 Ring Imaging CHerenkov (RICH) Counters*

**Geometry and Photon Detector**

The RICH detectors are designed to identify all hadrons from B decays as well as most leptons ( $\leq 20$ GeV ). Above 20 GeV electron identification is provided by the electromagnetic calorimeter. Each of the two spectrometers has a $C_6F_{14}$ freon liquid radiator of 10 mm thickness and a $C_5F_{12}$ freon gas radiator of 750 mm path length. Spectrometer 2 also has a second gas counter with a 1200 mm long higher-threshold $CF_4$ freon radiator. The two gas volumes in Spectrometer 2 are separated by a 3 mm thick fused quartz window and both ring images are detected at the focal plane, 1950 mm upstream from the spherical reflecting mirror. Fig. 18 shows the momentum ranges of unique separation for the indicated particles in the liquid and gas RICH counters.

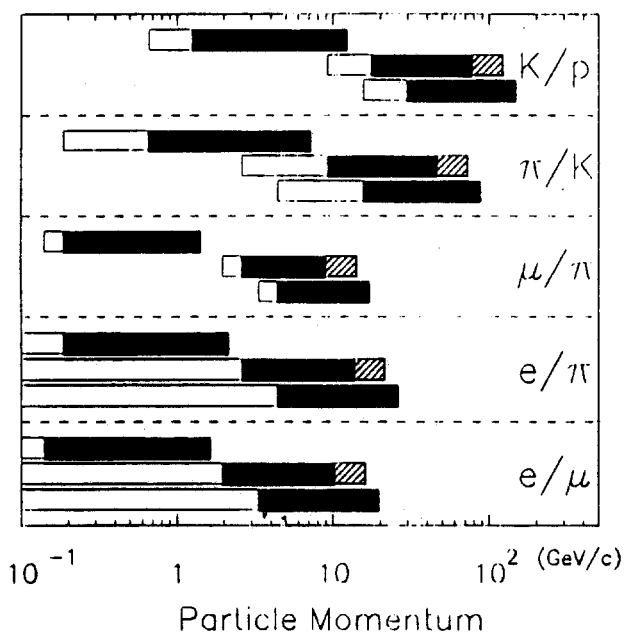


*Figure 18: Momentum Ranges of RICH Counter Identification.* For each indicated pair of particles, the upper bar in each set is for the the liquid RICH counters; the middle bar in each set is for the $C_5F_{12}$ radiators; the lower bar in each set is for the $CF_4$ radiator in Spectrometer 2. In all cases, the open bars show the momentum range between the thresholds for the lighter and heavier particles. The $3\sigma$ separation upper limits are indicated by the end of the solid bars, except for the $C_5F_{12}$ radiator in Spectrometer 2, whose upper limits extend to the ends of the hatched bars (since it is somewhat longer).

The liquid and gas radiator geometry is shown in Fig.s 14 and 15 and the proposed RICH detector geometry is shown in Fig. 19. The liquid radiator is contained by a 3 mm thick fused quartz window followed by a 25 cm Helium-filled flight path to its photon detector. This is immediately followed (back-to-back) by the gas image detector. Each detector consists of a 3 mm thick fused quartz window whose inner surface is coated with 100 $\mu$m wide metallic strips with 1 mm pitch (10% opacity) which

serve to define the equipotential surface, $V_0$. Cherenkov photons impinge upon the CsI/TMAE reflective photocathode[12] which is deposited on the pad structure shown in Fig. 19. The distance between the window and the pads is 3 mm and it is filled with 80% methane and 20% hexane at atmospheric pressure. Amplification is obtained on 20 $\mu$m diameter wires with 1 mm pitch placed 0.5 mm above the pad plane. The measured[13] pad efficiency for single photoelectrons exceeds 95% and the detector should be stable for gains up to $2 \cdot 10^6$.

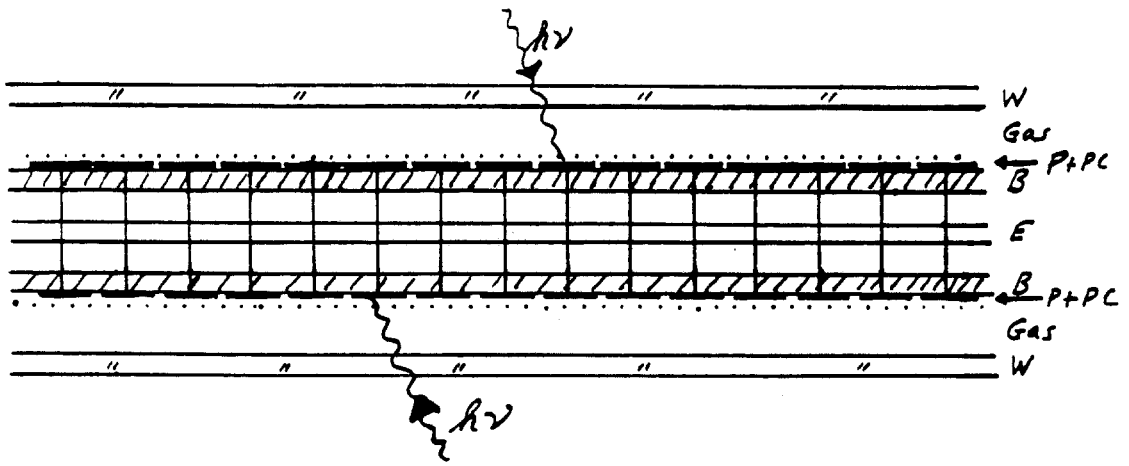


*Figure 19: Back-to-Back RICH Detector Geometry.* A schematic view of the quartz windows W, chamber body B, readout electronic E, and pad + photocathode structure P+PC. A Cherenkov photon is converted by the CsI/TMAE reflective PC and the produced primary photoelectron is amplified on a wire and induces a signal on nearby pads. The electronics readout is common to both chambers. The gas filling is 80% Methane and 20% Hexane at atmospheric pressure.

Secondary electron (feedback) production from the gas phase cannot occur since the TMAE partial pressure is negligible (i.e., TMAE gas flow is not necessary once the cathode has been sensitized). The primary avalanche process produces photons which irradiate the CsI/TMAE cathode and produce secondary avalanches. These pulses, however, merge with the primary avalanche because the amplifying wire is so near the cathode (i.e., 0.5 mm = 10 ns). The presence of hexane (with methane as the amplifying gas) defines the upper energy limit of the detector response (e.g., 7 eV) provides an absorber the $C^*$ emission lines at 7.47 and 7.95 eV (i.e., 166 and 156 nm). The $C^*$ emission line at 6.42 eV (193 nm) is then the only remaining source of feedback instability and has the same level of photon feedback as a TEA-based photoionizing gas detector. This is because the 156 and 193 nm lines are emitted with the same probability and because the quantum efficiencies of TEA and CsI/TMAE are similar at these respective wavelengths. A TEA pad detector with amplifying wires 0.5 mm from the pad plane

[12] J. Seguinot et al., Reflective UV Photocathodes with Gas Phase Electron Extraction: Solids, Liquids and Adsorbed Thin Films; CERN-EP/90-88 and NIM A297(1990)133.

[13] R. Arnold et al., Experimental Study of a Fast Photon Detector with Pad Readout, CRN/HE90-05 (available in French at CRN, Strasbourg – English version for NIM is in preparation).

has been successfully tested[13]. It showed enhanced stability to photon feedback compared to a TMAE gas detector and attained a gain of $2 \cdot 10^6$. It appears that the CsI/TMAE photocathode is suitable for fast operation ($\sigma_t$ = 10 ns) in the less dispersive energy range (6 to 7 eV), compatible with fused quartz windows.

The detector response parameter is $N_0 = (370\ eV^{-1}cm^{-1}) \cdot \Delta E \cdot \varepsilon$, where $\Delta E$ is the energy bandwidth of the detector and $\varepsilon = \int(Q \cdot T \cdot R)\, dE/\Delta E$ is the energy average of efficiencies (Q = quantum, R = reflectivity and T = transmissivity). Taking experimental values of R = T = 0.8 and an average Q = 27.5% (i.e., 12% at 6 eV and 43% at 7 eV), the detection efficiency $\varepsilon$ = 0.176. The resulting response parameter, $N_0 = 65\ cm^{-1}$, is used in Table 7.

The RICH detector surface area is 0.9 $m^2$ in Spectrometer 1 and 1.1 $m^2$ in Spectrometer 2, for a total of 2.0 $m^2$ corresponding to $3.8 \times 10^5$ pads ($3 \times 3\ mm^2$ in Spectrometer 1 and $2 \times 2\ mm^2$ in Spectrometer 2). The VLSI pad readout electronics[14] comprises a fast (25 ns) Bipolar analogue chain (preamplifier, discriminator, pipeline and memory), followed by a 50 MHz CMOS 2-dimensional shift register with priority encoding, zero suppression and output bus arbitration. The prototype system reads out $10^4$ pads in less than 300 ns. The first production chips have recently been tested with partial success. We are now proceeding to a second test production with a revised layout. Production of about $4 \cdot 10^4$ channels of electronics is scheduled for spring 1991 for use in a full-scale liquid RICH counter test.

**Resolution and Particle Separation Ranges**

The chromatic error $\sigma_\theta(E)$ in the determination of the Cherenkov angle $\theta$ may be expressed as

$$\sigma_\theta(E) = (\partial\theta/\partial n) \cdot (dn/dE) \cdot \sigma_E.$$

For the $C_6F_{14}$ liquid radiator (refractive index n = 1.278 at E = 6.5 eV and dispersion $dn/dE = 9.28 \times 10^{-3}\ eV^{-1}$), the proximity focused image is characterized by (see APPENDIX B):

$$\partial\theta/\partial n = (n\tan\theta)^{-1} \cdot (n^2\beta^2) \cdot (\cos\theta_p/\alpha).$$

The first factor is the canonical factor obtained from the Cherenkov relation $n\beta\cos\theta = 1$, the second factor $n^2\beta^2$ is due to refraction at the liquid surface and the last factor $\cos\theta_p/\alpha$ depends on the particle incidence angle $\theta_p$ with respect to the normal to the radiator plane. $\alpha$ depends on the Cherenkov azimuthal angle $\phi$ via the relation:

$$\alpha = \cos\theta_p - \sin\theta_p \cdot \tan\theta \cdot \cos\phi.$$

Therefore, this last factor is unity for normal incidence and averages to 0.9 at $\theta_p = 20^0$. The energy error $\sigma_E$ of a triangular response detector is $\Delta E/\sqrt{24}$ where $\Delta E$ is the base energy width. Combining these factors gives

$$\sigma_\theta(E) = (1/1.02) \cdot (1.63) \cdot (0.9) \cdot (9.28 \cdot 10^{-3}) \cdot (1.5/\sqrt{24}) = 4.1\ \text{mrad}.$$

At the chosen distance between the liquid radiator and detector (250 mm), the angular error $\sigma_{ze}$ due to a radiator of thickness 10 mm is about $\sigma_{ze} = 2.2$ mr when averaged over the accepted azimuthal angles $\phi$. With pad dimensions of $3 \times 3\ mm^2$, the measurement errors on the photon conversion point (x, y, z) are $\sigma_x = \sigma_y = 0.9$ mm and, with the CsI/TMAE photocathode, $\sigma_z = 0$. They contribute angular errors of 0.6 mr, 0.6 mr and 0 mr, respectively. Multiple scattering in the liquid radiator and quartz window contribute 2.8 mr/p to $\sigma_\theta$ and the uncertainty in particle direction contributes a term $(2/\pi)\ \sigma_{\theta p}$. Summing the above errors in quadrature gives a total angular error $\sigma_\theta$ = 4.6 mrad per de-

[14] See Figs. 34-41 in: J. Seguinot, **Fast RICH Detectors for LHC/SSC/ELOISATRON**, Proceedings of the Symposium on Particle Identification at High Luminosity Hadron Colliders, Fermilab, Batavia, IL, 5-7 April 1989 (Ed. T.J. Gourlay and J.G. Morfin), pps. 215-253 and 671-683.

tected photon. In the liquid radiator, the threshold momenta for e, $\mu$, $\pi$, K and p are, respectively, 0, 0.13, 0.18, 0.62 and 1.18 Gev. The relevant derivatives are given in APPENDIX B and summarized in Table 7.

*Table 7: RICH Resolution and 3σ Momentum Identification Limits*

| | LIQUID | | $C_5F_{12}$ GAS 1 | | $C_5F_{12}$ GAS 2 | | $CF_4$ GAS 2 | |
|---|---|---|---|---|---|---|---|---|
| $v_i$ | $\Delta v_i$ | $\sigma_\theta$(mr) | $\Delta v_i$ | $\sigma_\theta$(mr) | $\Delta v_i$ | $\sigma_\theta$(mr). | $\Delta v_i$ | $\sigma_\theta$(mr) |
| $z_e$ (mm) | 10 | 2.24 | 750 | 0.30 | 750 | 0.12 | 1200 | 0.04 |
| $x_e$ (mm) | – | – | 1.0 | 0.00 | 1.0 | 0.00 | 1.0 | 0.00 |
| z (mm) | 0.0 | 0.00 | 0.0 | 0.00 | 0.0 | 0.00 | 0.0 | 0.00 |
| x (mm) | 3.0 | 0.64 | 3.0 | 0.81 | 2.0 | 0.20 | 2.0 | 0.20 |
| y (mm) | 3.0 | 0.64 | 3.0 | 0.81 | 2.0 | 0.20 | 2.0 | 0.20 |
| E (eV) | 1.5 | 4.0 | 1.5 | 0.35 | 1.5 | 0.35 | 1.5 | 0.27 |
| $\theta_p$(mr) | 1.0 | 0.18 | 1.0 | 0.18 | 1.0 | 0.18 | 1.0 | 0.18 |
| $\sigma_\theta$(total) | 4.64 | | 1.25 | | 0.50 | | 0.44 | |
| $k_r$ [$10^{-6}$] | 730 | | 17.9 | | 7.2 | | 5.0 | |
| $p_{3\sigma}(e\mu)$ | 1.6 | | 10.1 | | 16.0 | | 19.2 | |
| $p_{3\sigma}(e\pi)$ | 2.1 | | 13.5 | | 21.3 | | 25.6 | |
| $p_{3\sigma}(\mu\pi)$ | 1.4 | | 8.9 | | 14.1 | | 16.9 | |
| $p_{3\sigma}(\pi K)$ | 7.1 | | 45.6 | | 71.9 | | 86.3 | |
| $p_{3\sigma}(Kp)$ | 12.1 | | 77.0 | | 121.4 | | 145.7 | |

These 3σ momentum discrimination limits are shown in Fig. 18.

The allowable average magnetic field inside a RICH radiator is

$$B < (\pi/2) \cdot (\sqrt{12}) \cdot \sigma_\theta \cdot p / (0.3L)$$

to insure that particle deflection inside the radiator does not cause additional smearing of the image. In the liquid radiator, $\sigma_\theta$ = 4.6 mr and L = 0.01 m. Hence, B < 8.4 T when p = 1 GeV, which is clearly satisfied.

The momentum p at which particles of mass $m_1$ and $m_2$ are discriminated at the level of $n_\sigma$ standard deviations is given by the formula:

$$p^2 = (m_2^2 - m_1^2) / (2n_\sigma k_T)$$

where

$$k_T = n \cdot \sigma_\theta / \sqrt{(N_0 L)}.$$

Experiments with the DELPHI barrel RICH prototype[15] have demonstrated ring images with 25 photoelectrons per liquid image (L = 1 cm), corresponding to $N_0 = 65\ cm^{-1}$ for the detector band base width $\Delta E = (7.1 - 5.6)$ eV. With $\sigma_\theta = 4.6$ mrad, $N_0 = 65\ cm^{-1}$, L = 1 cm and n = 1.278, the Cherenkov constant, $k_T = 7.3 \times 10^{-4}$. Hence, particles are discriminated at a level ($n_\sigma > 3$) up to momenta p = 1.6 GeV for $e\mu$, 2.1 GeV for $e\pi$, 1.4 GeV for $\mu\pi$, 7.1 for $\pi K$ and 12.1 GeV for Kp.

The gas radiator in Spectrometer 1 consists of atmospheric pressure $C_5F_{12}$, with Cherenkov threshold $\gamma_t = 17$, corresponding to momentum thresholds of 2.4, 8.4 and 15.9 GeV for pions, kaons and protons, respectively. These thresholds overlap with the upper discrimination limits of the liquid radiator, thus assuring complete coverage for particle identification in the low energy region.

The upper limits for particle identification in the gas radiators[16] are determined by the Cherenkov angular resolution $\sigma_\theta$. The relevant variables ($v_i$) are the photon emission point, $z_e$, the particle impact parameter, $x_e$, the photon detection point, (z,x,y), the photon energy E and the particle direction $\theta_p$ relative to the detector normal. Analytic expressions for the derivatives, $\partial\theta/\partial v_i$, can be found in footnote 16. A summary of the pixel sizes, $\Delta v_i$, and their contributions, $\sigma_\theta(v_i)$, to the total error, $\sigma_\theta$, are shown in Table 7.

The average magnetic field allowable in gas RICH 1 is B < 312 gauss × p, or 0.09T at 3 GeV (just above $\pi$ threshold) and 0.3T at 10 GeV. The shielding of the quadrupole field at the position of RICH 1 (0.5m to 1.25m from the quadrupole entrance plane) appears feasible, since the field direction is azimuthal and can be easily channeled by iron plates mounted on the outer part of the RICH gas box. In gas RICH 2, with its better resolution, only 0.05T and 0.16T are allowable (at 3 GeV and 10 GeV, respectively). However, it is further away from the entrance plane of the dipole (2.0 m to 2.8 m i.e. 2.0 to 2.8 half gaps). Some loss of resolution seems likely at low momentum, where it is acceptable, since many $\sigma$'s ($n_\sigma > 10$) are available for particle discrimination.

The momentum resolution of the RICH detectors is given by the relation, $\sigma_p = k_T p^3 / (m^2\beta)$, where $k_T$ is the Cherenkov factor calculated above. For example, $\sigma_p \leq 100$ MeV at $p_\pi \leq 4.8$ GeV and $p_K \leq 11.0$ GeV in Spectrometer 1 for the $C_5F_{12}$ radiator. In Spectrometer 2, $\sigma_p \leq 100$ MeV at $p_\pi \leq 6.5$ (7.3) GeV and $p_K \leq 14.9$ (16.8) GeV for the $C_5F_{12}(CF_4)$ radiators, respectively. It appears that the momentum resolution of RICH detectors can be useful for the heavier particles (K,p).

---

[15] R.Arnold et al., NIM A270, 255 and 288 (1988).

[16] T. Ypsilantis, CERN-EP/89-150;
**Particle Identification at Hadron Colliders**, Proceedings of Symposium on Particle Identification at High Luminosity Hadron Colliders, Fermilab, Batavia, IL, 5-7 April 1989 (ed. T.J. Gourlay and J.G. Morfin) pps. 133-158;
**Particle Identification at Hadron Colliders**, ECFA Study Week on Instrumentation Technology, Barcelona, Spain, 14-21 September, 1989, CERN 89-10, Vol. 2 (ed. E. Fernandez and G. Jarlskog) pps. 661-674.

### *5.7 Electromagnetic Calorimeter System*

The electromagnetic (EM) calorimeter system is shown schematically in Figs. 14 and 15. The surface areas covered are 17.3 $m^2$ and 4.5 $m^2$ in Spectrometers 1 and 2 respectively. As is discussed in Section 8.2, the electromagnetic energy resolution required is $\sigma_E < 4\% \cdot \sqrt{E}$. This may be achieved with a totally active liquid Krypton calorimeter[17] with $\sigma_E < 1\% \cdot \sqrt{E}$ or with scintillating glass[18] with $\sigma_E < 4\% \cdot \sqrt{E}$.

In the Krypton counter, a $25X_0$ calorimeter would be 1.15 m long, have a a volume of 25 $m^3$ and weigh 61 tons. The raw material cost is ≈$4.8M.

A $25X_0$ scintillating glass (HED-1, $\rho = 3.4\ g \cdot cm^{-3}$, $X_0 = 4.12$ cm) calorimeter would be 1.03 m long, with a volume of 22.5 $m^3$ and weigh 76 tons. We estimate a cost of ≈$7.7M (including phototubes).[19]

The spatial and directional resolutions of the Krypton calorimeter are extremely good (0.1 mm and 1.5 mrad for a 10 GeV electron or photon), whereas the corresponding spatial resolution of the scintillating glass is 2 mm, and its directional resolution is very poor. The Krypton (with 5% Xenon) scintillation is fast (20 ns), compared to the scintillating glass (87 ns), and with a 100 times larger photon yield (i.e. $3 \cdot 10^4$ compared to $3 \cdot 10^2$ $MeV^{-1}$). Since the overall costs of the two calorimeters would be similar, the improved resolution of Krypton is preferable if the cryostat does not seriously deteriorate its performance.

If the EM calorimeter were made of scintillating glass, the blocks would have area $5 \times 5$ $cm^2$, transverse to the beams. The number of blocks in Spectrometers 1 and 2 totals ≈8700. The phototube pulse heights would be digitized to 12 bits to allow for the large dynamic range in electron and photon energies.

If Krypton were used, the calorimeter would have towers with transverse size $3 \times 3$ $cm^2$ with 12 ionization samples (in depth). A photodiode placed at the end of each tower detects the fast scintillation light and could be used in the trigger. The ionization is detected in the drift cells with maximum drift time of 750 ns. The fast scintillation gives excellent energy resolution ($\sigma_E < 1\%\sqrt{E}$) while the ionization signal (detected by drift) gives precise determination of the direction and position (≈1 mrad and ≈0.1 mm for a 10 GeV electron or photon, respectively).

## *6. TRIGGER PROCESSORS & DETECTOR READOUT*

The demands made on the readout system and trigger processor by the proposed experiment are particularly severe. The lack of an effective fast trigger criterion that can be calculated in less than the time between interactions means that, for each interaction, all detector information must be read out and stored in a pipeline until the Level-1 trigger decision is taken. Moreover, in order to minimize the number of events which must be stored, the estimated $10^4$ instructions per event needed for the Level-1 trigger algorithm described in Chapter 4 must be made in the shortest possible time, say 15 μsec. An additional requirement is that the fewest number of processors should be used, in order to minimize the complexity of the channel used to distribute the data from the detectors to the processors. We note that the total required computing power of the Level-1 trigger processor is given by the $10^4$ instructions per event, times the interaction rate of 600 KHz, or 6000 MIPS (million instructions per second).

---

[17] J. Seguinot et. al., CERN/DRDC/90-70,DRDC/P17;

[18] U. Buchner et. al., NIM A272(1988)695.

[19] J. Spengler MPI-H-1990-V6

The Level-1 algorithm discussed in Chapter 4 and also in APPENDIX A will be implemented using a processor with Data-Flow architecture with the processing elements imbedded in the data readout channel. The algorithm is precisely defined and amenable to implementation in hardware. Speed is of the utmost importance because it also translates directly into decreased costs for the buffer system used for the spectrometer detector information.

Five years ago, the UCLA group had a very successful experience building and using a Data-Driven processor[20] with 240 MIPS capability. This device, which was built for a Level-1 trigger for experiment UA8 at the CERN Sp$\bar{p}$S-Collider, illustrates the power of such architectures. This processor used 40 modules of two types to calculate the momentum and intercept position of fast protons traversing the UA8 roman pot spectrometers. The TDC readout, calculation and the final trigger decision were made in 1.4 $\mu$sec, of which only $\approx$450 nsec was used for the actual calculation.

The Data-Driven processor designed and built by the Nevis-Univ. Mass. group[21] for Fermilab experiment E690 is a much more powerful system and could provide our necessary online computing power this year. Thus, we have undertaken an R&D project to build and interface a version of their processor to our silicon system and test it in a beam in 1991. It is extremely cost-effective compared to, for example, a RISC processor farm of similar power. The processor configuration for our application is about one-third the size (in number of modules) of the configuration in use by E690 and should be relatively straight forward to build.

For the proposed experiment, we plan to update the technology we will actually use, to include such things as optical fiber data transmission, application specific integrated circuits (ASIC's), Digital signal processors (DSP), etc. Improvements in speed, flexibility and reliability will be sought.

Both the readout system and the Level-1 trigger processor are pipelined. Data read from the spectrometer detectors are transferred to FIFO memories in a very high speed data transport system, while the silicon vertex detector data enter the first stage of the data-driven processor described in Section 6.2. Data entering the first stage of the processor are quickly processed and sent on to the following processor segment. This frees the starting set of processor modules for the subsequent event. The results of the trigger calculation are used to direct the transfer of data through the transport system. Events emerging from the transport destination modules are sent to a VME or Fastbus-based data acquisition system for further Level-2 processing in a system of RISC processors, as well as data monitoring and recording.

## *6.1 Detector Readout System*

All detectors in the apparatus will be gated at every bunch crossing for which the readout is idle. The readout is started only if a Level-0 interaction trigger is present. Once initiated, the digitization and readout of the detector information will take two or more bunch crossings depending on the number and distribution of hits in the event. The minimum readout time is limited by the 1 $\mu$s drift time of the jet chambers. Data read from the spectrometer detectors are entered into digital pipelines (FIFO buffers) for storage until the trigger processor has completed its calculation. The data for accepted events are then passed on to the Level 2 processor farm.

Table 8 shows the numbers of detector elements, the average number of elements with hits, and the expected data lengths for each of the subdetectors in a single arm apparatus. In addition to the expected signal data length (35 Kbytes), we assume a 1% average noise rate with an average 4 bytes/hit. This yields a total average data length of 60 Kbytes/event.

---

[20] J.G. Zweizig et al.(UA8 Collaboration); Nucl. Instruments & Methods A263 (1988)188.

[21] W. Sippach et al., IEEE Trans. Nucl. Sci., 27 (1980) 578;
E.P. Hartouni et al., IEEE Trans. Nucl. Sci., 36 (1989) 1480;
B.C. Knapp, Proceedings of 4th Pisa Meeting on Advanced Detectors (1989), Nucl. Instr. & Meth. (in press - 1989)

*Table 8: Data Lengths by Detector*

| Detector | No. Elements | Hit Elements | Data Length(bytes) |
|---|---|---|---|
| Silicon | 115200 | 1000 | 4000 |
| Si Pixel | 4500 | 35 | 140 |
| Pixel DC 1 | 4480 | 18 | 72 |
| Jet Cham 1 | 7000 | 1000 | 4000 |
| Jet Cham 2 | 9600 | 1000 | 4000 |
| RICH 1 | 100000 | 1250 | 5000 |
| EM Cal 1 | 35000 | 540 | 2160 |
| Pixel DC 2 | 11040 | 15 | 60 |
| Jet Cham 3 | 5700 | 1300 | 5200 |
| Jet Cham 4 | 7100 | 1300 | 5200 |
| RICH 2 | 280000 | 1000 | 4000 |
| EM Cal 2 | 36000 | 420 | 1680 |
| Total | 615620 | | 35412 |

Emphasis is being placed on implementing a greater than usual concentration of intelligence near the front end through the use of integrated VLSI readout electronics. This will result in better compaction of the detector data and hence higher live times. As discussed in the following paragraphs, the development of VLSI readout electronics for the RICH and Silicon is already well underway.

**Silicon:** The silicon detectors will be read out using a high density (128 channels per IC) VLSI chip which employs sparse data scanning to minimize the number of cycles needed to read the data. The Berkeley SVX chip, which was developed for the CDF silicon-strip vertex detector, would be well suited to this application, but the current version may not be fast enough. However, the success of the present SVX and other chips gives us confidence that an IC which will meet our needs can be built within the time scale of this experiment.

We are presently designing a gate sequencing and readout control system for the silicon-processor interface, which we plan to test at CERN this year. In this system, the readout electronics is divided into three types of modules. A ReadOut Sequencer Module (ROSM) generates the signals necessary to gate the silicon readout chip (i.e. the SVX), and transfer the encoded hit data. Hit data is sent via a ReadOut Control Module (ROCM) associated with each set of 4 SVX daisy-chains (x and y of left and right detectors for a single half plane) to a ReadOut Link Module (ROLM) which interfaces with the Level 1 processor system. The data are then used by the processor system, and passed on for recording if the event is accepted.

**Chambers:** The chamber-hit times will be encoded and recorded using a 8-bit, 10 nsec bin, multiple hit TDC system. In this system, each sense wire signal is tested every 10 nsec starting from the bunch crossing (gate) signal. If a signal appears on a wire, the arrival time is saved in one of two 4 word × 8-bit 100 MHz FILO stacks. The encoding process will require 1$\mu$s (the maximum drift time) during which additional gates will be inhibited. This will result in a dead time of $\approx$20%. If no Level-0 signal arrives, a reset is generated and the chamber readout is aborted with no loss of live time. At the end of the readout cycle, the second FILO is enabled for readout of the next event, while data are transferred from the first set to FIFO buffers. Hit data from each chamber is transferred to the FIFOs over 20-32 parallel data streams arranged so that each stream receives approximately the same amount of data.

It would be desirable to incorporate some intelligence into the drift chamber readout electronics which would perform line-segment finding within the drift cells. This would reduce the amount of data transferred to, and saved in the FIFOs, and facilitate track reconstruction in the second level filter. This possibility is under investigation.

**RICH:** Cherenkov photons will be detected on pad detectors which are segmented into 27 groups of 64 row × 128 columns for the purposes of readout. The pad signals will be amplified and shaped by a 16-channel VLSI chip currently under development. The discriminated signals produced by these chips are latched into a 50 MHz shift register. Data readout proceeds by shifting out the hits a row at a time into a 128-bit row latch. Words which contain at least one set bit are latched in a second word from which the hit coordinates are encoded. The row number is given by counting the number of rows which have been shifted out, and the column number is determined by priority encoding. One hit is recorded and erased from the encoding register every 20 nsec until it is empty. Shifting of rows continues in parallel to the hit encoding unless a second non-zero row is found while encoding of a previous row is still in progress. One or more additional row buffers may be added to decrease the likelihood of stopping the row shifting process.

**Pixel Detectors:** The Pixel Drift Chambers will be read out with the same type of modules used for the tracking chambers. The silicon pixel detector will be read out with the same electronics used for the silicon vertex detector.

**Electromagnetic Calorimetry** The Electromagnetic Calorimetry will be read out by 64-channel 10-bit FADC modules. Each module will have 64 charge integrators with two FADCs for digitizing the latched analog signals and circuitry for suppression of empty channels.

**Data Transport System:** The data transport system is a crate-oriented, 200 Mbyte/sec synchronous backplane through which all accepted events are passed. The extremely high throughput of this system allows the transfer of all accepted event data over a single channel, facilitating the dispersal of event data to acquisition, monitor, and high level processors. Modules connected to a backplane can be either data sources or data sinks. Each source module in turn transfers all the data for one event in a broadcast mode. Any sink modules which are enabled may save the same event simultaneously. Multiple transport crates can be linked together in a tree structure for merging data from an arbitrary number of input sources or fanning out the data to an arbitrary number of destinations. A minimal programability will make it possible to configure the destination modules to select a subset of events.

## *6.2 Level-1 Trigger Processor*

Briefly, the properties of the Nevis-Univ. Mass Data-Driven processor are:

- **No centralized control:** There is no CPU in the system. The processor consists of an array of function modules, in which the arrival of data at a module initiates its operation.

- **Parallel:** Several data streams are processed in parallel. In our case, track finding in the silicon detectors is done in parallel in 8 identical processors (4 quadrants × 2 views). Other parallelism can be intrinsic to a processor structure.

- **Pipelined:** Several events are in the processor simultaneously. For example, with an interaction rate of 600 KHz and an event processing time of about 15 $\mu$s, about 10 events would be in the pipeline at a time.

- **Synchronous:** All registers in the system are latched simultaneously by a 40 MHz central clock.

- **Expandable:** The processor may be increased to solve an arbitrarily complex problem by the addition of more modules. Since there are no resources like central memory or common I/O paths, bottlenecks do not appear. Also, because there is very little overhead, an increase in the number of processor modules yields a proportional increase in processor speed. This will be a very valuable attribute in the future, when there will be a need to upgrade the data acquisition system to handle the higher luminosities which will be available at the new proton-proton colliders.

The processor modules are themselves quite simple. Each module takes one or two 24 bit (16 data + 8 control) input data words, performs some simple operation on them and produces an output which is passed on to the next module. All modules in the system are clocked synchronously and the input and output data words are latched into registers on each clock cycle. Care has been taken to provide access to all of the input and output registers in the system, either for reading data or inserting data. This greatly simplifies the task of debugging and diagnosing problems, since the state of the system can be determined and checked on a cycle by cycle basis.

Fig. 20 is a block diagram of the processor. There are five subroutines shown, which are isolated from each other by control buffers. The 3-plane line-finder, discussed below, contains most of the hardware, with 8 identical sections (corresponding to 4 quadrants × 2 views). Each of the 8 line-finders utilizes about 20 existing modules, for a total of 160 modules.

**Line-Finder**

Of the subroutines listed above, the track finding step is the most complex, and provides the greatest challenge for optimal design and construction. Fig. 21 shows a diagram of this subroutine,[22] which uses the processor modules in a configuration similar to that used by FNAL experiment E690. Depending on the required throughput, the line-finding may be performed by a single set of modules which would process each detector triplet in succession, or by many similar sets, each of which would perform the line-finding in one or a few plane triplets. With multiple independent line-finders, the effective throughput is increased by the same factor as the number of line-finders.

The following is a somewhat simplified description of the operation of the line-finding subroutine illustrated in Fig. 21. Hit strip addresses enter on the readout bus. Data from different detectors in the same quadrant appear on the same bus, and are distinguished by a 4-bit identification field (Tag). The **Buffer** modules (Labeled B in Fig. 21) select the hits from a single detector, and store them in a First-In-First-Out (FIFO) memory for eventual retransmission into the remainder of the subroutine. The hits from the first and third planes of a detector triplet are then associated into clusters by the **Associator** (A) modules and entered into lists in the **List** (L) modules. In addition, as cluster positions are entered into the lists, they are counted by the **Index Generator** (I) module. The **Index Generator** starts immediately to generate all pairs of indices of clusters in the lists. Each generated index pair causes the two **List** modules to output the cluster positions specified by those indices. The positions are then multiplied by a constant in the **Normalizer** (N) module and added together (⊕ module) resulting in a prediction of a hit position in the second plane of the triplet. If there is a hit in the second plane corresponding to the value thus predicted, it is taken to indicate the existence of a track, and the hits which define the track are added to a track list. This last function is performed by a **Map** (M) module which saves the hits from the second plane in an internal bit map. It then uses the incoming hit predictions to fetch the hits in the region of the prediction. The **Table** (T) module which follows the **Map** determines whether the neighboring hits meet the track acceptance criteria by table lookup. The hits from the first and third planes associated with the accepted lines are added to the list by the **List Counter** (Lc) modules. The resulting list of hits on tracks is then entered into buffers for use by the subsequent stages of the processor.

---

[22] We thank Bruce Knapp for his design of this hardware "subroutine"

FERMILAB-Proposal-845

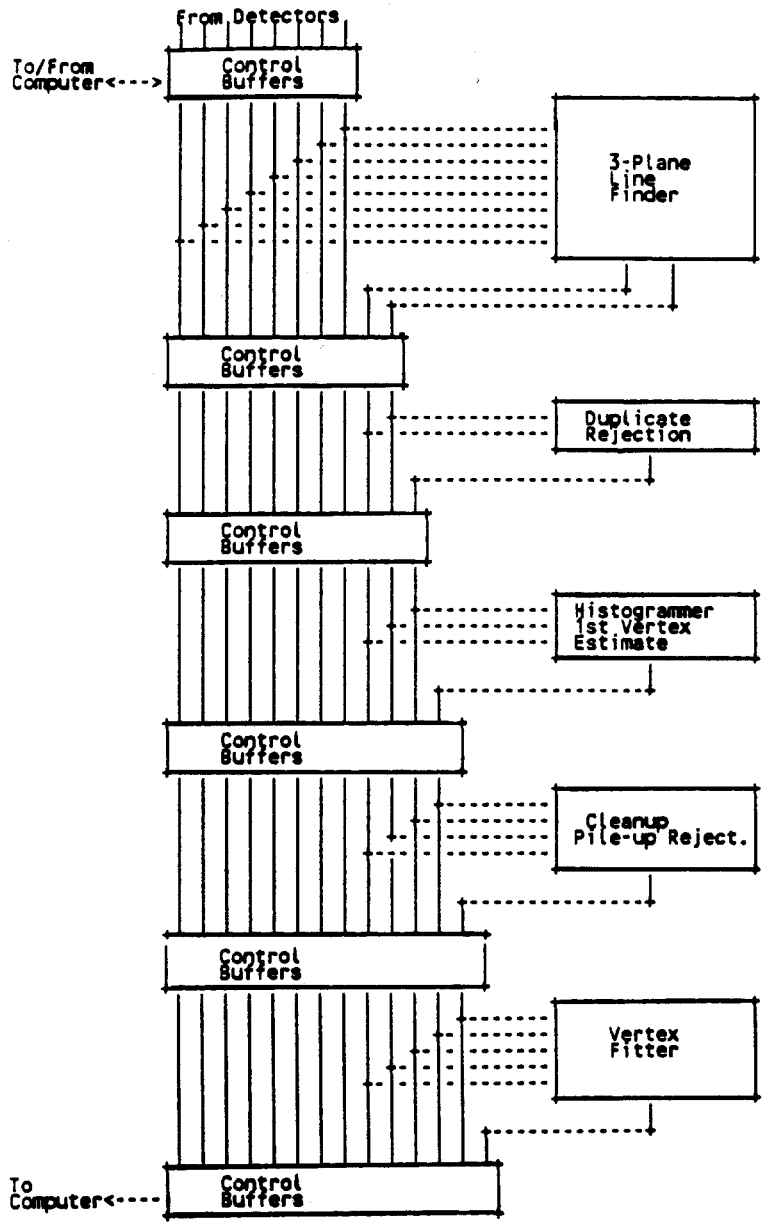


*Figure 20: Block Diagram:* Level-1 Trigger Processor with Data-Flow Architecture

The final translation of the algorithm described above into a hardware configuration will be made using emulation and analysis of the processor's response to the silicon data have obtained in our P238 Sp$\bar{p}$S-Collider test run. Preliminary design work indicates that we will need fewer than 100 additional modules for the remainder of the system, for a total of about 250 modules (compared to about 700 modules for the E690 processor). Almost all module types already exist and are in use by the E690 Collaboration. The remaining 1-2 modules are simple extensions of the existing architecture.

**Processor Emulator**

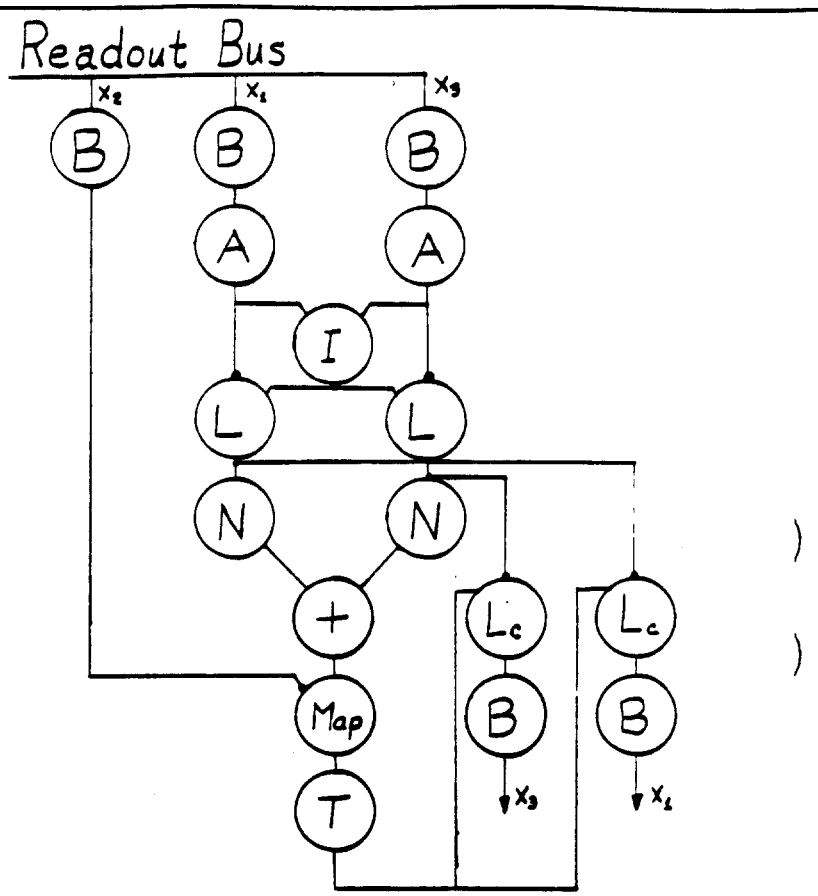


*Figure 21: Block diagram of the Data-Driven Line-Finder.*

The operation of the entire processor structure is being emulated in software. The processor emulator is a package designed to duplicate in software the action of the processor on a cycle by cycle basis. A FORTRAN subroutine is written for each type of module, of which there are about 20. One subroutine call corresponds to one clock cycle.

A processor algorithm consists of a list of boards, the specification of the contents of any memory elements on those boards and the specification of how these boards are cabled together. Such a list is known as a **Configuration File.** The emulator reads this file in its initialization phase and thus determines which board subroutines are to be called. It calls these subroutines, which in turn reserve enough memory to hold any tables which must be down-loaded as well as memory locations for the input and output registers. Storage is also reserved to hold cable contents and pointers are set up to the memory locations which hold the contents of the input and output cables. After this initialization phase, the memory locations, reserved to hold on-board tables, are loaded by simulating the cycles that would be executed by the processor hardware in performing this function.

After the initialization phase, the emulator is ready to process data. Data is loaded into the locations which correspond to the input cables and the board subroutines are called as specified in the **Configuration File.** Each board subroutine checks for data on the input cables and, if present, performs its operations and modifies the memory locations which correspond to its on-board registers and out-

put (and possibly input) cables. This procedure precisely emulates the processing performed in one clock cycle. The process is repeated for subsequent cycles until the data (and control "signals") propagate through the entire "processor" and appear in those locations which correspond to the processed data cables and the output control buffers.

Using the emulator, it is possible to precisely predict the operation of a given algorithm on any set of simulated event data. For example, the average number of clock cycles per event can be easily determined, problems of precision can be investigated and bottlenecks in the algorithm calculations can be located.

The emulator can be used not only for the design and evaluation of processor configurations, but also can serve as a powerful diagnostic tool when the same data is given to both the emulator and the hardware processor and the results of the computation compared. The operation of a single board can thus be evaluated, as can the operation of an entire subroutine.

### *6.3 Level-2 Trigger Processor*

A second level of filtering for all events which pass Level-1 will be implemented as a farm of high-speed (50 MHz or greater) RISC processors which would have access to all the data for a given event. These processors may perform some or all of the following functions:

- Perform complete track reconstruction,
- Eliminate most pileup events by requiring that the total longitudinal momentum of all tracks in either the forward or backward hemisphere does not exceed the beam momentum (as required by conservation of momentum and energy), and that there is at most one vertex with tracks in both the forward and backward hemispheres.
- Repeat the Level-1 test with matched views, and correct weighting based on the track momenta.
- Determine the event topology.

To determine the size of the RISC farm necessary to perform these functions we assume that the average event will require $5\times 10^6$ RISC instructions.[23] To handle the 6.7 KHz rate we estimate that we will need a "farm" with about 670 × 50MIPS RISC processors. Clearly, should faster processors become available, this number can be reduced.

## *7. FLAVOR TAGGING: LEPTONS VS. KAONS*

To avoid the very large event loss which arises from requiring full reconstruction of both B and $\bar{B}$ in the spectrometer, we advocate just using as tags, supplementary particles in the spectrometer which are inconsistent with coming from the primary vertex (as determined using the vertex detector information). As discussed in the following paragraphs, these can be either charged kaons or leptons. In order to understand the tagging possibilities of $K^{\pm}$ and leptons, an analysis was made of Monte-Carlo generated $B\bar{B}$ events using PYTHIA. In the event generation, no requirements are made on the hadronization or decay of the associated b-quark which provided the potential tag. Of course, these esti-

[23] Note that the $5\times 10^6$ instructions is an average figure, some events will take considerably more or less than this mean. Note also that some of the reconstruction tasks will have already been performed by the Level 1 processor (e.g. line finding in the silicon) and readout system.

mates depend greatly on the correctness of PYTHIA's hadronization scheme, which could be verified by measurements at existing hadron colliders.

For a $B_s$-Mixing experiment, charged kaons from the primary vertex can also be used, because their flavor is potentially correlated with the flavor of a reconstructed $B_s$-Meson. Such kaons have an advantage over those from secondary sources, in that there are no oscillation effects of the tag-providing system

**The Use of Muon Tags:** For events in which a Beauty meson is detected in a 600 mrad spectrometer at the Tevatron Collider, what are the momenta and angles in the laboratory of an accompanying muon ? This question is answered in Fig. 22, which is a scatter plot of $p_\mu$ vs. $\theta_\mu$ in the laboratory, for Tevatron events which contain both a B accepted in the 600 mrad spectrometer and a muon from any source with momentum transfer, $p_t > 1.2$ GeV. The correlation which is expected between a B and a $\mu$ from its partner $\bar{B}$ is clearly visible. Most muons are in the same hemisphere as the B detected near 0° and correlated within ~1 unit of rapidity. Furthermore, the muons within the spectrometer aperture of 34.9° (600 mrad) are seen to have much larger momenta than those outside the spectrometer. We can conclude that, for Beauty particles detected in the 600 mrad spectrometer, there is not much to be gained by constructing additional lepton detection outside the 600 mrad aperture.

At $\sqrt{s} = 1.6$ TeV, we find that 5.7% of B-Mesons which are accepted in the spectrometer have an accompanying $\mu^\pm$ also in the spectrometer with $p_t > 1.2$ GeV (necessary to suppress muons from the $c \to s$ transition). The tag quality factor, (good tags/all tags), is found to be 73%. The quality factor can be improved by selecting larger $p_t$, but with a loss of muons. If electron tag are also used, the fraction of tagged events could increase to an upper limit of 11.4%. However, additional losses arise from cuts needed to minimize the background from other sources. We have not attempted to estimate these losses since, as discussed in the next section, the use of $K^\pm$ tags is more promising.

**The Use of Secondary $K^\pm$ Tags:** The overall strategy is to examine supplementary kaons in the spectrometer (those not associated with the reconstructed B). There are two major sources of such kaons. They either come from the accompanying $\bar{B}$ meson or they come from the primary vertex. Those from the primary vertex are only useful for tagging reconstructed $B_s$-Mesons and we return to them below.

A $K^\pm$ which contains the s-quark at the end of the $b \to c \to s$ chain uniquely identifies the flavor of its $\bar{B}$-meson at decay. However, there are many sources of mis-tagging, such as kaons which are produced from the $s\bar{s}$ sea or from a $W^\pm$ in either the $b \to c$ or $c \to s$ transitions (which can have either sign). All these possibilities are accounted for to some approximation in the PYTHIA event generation and can be investigated by tabulating the supplementary kaons which are found in the spectrometer. For Tevatron events with $\sqrt{s} = 1.6$ TeV, 25.5% of the B-mesons in the spectrometer are found to have a supplementary $K^\pm$ with reconstructed impact parameter greater than $3\sigma$ from the primary vertex. The correct charge was found in 82.2% of these tags (good tags/all tags). Thus, secondary $K^\pm$, $\mu^\pm$ and $e^\pm$ together can tag as much as 35% of all Beauty particles reconstructed in the spectrometer.

**The Use of Primary $K^\pm$ Tags in $B_s$-Mixing Measurement:** A primary $K^+$ or $K^-$ potentially contains the $\bar{s}$ or s quark which is created in association with the s or $\bar{s}$ quark used in a reconstructed $B_s$ or $\bar{B}_s$, respectively. They should be produced nearby in rapidity. Note that the sign of such a primary $K^\pm$ has exactly the opposite tagging significance as does a secondary $K^\pm$.

Background comes from kaons produced from the $s\bar{s}$ sea in the numerous hadronization processes at the primary vertex which are not associated with the $B_s$ or $\bar{B}_s$ mesons. Such kaons can be of either flavor and thus dilute the kaon tagging. We have performed a complete detailed analysis of Monte-Carlo $B_s$ events at the lower energy $Sp\bar{p}S$-Collider and find that the primary kaons are just as effective in flavor tagging reconstructed $B_s$ mesons as are secondary kaons. 26% were tagged by secondary $K^\pm$. An additional 26% were tagged by primary $K^\pm$ and a further 7% were tagged by both types of $K^\pm$. Thus, a total of 58% of all reconstructed $B_s$ were tagged in this way. The tagging quality of these events ranged from 70-76%.

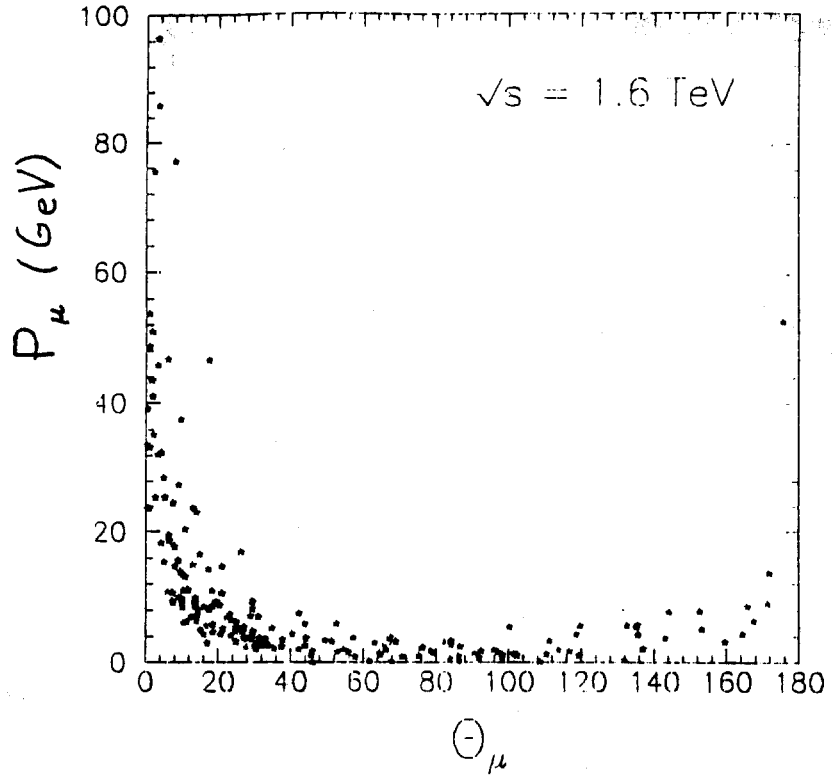


*Figure 22: Laboratory Momentum vs. Angle of* Muons Accompanying an Accepted B at the Tevatron. The detected B is on the 0° side. The muons have $p_t > 1.2$ GeV.

We are presently repeating this analysis for $B_s$ events at the Tevatron and expect that some additional contribution will indeed be offered by primary kaon tagging. However, it may be a somewhat smaller amount at the Tevatron energy because of enhanced kaon production from the $s\bar{s}$ sea.

**Dilution Effects:** There are two types of dilution (decrease in statistical effectiveness) due to mis-tagging. One arises simply from using a tagging particle (kaon or lepton) which has the wrong sign because its source is extraneous. The other arises from the fact that the B (or $\bar{B}$) which provides the tagging particle may itself oscillate and thereby give the wrong sign tag. The estimates of mis-tagging given in the previous paragraphs are obtained with the use of a Monte-Carlo generator which does not have B-oscillation built into it. Thus the estimates are of the first type of mis-tagging. As pointed out in Chapter 2, the relevant factor is not the "tag quality", but rather the quantity, $k_1$ = (good tag − bad tag)/(good + bad). For example, a "tag quality" of 0.8 yields for this dilution factor: $k_1 = 0.60$.

To estimate the dilution factor, $k_2$, from the second type of mis-tagging due to the oscillation of the tag-providing B (or $\bar{B}$), we must use the time averaged probabilities for oscillation and non-oscillation: $x^2/[2(1+x^2)]$ and $(2+x^2)/[2(1+x^2)]$, respectively. Here $x \equiv \Delta M/\Gamma$ for the source B. Because the expected decay time dependences of the tagged-B (or $\bar{B}$) are of the general form $1 \pm a(t)$, it is explicitly shown in Chapter 2 on $B_s$-Mixing that the dilution factor multiplies the a(t) term and is given by the weighted average of the quantity $1/(1+x^2)$ over the three types of tag-producing B's according to their relative production frequency.[24] A weighted average, of $[1/(1+x^2)]$ over $B_u$ (40%), $B_d$ (40%) and $B_s$ (20%) is found to be: $k_2 \approx 0.67$, if we assume x to be 0, 0.7 and 15, respectively, for

[24] P. Krawczyk, D. London & H. Steger, DESY-163 (Nov. 1988).

the 3 cases. Thus, the net dilution factor can typically be expected to be: $K = k_1 \cdot k_2 \approx 0.40$.

## 8. RECONSTRUCTION OF B-EVENTS, YIELDS & BACKGROUNDS

### 8.1 General Considerations and Lifetime Measurements

We present here a study of the problems of B event reconstruction and sources of combinatoric background which was done for a c.m. energy, $\sqrt{s} = 0.63$ TeV, where the mean momentum of reconstructed B-mesons is 35 GeV. Since this momentum is expected to be about 45 GeV at the Tevatron, and since there is not much increase in track multiplicity through the silicon detectors, the conclusions should also be valid for the Tevatron.

Software was written to reconstruct Monte Carlo Beauty events which were generated using PYTHIA. In addition to minimum bias and charm events, two types of Beauty Monte Carlo event samples were studied: (a) a general or inclusive $B\bar{B}$ sample, in which B-mesons decay according to the "natural" B decay modes given by PYTHIA, and: (b) events in which all B's decay via the particular mode under study. In both cases, PYTHIA generated an underlying event, similar in structure to a minimum bias event, in addition to the decay tracks from the B and $\bar{B}$ states. Unit vectors describing track direction and position were obtained from a full silicon detector simulation using the program GEANT. Momentum measurement errors were simulated by randomly varying the generated Monte Carlo momentum, in accordance with expected spectrometer resolutions. We assumed that x/y view matching as well as track matching between the spectrometer and silicon detector could be done without significant error.

For the exclusive decay mode samples, events whose B-meson decay products are completely contained in the spectrometer aperture are passed through the trigger algorithm simulation software. Surviving events are used to evaluate the reconstruction efficiency. Minimum bias and inclusive $B\bar{B}$ events are passed through the same software chain used for the exclusive final state in order to determine the combinatoric background level.

Studies were also made of the response of our trigger algorithm and Beauty reconstruction software to inclusive $c\bar{c}$ (charm) states. We found that the topological information in the silicon detectors, together with the larger energy release in Beauty decay, allowed us to reject background from $c\bar{c}$ states to a negligable level.

On the question of final states with a single $\pi^0$, we have not yet been able to demonstrate that acceptable signals with low-background can be extracted from the data. On the other hand, final states with a single $\gamma$, such as Reaction (20) discussed in Section 8.2, can be cleanly extracted. This should also be the case for $D^{0*} \to D^0\gamma$, as has been mentioned above. In general, we find that if an e.m. calorimeter with the superb resolution of $\sigma = 0.5\% \cdot \sqrt{E}$ is assumed, the invariant mass resolution for the B is comparable to that obtained for final states with all charged particles. See the discussion in Section 8.2.

Reconstruction software for exclusive final states proceeds in the following way. A vertex-finding algorithm which consists of the repeated application of a vertex search among tracks that do not come from previously found vertices is applied. After vertex finding each individual decay mode is reconstructed using separate subroutines. In all of these subroutines, relevant invariant masses are calculated for all possible track combinations consistent with the desired topology. Also, for most decay modes, a minimum flight path of 0.5 mm is required for the B-meson, making it possible to impose transverse momentum balance with respect to the B direction of motion. This is found to greatly suppress combinatoric background under the B signal.

We present details of the analyses of some exclusive final states in the succeeding sections. The general conclusions of these analyses are that clean signals can be found and that the chief sources of

combinatoric background to B-meson signals are: (a) those $B\bar{B}$ events which have similar topologies but which decay via modes other than the one under study; or (b) from the same mode, but where one or more tracks can not be uniquely assigned to the B decay vertex. In a sample of 4000 minimum bias events, no events survived Level-1 trigger cuts and produced a secondary vertex other than from strange particle decay. Thus we conclude that background from minimum bias is less than a third the background from events which contain Beauty.

**Analysis of:** $B^0 \rightarrow \bar{D}^0\pi^+\pi^- \rightarrow (K^+\pi^-\pi^-\pi^+)\pi^+\pi^-$

We start by calculating the invariant mass for each $K^+\pi^-\pi^-\pi^+$ track combination which is consistent with having a common vertex. For combinations with a mass near to that of the $\bar{D}^0$, we loop over the remaining $\pi^+\pi^-$ pairs which have a common vertex at least 0.5 mm downstream of the primary vertex but no further downstream than the $\bar{D}^0$ vertex. Finally, we reconstruct the momentum vectors of the $B^0$ and $\bar{D}^0$ requiring that the $\bar{D}^0$ momentum vector be collinear with the line connecting the $B^0$ and $\bar{D}^0$ vertices and that the $B^0$ momentum vector be collinear with the line connecting the $B^0$ vertex with the primary vertex. For these events, the $\bar{D}^0\pi^+\pi^-$ invariant mass is calculated.

Fig. 23 shows the $K^+\pi^-\pi^-\pi^+$ and $\bar{D}^0\pi^+\pi^-$ invariant mass spectra. In both Figs. 23(a,b), the unshaded histograms show all possible track combinations with no cuts on vertex topology. The shaded histograms show the effects of imposing the vertex topology and momentum conservation cuts referred to in the preceding paragraph.

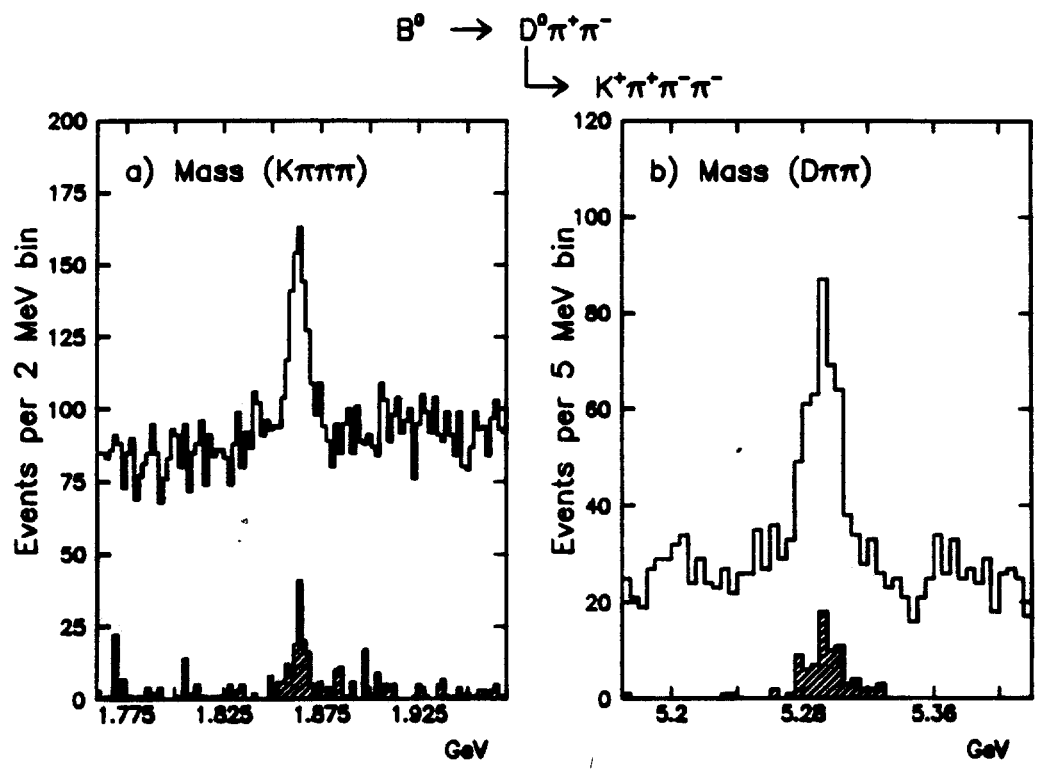


*Figure 23: Invariant Mass Spectra for the Final State* $\bar{D}^0\pi^+\pi^-$. (a) $\bar{D}^0$ signal in $K^+\pi^-\pi^-\pi^+$ spectrum; (b) $B^0$ signal in $\bar{D}^0\pi^+\pi^-$ spectrum, both with no vertex cuts. The shaded areas in each plot show the signals which remain after applying the vertex cuts discussed in the text.

This figure does not reflect the true background level since it contains only the combinatoric background from events containing $B^0$ mesons decaying according to the reaction $\bar{D}^0\pi^+\pi^-$. When background generated from all other sources is included, the B-signal/background ratio is estimated to be larger than 5/1.

**Analysis of:** $B^0 \rightarrow D^{*-}\pi^+\pi^+\pi^- \rightarrow ((K^+\pi^-\pi^-\pi^+)\pi^-)\pi^+\pi^+\pi^-$

We start by calculating the invariant mass of all $K^+\pi^-\pi^-\pi^+$ combinations which are consistent with a common vertex. For each such combination which has a mass near to the $\bar{D}^0$ mass, we calculate the $\pi^-K^+\pi^-\pi^-\pi^+$ invariant mass using all remaining $\pi^-$ tracks in the spectrometer. Fig 24(a) shows the distribution of the mass difference between these two combinations. The peak is quite clean. For combinations which are consistent with being from the decay of a $D^{*-}$, we calculate $(\pi^-K^+\pi^-\pi^-\pi^+)\pi^+\pi^+\pi^-$ invariant mass. We demand that the $D^{*-}/D^0$ mass difference be small, and use the momentum conservation cut described above and somewhat less stringent cuts on event topology. The $(D^{*-}) - (\bar{D}^0)$ mass constraint is sufficiently powerful that a reconstruction efficiency of more than 40% can be obtained. The resulting mass distribution is shown in Fig. 24(b). For this mode, we find that little background is contributed by events with B's decaying inclusively, thus the figure represents the true background level.

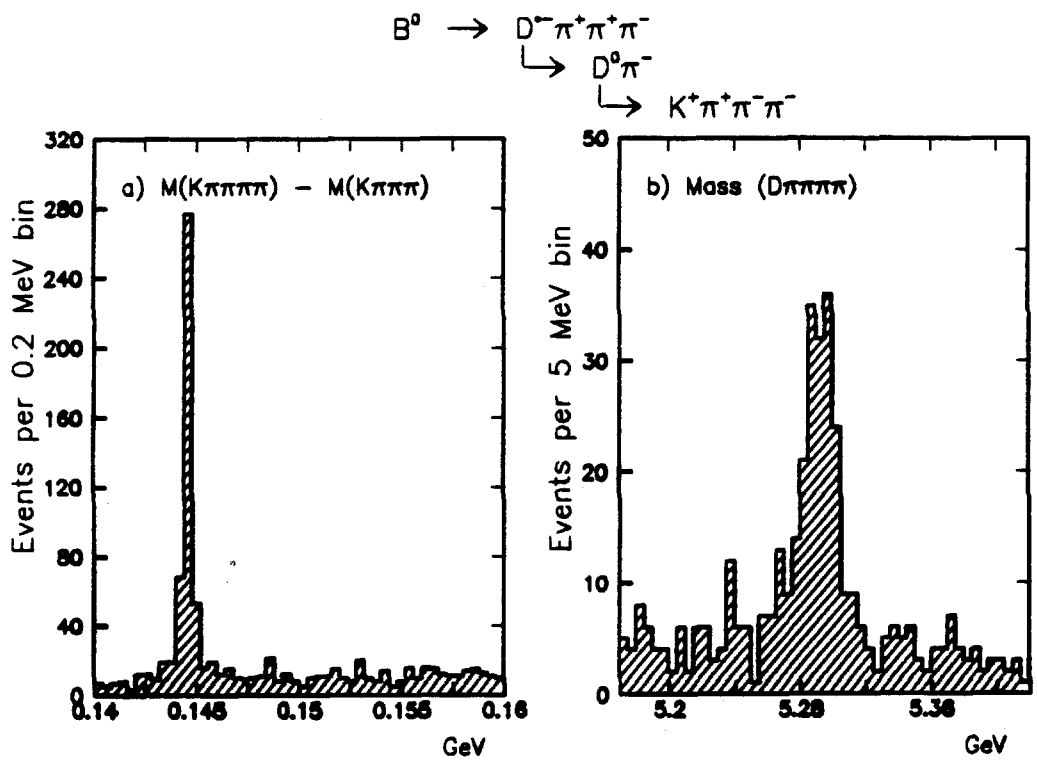


*Figure 24:* (a) The distribution of the difference in invariant mass between $K^+\pi^-\pi^-\pi^+$ and $\pi^-(K^+\pi^-\pi^-\pi^+)$ combinations as explained in the text. (b) The $B^0$ signal in the $(\pi^-K^+\pi^-\pi^-\pi^+)\pi^+\pi^+\pi^-$ mass spectrum when $\pi^-(K^+\pi^-\pi^-\pi^+)$ satisfies the $\bar{D}^{*-}$ mass constraint, $K^+\pi^-\pi^-\pi^+$ satisfies the $\bar{D}^0$ mass constraint and after topology and momentum conservation cuts have been applied.

**Analysis of $B^0 \rightarrow J/\psi^0 K^0 \rightarrow (e^+e^-)(\pi^+\pi^-)$**

The analysis proceeds by forming the invariant mass for all $e^+e^-$ pairs. The resulting mass plot is shown in Fig. 25(a). Next, the invariant mass for all $\pi^+\pi^-$ combinations is calculated and $K^0$ candidates defined by requiring that this mass be near the $K^0$ mass. We then calculate the invariant mass for all $J/\psi^0$ candidates (defined only by a mass cut) with all $K^0$ candidates. The resulting mass plot (with no vertex cuts) is shown in Fig. 25(b).

The $J/\psi^0$ cut alone suppresses virtually all background from $B^0$ decays. Background from direct $J/\psi^0$ production has not been studied but a combination of topology and transverse momentum cuts should reduce it to manageable levels with some sacrifice of signal.

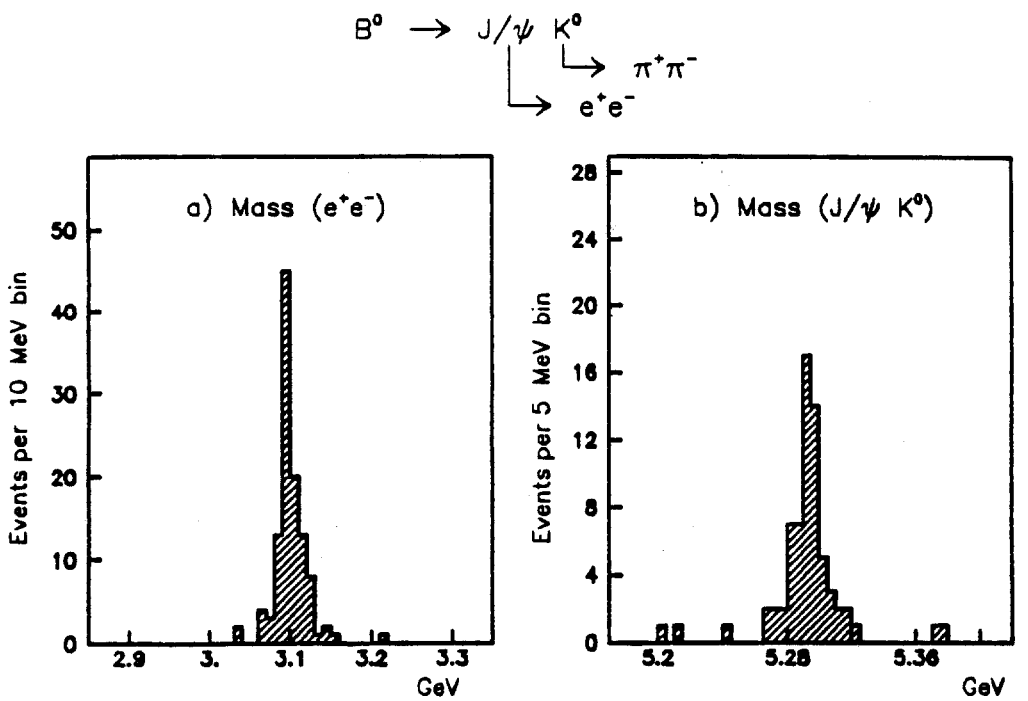


*Figure 25: Invariant Mass Spectra for the Final State $J/\psi\ K^0$.* (a) $J/\psi$ signal in $e^+e^-$ spectrum; (b)$B^0$ signal in $J/\psi\ K^0$ spectrum, both with no vertex cuts.

**Lifetime Measurements**

The mean reconstructed B-meson momentum of about 45 GeV/c (see Fig. 9 in Chapter 3) and the mean distance of 2 cm between event vertices and first silicon detector plane allow rather good measurements of proper flight time for each event.

Fig. 26 displays the simulated proper time distribution (in units of B mean life) expected for a 9000 event sample.

It is seen in Fig. 26 that we have excellent acceptance in t above about one mean life. The departure from a pure exponential in Fig. 26 illustrates the combined effect of the geometrical acceptance

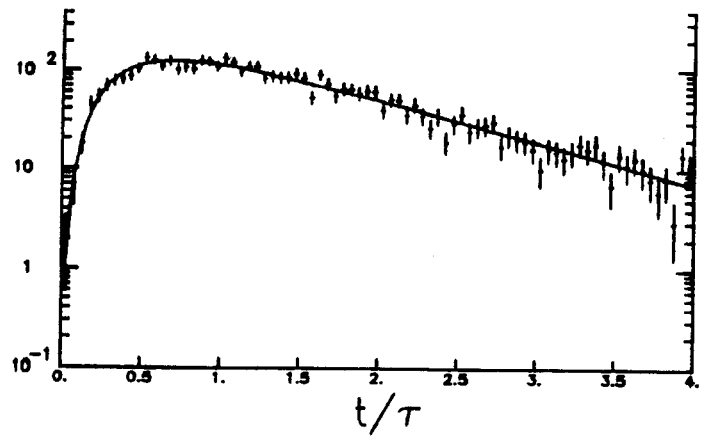


*Figure 26:* Simulated proper time distribution (in units of B mean life) for 9000 reconstructed $B_s$ events. The departure from a pure exponential illustrates the acceptance effects of geometry, trigger and event reconstruction. The superimposed curve is the empirical acceptance function $A(t) = 4t^2/(1+4t^2)$ multiplied by $e^{-t}$ This curve is a reasonably good fit to the B events which have been accepted by our trigger simulation and reconstruction programs.

(aperture) and trigger efficiency. The acceptance function, $A(t) = 4t^2/(1+4t^2)$, approximately describes the net acceptance and is used in the generation of Monte-Carlo events in the mixing and CP violation studies summarized in Chapter 2. This function is multiplied by $e^{-t}$ and superimposed on the generated data in Fig. 26. In our mixing studies, simultaneous fits to the data shown in Fig. 26 and to the subset which is flavor tagged (as described in Chapter 7) are performed to obtain the B mean life, $x = \Delta M/\Gamma$ and the dilution factor, K.

The experimental resolution in the measured proper time is obtained by comparing the generated $B_s$ flight path with its reconstructed value for a large number of Monte-Carlo events. This difference quantity is plotted in Fig. 27 and is seen to have a standard deviation, $\sigma_z = 180\ \mu m$.

The error in proper time, $\sigma_t$, is obtained from the relation $z = ctp/m$ and $\sigma_z = 180\ \mu m$. With a mean $p = 45$ GeV, we find $\sigma_t = 5.8$ %. For a number of reasons, the expected value will be somewhat smaller than this. First, the data in Fig. 27 are calculated using a distance of 6 cm between silicon detector planes used in the P238 silicon configuration. We have since decided to decrease this distance to 4 cm. Second, it is likely that the algorithm used in the calculation of the data in Fig. 27 can be further improved.

## 8.2 $B_s$ Reconstruction: Signal Yields & Background Estimates

The previous section contains a discussion of the B-meson reconstruction procedure and combinatoric background problem in some detail, for specific exclusive final states. However, for a $B_s$-mixing measurement, we anticipate using a final state such as:

$$B_s \to D_s^* \pi\pi\pi$$
$$\to D_s \gamma$$
$$\to \phi\pi$$

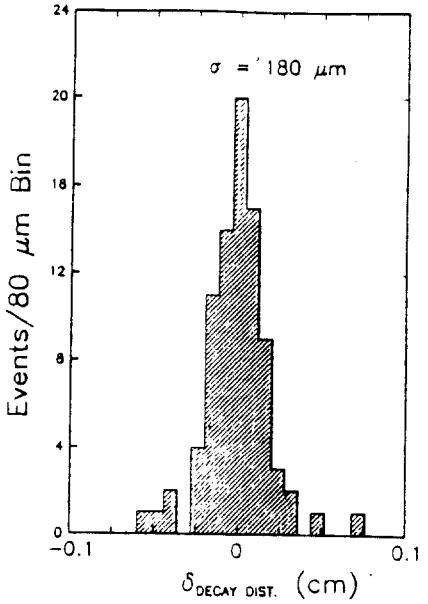


*Figure 27:* Difference between Monte-Carlo generated and reconstructed B track length. The width of this distribution (standard deviation, $\sigma_Z$ = 180 $\mu$m) gives the uncertainty in our measurement of the B track length. As discussed in the text, several improvements in software and hardware will result in $\sigma_Z$ actually being smaller than this value.

which introduces a new factor, namely the effect of using electromagnetic calorimeter information in the $B_s$-meson reconstruction.[25] We have thus studied the effect of calorimeter energy and spatial resolutions on both the reconstruction yield and the $B_s$ signal/background ratio.

Following the procedures of the last section, we construct the invariant mass difference, $M(D_s^*) - M(D_s)$ for the $B_s$ decay in Reaction 20. We plot the resulting mass difference distributions in Fig. 28 for 12 combinations of calorimeter parameters. Calorimeter energy resolutions ($\sigma/\sqrt{E}$) of 0.5%, 1%, 2% and 4% and spatial resolutions of 0.3 mm, 1.0 mm and 10 mm are considered. In constructing these plots, we randomly vary all charged track and $\gamma$ parameters in accordance with the expected energy and angular resolutions. Since the purpose of these plots is to demonstrate the effect of different calorimeter resolutions on the invariant mass resolution, we do not include the combinatoric background resulting from all possible track combinations – only the correct $B_s$ decay tracks are used.

Although there is very little dependence of the invariant mass difference resolution on calorimeter spatial resolution seen in Fig. 28, there is a very large dependence on its energy resolution. For a $0.5\% \cdot \sqrt{E}$ calorimeter, the FWHM is 2 MeV, while for $4\% \cdot \sqrt{E}$, the FWHM increases to about 12 MeV. As will be demonstrated below, the effect of this poorer resolution is to allow more combinatoric background into the signal region and also to lose some signal because some of the tails in the $M(D_s^*) - M(D_s)$ distribution will be cut off. In addition, a larger fraction of the $\gamma$'s from $D^*$'s combine with other $\gamma$'s in the event to form a $\pi^0$ mass; these are then cut out in our selection procedure.

[25] With electromagnetic calorimetry, we would also have the capability to detect B final states which contain $D^{*0} \to D^0\gamma$ (BR = 48%) for the first time, thereby opening the door to the study of entire new classes of final states..

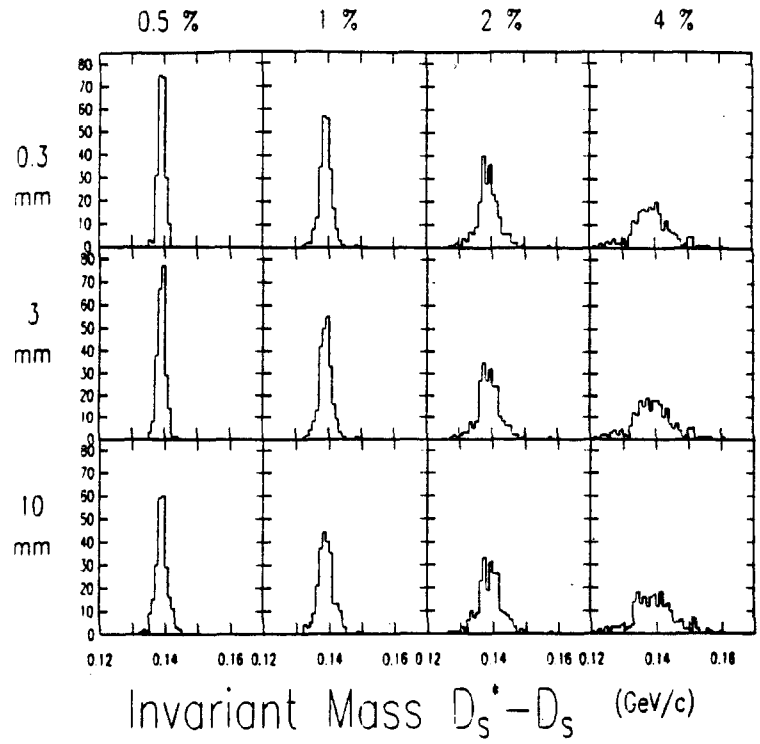


*Figure 28:* Invariant mass differences, $M(D_s^*) - M(D_s)$, for the indicated 12 combinations of electromagnetic calorimeter energy and spatial resolutions. The spatial resolution is the standard deviation, $\sigma_x$. The mass bins are 1 MeV. No combinatoric background is shown. In each case, the energy resolution $\sigma_E/E$ is the indicated constant (e.g. k = 0.5%) divided by $\sqrt{E}$ in GeV.

Using appropriate mass cuts in Figs. 28 to select most of the signal peaks leads to the $B_s$ invariant mass distributions shown in Figs. 29 for the same sets of calorimeter parameters. Although there is a significant dependence of the mass resolution on calorimeter parameters, the dependence is weak, due to the fact that, in general, the $\gamma$ possesses only a small part of the $B_s$ energy (average $\gamma$ energy is about 1 GeV for a $B_s$ energy of 35 GeV).

Before discussing the matter of how the signal/background ratio depends on calorimeter resolution, we show in Fig. 30(a) the expected $B_s$ signal for the best calorimeter case (0.5%·$\sqrt{E}$ and 0.3 mm), with all combinatoric background. Fig. 30(b) shows the expected $D_s$ signal with its combinatoric background.

The $B_s$ signal size and signal/background ratio have been evaluated for all 12 sets of calorimeter resolutions considered (we include the expected background from the general B event sample, in addition to the combinatoric background arising from Reaction (20). Figs. 31 shows the signal/background results. For the 4%·$\sqrt{E}$ and 0.5%·$\sqrt{E}$ calorimeters, the signal/background is about 4 and 10, respectively. The degradation of the $B_s$ reconstruction efficiency with worsening calorimeter energy resolution is also noticable. We find 29% and 43%, respectively for the two calorimeter types.

**Yields of $B_s$-Mesons**

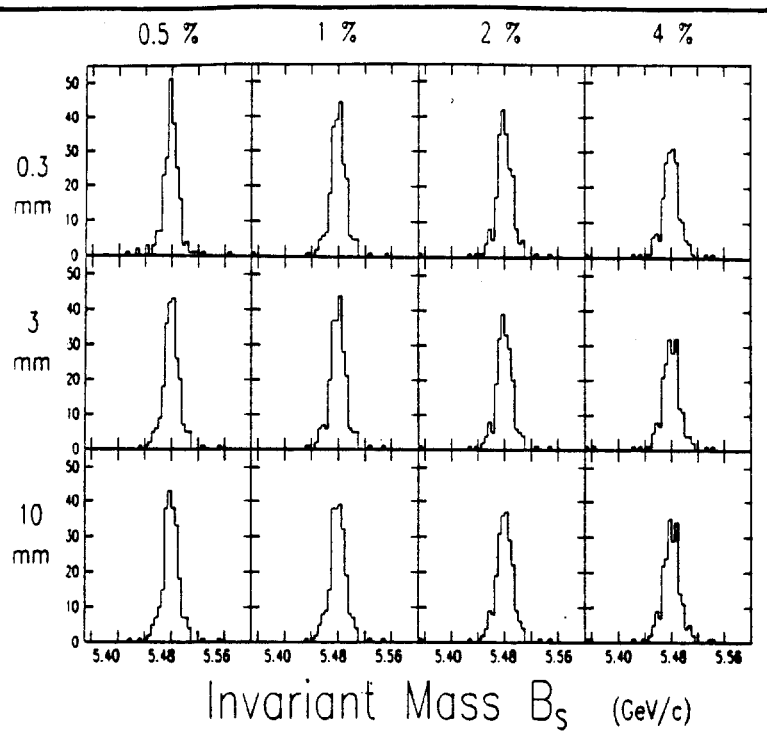


*Figure 29:* Reconstructed $B_s$ Invariant Mass for the indicated 12 combinations of electromagnetic calorimeter energy and spatial resolutions as in Fig. 28. In each case, an appropriate cut is made on the mass difference, $M(D^*) - M(D_s)$, of the corresponding plot in Fig. 28. The mass bins are 5 MeV. No combinatoric background is shown.

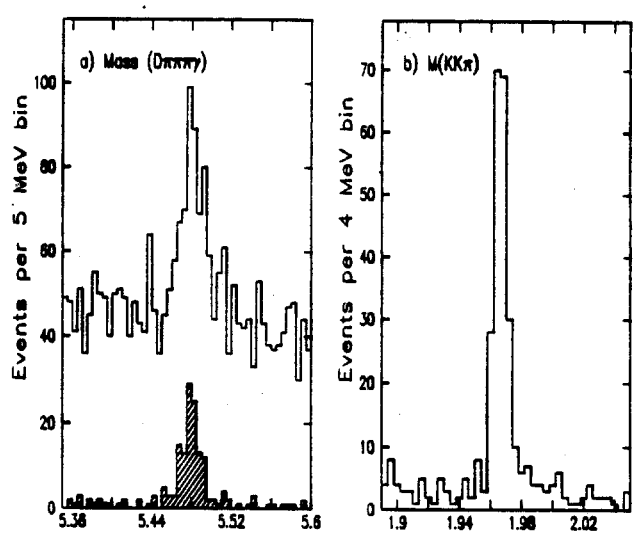


*Figure 30:* (a) Reconstructed $D^*\pi\pi\pi$ invariant mass and (b) $KK\pi\gamma$ invariant mass. Both plots assume calorimeter energy resolution $\sigma_E = 0.5\% \cdot \sqrt{E}$ and position resolution = 0.3 mm. All expected combinatoric background is shown.

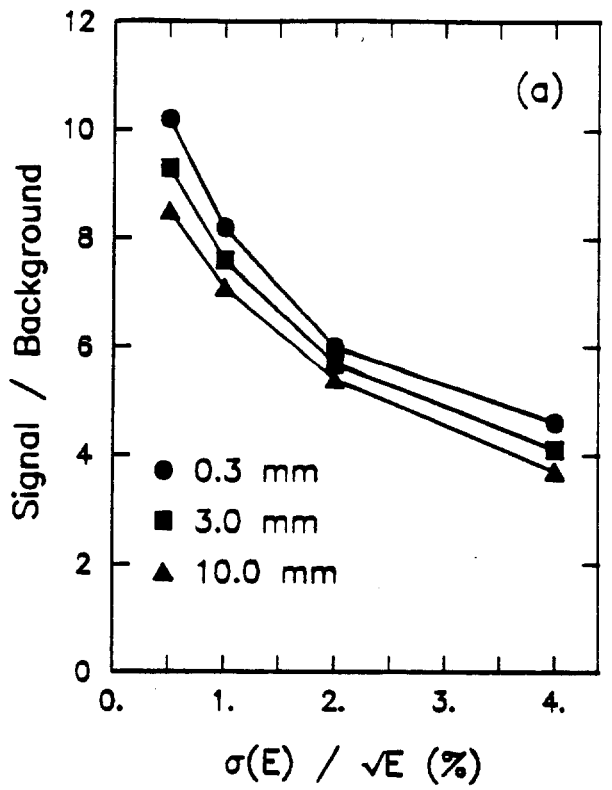


*Figure 31: $B_s$ Signal/background vs. Calorimeter Resolution:* The $B_s$ Signal/Background is shown vs. k in $\sigma_E = k\% \cdot \sqrt{E}$. Curves are given for three different spatial resolutions of the calorimeter.

We base our estimate of the expected yields of reconstructed and tagged $B_s$ and $\bar{B}_s$ mesons for a run with integrated luminosity, $\int \mathscr{L} dt = 10\ pb^{-1}$. The following losses and efficiencies are tabulated in Table 9:

- **$B_s$ Production Probability:** We assume that a $\bar{b}$-quark has a 12% probability[26] to combine with an s-quark to make a $B_s$-meson. This should allow, for example, for the loss of excited $B_s$ which can decay into B + K.

- **2-Arm Geometric Acceptance:** As discussed in Chapter 3, the decay tracks of 30% of all PYTHIA-generated $B_s$ mesons and 30% of all $\bar{B}_s$ mesons are fully contained by a system of two 600 mrad aperture forward spectrometers. There is a 14% overlap, in which both are contained.

- **$B_s$ Branching Ratios:** We assume BR = 9% for the total of all reactions of the type:

$$B_s \rightarrow D_s^* + n\pi^\pm\ ,\ D_s + n\pi\ ,\ D_u + Kn\pi$$

[26] V. Khoze [private communication].

The ARGUS group has reported a branching ratio[27] BR = 6.7%, for final states of the type $B_d \rightarrow D^* + n\pi$ with n = 1,2,3 We also assume that the $D_s^*$ to direct $D_s$ ratio is 3/1 and that the final state $D_u K n\pi$ contributes at least 0.2 %, giving us the total of 9%. Since it seems likely that we shall also be able to reconstruct such final states with n > 3, our effective useful BR should be larger than this.

- **$D_s^\pm$ Branching Ratio:** We take BR = 5% for all known charged final states:[28] $K^+K^-\pi^\pm$, $K^+K^-3\pi$, $K^0K^\pm$

- **$D_s^*$ Branching Ratio:** We assume that all $D_s^*$ decay via the mode: $D_s^* \rightarrow D_s\,\gamma$

- **Live time:** We assume a net 70% live time for the experiment.

- **Trigger Efficiency:** The trigger simulation is discussed in detail in Chapter 4. We find an efficiency of about 45% for Reaction 20 at the Tevatron.

- **Tagging Efficiency:** The tagging efficiency is estimated in Chapter 7 to be larger than 35%. We assume a value of 35% in constructing Table 9

- **Reconstruction Efficiency:** As mentioned above, a $\sigma = 4\% \cdot \sqrt{E}$ e.m. calorimeter yields a reconstruction efficiency of 29% for an average $B_s$ momentum of 35 GeV. The larger $B_s$ momenta at the Tevatron and somewhat larger track multiplicity may decrease this. Thus, for the Table 9 estimates, we assume the conservative value of 15%.

A total of ≈2700 tagged reconstructed $B_s$ events is about four times the estimated need in Chapter 2. Since 10 $pb^{-1}$ is an integrated luminosity that may be reached in a 10 day run in 1994, we see that a $B_s$-Mixing measurement constitutes a relatively modest goal for this experiment.

## *8.3 Monte-Carlo Simulation and Analysis of RICH Counter Data*

We have attempted to make a realistic estimate of the RICH identification efficiencies by simulating the RICH counter response to events containing $B_s$ decays. These simulated RICH data are then analyzed, in order to extract identification information for the particles.

We have started by doing an accurate simulation of the Liquid RICH counter in the first (100-600 mrad) spectrometer. Particle identification in the Liquid RICH counters are the most difficult for the following reasons:

- The number of particles which produce Cherenkov light in the liquid radiator is larger than in the gas counters (pion threshold is about 0.2 GeV in the liquid and is about 2.6 GeV in the gas counters).

- The "rings" are only rings for particles at normal incidence. Away from normal incidence, the light is seen in conic sections which have been truncated by light loss due to total internal reflection in the liquid radiator.

---

[27] H. Schroeder, Rapporteur Talk at XXIV International Conference in HEP (August 1988 - Munich, FRG) and DESY 88-101.

[28] [P. Karchin, Rapporteur Talk at SLAC Lepton-Photon Conference (August 1989)].

*Table 9:* *$B_s$ & $\bar{B}_s$ Event Yields at the Tevatron Collider*

$5 \times 10^8$ $b\bar{b}$ using: $\int \mathscr{L} dt = 10$ pbarn$^{-1}$ ($10^{31} \times 10^6$)
$\sigma(b\bar{b}) = 50\ \mu b$.

| | | |
|---|---|---|
| $6.0 \times 10^7$ $B_s$ | $6.0 \times 10^7$ $\bar{B}_s$ | 0.12 = $B_s$ Production |
| $1.8 \times 10^7$ | $1.8 \times 10^7$ | 0.30 = 2-Arm Geometrical Acceptance |
| $8.1 \times 10^4$ | $8.1 \times 10^4$ | $4.5 \cdot 10^{-3}$ = Branching Ratios ($B_{s*} \to D_s^*$, $D_s$ and $DK^-$ with $n\pi$) ($D_s^* \to D_s\,\gamma$) ($D_s \to KK\pi$, $KK3\pi$, $K^0K$) |
| $5.7 \times 10^4$ | $5.7 \times 10^4$ | 0.70 = Live Time |
| $2.6 \times 10^4$ | $2.6 \times 10^4$ | 0.45 = Trigger Efficiency ($D_s^*\ 3\pi \to D_s\gamma\ 3\pi$) |
| $8.9 \times 10^3$ | $8.9 \times 10^3$ | 0.35 = Tagging Efficiency |
| $1.3 \times 10^3$ | $1.3 \times 10^3$ | 0.15 = Reconstruction Efficiency (allowing for $\gamma$) |
| $2.7 \times 10^3$ | | Total Reconstructed $B_s$ and $\bar{B}_s$ Events |

- The radii of the liquid RICH "rings" are large. Thus, there is considerable overlap of the rings from different particles. There is also some light loss to the walls of the counter.

In order to obtain an overall efficiency for the RICH identification procedure, we have generated 200 $B_s$ events, in which all particles in the final state $K^+K^-\gamma 4\pi$ are contained in the spectrometer aperture. Fig. 32(a) shows the momentum distribution for kaons which emerge from the decay of the $B_s$. Fig. 32(b) shows the momentum for kaons in the spectrometer which are not from the $B_s$ decay (they provide the candidate tagging sample discussed in Chapter 7).

To illustrate the enormous difference between the signals in the detector planes of both types of counters, we show in Figs. 33(a,b) the detector planes for typical events in the liquid and gas RICH counters, respectively. For the gas counter, the signals from nine events are superimposed. Note also that the noise signals referred to below are not shown in these figures.

Because the rings in the gas RICH are much much smaller and relatively well isolated, for the purposes of this study, we provisionally assume that the Gas RICH counter perfectly identifies all particles for which at least 4 photons are detected. We are in the process of extending our modeling to the entire system and should soon have a more complete answer. We first describe the RICH counter simulation, then the reconstruction algorithm and finally present the results of this study.

**RICH Data Simulation**

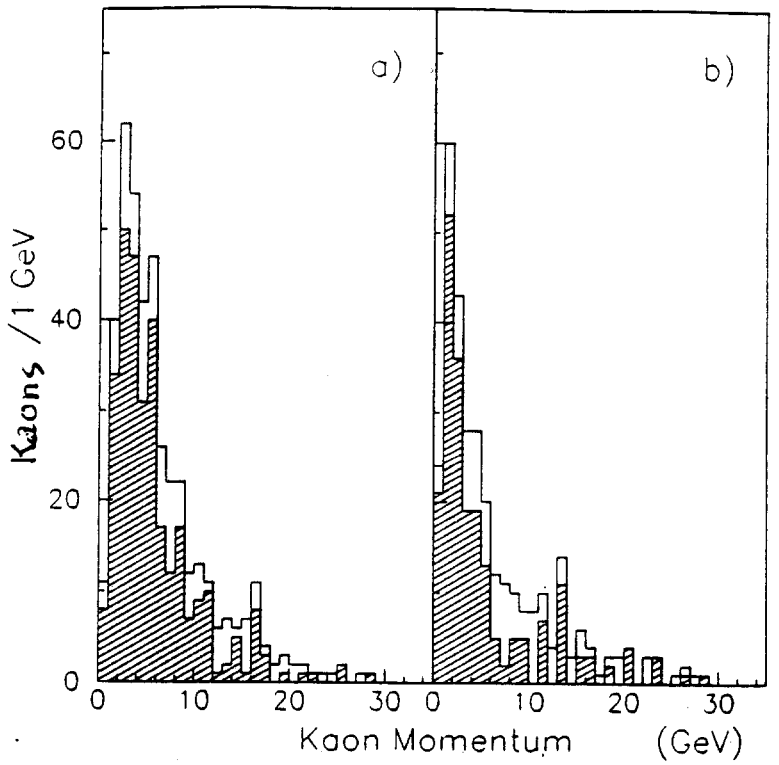


*Figure 32:* (a) Momentum distribution of $K^{\pm}$ which emerge from $B_s \to D_s^* 3\pi$ decay. Shaded histogram shows those that enter the first spectrometer (100-600 mrad); (b) Momentum distribution of $K^{\pm}$ in the detector, which do not come from the decay of $B_s$. Shaded histogram is same as in (a).

As explained above in Section 5.6, each liquid RICH counter consists of a 1 cm thick radiator which is followed by a 3mm thick quartz window. Cherenkov photons which are emitted in the radiator pass through the window into a 25 cm long, helium-filled volume. After traversing the helium, the photons pass through a second quartz window into the photon detector.

For ease of simulation, all windows, detectors and radiators were assumed to have surfaces perpendicular and parallel to the beam axis. This differs slightly from the proposed geometry in which the normals to the windows are along the average particle direction (see Fig. 14). This approximation slightly decreases the number of photons detected in a ring image (because of increased losses due to total internal reflection), but should have little effect on the the ring reconstruction problem. In fact, the average number of "detected" photons generated by the program (20) is very close to the 23.4 photons, measured[29] for a $\beta = 1$ track normally incident on a similar prototype module.

All physical effects relating to the generation and propagation of the Cherenkov photons were carefully simulated. Tracks entering the RICH radiator are multiple-scattered between emission of photons. The photons are propagated through the radiator, the two quartz windows and the helium space, taking into account the energy-dependent index of refraction and absorption lengths in each medium. Reflection probabilities are calculated at each interface between two materials with differing indices of refraction and photons were eliminated if reflection takes place. The distance each photon

[29] R. Arnold et al. [CRN/HE 87-08]

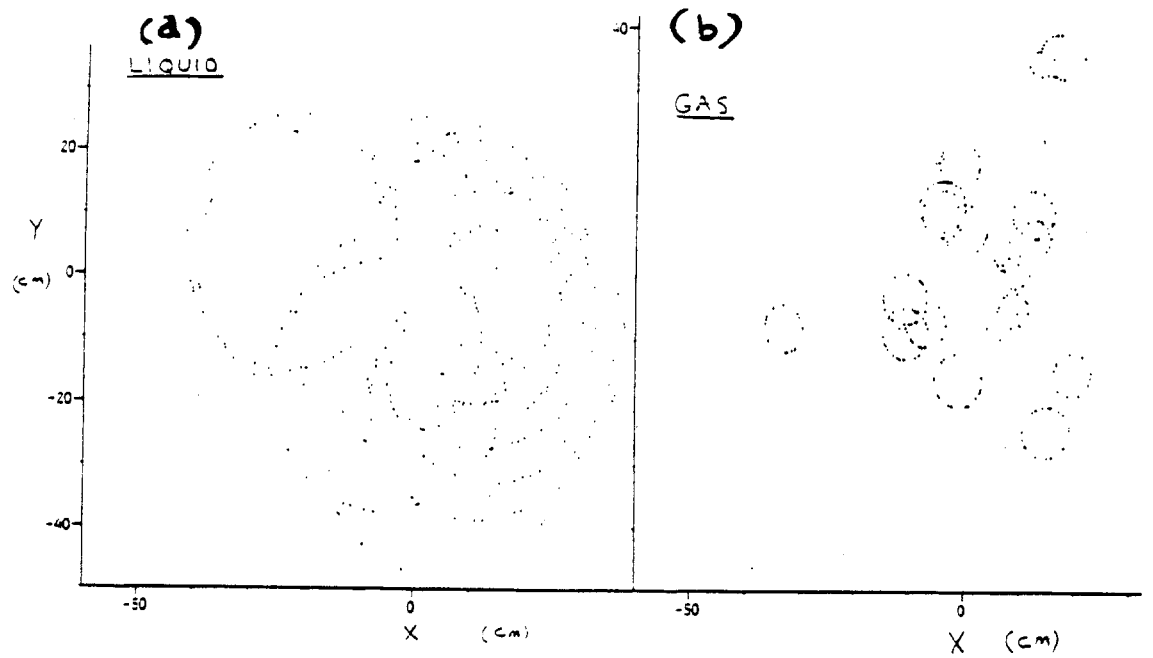


*Figure 33:* (a) Photon Images for One Typical Event in Detector Plane of Liquid RICH; (b) Photon Images in Detector Plane of Gas RICH. The signals from 9 events are superimposed in the gas RICH figure. Noise signals referred to in the text are not shown in either figure.

indices of refraction and photons were eliminated if reflection takes place. The distance each photon travels in the detector before absorption is then calculated, and the detected photon position is digitized, assuming $3 \times 3$ mm$^2$ pads.

Cherenkov light is also generated by all tracks as they traverse the quartz windows (this effect is expected to account for the major fraction of noise photons). These photons are propagated through the counter to the detector in the manner described above. It may be noted that the counter configuration used in the present simulation (perpendicular to the beam axis, rather than rotated as in Fig. 14) overestimates the number of photons from this source, since most photons from tracks normally incident on the quartz are internally reflected in the windows.

**Analysis of Simulated RICH Data**

The input to our provisional reconstruction algorithm is the list of tracks and their trajectories and momenta, as well as the list of hit RICH detector pads produced by the simulation program. As described below, we assume that, if a particle's velocity is above Cherenkov threshold for pions in the gas RICH counter, the gas counter gives a correct particle identification.

For a given measured charged track, the analysis is based on the reconstruction of a Cherenkov emission angle, $\theta$, for each detected photon (at present, each struck $3 \times 3$ mm$^2$ pad is interpreted as one photon). A straightforward ray calculation, which includes refraction at the interfaces, gives two equations for the coordinates (x,y) of converted photons in the photon detector as a function of $\theta$. and the azimuthal Cherenkov emission angle, $\phi$. For each track, we use these equations and standard numerical techniques to give $\theta$ and $\phi$ for each detected photon (if a solution exists).

The subsequent analysis is facilitated by the removal of hits in the Liquid RICH detector, which constitute background from two sources:

- For the relatively few tracks in each event which are above Cherenkov threshold in the Gas RICH, a random number, n, is generated according to a Poisson distribution, whose mean is the expected $\beta$-dependent photo-electron yield (20 for $\beta = 1$). If $n > 4$, we assume that the Gas RICH counter correctly identifies this track (tracks whose momenta are between pion and kaon thresholds in that counter, and which have no light, are assumed to be kaons). We then remove, from the Liquid RICH hit list, all photons from these tracks which are within 2 standard deviations of their expected $\theta$ (this standard deviation is discussed in Section 5.6).

- Cherenkov photons produced in the quartz detector window are removed by removing all hits produced in a 1 cm radius circle about the point where the particle enters the photon detector.

Since, as discussed above, the gas RICH counter is assumed to correctly identify all tracks which are above about 2.6 GeV (pion threshold in that counter), we now investigate with our detailed simulation how well the liquid RICH counter can be used to identify tracks with momentum below 2.6 GeV. Fig. 34 shows a histogram of the values of $\theta$ for an identified kaon track in a typical $B_s$ event after the above cleanup procedure. A peak is seen at an angle which corresponds to the Cherenkov emission angle for the track in question. In general, the situation may not be so obvious.

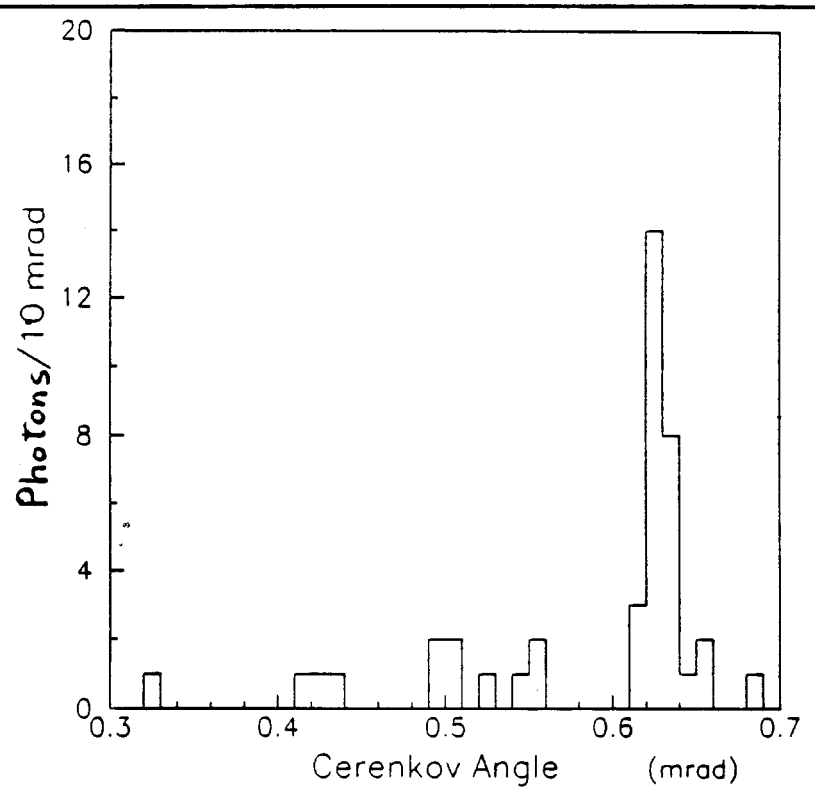


*Figure 34:* Histogram of reconstructed Cherenkov emission angles for a typical kaon track that is identified by the liquid RICH counter. The momentum of this kaon is 1.7 GeV.

In order to quantify the RICH identification picture, we have tentatively employed the following, somewhat arbitrary, algorithm. For each track with momentum below 2.6 GeV, and for each possible mass identity, we count the number of the photons within a "road" of width, $2\sigma$, where $\sigma$ is the expected standard deviation on $\theta$ referred to above. A photon count thus results for each mass identity possibility. For the particle to be uniquely identified as a particular type, the algorithm requires:

- The photon count, $n_\gamma > 5$, within the "road" for that particle type.
- For all other particle types, their photon counts, $n_\gamma' < n_\gamma - 4$.

We are also exploring other more sophisticated algorithms but this relatively simple one already gives rather good results. Table 10 gives the results of the analysis for the sample of 200 events. The rows are the "true" identities of the tracks and the columns are the identities deduced using the above algorithm.

*Table 10:* *RICH Counter Identification Matrix for 200 $B_s$ Events**

| | | Identification from RICH counters | | | |
|---|---|---|---|---|---|
| | | p | K | $\pi$ | pK$\pi$ |
| "True" ID | p | 22 | 22 | | 26 |
| | K | 3 | 372 | 5 | 62 |
| | $\pi$ | 10 | 30 | 1277 | 673 |

(*) For simplification, muons are not included here. Their contribution is small, however.

We see in Table 10 that 85% of all "real" kaons are called kaons by the RICH counters. On the other hand, of all tracks that are called kaons by the RICH counters, 88% of these are real kaons. As commented above, we are fairly confident that these efficiencies can be improved, as we use increasingly more sophisticated reconstruction algorithms.

## *8.4 Yields of Potential CP-Violating Channels*

Table 11 gives a summary of the various factors which determine the event sample size available for a CP-Violation measurement at the Tevatron Collider. The estimates assume a 50 $\mu$b cross section for $B\bar{B}$ production and are given for an integrated luminosity, $\int \mathscr{L} dt = 200$ pbarn$^{-1}$. Referring to Fig. 6, we can see that the 1150 tagged events obtained in this run would permit a $3\sigma$ or more measurement of $\sin(2\beta)$ only for asymmetries larger than about 0.3.

*Table 11:* $B^0_d \to J/\psi\, K^0_s$ *Event Yields at Tevatron Collider*

$10^{10}$ $b\bar{b}$ using: $\int \mathscr{L} dt = 200$ pbarn$^{-1}$ ($10^{31} \cdot 2 \cdot 10^7$)
$\sigma(b\bar{b}) = 50$ $\mu$b.

| | | |
|---|---|---|
| $4.0 \times 10^9$ $B_d$ | $4.0 \times 10^9$ $\bar{B}_d$ | 0.40 = $B_d$ Production |
| $1.2 \times 10^9$ | $1.2 \times 10^9$ | 0.30 = 2-Arm Geometrical Acceptance |
| $4.7 \times 10^4$ | $4.7 \times 10^4$ | $3.9 \cdot 10^{-5}$ = Branching Ratios $B \to J/\psi K_s \to \ell^+\ell^-\pi^+\pi^-$ |
| $3.3 \times 10^4$ | $3.3 \times 10^4$ | 0.70 = Live Time |
| $6.6 \times 10^3$ | $6.6 \times 10^3$ | 0.20 = Trigger Efficiency |
| $2.3 \times 10^3$ | $2.3 \times 10^3$ | 0.35 = Tagging Efficiency |
| $5.7 \times 10^2$ | $5.7 \times 10^2$ | 0.25 = Reconstruction Efficiency |
| $11.5 \times 10^2$ | | Total Reconstructed $J/\psi K_s$ Events |

Our preliminary estimates indicate that substantial radiation damage may occur during the course of a 200 pb$^{-1}$ run and it may be necessary to replace the silicon once or twice during the course of a CP experiment. However, radiation damage to the silicon at high luminosities is not a fundamental limitation, although it will probably be necessary to regard the silicon detectors as expendable, at a cost which is quite tolerable compared to the cost of the entire detector and of running the machine.

# 9. DISCUSSION & COST ESTIMATES

## Discussion

Assuming eventual approval by summer 1991, we would endeavor to have the experiment designed, built and tested in time for a run beginning during the last half of 1994. There remains one key question to answer:

- **Should one or two spectrometer arms be instrumented ?**

To answer this question, there are two important points to note. This experiment would be the first of its kind and it would seem desirable to build one arm and after running and obtaining experience with it, to consider "how things should have been done". But, equally important is our observation that CP-Violation is probably beyond the reach of any Tevatron collider experiment. On the other hand, physics items such as $B_s$-Mixing are easily done with the available luminosity and the loss of 50% statistics that a single instrumented arm implies. **Thus, we propose to build a single arm spectrometer system** at this time.

## Cost Estimates

The major items which we consider here are 1) The silicon vertex detector, 2) The tracking system (wire and pixel drift chambers), 3) RICH, 4) Electromagnetic Calorimeters, 5) Magnets, 6) Trigger Processors, 7) Readout system, 8) Other computing needs, and 9) Mechanical devices for transport and support.

The wire drift chambers contain about 30000 sense wires with building costs estimated at \$24/wire. The electronics costs add an additional \$48/wire giving a total of \$72/wire. The pixel drift chambers, which have about 15000 wires, will use cheaper electronics and cost \$48/wire. The total electronic and mechanical costs are thus estimated to be \$2,880K. An additional \$144K will be needed for a laser alignment system and a gas delivery system for a system total of \$3,024K.

The RICH detectors contain about 7 $m^2$ of quartz costing \$168K. Mechanical construction of the 2.0 $m^2$ of RICH detector is estimated at \$80K, The gas system at \$40K, liquid transport and cleaning system \$40K and mirrors \$16K. Other items include thermal regulation, Freon liquids and gasses, and mechanical mounts. The largest item is the readout electronics for $3.8 \times 10^5$ channels which is estimated to cost \$3/channel for the RICHIP. Development of this chip is almost finished and a 15,000 pad detector is expected to be equipped soon. Pad detectors have recently been tested and work as expected. A full scale operating detector is scheduled for spring 1991, and a full scale test of the combined radiator and detector system will take place early in 1992. Design, construction and testing of the full RICH system during the ensuing two years appears eminently feasible. The total cost of the RICH system is estimated to be \$1,604K.

*Table 12: Experiment Cost Estimates in U.S. Dollars*

| Device | Quantity | Unit Cost | Total (K$) |
|---|---|---|---|
| **Silicon Vertex Detector System** | | | |
| Si Detectors | 96 | 5,000 | 480 |
| Readout electronics | $4 \cdot 10^5$ | 0.50/ch | 200 |
| Mechanical Support | | | 200 |
| VLSI Development | | | 200 |
| Subtotal | | | 1,080 |
| **Wire Chambers (Tracking & Pixel)** | | | |
| Mechanical | $4.5 \cdot 10^4$ | 24 | 1,080 |
| Electronic Preamp | $4.5 \cdot 10^4$ | 8 | 360 |
| Multihit TDC(8 bits, 4 ns) | $3.0 \cdot 10^4$ | 32 | 960 |
| Multihit TDC(4 bits, 25 ns) | $1.5 \cdot 10^4$ | 8 | 120 |
| Cables, Housing, Power | $4.5 \cdot 10^4$ | 8 | 360 |
| Laser Alignment | | | 100 |
| Gas Transport | | | 40 |
| Subtotal | | | 3,020 |
| **RICH System** | | | |
| Quartz Windows | 7 $m^2$ | 24K/$m^2$ | 168 |
| Detectors | 2 $m^2$ | 40K/$m^2$ | 80 |
| Gas System | | | 40 |
| Liquid transport & cleaning | | | 40 |
| Mirrors | | | 16 |
| Thermal Regulation | | | 40 |
| Mechanical Mounts | | | 40 |
| Liquids & Gases | | | 40 |
| Electronics | $3.8 \cdot 10^5$ | 3/ch | 1,140 |
| Subtotal | | | 1,604 |
| **Electromagnetic Calorimeter** | | | |
| Subtotal | | | 7,700 |
| **Magnets** | | | |
| Quadrupole ($\phi$4m·2m) | | | 1,600 |
| Superconducting Dipole ($2 \cdot 2 \cdot 2m^3$) | | | 2,600 |
| Subtotal | | | 4,200 |

*Table 12: Experiment Cost Estimates in U.S. Dollars*

| Device | Quantity | Unit Cost | Total (K$) |
|---|---|---|---|
| **Data-Driven Trigger Processor** | | | |
| Computational Modules | 300 | 300 | 90 |
| Control, Power, and Housing | | | 50 |
| Development | | | 200 |
| Subtotal | | | 340 |
| **Readout System** | | | |
| Detector Encoding | 200 | 800 | 160 |
| Data Buffering/Transport | 200 | 800 | 160 |
| Housing & Power | 30 | 3,200 | 96 |
| Subtotal | | | 416 |
| **Other Computing** | | | |
| Online Host Computer | | | 80 |
| Monitoring/Selection $\mu$P Farm | 700 | 2,000 | 1,400 |
| Subtotal | | | 1,480 |
| **Mechanical** | | | |
| Supports | | | 80 |
| Transport | | | 80 |
| Subtotal | | | 160 |
| TOTAL | | | 20,000 |
| CONTINGENCIES (20%) | | | 4,000 |
| GRAND TOTAL | | | 24,000 |

## APPENDIX A – Trigger Algorithm & Simulation

This is a detailed description of the Monte-Carlo study of the trigger algorithm and its performance which was done for a c.m. energy, $\sqrt{s}$ = 0.63 TeV, where the mean B momentum is 35 GeV. Since the mean momentum at the Tevatron only increases to about 45 GeV, and since there is not much increase in track multiplicity through the silicon detectors, the conclusions should still be valid.

**Silicon Data Simulation and Detector Response** In order to understand the properties of the silicon system, we have generated Monte-Carlo event samples of different types using the Lund program, PYTHIA 4.8, imbedded in the CERN detector simulation Monte-Carlo program, GEANT (We have compared PYTHIA event distributions with the corresponding distributions from UA5 data and have found reasonable agreement).

Silicon response data for the various classes of Monte-Carlo events are simulated in GEANT. We have included the following effects into the generation:

- **Multiple Scattering** Both Gaussian and Moliere scattering were tried. The Gaussian form results in a somewhat more pessimistic estimate of the trigger suppression for minimum bias events and we use it for the results presented below.
- **Nuclear Interactions** We have tried both the Tatina and Geisha packages, but see little difference between the two. The samples discussed below were generated with the Tatina package.
- **$\pi^0$ decays** $\pi^0$s are allowed to decay into either $\gamma\gamma$ or $\gamma e^+e^-$.
- **$\gamma \to e^+e^-$ conversions in the detector** Here, as above, the electrons are added to the track list and are followed through the detector as far as they go.
- **$\delta$-rays** Charged particles traversing the detector are allowed to generate electrons with energies above 10 keV, which are subsequently tracked until they stop.

The first step in generating the silicon response is to assign a quantity representing the amount of energy deposited in the detector by each charged track in an event. For example, Fig. 35 shows the distribution of energy generated for tracks with momenta greater than 10 GeV which impinge on the detector at normal incidence. The energy deposited by delta rays associated with the tracks is included.

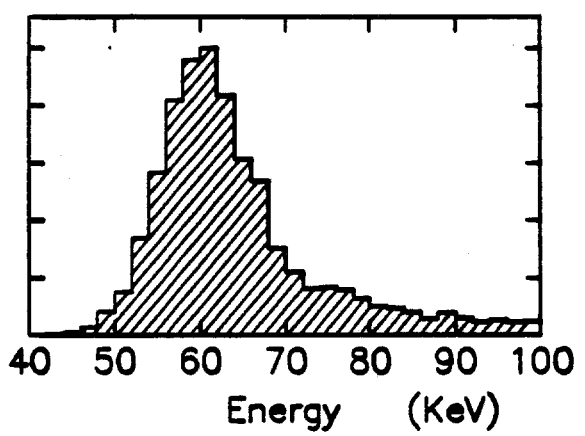


*Figure 35: Energy Deposition in 200 μm of Silicon*

The energy is divided between strips based on the path length spent in the depletion layer of each strip. Next, the number of electron/hole pairs is calculated assuming 270 pairs per KeV of deposited

energy. Detector noise is accounted for by generating a normally distributed random number with a width ($\sigma$) of 1000 electrons and adding it to the signal. The resulting total charge is then compared to a threshold of 4000 electrons, and a yes/no response is generated for each strip. We decided not to make use of pulse height information, since it is currently impossible to read out such information from a real detector at a high enough rate to satisfy the requirements of our on line trigger calculations. This algorithm results in a detector which is essentially fully efficient for tracks impinging at angles less than about 500 mrad, but rapidly loses efficiency for larger angle tracks.

## TRIGGER ALGORITHM AND SIMULATION:

Fig. 36 shows the flow diagram of the proposed trigger. We describe each step of the algorithm in detail. We refer to a coordinate system in which z is along the beam direction, with x (horizontal) and y (vertical) perpendicular to z.

### • POINT FINDING

First, the raw silicon hit information is transformed into points independently in the xz and yz planes. The problem here is to dispose of the clusters (contiguous hit strips). Fig. 37(a) is the distribution of the number of contiguous hit strips generated in the Monte-Carlo simulation. The average cluster width is 1.6 strips. A point is defined as the geometrical center of a cluster. A comparison of the points found in this way with the original track coordinates shows that they have a resolution of 16 $\mu$m (full width half maximum) as demonstrated in figure 37(c).

The distribution of the number of points per silicon detector (i.e. one quadrant of one plane) is shown in Fig. 37(b). Although the charged track multiplicity is high, one quadrant sees on average, less than 1/8 of the total, resulting in the rather modest mean multiplicity of 2.5 points per quadrant.

### • TRACK FINDING

Next, straight lines in both hemispheres, which traverse at least three planes of silicon, are found independently in their xz and yz projections. We demand that the points be collinear to better than $\pm 25$ $\mu$m. This rather stringent cut corresponds to the multiple scattering of a 2 GeV/c track and thus tends to reject tracks with lower momentum which could degrade the vertex algorithm. Figure 38(a) shows the number of tracks found in the xz vs. yz projections using this procedure. The correlation is clear, although mainly because of the loss of lowest momentum tracks, there is a smearing. On average, the algorithm finds about 13 tracks in each view. Fig. 38(b) is a histogram of the number of particles which have traversed at least 3 detector planes minus the number of tracks found per event. As can be seen from this figure, the algorithm usually finds fewer tracks than are actually present (the overall efficiency is about 80%) because of the loss discussed above of tracks with momentum less than 2 GeV which fail the collinearity test.

### • ESTIMATE PRIMARY VERTEX

We use the tracks found above to estimate the position of the vertex. As shown below, this step is mainly needed to define the subset of found tracks whose origins are near the primary vertex.

We histogram together in 5 mm bins the z intercept of all found tracks in both the xz and yz views. (We use only the two hits closest to the beam to estimate the track parameters.) A z-intercept histogram of a typical event from the minimum bias sample is shown in Fig. 39(a). Part (b) of this figure contains a histogram from a typical B event. For both events, most tracks are contained in two bins. There is seen to be very little difference on this scale between minimum bias events and B events.

We next loop over the histogram bins and find the two adjacent bins which contain the most hits. For our first estimate of the event vertex, we assume that the z coordinate is the average position of these 2 bins, weighted by the number of hits in each bin, and that $x=y=0$. Using this method, the vertex is located with a precision of 1 mm along the z axis.

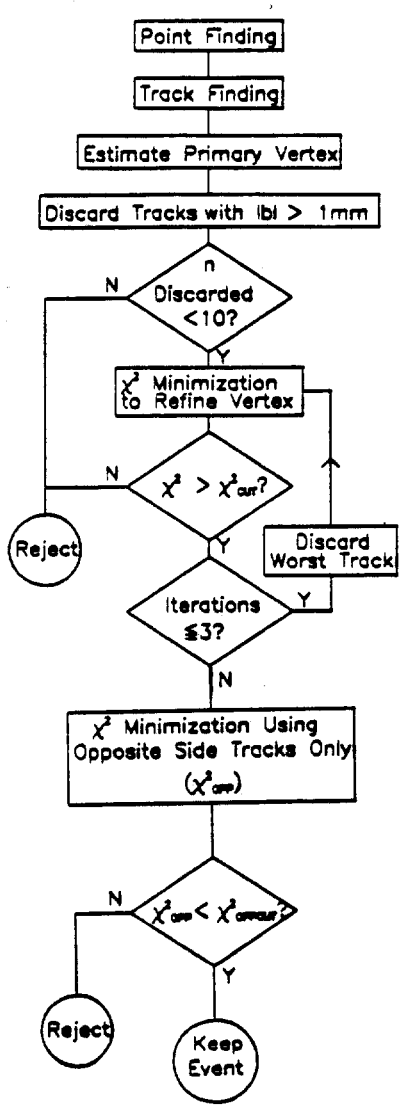


*Figure 36: The Trigger Algorithm*

- **EXCLUDE TRACKS WITH IMPACT PARAMETERS > 1 mm**

This cut serves the dual purpose of discarding tracks which come neither from the primary vertex nor a B decay vertex (such as strange particle decay products or spurious tracks) and as a basis for rejection of pileup (multiple interactions in a bunch crossing) as is discussed below and earlier in Section 3.2.

We define the impact parameter as the distance between the point on the track at the z of the first vertex estimate and the z axis. Fig. 40 shows the impact parameter distributions for various classes of

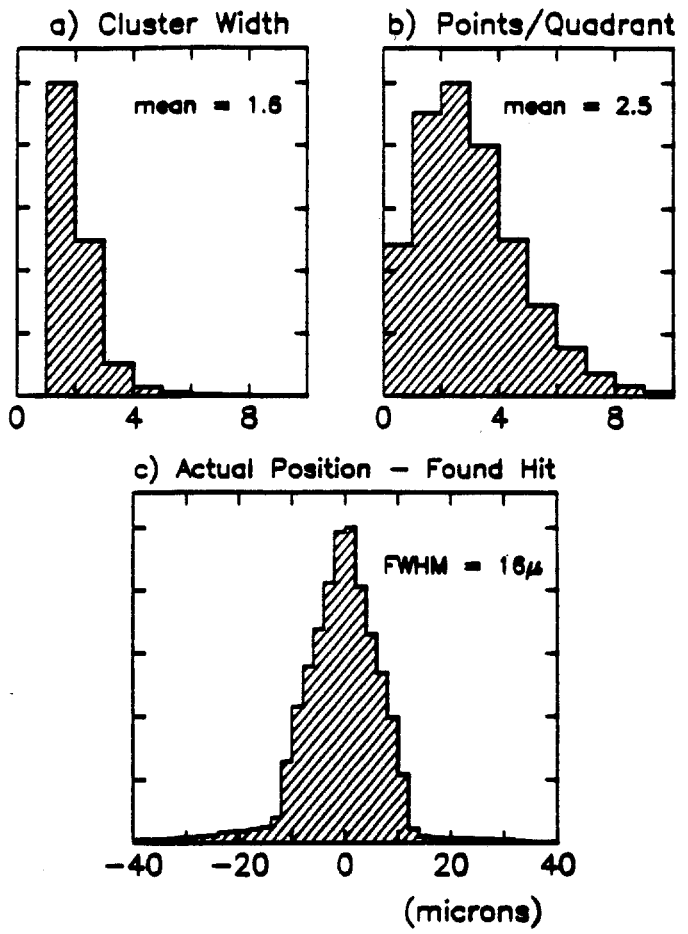


*Figure 37: Point finding details*

tracks. Fig. 40(a) is for tracks from the primary vertex only. Most of these tracks are in two 200 $\mu$m bins. Very few are actually outside the 1 mm cut. On the other hand, Fig. 40(b) shows that tracks from $K^0$ and $\Lambda$ decay have a considerably broader distribution. Roughly half of all $K^0$ and $\Lambda$ decay tracks are thrown out by this cut. The impact parameter distribution for tracks from B decays is somewhat broader than that of primary vertex tracks as can be seen in Fig. 40(d). On average the 1 mm cut discards about 1 more track from B events than from minimum bias events.

- **REJECT EVENT IF MORE THAN 10 TRACKS HAVE b > 1 mm**

This cut is aimed at pileup suppression. Fig. 40(c) shows the impact parameter distribution obtained from Monte-Carlo generated double events (two minimum bias events in one bunch crossing). Except for the broad tail, the distribution is very similar to Fig. 40(a). The histograming method used to find the first vertex estimate usually picks out one or the other vertex when two events occur at the same time. The tracks from the found vertex are mainly in the b = 0 peak, while the tracks from the second vertex form a broad background, also centered at b = 0.

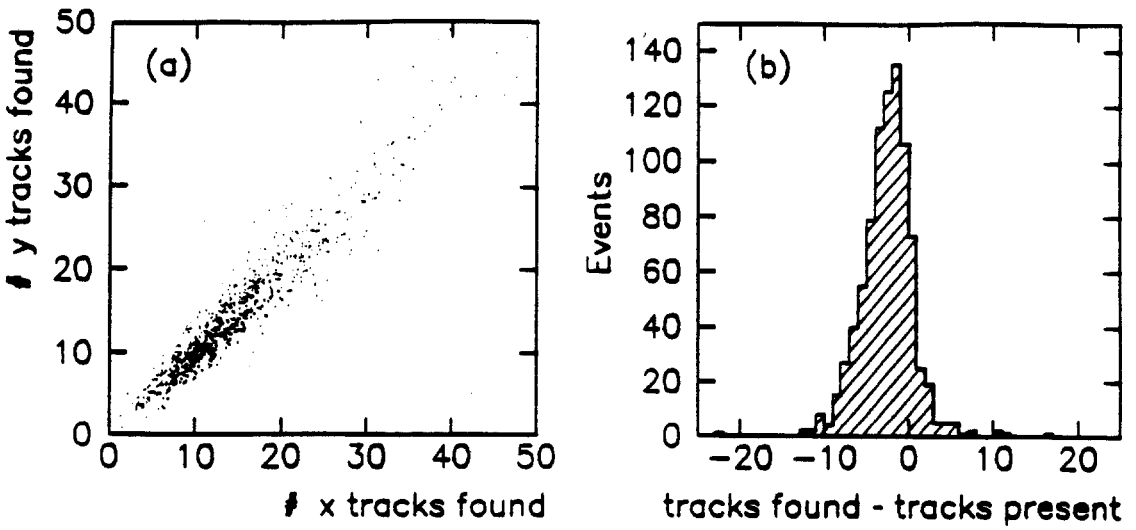


*Figure 38:* (a) The number of y-view tracks found, vs. number of x-view found. (b) the number of tracks found minus number of tracks present.

Fig. 41 shows the number of tracks per event whose impact parameters exceed 1 mm for three classes of events. Demanding that fewer than ten tracks be excluded results in a loss of a few percent of B events while suppressing pileup by a factor of ten.

- **VERTEX FINDING BY $\chi^2$ MINIMIZATION**

Events which pass the above track cut proceed to the next phase which consists of refining the vertex estimate by minimization of the $\chi^2$ given by:

$$\chi^2 = \sum_{i=1}^{N_x} \frac{b_{xi}^2}{\sigma_{xi}^2} + \sum_{i=1}^{N_y} \frac{b_{yi}^2}{\sigma_{yi}^2}$$

This equation contains independent sums over x and y view tracks. $b_{xi}$ ($b_{yi}$) is the impact parameter of the i'th track in the x (y) view. Here, the impact parameter is the distance between the point on the track at the z of the vertex and the vertex point which is no longer constrained to be at $x = y = 0$. Track parameters are estimated using the two measured points closest to the first vertex estimate. A weight, $\sigma_{xi}$ or $\sigma_{yi}$, is assigned to each impact parameter based on the track's slope (which gives a very rough indication of the track's momentum) and the extrapolation distance between the vertex and the closest measured point on the track.

Fig. 42 shows the $\chi^2$/DOF (Degree of Freedom) distribution obtained from a sample of minimum bias events. The distribution is far from the ideal $\chi^2$/DOF distribution. It peaks at $\chi^2$/DOF

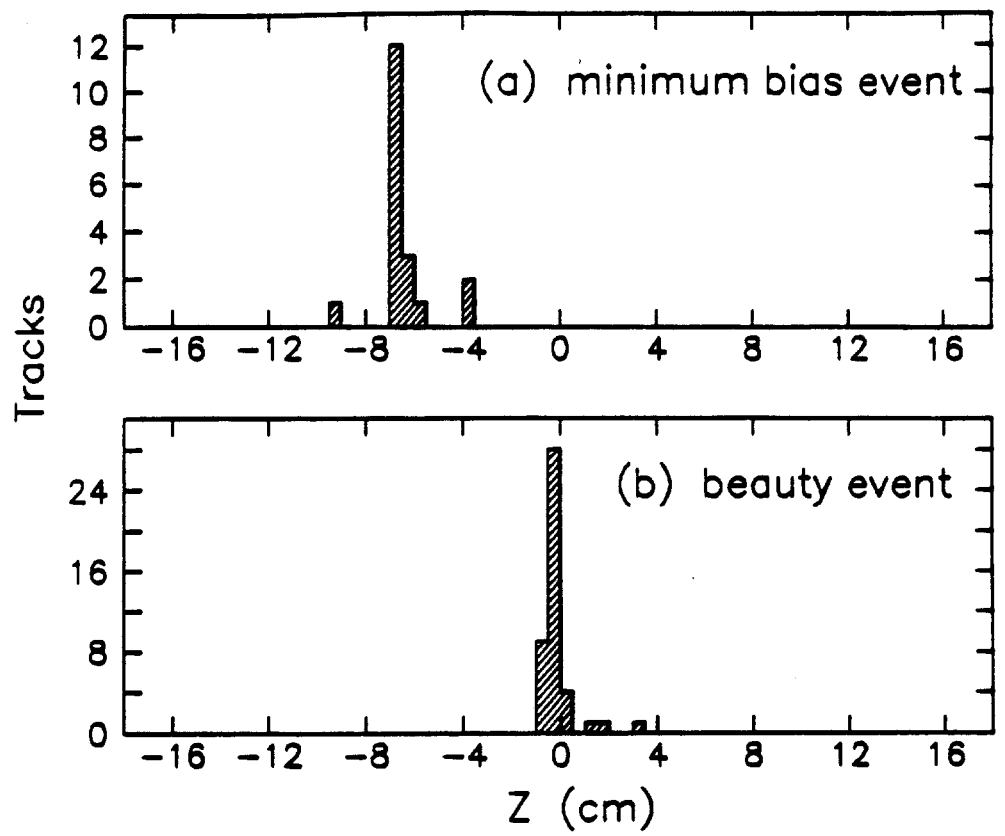


*Figure 39:* z-Intercept Distributions for (a) Typical Minimum Bias Event (b) Typical $B\bar{B}$ Event

= 4 and has a tail extending to very high values. This is due in part to the presence of non-vertex tracks in the sum and to the rather crude estimate of track momentum that is used in evaluating the weight.

- **$\chi^2$ CUT AND ITERATION**

The $\chi^2$-distribution shown in Fig. 42 with its very long tail (not shown) is insufficient to obtain the required suppression of minimum bias events without simultaneously rejecting an unacceptably large portion of the B events. However, we find that if we discard the track with the largest contribution to the $\chi^2$ and refit, we can obtain substantially greater minimum bias suppression with acceptable additional losses of B events. The procedure is optimized by iterating and discarding up to 3 tracks. The results of applying this procedure to minimum bias, $b\bar{b}$ and $c\bar{c}$ event samples are shown in the next section.

Additional suppression of minimum bias events relative to B events can be obtained by using only the tracks which point in the hemisphere opposite the spectrometer and forming a $\chi^2_{opp}$. The basic rationale behind this is the observation that if a B meson is produced and decays into the spectrometer, the accompanying $\bar{B}$ meson is very likely to be in the same hemisphere and therefore $\chi^2_{opp}$ should be small. However, a minimum bias event which happens to have a large $\chi^2$ is equally likely to

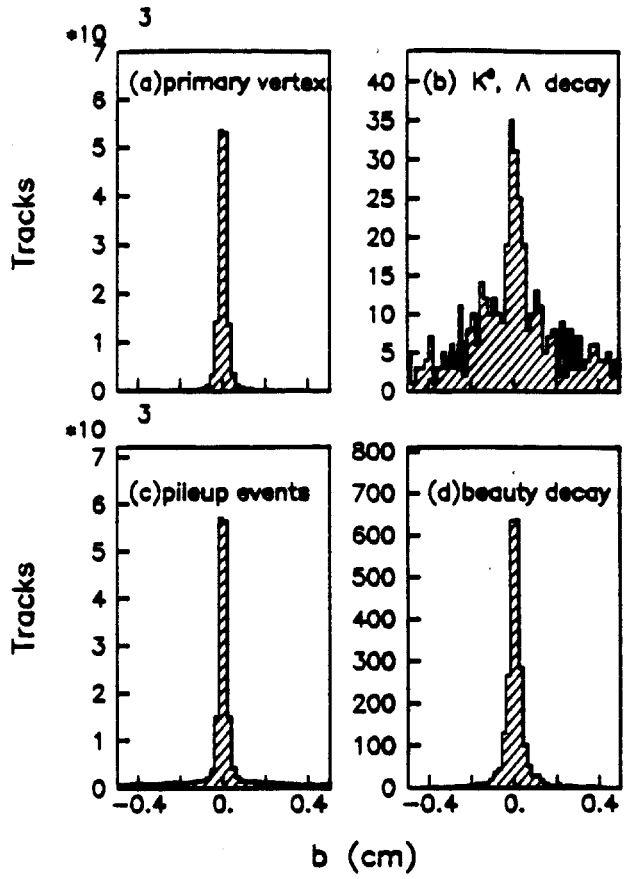


*Figure 40: Impact parameter distributions* (a) tracks from the primary vertex. (b) tracks from $K^0$ and $\Lambda$ decay. (c) tracks from two superimposed events. (d) tracks from B-meson decay.

have its largest contributions from tracks in either hemisphere. Thus, an additional factor of two suppression should be obtainable by requiring that $\chi^2_{opp}$ is small. Moreover, since two superimposed (pileup) events with a large $\chi^2$/DOF are likely to have a mix of tracks from both events going into both hemispheres, a $\chi^2_{opp}$ cut will yield a similar suppression here as well. Thus, for events which have a $\chi^2$ larger than the cut value and which have at least 2 opposite-arm tracks in each view, we make one more iteration of the vertex minimization procedure, using only those tracks.

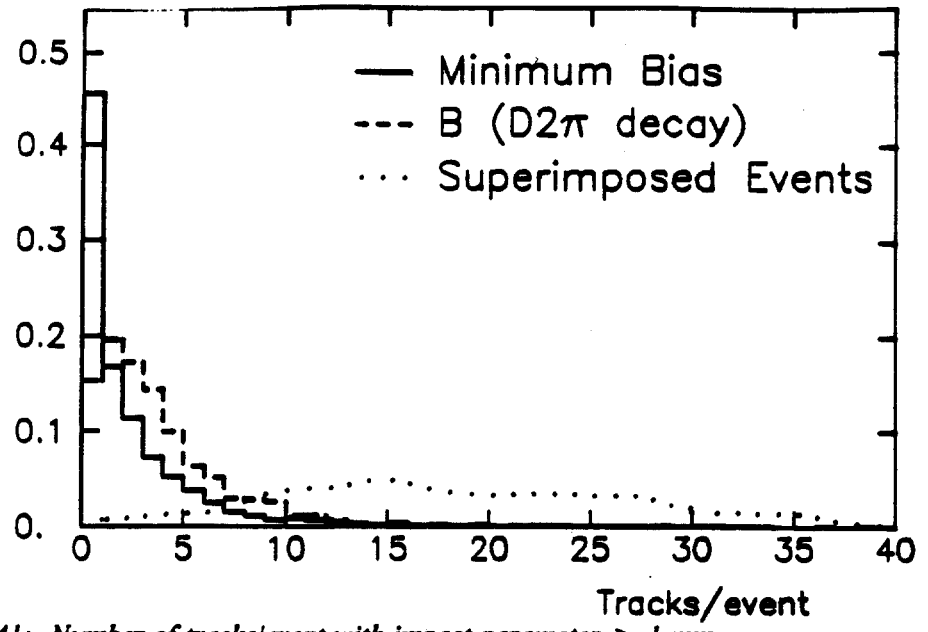


*Figure 41: Number of tracks/event with impact parameter > 1 mm*

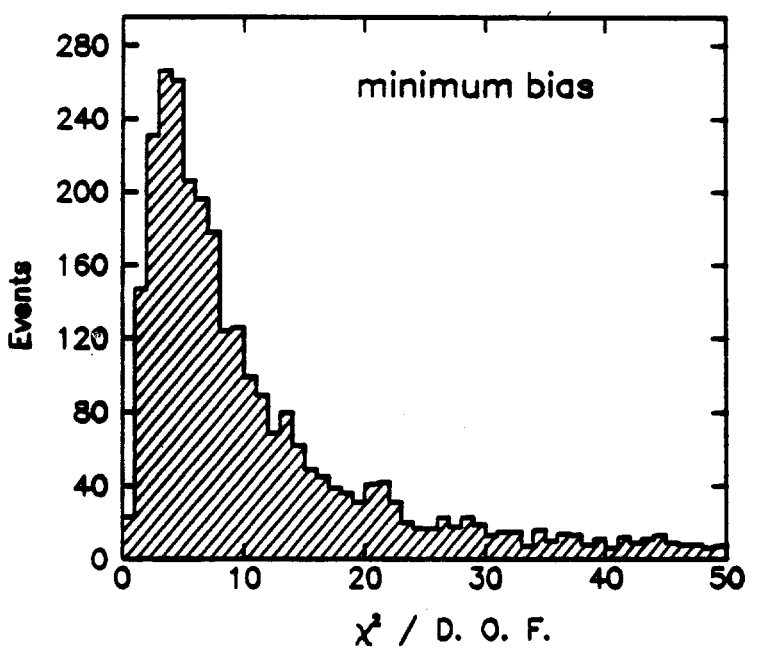


*Figure 42:* $\chi^2$ *Distribution for Minimum Bias Events.* This $\chi^2$ is obtained from the first minimization, before discarding worst tracks and iterating.

## APPENDIX B – Liquid-Radiator Rich Resolution

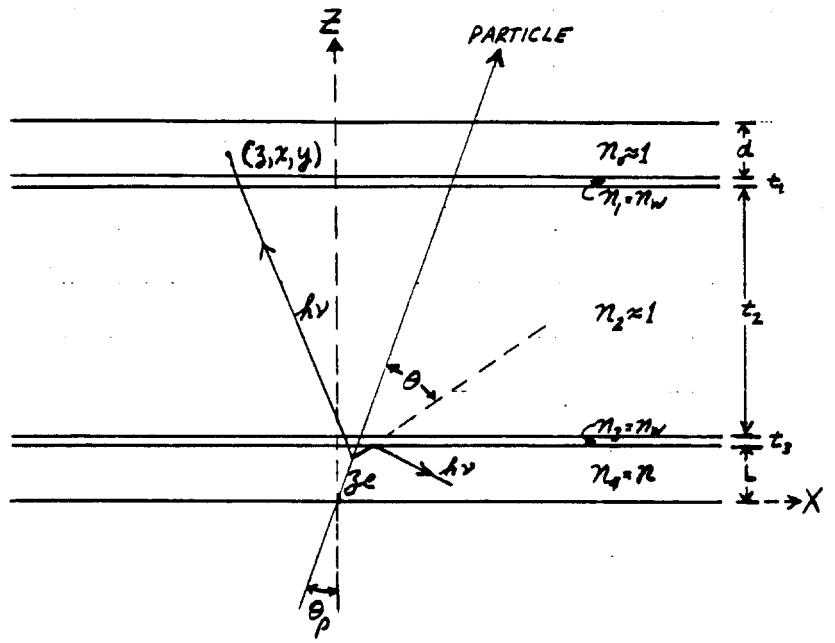


*Figure 43: Liquid-Radiator Geometry.*

The xz plane is defined to contain the radiator normal (z) and the particle momentum vector ($\vec{p}$) as shown in Fig. 43 The photon emission point $z_e$ along the particle direction varies between $-L/(2\cdot\cos\theta_p) < z_e < +L/(2\cdot\cos\theta_p)$ and is unmeasurable. Hence $\sigma_{ze} = L / (\sqrt{12}\cdot\cos\theta_p)$. The photon energy is also unmeasurable and has an energy width $\Delta E$ determined by the detector response, in this case $\sigma_E = \Delta E/\sqrt{24} = .31$ eV. The photons are detected at points (z, x, y) in the detector volume with r.m.s. errors $\sigma_z$, $\sigma_x$ and $\sigma_y$. The Cherenkov angle $\theta$ may be reconstructed from the measured quantities z, x, y, $\theta_p$, $z_e = \langle z_e \rangle = 0$, $n = \langle n \rangle = 1.278$ with the formulas (valid for vanishingly thin window and radiator)

$$\cos\theta = (\sin\theta_p/n)\cdot(x/r) + (\cos\theta_p/n)\sqrt{[n^2-(x^2+y^2)/r^2]}$$

$$\tan\phi = y / [x\cos\theta_p - \sin\theta_p \cdot \sqrt{(n^2r^2-x^2-y^2)}]$$

The derivatives of these reconstruction formulas allow calculation of the angular error at a given $\phi$ via the relation $\sigma_\theta = (\partial\theta/\partial v_i)\,\sigma_{vi}$ The derivatives are:

$$\partial\theta/\partial x = (\beta\sqrt{K/z})[K\cos\phi/\alpha - \sin\theta_p\tan\theta\sin^2\phi/\beta^2]$$

$$\partial\theta/\partial y = (\beta\sqrt{K/z})\sin\phi[1/\beta^2 - \cos\theta_p(n^2-1)/\alpha]$$

$$\partial\theta/\partial z = -(K/z\alpha)(\cos\theta_p\tan\theta + \sin\theta_p\cos\phi)$$

$$\partial\theta/\partial\theta_p = -\cos\phi$$

$$\partial\theta/\partial z_e = (\tan\theta\sqrt{K/z\beta})[(\beta^2K/\alpha^2)(1-\sin^2\theta_p\sin^2\phi) + \sin^2\theta_p\sin^2\phi]$$

$$\partial\theta/\partial n = (n\tan\theta)^{-1}(n^2\beta^2)(\cos\theta_p/\alpha)$$

with $\alpha = \cos\theta_p - \sin\theta_p\tan\theta\cos\phi$ and $K = 1 - n^2 + \alpha^2/\beta^2$.

Appendix

UROPEAN ORGANIZATION FOR ! ;LEAR RESEARCH

DRAFT

18 December 1990

# Development and Test of a Large Silicon Strip System for a Hadron Collider Beauty Trigger


J. Ellett, S. Erhan, P. Kreuzer[1], D. Lynn, M. Medinnis, P. Schlein, J. Zweizig
University of California*), Los Angeles, U.S.A.

A. Czermak[2], G. Engelmann, O. Klingsheim[3], K. Ley, A. Rudge, H. Wahl, P. Weilhammer
CERN, Geneva, Switzerland

G. Borreani
University of Ferrara and INFN, Italy

R. Ely, C. Haber
Lawrence Berkeley Laboratory, Berkeley, CA, U.S.A.

W. Hofmann, B. Wilkens
Max Planck Institut fur Kernphysik, Heidelberg, F.R.G.

M. Calvetti, M. Punturo
University of Perugia and INFN, Italy

Y. Guz, Y. Ivanuschenkov
IHEP-Serpukhov, Protvino, U.S.S.R.

C. Biino, S. Palestini, L. Pesando
University of Torino and INFN, Italy

R. Harr, P. Karchin
Yale University**), New Haven, Connecticut, U.S.A.


## Abstract


Large aperture forward spectrometers with planar geometry perpendicular to the beam line are the natural detectors to accomodate the expected forward peaking of heavy flavor production at high energy hadron colliders. Such systems, together with silicon strip detectors for triggering, which are configured perpendicular to and close to the beam inside the vacuum pipe at the center of the interaction region should make possible the exploitation of hadron colliders as Beauty Factories. We have designed, built and tested such a silicon system at the CERN Sp$\bar{p}$S-Collider. Running 1.5 mm from the Sp$\bar{p}$S beams, clean background-free events are seen.



To be submitted to Nuclear Instruments and Methods


---


*) Supported by U.S. National Science Foundation, Grants PHY90-08221 and PHY85-09175.

**) Supported by the U.S. Department of Energy



1) Ecole Polytechnique, Lausanne, Switzerland

2) Visitor from Institute of Nuclear Physics, Krakow, Poland.

3) Present Address: Stavanger Tekniske Fagskole, Stavanger, Norway.

# Contents


**1 Introduction** 1

**2 The Detector** 2
- 2.1 Overview . . . 2
- 2.2 Silicon Detectors . . . 2
- 2.3 SVX Chips . . . 2
- 2.4 Hybrid Design . . . 3
- 2.5 Detector Mount . . . 3
- 2.6 Assembly and Testing . . . 4

**3 Installation and Roman Pots** 5
- 3.1 Roman Pots . . . 5
- 3.2 Positioning Mechanism . . . 5
- 3.3 Pumping system . . . 5

**4 Silicon Power System** 6

**5 Triggering and Readout System** 6

**6 System Performance & Data Analysis** 8

**7 Conclusions** 9


# 1 Introduction

The exploitation of hadron colliders as beauty factories would be impossible without a high resolution vertex detector and an efficient and highly selective beauty trigger. A scheme for realizing such a detector and trigger was explored and extensively modeled in the context of a proposal to the CERN SPS committee[1]. Although this proposal was for an experiment at the Sp$\bar{p}$S-collider, it was recognized that the apparatus built for the Sp$\bar{p}$S collider experiment could serve as a basis for the more elaborate apparatus needed to cope with the higher energies of the next generation of hadron colliders. Indeed, the long range goal of the collaboration is an experiment with sufficient sensitivity to measure CP violation parameters in the decay of B mesons. The attainment of this goal awaits the high luminosites and high cross-sections of the next generation of hadron colliders.

We report here on the design and construction of a test version of the proposed detector and present a preliminary analysis of the results obtained with it during the Fall 1990 Sp$\bar{p}$S-collider run. The purposes of this test were to assess the feasibility of operating a silicon detector at a few millimeters from the beam axis, and to gather data for the off-line testing of trigger algorithms based on silicon hit information, which would select events containing beauty production.

Fig. 1(a) shows a side view of the detector used for this test. Part (b) of this figure shows a perspective drawing. The detectors are organized into 6 planes perpendicular to the beam axis. Each plane has 8 silicon detectors: 4 with vertical (x-view) and 4 with horizontal (y-view) strips.

The "fixed-target" type geometry was adopted to accomodate the anticipated sharp peaking of B production in the beam directions[1]. The forward peaking of reconstructable B mesons is even sharper since the decay products of B mesons produced near Feynman-x = 0 tend to have low momentum and therefore become easily lost in pattern recognition. The detector was therefore optimized for particles traveling in the forward and backward directions, at angles less than about 600 milliradians.

In order to minimize extrapolation distance to the primary vertex, the detector was positioned at the center of the interaction region and the gap between upper and lower halves was reduced to the minimum distance consistent with clean running conditions. The detector is

mounted in a device (called a Roman Pot) which allows retraction of the detector to a safe distance during beam manipulations and setups.

The detector assembly and associated systems are discussed in Sections 1 through 5. A discussion of the performance of the detector during the collider test run and a preliminary analysis of the data taken during that run is presented in Section 6.

# 2 The Detector

## 2.1 Overview

A photograph of a detector with its associated readout hybrid is shown in Fig. 2. The assembly pictured here was appropriate for readout of the horizontal coordinate. The silicon detector is on the left in this view. The seven chips next to the detector are SVX pre-amplifier/readout chips. A Kapton readout cable is shown plugged into connectors near the right-hand edge of the hybrid.

The detectors were supported by aluminum brackets glued to the back of the alumina hybrids. Fig. 3 shows a side view of two detector planes. Each detector is shown attached to its hybrid and heat sink. The distance between adjacent x- and y-view detectors was 2 mm and the distance between the center lines of adjacent planes was 3.8 cm.

As shown in Fig. 4, the aluminum support brackets were afixed to a water-cooled mounting plate which was in turn attached to a vacuum bulkhead. As shown in Fig.s 3 and 4, a thin corrugated window separated the detector volume from the main SPS vacuum. Since the window was required to be thin, the detector volume was also evacuated.

## 2.2 Silicon Detectors

The silicon strip detectors were fabricated by the Central Institute for Industrial Research (S.I.) in Oslo and are functionally similar to those used by the DELPHI experiment[2]. They have an active area of $44.8 \times 44.8\,\mathrm{mm}^2$ and thickness $280\,\mu\mathrm{m}$. Each detector has a total of 1793 diodes with a pitch of $25\mu\mathrm{m}$, only half of which (every second one) is read out. The charge deposited on diodes between read out strips capacitively induces signal on neighboring strips, thus enhancing charge sharing and improving spatial resolution. Metal strips, which are bonded to preamplifier inputs, run the length of the diodes and couple capacitively to the underlying p-strips via a 200 nm thick oxide layer. Each p-strip is connected to a common bias bus through individual $\sim 6\,\mathrm{M}\Omega$ polysilicon bias resistors. We find more than a 99% yield of good strips and leakage currents in the range of 50 pA/strip to 1 nA/strip.

## 2.3 SVX Chips

A detailed discussion of the properties of the Lawrence Berkeley designed SVX-D chip can be found elsewhere[3]. We present only a functional description relevant to the design of the support electronics.

The SVX-D is a CMOS chip which contains 128 charge-sensitive preamplifiers with an overall gain of about 15 mv/fc as well as circuitry for multiplexing and optionally "sparsifying" pulse-height information (i.e. reading out only those strips whose charge is above a set threshold).

In addition to the 128 preamplifier inputs, the SVX has the following input/output lines:

- A set of eight bi-directional data lines which is used to read addresses of hit strips, to set and reset various switches in the pre-amplifiers, and to write a chip number during initialization.
- Three control signals which determine the function of the data lines.
- A calibration line by which charge is injected to set a threshold for sparse readout.
- Input and output priority signals which allow daisy-chaining of an arbitrary number of SVX chips.

- A gated analog line which, during readout, outputs a voltage proportional to the charge on the strip currently being read out. The analog line is only active when the chip currently has priority.

The SVX requires two sources of power, an analog power of six volts which is supplied to the bottom of the chip as well as a bonding pad, and a digital power of between five and six volts which is supplied to a bonding pad.

For each strip read out, the SVX first outputs the chip number (which is written to the chip during initialization) followed by the strip number onto the eight data lines while simultaneously outputting the analog pulse height onto a common bus.

## 2.4 Hybrid Design

Each silicon detector (896 strips) requires seven SVX chips, which were mounted on ceramic alumina hybrid circuit boards. There were two different but similar hybrid designs for the x- and y-view detectors. The two designs were needed since connections could only be made near the outer vertical edges due to space limitations.

Both hybrid types contain five main layers silk-screened onto the alumina substrate. The lowest two layers have horizontal and vertical gold traces intended to bring the control, data, calibration, and analog signals to and from the SVX chips. An SVX analog power plane, an SVX digital power plane, and then a ground plane are layered above. Dielectric material electrically isolates the various layers. Surface mount capacitors provide filtering for the SVX power. The SVX chips are glued with conducting epoxy onto an exposed section of the analog power plane. Connections to the input/output pads of the SVX chips and the gold traces on the hybrid are made via an ultrasonic wire bonding process using one mil diameter aluminum wire. Two sixteen-pin surface mount connectors manufactured by DuPont (Microflex) were mounted on each hybrid.

## 2.5 Detector Mount

The individual silicon detectors were glued to hybrids along one edge, with a two millimeter overlap. The hybrids were then glued to aluminum brackets, which also served as heat sinks, using silver-impregnated epoxy for good heat conduction. The gluing was done under microscope and on a vacuum jig with a precision of ten microns perpendicular to the strips and one hundred microns parellel to the strips. The detectors were positioned for gluing with reference to alignment holes on the heat sink and to the heat sink surface which abuts the mounting plates. Each assembled detector was attached to its mounting plate with a single screw. The x-view detectors were held in position with alignment pins.

The two water-cooled mounting plates (for top and bottom hodoscopes) each consisted of two 2 cm thick plates glued together. Before gluing, a channel for cooling water was machined into the inner surface of one of the disks and matching slots were machined into both disks for the passage of readout cables. Fig. 5 shows a photograph of a partially assembled hodoscope. Five of the six planes had been mounted at the time the photograph was taken. The x- and y-view detectors for each quadrant were mounted with diode strips facing each other across a 2 mm gap. The cable slots for the sixth (as yet unmounted) plane are visible on the right-hand side of this photograph.

Each mounting plate was attached to vacuum bulkheads by means of four precisely-machined aluminum bars. The vacuum bulkheads were made from 3 cm thick aluminum plates, which bolted onto the Roman Pot assembly (described below). Signals to and from the SVX chips traversed from vacuum to atmosperhic pressure on printed-circuit boards ("feed-through boards") which were glued with Araldite into the bulkheads. The bulkheads also contained ports for vacuum pumps and cooling water. Fig. 6 shows the same five-plane assembly pictured in Fig. 5 after it had been joined to the vacuum bulkhead. The bulkhead is at the bottom of the figure. The vacuum-side portions of the printed-circuit boards can be seen traversing the bulkhead and a cooling-water tube is visible in the forground.

## 2.6 Assembly and Testing

Upon receipt from the manufacturer, the silicon detector wafers were subjected to a thorough visual inspection at a microscope station with the intention of catching physical defects such as shorts between strips, breaks in the bias and guard rings or diffusion strips, and poorly cut wafer edges.

After visual inspection, electrical measurements were made of the coupling capacitance and the interstrip capacitance and resistance. Additionally, the leakage currents of the guard ring and bias strip were monitored for a period of 40 to 50 hours. Typically, bias strip currents were in the range $0.1 - 1.0\,\mu$amps while the guard ring currents would increase over a period of about one day from an initial value of about $1 - 10\,\mu$amps to $20 - 100\,\mu$amps and then stabilize. Approximately 10% of the detectors were rejected either for physical or electrical defects.

The SVX chips were tested at Lawrence Berkeley Lab using a procedure developed for the CDF $\mu$vertex detector. Our batch had the unusually low yield of 13% good chips. Using the test results, an attempt was made to match as closely as possible the nominal analog output voltage for each set of seven SVX chips on a given detector. No additional tests were performed on the SVX chips before mounting on the hybrid assembly.

The alumina hybrids were designed by our group and manufactured at CERN. After manufacture, they were visually inspected for obvious defects, then passive components (resistors, capacitors and connectors) were mounted. The hybrids were tested for continuity between bonding pads and connectors and for shorts between adjacent lines. The SVX chips were then glued in place and wire-bonded to the hybrids.

At this point, the hybrid assembly was tested. The test setup was similar to the experimental readout system which is discussed in Sec. 5. It consisted of a MicroVax controlling a CAMAC crate which contained a sequencer module (SRS)[4] to generate the SVX clocking signals, and a readout module (SDA)[4] to read and store the analog and digital address information from the SVX's. A test board provided the electrical interface to the detector assembly and contained a variable charge injection circuit as well as oscilloscope test points. The following checks were made:

- analog output voltage responds to charge injection onto the calibration line;
- priority propagates through the SVX chain;
- average analog outputs of most channels are correct;
- noise levels of most channels are small;
- correlated shifts of baselines (common-mode) on all channels of a chip not too large;
- no (or few) skipped, out of sequence, or multiple occurrences of digital addresses.

Problems detected by the testing were repaired, sometimes with the use of a probe station for tracking down less obvious malfunctions. Not all problems were considered serious enough to warrant the risk of creating a worse condition by attempting repairs. An example would be a channel which was always skipped during readout.

After gluing the hybrids to the heat sinks and the detectors to the hybrids, the 896 readout strips were bonded to the inputs of the SVX preamplifiers using a semi-automatic bonding machine. This process took approximately two to three hours per detector. The detector pictured in Fig. 2 does not have an attached aluminum heat sink (it was a test assembly) but otherwise shows a detector at this stage of assembly.

The above tests were then repeated with the detector attached and biased. As a final test each detector was scanned with a tightly focused, pulsed LED light source to verify that all (or most) channels responded and to get a rough measure of the relative analog gain differences between the SVX's. The detectors were then assembled onto the mounting plates as shown in Fig. 5.

# 3 Installation and Roman Pots

## 3.1 Roman Pots

The silicon detector must be isolated from the Sp$\bar{p}$S machine vacuum for two reasons:

1. The pressure in the vacuum system around experimental areas of the Sp$\bar{p}$S must be in the low $10^{-10}$ mbar range. However, the gas load ($\sim 10^{-3}$ mbar $* \ell/s$) of the complete silicon detector assembly precludes pumping to this pressure range.

2. The detector must be electromagnetically shielded from the beam bunches which set up strong image currents in the vacuum chamber walls which could cause very serious noise pickup in the detectors.

Thus, a metallic, vacuum-tight separation with low outgassing rate was needed. The separator was also required to present a minimum thickness to particles traversing the detector's active volume in order to minimize multiple scattering, particularly of small angle tracks. We therefore developed a special aluminium vacuum vessel which had a very thin ($200\mu$m) corrugated Al-foil in the sensitive volumes of the detectors as shown in Fig. 3. Since such a thin Al-foil could not withstand the pressure difference of one atmosphere, the silicon detector assembly was designed such that it could be pumped down to about $10^{-4}$ mbar and therefore exclude all forces on the Al-foil.

For reasons of expediency, the whole arrangement, pot and silicon detector, had to be designed such that it could be fitted into the existing Roman Pot driving mechanism which is described below.

Fig. 7 shows the aluminum vacuum vessel with its two corrugated side walls. This piece was machined from a single piece of aluminum using a numerical-controlled milling machine. The free space between the two side walls, which housed the silicon detector planes, was later covered with the 200 $\mu$m thin Al-foil.

The corrugated shape of the Al-foil was produced using special tools as shown in Fig. 8 and afterwards annealed in order to stabilize the corrugated shape. It was then glued to the side walls of the pot with a special silver charged Araldite to ensure good electrical contact between the Al-foil and pot, and thus maintain adequate electromagnetic shielding. Fig. 9 shows a close-up of the corrugated region of the pot, after installation of the Al-foil.

Since the total surface of glue ($\sim 50\,\mu$m thick line over the length of the corrugated shape) exposed to the Ultra High Vacuum (UHV) system of the SPS is less than 1% of the surface of the complete pot, its contribution to the total outgassing rate is negligible. Fig. 10 shows a detail of the connection of the Al-foil to the pot.

## 3.2 Positioning Mechanism

Given the short time allowed for construction of equipment for this test, it was not possible to design and build an optimized positioning mechanism. We therefore used, with minimal compromise, an existing Roman Pot mechanism which had previously been used for diffractive measurements by two experiments at the Sp$\bar{p}$S-collider. A photograph of the mechanism is shown in Fig. 11.

The mechanism allows detectors, mounted inside pots above and below the beam, to be displaced along the vertical axis. The pot flanges are connected to the vacuum chamber of the machine by bellows. During beam manipulations, the inner edge of the vacuum shield was retracted to a distance of about 5 cm from the nominal beam position. During data-taking runs, the two pots were brought close to the beam axis as shown in Fig. 4. The pot position was adjusted and monitored using a linear position transducer with an accuracy better than 50 $\mu$m.

## 3.3 Pumping system

Fig. 12 shows the schematic layout of the special pumping system installed for this test. The line between the SPS sector valves VVS1 and VVS2 represents the SPS vacuum system with

the pot assembly in the center. VPRS1 to VPRS3 are turbomolecular pumps backed by rotary vane pumps. VG1, VG2 and VG-SPS are vacuum gauges and V1 to V4 are roughing valves. On each side of the pot, a combination of a 400 $\ell$/s sputter-ion with a 1000 $\ell$/s sublimation pump (VPS) was installed for UHV production.

The initial pump down from atmospheric pressure of the SPS vacuum system and of the pots down to about $10^{-1}$ mbar is made with VPRS1 via the valve V1 and V2. Below a pressure of $10^{-1}$ mbar, measured on VG2 and VG-SPS, valve V2 closes automatically and VPRS1 is pumping via V1 only the pots. At the same time V3 and V4 are opened to pump the SPS vacuum system with the help of VPRS2 and VPRS3. After a bakeout at 150 $^0$C of the SPS vacuum system, UHV production with the VPS's was started.

In case of a sudden pressure rise higher than $10^{-1}$ mbar in the SPS vacuum system or in the pots, VVS1 and VVS2 as well as the roughing valve V1 close and the separation valve V2 open in order to equalize the pressures in both vacuum systems and therefore avoid damage to the detector or thin Al-foil of the pot.

After a short power cut the pumping system restarts automatically. If there is however a slow pressure rise above $10^{-1}$ mbar due to an extended power failure of a few hours, the complete pumping system will be blocked and can, for safety reasons, only be manually restarted.

The best pressure obtained in the SPS vacuum system after a few weeks of pumping was about $5 \times 10^{-10}$ mbar with a residual gas composition mainly composed of hydrogen and water vapor. The pressure in the pots was maintained at about $5 \times 10^{-4}$ mbar.

# 4 Silicon Power System

The power system supplies the DC voltages to run the detectors, with the requirements that these voltages have low noise ($<$ 1 mV at the detector) and that every bias current is monitored. The system consists of a switch panel in the counting room for individual control of each of the 48 detectors; the supplies, mounted in a rack next to the detector; and a monitoring system composed of a CAMAC multiplexer and ADC module, read out by a Caviar unit in the counting room. The use of opto-couplers to switch individual detectors assures total electrical isolation of the control circuitry thus minimizing noise pick-up.

The SVX analog and digital voltages as well as voltages to power the PID boards (described below) were generated by commercial supplies (Ultronix).

Ninety volt batteries (Eveready No. 490) were used to bias the detector back planes, since suitably decoupled batteries provide ripple-free voltage, and make individual detector current monitoring relatively simple. Four batteries were mounted in a double-width NIM module. The output voltage for each channel could be independently adjusted in the range 0 to 90 V and was determined by a combination of an external reference voltage, common to all supplies and potentiometers for each channel as shown in Fig. 13. Two Darlington connected transistors provide a low output impedance, and independence from battery voltage changes. With typical bias voltages of 50 V and currents of 1 to 100 $\mu$A (due mainly to guard ring leakage), battery life is greater than 6 months.

The voltages and currents of all supplies were continuously monitored by a CAMAC analog scanner and DVM (Lecroy LG5310), and displayed in the counting room in bar graph form. The SVX analog and digital voltages and the detector bias voltage are interlocked to insure that they could be turned on only in the correct order.

# 5 Triggering and Readout System

The control signals necessary for operation of the SVX chips were generated by the Lawrence Berkeley designed SRS (SVX Readout Sequencer)[4] CAMAC module. This module contains an AMD2910 sequencer and 12 kbytes of program memory which may be downloaded from the host computer. Approximately 6 kbytes of the memory are used to store bit patterns which are sent to front panel outputs to drive the SVX's. The AMD2910 addresses successive locations of the internal memory to access these bit patterns, but may jump to any specified address depending

on the state of front panel input signals (e.g. scintillator trigger signal). This permits access to the different sets of bit patterns required either by the sampling sequence or by the SVX readout sequence.

The SRS control signals were converted to differential levels and sent over a 50 m flat twisted pair cable to the interaction region, where a repeater board converted them to single ended TTL levels. The control signals then traveled another two meters over two flat cables to twelve Plug-In-Driver (PID) printed circuit boards of the top and bottom half detectors. This signal path is indicated in Fig. 14 for the upper detector hodoscope. As shown in this figure, there is one PID board for each detector plane. The PID boards plug into feed-through boards which together with short Kapton cables, relay signals to and from the hybrids, through the vacuum bulkhead . Two analog output daisy-chains from each PID board are routed to the control room on shielded twisted-pair cable.

The purpose of the PID was to:

- fan out control and data signals to the hybrids;
- daisy chain the readout of the x- and y-view hybrids from each quadrant to produce two daisy-chains of 1792 channels per PID board (for a total of 24 daisy-chains);
- convert the single-ended SVX analog output signals to differential levels which are sent to the counting room via approximately 50 m of shielded twisted pair cables;
- mulitplex the digital data signals (strip number and chip number) from the SVX chips onto a bus common to all PID boards. Signals from any daisy-chain could be selected from the counting room for diagnostic purposes. (This bus is not shown in Fig. 14.)

The detector readout was triggered by a coincidence of scintillation counters, which detected particles produced at polar angles between 0.027 and 0.11 rad. The trigger was sensitive to approximately 45% of the total cross section and introduced minimal bias.

Synchronization with the beam crossing was accomplished by means of a signal from a directional coupler which sensed the beam passage. When live, the SRS generated a double-correlated sample and hold sequence for every beam bunch crossing (3.8 $\mu$sec). Upon receipt of a scintillator trigger, the SRS initiated and controlled the SVX readout.

We did not utilize the sparsification feature of the SVX since, in the short time available to us, we were not able to adequately evaluate its performance. We were particulary concerned that charge fluctuations at the inputs to the preamplifiers on time scales comparable to the readout cycle would result in common baseline shifts which would render the sparsification useless. Rather, we chose the CERN-designed SIROCCO II[5] (SIlicon ReadOut Camac COntroller) module for analog to digital conversion. This module features optional hit sparsification as well as common mode and pedestal subtraction. It contains a 10-bit flash ADC, and internal memory to store pedestals and pedestal subtracted pulse heights for up to 2048 channels. Twenty four of these modules were used (one for each daisy chain).

Readout to the host computer (MicroVAX II) was implemented using standard CAMAC and ROMULUS/REMUS modules. Silicon hit data together with pulse-height, pulse arrival time and scaler information from the scintillators were written to 8 mm tape cassettes using Exabyte tape drives.

Data was collected with full detector readout as well as under SIROCCO II sparsification. Approximately 1.4 million events were written in the full readout mode. The data acquisition rate was limited to approximately 3 Hz by the tape writing speed. The full event size was 172 kbytes.

For readout sparsification, the threshold was set at three times the average r.m.s. noise found in the two daisy-chained detectors for each SIROCCO II . Only channels passing the threshold were read out and written to tape. In order to monitor pedestal stability and common mode noise, 21 additional "monitor" channels (2% of the total), were always read out. Thresholds for hot channels were set such that those channels were never read out. The event size was typically 9 kbytes, and the acquisition rate was approximately equal to 35 Hz. About 5 million events have so far been collected in this mode.

# 6 Syst ı Performance & Data Anal .s

The silicon Microvertex detector was tested under high luminosity (typically $2 \times 10^{30} cm^{-2} s^{-1}$) collider operating conditions during the Fall 1990 run. The most important result obtained from run is that it is possible to cleanly and routinely run a silicon detector at a distance of 1.5 mm[1] (approximately 15 beam widthes) from the beam.

In more detail:

1. We saw no increase in scintillator counting rates as the pot window was brought from 5 cm to 1.5 mm, indicating that the beam scrapers which were positioned at 6 beam widthes were still effectively shadowing the detector assembly. We found however, that when positioning the window to a distance of 1.2 mm from the beam, we experienced an increase in scintillator counting rates of about a factor of two, which can be accounted for if aproximately one halo track per bunch crossing interacts in the aluminum shield. Thus, we chose to run regularly at the 1.5 mm distance.

2. We saw no evidence for run-to-run variations in the average vertical position of the beams and were thus able to set the detectors to the same position at the start of every Sp$\bar{p}$S fill. Preliminary analysis of reconstructed verticies shows that over the course of a run, the Sp$\bar{p}$S beams were steady to better than 100 $\mu$m.

3. Forty seven of the 48 detectors functioned properly when installed into the Roman Pots and subjected to vacuum. The back-plane of the one failed detector developed a short to ground. Two SVX chips (256 channels) of another detector failed during the run due to a power glitch. Of the remaining 46 detectors, 386 ( 1% of remaining channels) were unusable due to high noise levels caused mainly by defects in the silicon (e.g. holes in the $SiO_2$ layer resulting in shorts between a diode and its readout strip). Therefore, a total of 96.4% of the 43008-strip system was found to work.

4. Electronic effects, such as pedestal shifts, due to RF pickup of the passing beams was not seen.

5. Total detector leakage current decreased when the detector was put into vacuum and remained low during the course of the run. Typical total leakage currents varied between 1 and 20 $\mu$amps while in vacuum. This compares to values in the range of 100 to 200 $\mu$amps as measured on the test bench in air.

6. Strip noise showed no noticable increase during the course of the run, thus no significant radiation damage was observed. This is further illustrated by Fig. 15(a) which shows the rms noise levels in units of ADC channels of a typical detector as a function of channel number. The data for this plot were taken near the end of the collider run. Since the beam passes nearest to strip 896, the radiation dose from interactions increases with increasing strip number. The fact that the rms noise shows no corresponding increase indicates that no significant interaction-induced radiation damage had occurred.

7. Based on an event scan, the number of tracks coming from a sources outside the p$\bar{p}$ interaction region (e.g. "beam halo") was neglible.

8. The detectors and associated readout electronics displayed excellent signal to noise characteristics. The average cluster[2] pulse height distribution for a typical detector is plotted in Fig. 15(b) for all clusters with width less than four strips and (cross-hatched) all clusters with width equal two. The average of the uncut distribution is 94.5 ADC counts while the average of the cluster width equal two distribution is 74.9 ADC counts. Dividing

[1] The inner edge of the aluminum window was positioned at 1.5 mm. The edge of the sensitive region of the silicon was 3.0 mm from the beam.

[2] A cluster is defined as a contiguous series of strips each with a pulse height more than 4 times the rms noise and with total cluster pulse height more than 5 times the rms of all strips in the cluster

this last , .ue by the average rms noise shown in Fi. .5(a) of about 2.2 ADC counts gives an average signal to single channel noise of 34.0. (When no cut is made on cluster width, the average signal to single channel noise is 43.4 but there is evidence for significant contribution from hits originating from two nearby tracks.)

9. The distribution of cluster hit multiplicity in one typical detector is shown in Fig. 16(a). The average hit multiplicity per detector is 1.8. The distribution of hits as a function of strip number is shown in Fig. 16(b). The comparison of these and other distributions with Monte Carlo is under study.

10. Event dispays tend to be clean and contain few clusters which are not associated with tracks from a common vertex. Fig. 17 shows a relatively high multiplicity but otherwise typical event.

## 7 Conclusions

A large silicon system was assembled and operated at very short distance from the Sp$\bar{p}$S-collider beam, in the LSS5 high luminosity interaction region.

The detector performance was satisfactory with signal to noise ratios in the range 20 to 30, which allows an on-line pedestal subtraction and zero suppression with high efficiency.

The background due to beam halo particles, and the effect of RF induced signal from bunch crossing was found to be negligible.

The success of this test leads to the conclusion that a detector of this kind might be very effective in tagging beauty particles produced in the forward region in high energy hadronic collider, at the level of both on-line trigger and off-line analysis.

## References


[1] Proposal P238, Study of Beauty Physics at the SPS-Collider with Real-Time Use of Silicon Microvertex Information, CERN-SPSC/88-33;
P238Add.1, Measurement of $B_s$ Mixing, CERN-SPSC/89-43;
P238Add.2, Request For Collider Test of Silicon Microvertex Detector, CERN-SPSC/89-55;
P238Add.3, Further Comments on Collider Test of Silicon Microvertex Detector, CERN-SPSC/89-61.

[2] M. Caccia et al., NIM A260 (87)124.

[3] S.A. Kleinfelder et al., IEEE Trans. Nucl. Sci. 35 (1989) 171.

[4] F. Kirsten and C. Haber, IEEE Trans. Nucl. Sci. 37 (1990) 288.

[5] A. Lang and J.P. Vanuxem.

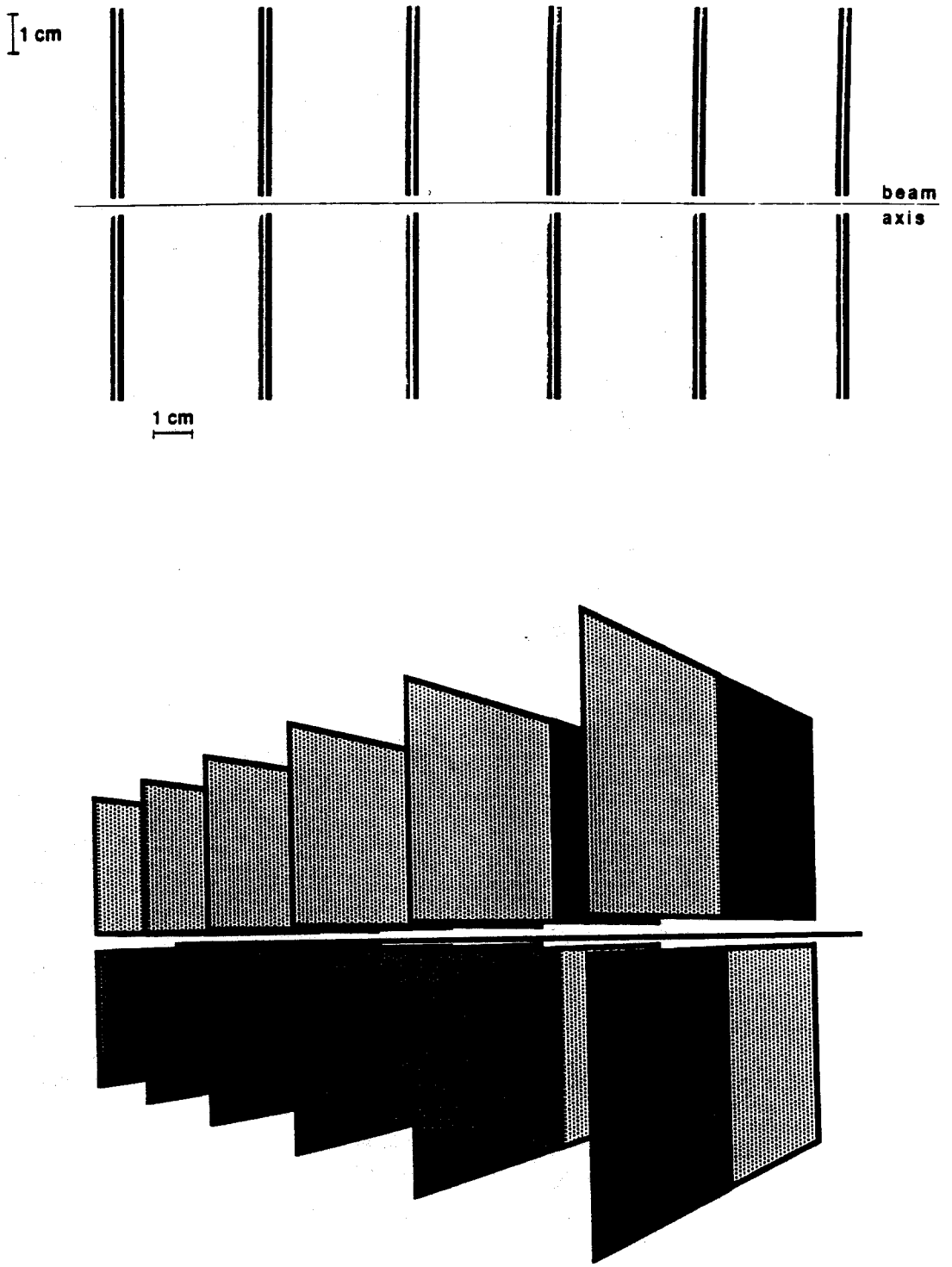


Figure 1: (a) Side view of the detector configuration. The black lines indicate the x-view detector positions and the gray lines indicate the y-view detector positions. (b) Perspective drawing of detector. Only four of the eight detectors in each plane are visible. The strip orientation of the hidden detectors is perpendicular to that of the detectors they face.

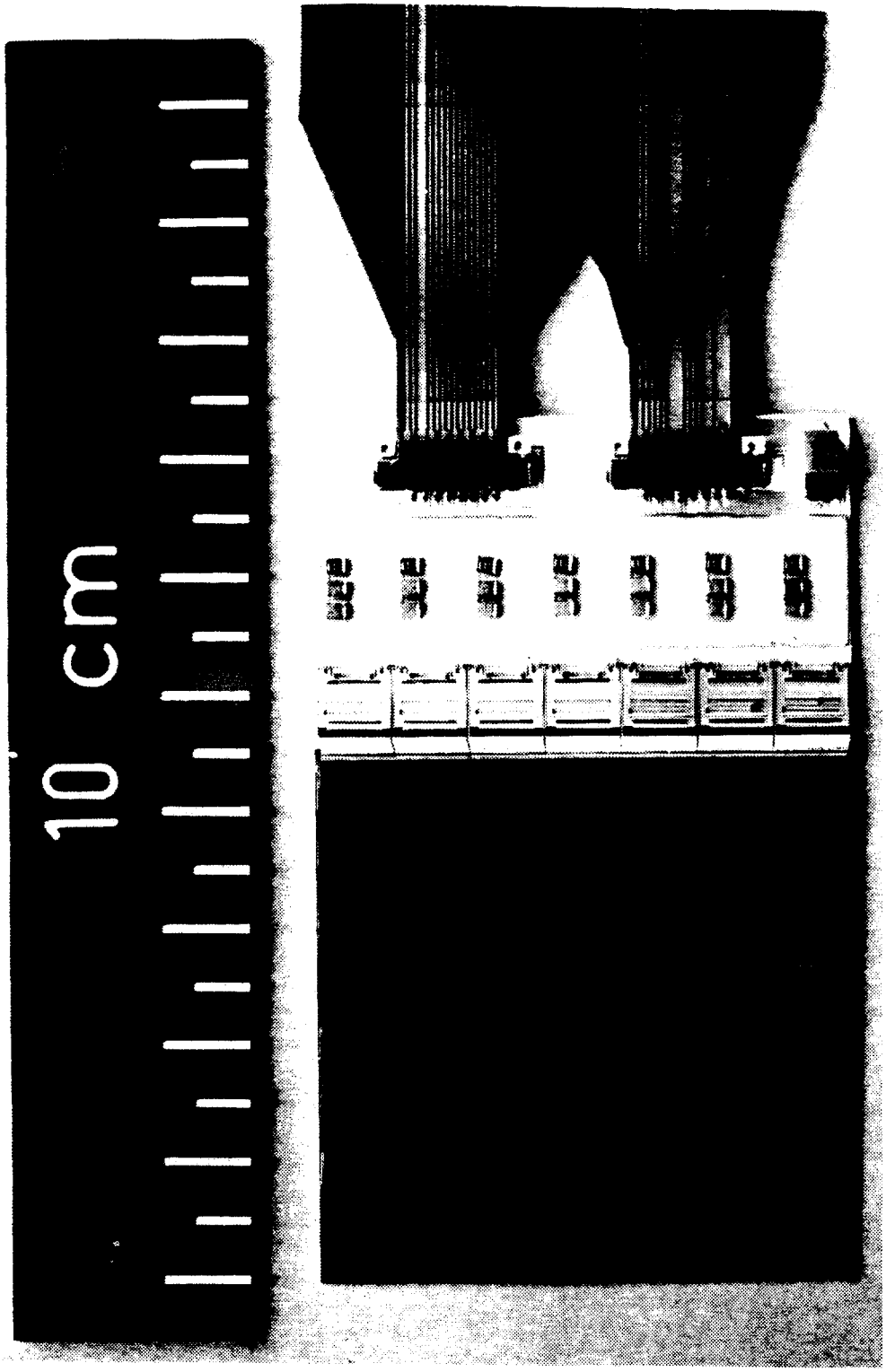


Figure 2: Photograph of a single silicon strip detector with its associated alumina hybrid and readout chips.

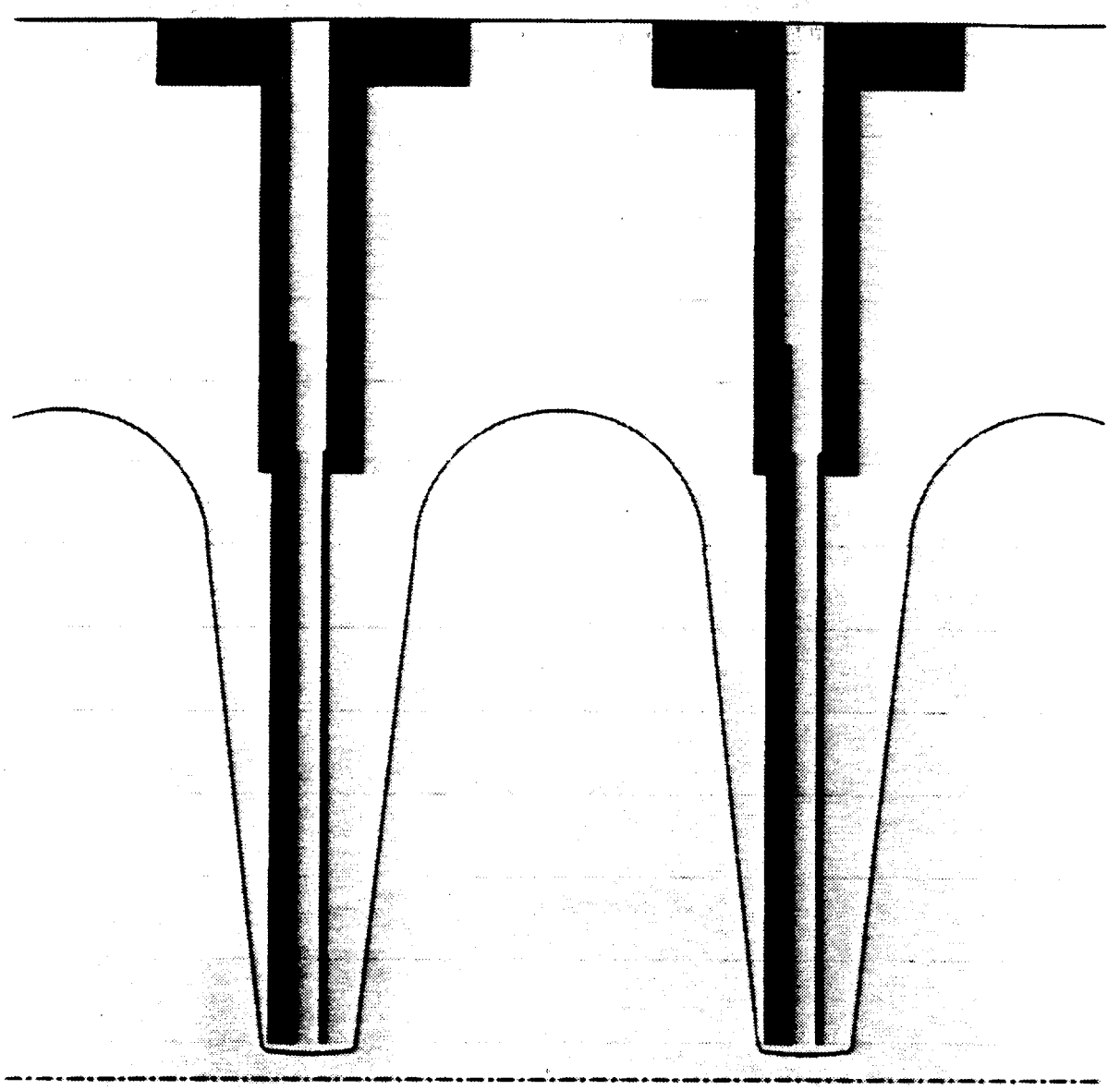

Figure 3: Side view showing two detector planes. The y-view detectors for each plane are on the left of the corresponding x-view detectors.

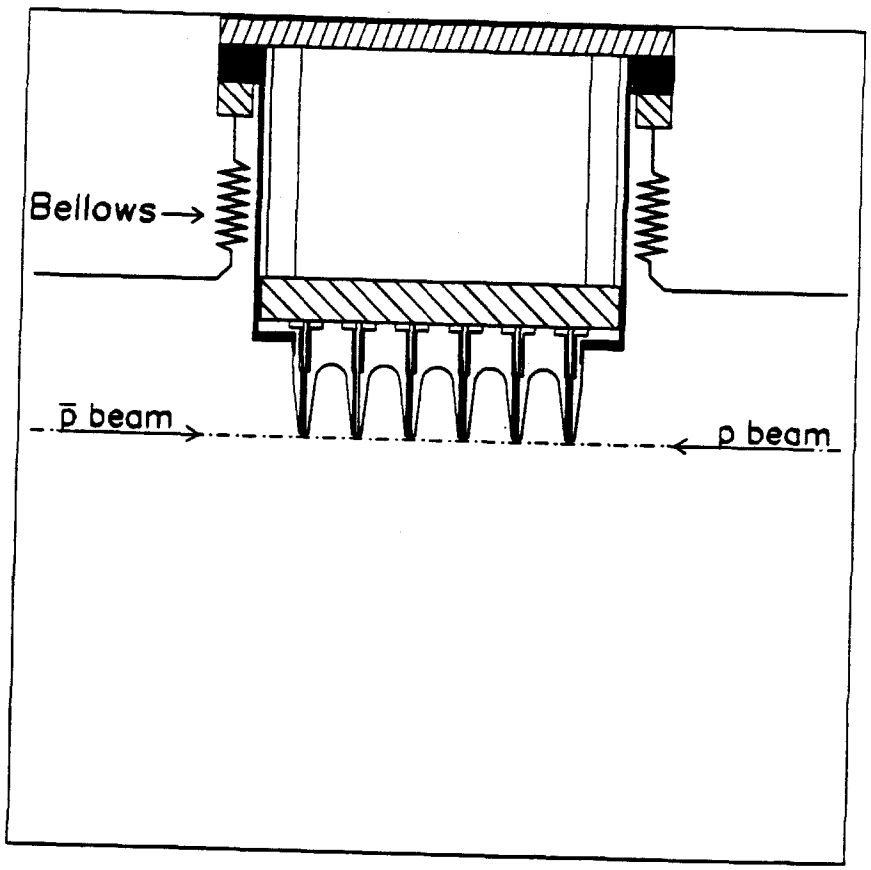


Figure 4: Sketch of the upper silicon half-detector mounted inside a Roman Pot. The bottom of the corrugated window is shown at a distance of 1.5 mm from the beam.

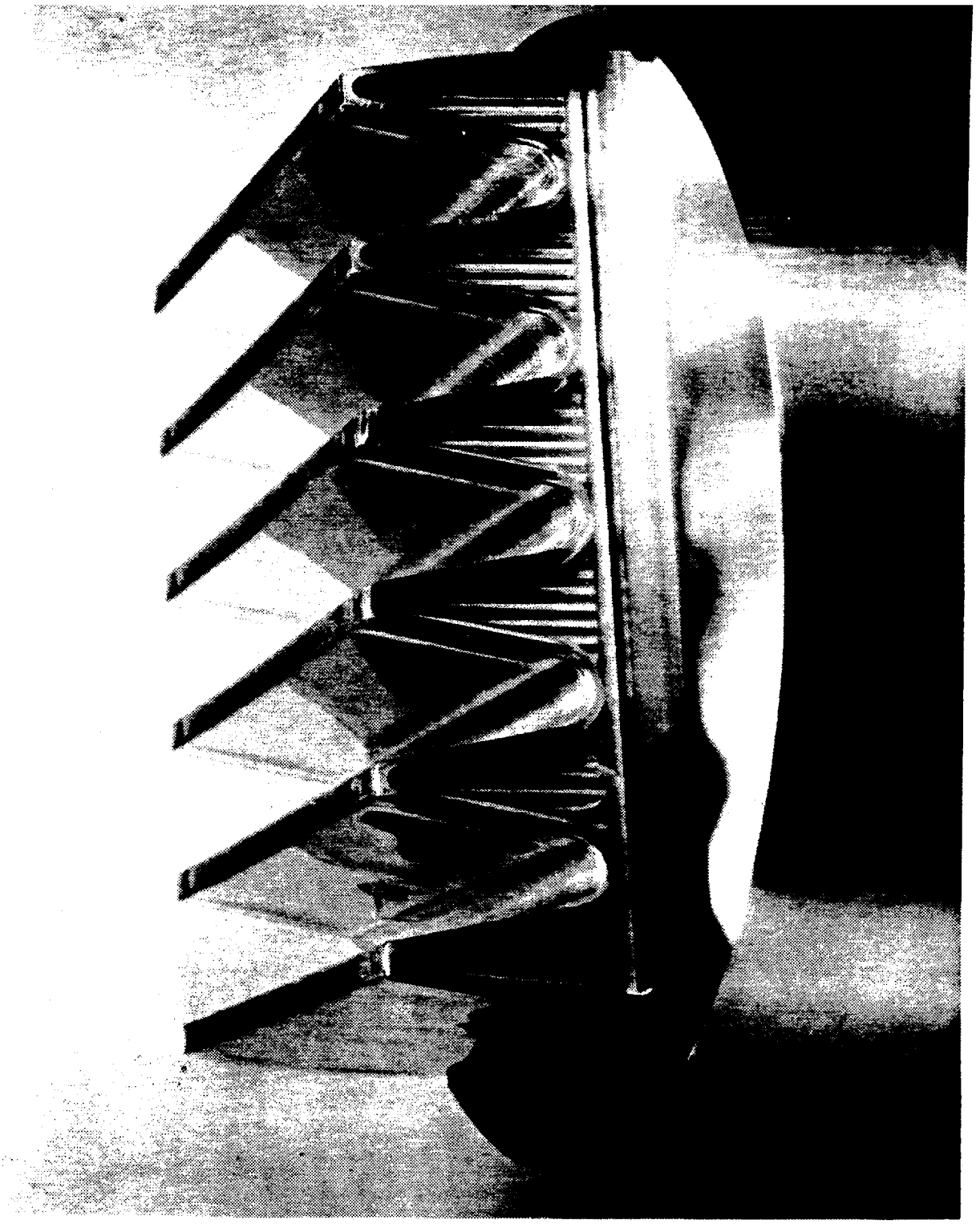

**Figure 9: Close up photograph of the corrugated window on the Roman Pot designed for this test.**

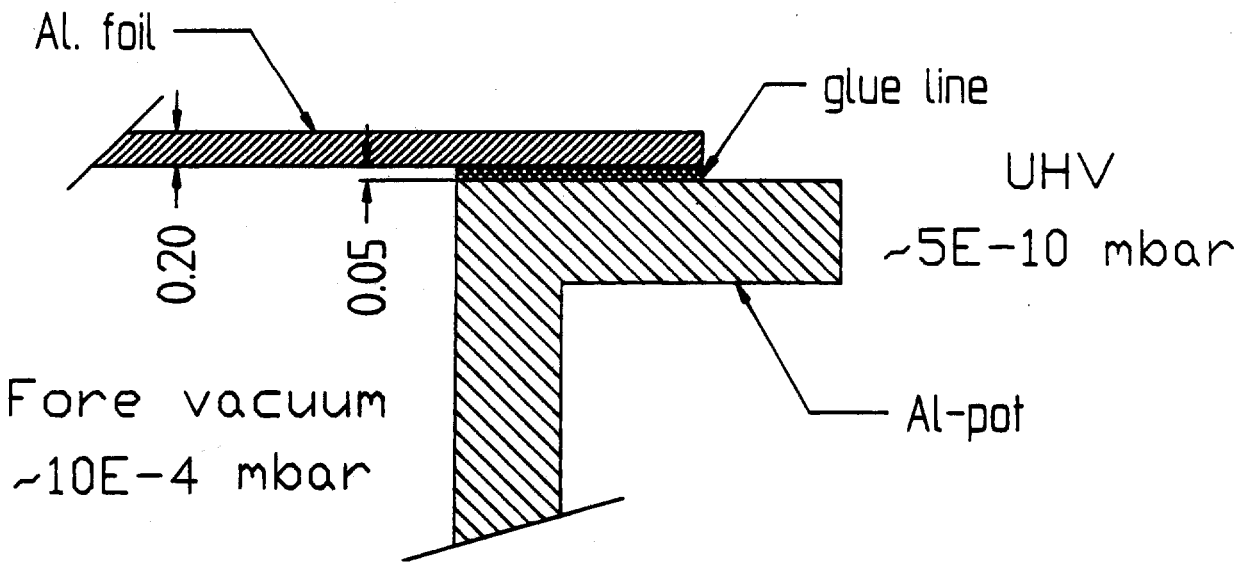


**Figure 10: Detail of the joint between the 200 $\mu$m window and the Roman Pot.**

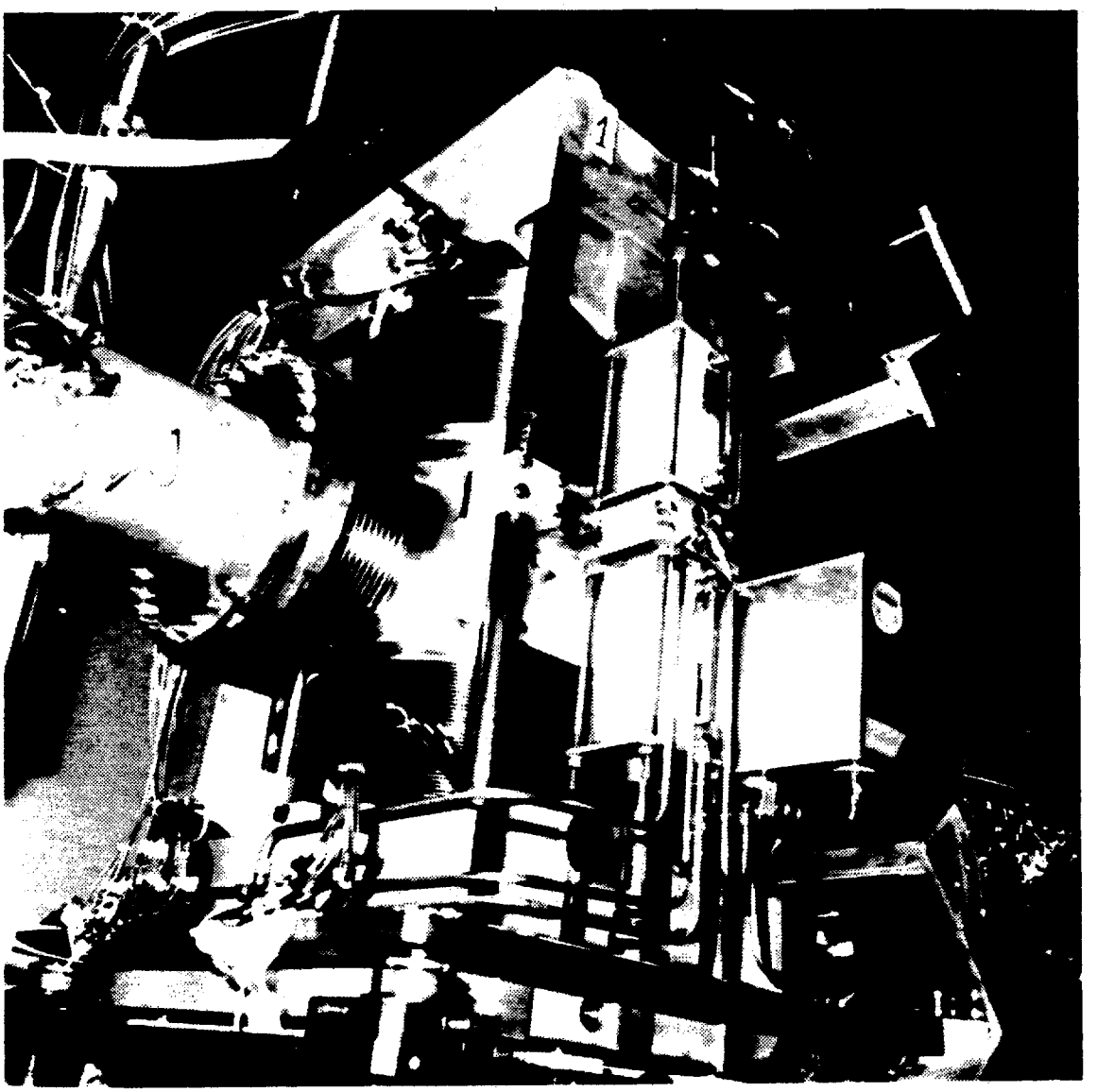

**Figure 11: Pot positioning mechanism, after installation in LSS5.**

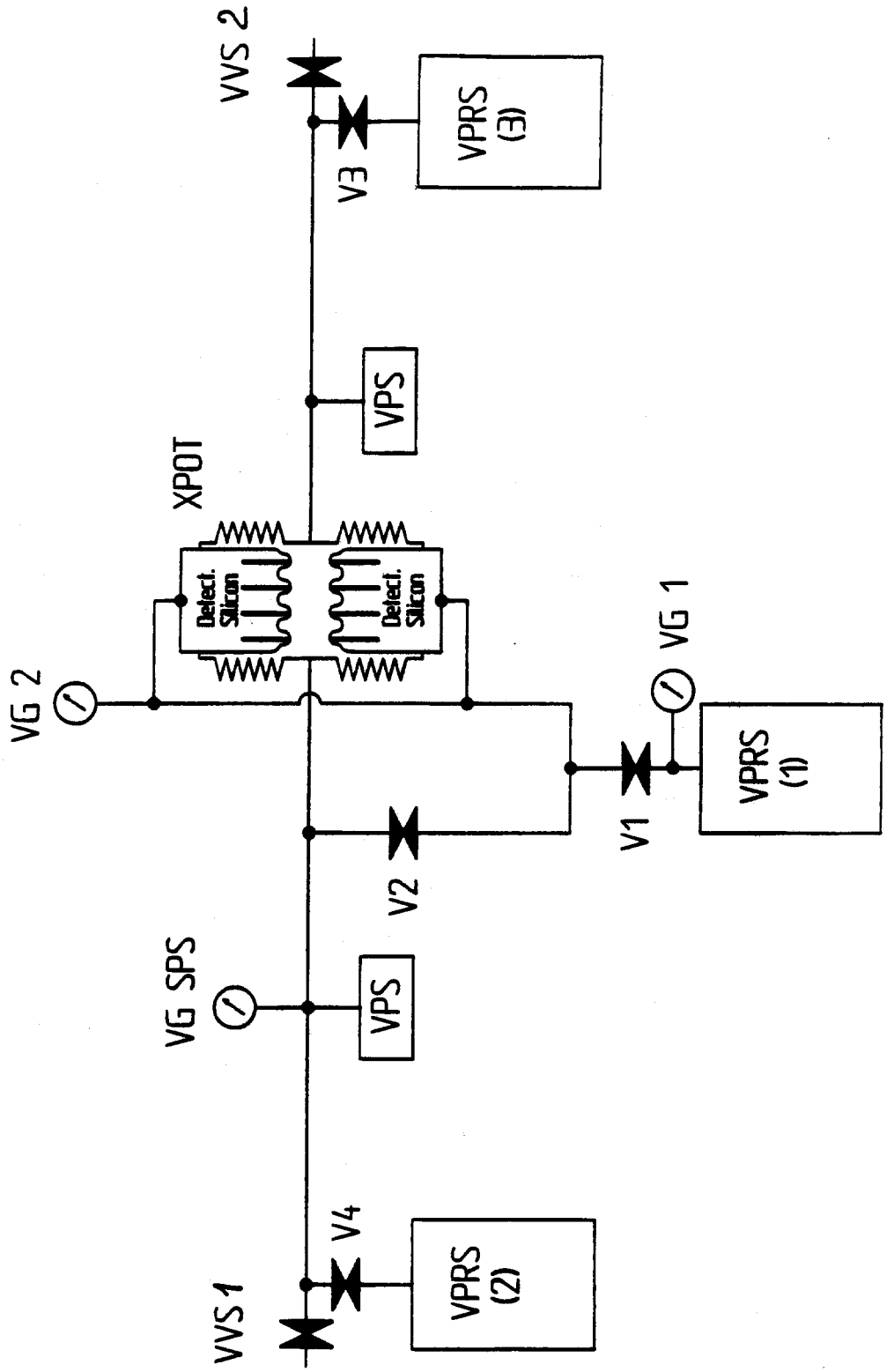


**Figure 12: Schematic layout of the vacuum pumping system.**

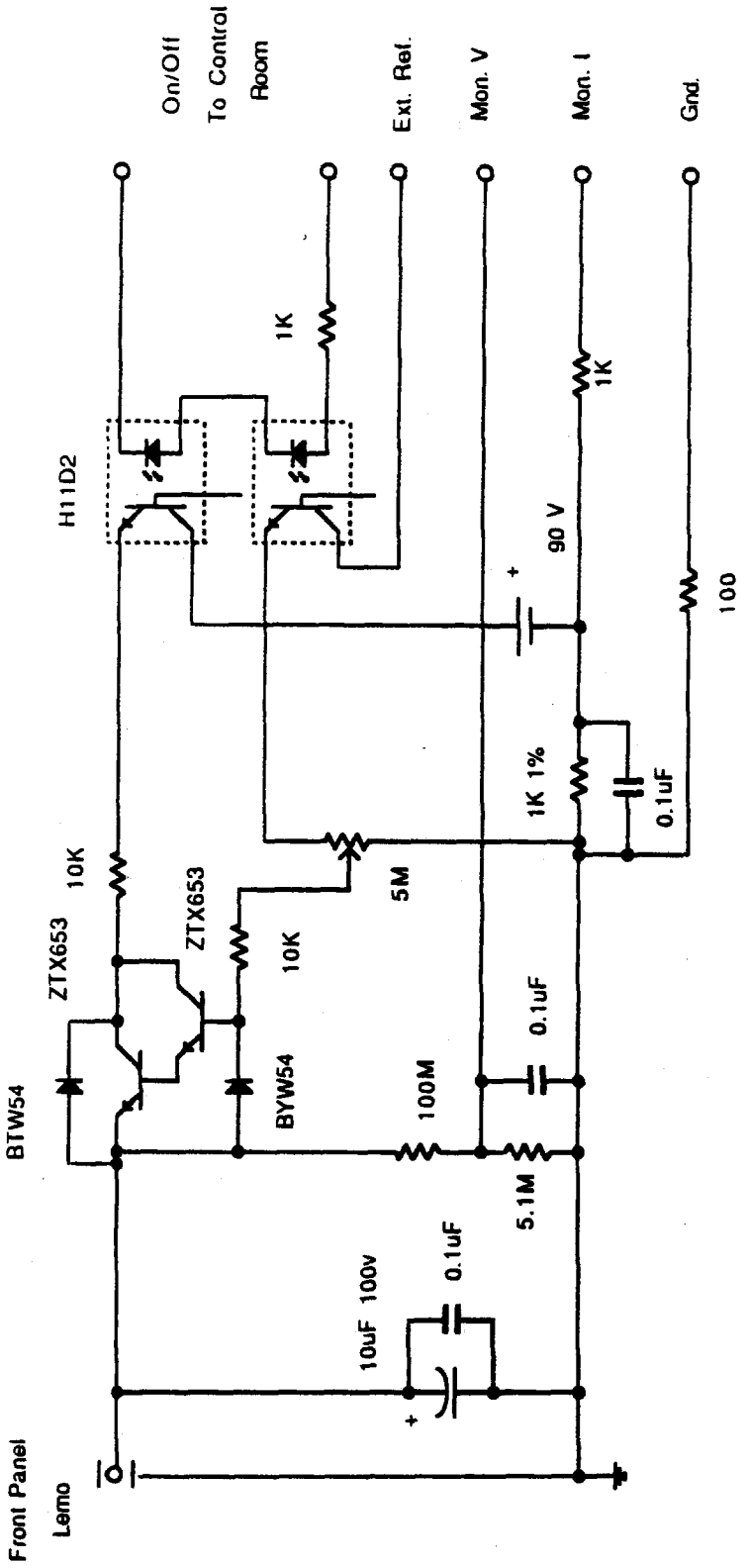


Figure 13: Power supply bias and control circuit.

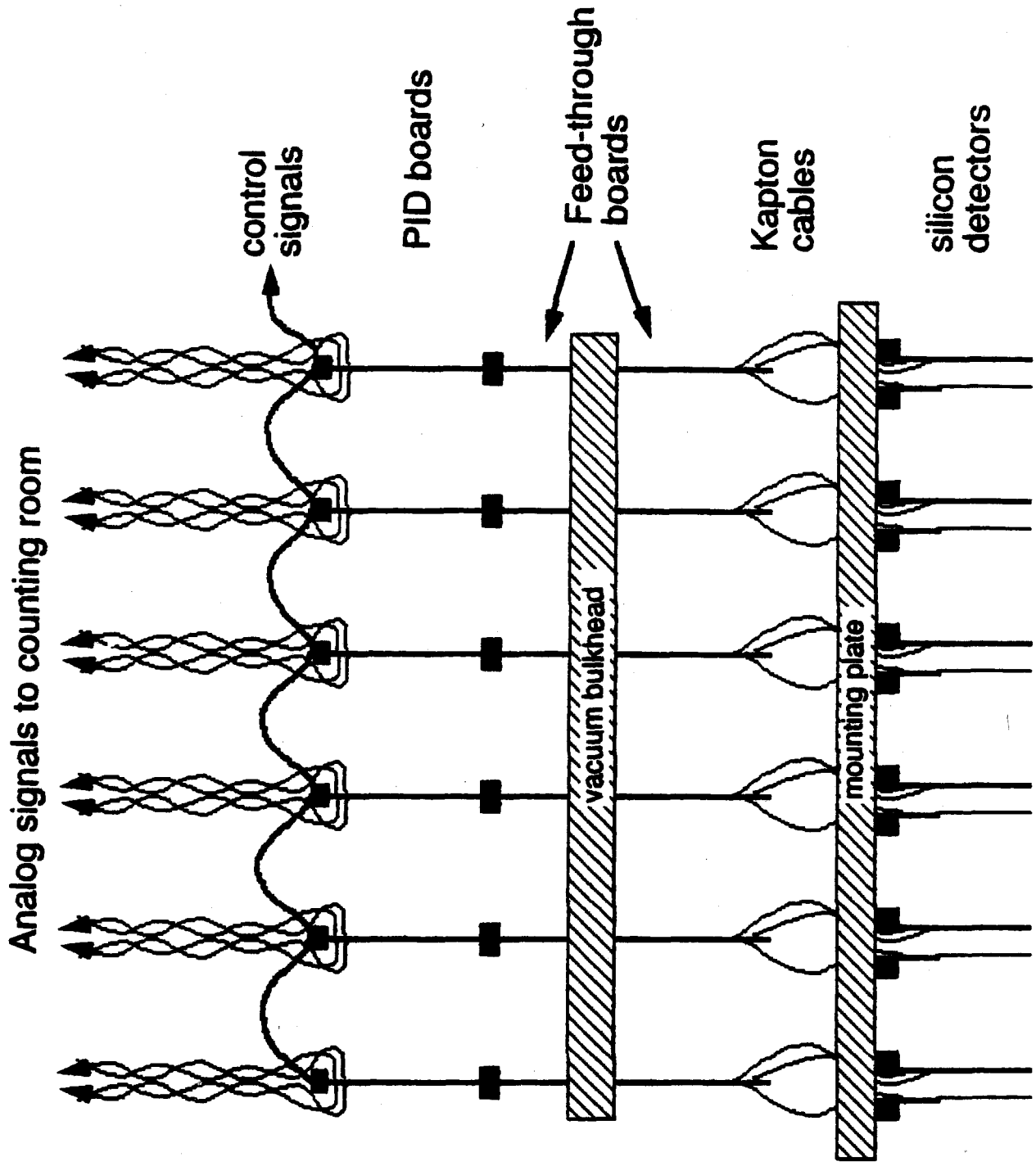


Figure 14: Schematic of readout and control pathes for one detector hodoscope.

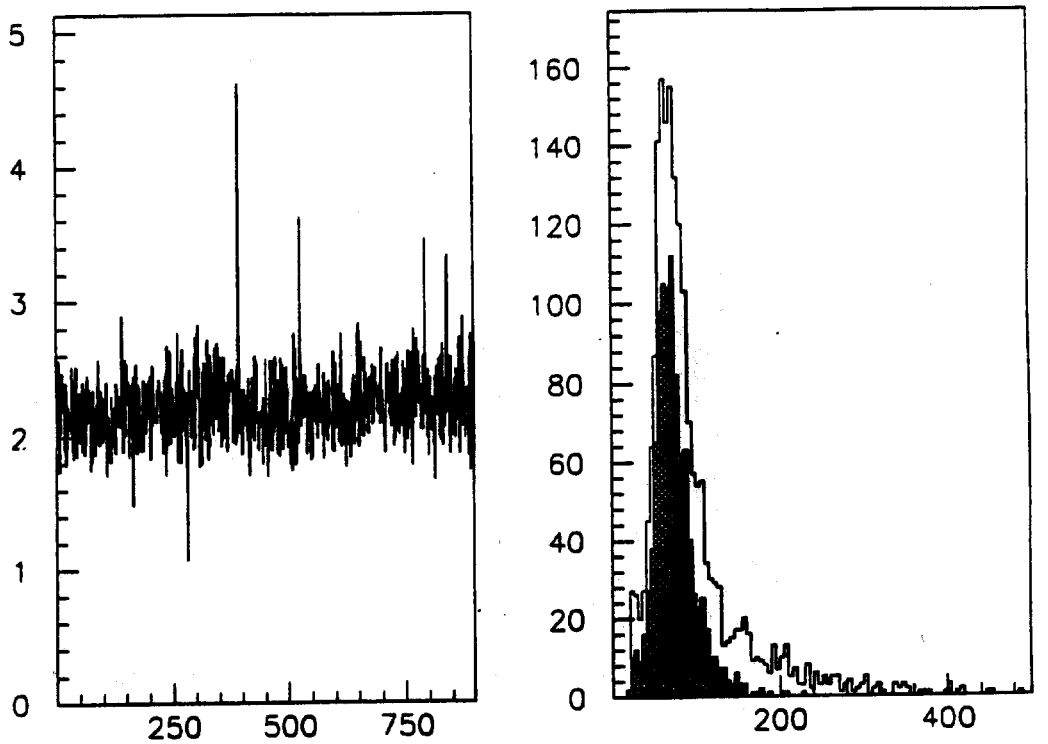


**Figure 15: (a) The rms noise of a typical detector plotted vs. channel number. (b) Cluster pulse height distributions. The unhatched histogram is for all clusters with width less than four strips. The hatched histogram is for all width=2 clusters.**

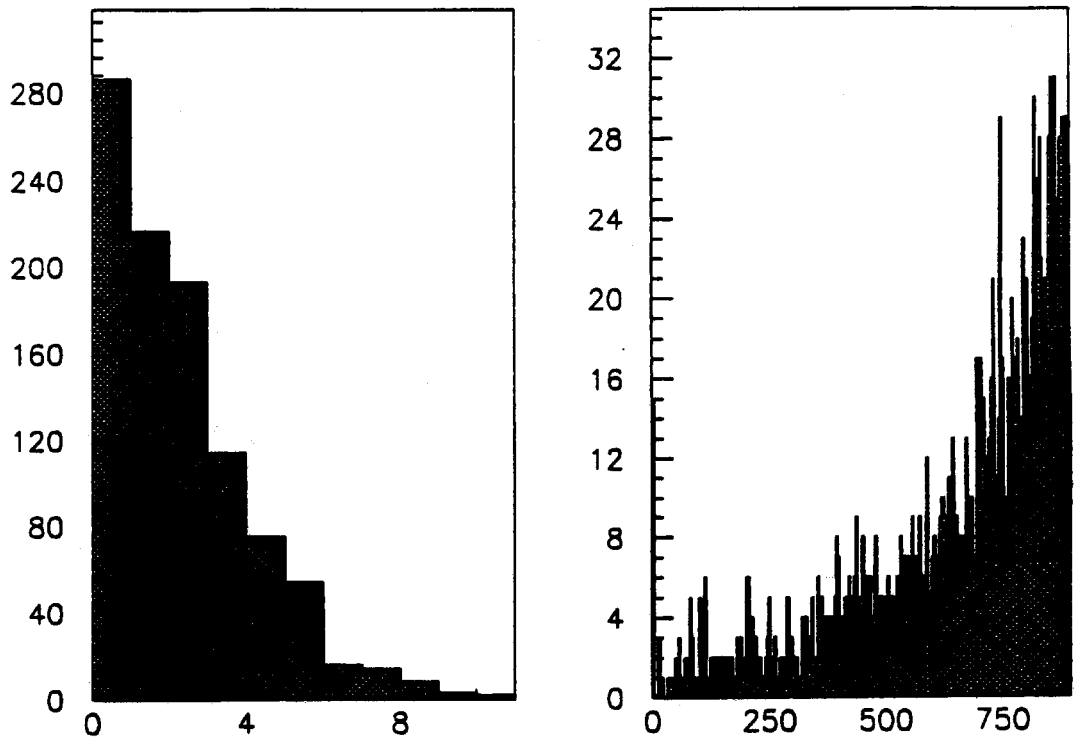


**Figure 16: (a) Hit multiplicity distribution on one detector. The average hit multiplicity is 1.8. (b) Hit distribution vs. channel number for a typical detector.**

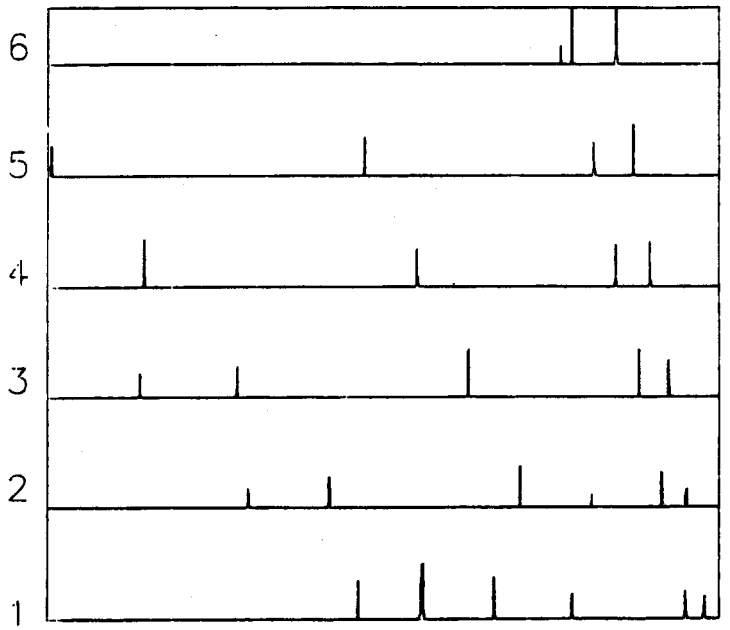


**Figure 17: Pulse height distribution vs.channel for the six planes of one detector quadrant for a single event. Only pulse heights greater than 4 times the rms noise are plotted.**